UNIVERSIDAD COMPLUTENSE DE MADRID
FACULTAD DE CIENCIAS FÍSICAS
Departamento de Física de la Tierra, Astronomía y Astrofísica II

TESIS DOCTORAL

A study of the X-ray and optical variability of the active galactic nucleus ESO 362-G18: from days to years

Estudio de la variabilidad del núcleo galáctico activo ESO 362-G18 en las bandas óptica y de rayos X: escalas de tiempo desde días a años

MEMORIA PARA OPTAR AL GRADO DE DOCTOR

PRESENTADA POR

Beatriz Agís González

Director

Giovanni Miniutti

Madrid, 2017

UNIVERSIDAD
COMPLUTENSE
MADRID

Doctoral Thesis

A study of the X-ray and optical variability of the active galactic nucleus ESO 362-G18: from days to years

Estudio de la variabilidad del núcleo galáctico activo ESO 362-G18 en las bandas óptica y de rayos X: escalas de tiempo desde días a años

Author:	*Supervisor:*
Beatriz Agís González	Dr. Giovanni Miniutti

A thesis submitted in fulfilment of the requirements
for the degree of Astrophysics in the

Departamento de Física de la Tierra, Astronomía y Astrofísica II
(Facultad de Ciencias Físicas, UCM)
Centro de Astrobiología
(CSIC-INTA)

CENTRO DE ASTROBIOLOGÍA
ASOCIADO AL NASA ASTROBIOLOGY INSTITUTE
CSIC INTA

Madrid, November 2016

A Beni, mi estrella.
A mis padres, que me indican el camino tal cual la Vía Láctea.
A Buum, mi mejor compañero de viaje.

Agradecimientos

Tienes entre tus manos lo que un día fue un sueño, aunque en los últimos años haya adquirido ápices de verdadera pesadilla infernal. Hoy la pesadilla se ha terminado y el sueño se ha cumplido. En estos momentos el enorme cansancio no me permite disfrutar de toda la felicidad que esto conlleva, pero espera a que pasen un par días, ¡no cabré en mí de tanta felicidad! También sé que ese mismo cansancio no me va a permitir expresar todo lo que me gustaría hacia las muchísimas personas que me han ayudado a superar los baches para llegar hasta aquí y han conseguido que el camino fuese más agradable. Lo voy a intentar con el corazón.

Hay dos personas que siempre han estado ahí desde el principio de forma incesante: mis padres. No solo sois un ejemplo a seguir de fortaleza y superación sino que también sois el apoyo incondicional que cualquiera desea tener. Nunca jamás me habéis negado vuestro apoyo y amor incondicionales a pesar de que mis pasos se iban alejando cada vez más de casa. Gracias por cuidarme y por hacerme como soy, con mis defectos y mis virtudes, sois mi vida. Os quiero de manera infinita

Ana, crecer sin ti no hubiese sido lo mismo. Risas, juegos, enfados, diversión incansable de hermanas, peleas que acababan siempre en abrazos ... Gracias por cuidarme y quererme tanto. Y gracias también a ti, Benja. Eres el cuñi ideal y estoy orgullosa de tenerte entre la familia.

Sin duda, hay una persona que sin saberlo ha marcado profundamente mi vida: Beni. Hace ya 20 años que te fuiste, pero nunca, nunca dejarás de estar presente ni un sólo día. Lo único que tengo que hacer para coger fuerzas en momentos difíles es pensar en ti. No hay palabras que puedan describirte, tus niveles de bondad y superación superan cualquier límite imaginable. Ójala hubiese podido compartir más tiempo contigo, ójala el destino no fuese como fue, hubiese hecho cualquier cosa. Eres y siempre serás mi estrella.

Tía Isabel, tú también mereces mi admiración congelada. Beni tenía a quién parecerse. Tu templanza ante la vida es la más admirable que he visto nunca. Gracias por ese espíritu de lucha incansable.

A mi segunda mamá, Ade, y a mis dos otras hermanas, Cris y Pati. Sois mi familia, no pude ser más féliz a vuestro lado junto con Carlos y Pepe. Os quiero muchísimo.

A mi familia en general, tíos y primos, tengo que agradecerle todo el cariño que me brindan. No tenemos una relación extremadamente estrecha pero los lazos familiares son muy especiales.

Ne, mi amiga del alma. Desde que íbamos al cole agarradas de la mano, pasando por los “walkie talkies”, el insti, nuestra casa juntas... hasta hoy en día. No puedo ser más afortunada de tenerte. No solo por estar siempre que lo necesito o porque puedas entenderme sin más que mirarme a la cara, sino por ser una fuente inagotable de alegría constante y positivismo capaz de contagiar a cualquiera. Te quiero a más no poder.

Ro, ahora estás lejos, pero no me olvido de mi pareja. Son muchos años reina, y los que nos quedan... Gracias por ser como eres.

Sin duda alguna, gracias a mi director de tesis, Giovanni. Por darme la oportunidad de poder empezar este trabajo. Por transmitirme y contagiarme tu pasión por los AGNs. Por todo lo que me has enseñado a largo de estos años. Y sobre todo, por ayudarme a llegar al final.

Tampoco puede faltar aquí otra persona fundamental en mi día a día: Benja. Sigo preguntándome qué hubiese hecho yo sin tu apoyo diario, sin tus ánimos y sin tus cuidados. Gracias por tus largas clases de MIDAS, Dipso, espectroscopía y cualquier cosa. Porque para cualquier pregunta me ayudas a buscar una respuesta, da igual que tratemos de estrellas, AGNs, polarimertría, barcos o la vida misma. Te voy a echar mucho de menos en Liège.

Resumen de la tesis en castellano

El modelo unificado de los núcleos galácticos activos (AGN, por sus siglas en inglés), establecido hace 30 años, ha sido clave para esclarecer la complicada taxonomía de esta clase de objetos tan heterogénea. Su base se fundamenta en la existencia de una estructura toroidal, compuesta por gas y polvo, capaz de absorber la emisión central del AGN y que rodea el agujero negro supermasivo (SMBH, por sus siglas en inglés) y el disco de acreción, de modo que la diversidad observada simplemente refleja diferentes ángulos de visión de una geometría con simetría axial . Consecuentemente, en los AGNs tipo 1 tenemos una visión directa del material próximo al SMBH, es decir movíendose a gran velocidad, lo que permite que surjan líneas anchas de emission en los espectros ópticos/UV. Por el contrario, los AGNs tipo 2 son observados desde una línea de visión (LOS, por sus siglas en inglés) que permite interceptar el toro, bloqueando y absorbiendo la región de las líneas anchas. Este esquema se consolidó con el descubrimiento de líneas anchas de emisión polarizadas (PBLs, por sus siglas en inglés) en AGNs tipo 2. Es decir, aunque no podemos verlas en luz directa, los AGNs tipo 2 también presentan líneas anchas en luz polarizada, confirmando una naturaleza común entre ambos tipos de objetos.

Hoy en día, existen claros indicios observacionales que no concuerdan con las predicciones, como por ejemplo la estructura del toro. El modelo unificado establece un toro homogéneo e uniforme. Sin embargo a partir de diversos estudios, sobre todo en longitudes de ondas infrarrojas, se obtienen evidencias de que esta estructura es más bien grumosa.

Precisamente, el principal objetivo de esta tesis es avalar la necesidad de un toroide más complejo desde las bandas óptica y de rayos X. Para ello, nos centraremos en estudiar la variabilidad de absorción de una interesante galaxia Seyfert: ESO 362-G18. Esta fuente merece toda nuestra atención debido a su intrigante comportamiento: usualmente se clasifica como Seyfert tipo 1, sin embargo, se ha recuperado un espectro contenido en el catálogo 6dfGS que no muestra líneas anchas, es decir, un espectro tipo 2. Estos extraños AGNs clasificables en ambos tipos representan una violación del esquema unificado estándar y constituyen una prueba más de que un modelo dependiente en exclusiva del ángulo que forma nuestra LOS con el eje de simetría del AGN es insuficiente. Con el fin de ahondar más en la naturaleza de estos objetos claves, y a la vez poco frecuentes, decidimos emprender un profundo estudio multi-longitud de onda que nos permitiese obtener diferentes visiones complementarias.

Debido a que se ya conocía que ESO 362-G18 también era un potencial candidato para presentar variabilidad en rayos X, decidimos llevar a cabo un seguimiento multi-época en estas longitudes de onda (9 observaciones tomadas con distintos satélites: *Swift*, *XMM-Newton*, *Suzaku* y *Chandra*) para determinar sus cambios espectrales y de flujo en escalas temporales desde días a años. Las observaciones de mayor calidad nos permitieron descomponer su complejo espectro de rayos X, hallando entre sus componentes espectrales una reflexión relativista originada en las regiones más internas del disco de acreción. Por lo tanto la forma espectral de esta componente se verá distorsionada con los fuertes efectos gravitatorios causados por el SMBH. Analizar estas distorsiones nos permitirá obtener valiosos datos acerca del agujero. Concretamente fuimos capaces de medir un “spin” $a \geqslant 0.92$ al 99.99% de nivel de confianza, lo que implica que ESO 362-G18 presenta un SMBH de máxima rotación, y un índice de emisividad de $q = 4.3^{+0.8}_{-0.6}$, lo que sugiere que la fuente primaria de emisión de rayos X (concocida como corona de rayos X) es compacta y se concentra en las zonas centrales del disco de acreción. Por otro lado, ya que las distorsiones relativistas dependen del ángulo de inclinación del sistema, derivamos $i = 53° \pm 5°$. Este valor relativamente alto de la inclinación se corrobora a través de estimaciones asumiendo condiciones viriales a través la establecida relación entre la masa del SMBH y la velocidad de dispersión estelar, lo que confiere un soporte independiente a nuestra intepretación de reflexión relativista de la forma espectral de ESO 362-G18.

Por otro lado, también fuimos capaces de medir un retraso temporal entre el contínuo primario y el contínuo reflejado. Este retraso de la luz emitida en dos regiones diferentes, la emisión primaria que tiene lugar en la corona de rayos X y la emisión reprocesada o reflejada por el disco acreción, puede traducirse en la distancia que separa esas misma regiones. De este modo, obtenemos que una distancia de separación entre la corona de rayos X y el dsico de acreción de $\sim$ 7 radios gravitacionales y confirmamos nuevamente de un modo independiente del modelado espectral, la detección de refelxiíon relativista.

Dada la alta inclinación obtenida lo más probable es que nuestra LOS esté interceptando las parte superior del toro (cuyo ángulo típico de abertura es $\sim 45°$), de modo que su supuesta grumosidad podrá explicar los cambios de estado (de tipo 1 a tipo 2 en solo 1 año y 8 meses) encontrados en ESO 362-G18. De hecho, en nuestro estudio multi-época en rayos X probamos que una de la observaciones es absorbida por una una nube polvorienta perteneciente al toro que cubre por completo la fuente y aumenta la densidad de columna $\sim$ 2 órdenes de magnitud en un tiempo menor que 2 meses. Este evento nos permite confirmar una vez más la naturaleza compacta de las regiones emisioras de rayos X dentro de 50 radios gravitacionales, como ya habíamos derivado del modelado de la reflexión relativista.

Durante otro seguimiento con el telescopio espacial *Swift* (36 observaciones a lo largo de 2 meses), pudimos detectar otro evento de absorción en ESO 362-G18, pero esta vez de forma mucho más detallada, siguiendo su progresión desde practicamente el inicio del “eclipse” hasta el final. Gracias a ello derivamos con mejor precisión el tamaño de la región emisora de rayos X (que resulta ser un poco menor de 50 radios gravitaciones, entre 17 y 33) y las propiedades de la nube absorbente, demostrando una vez más la naturaleza dinámica de la absorción en rayos X.

Nuestro estudio de ESO 362-G18 prosigue en la banda óptica analizando 4 espectros de baja resolución, dos de ellosmostrando líneas anchas, y dos donde esas líneas anchas desaparecen, lo que confirma que ESO 362-G18 es ciertamente una galaxia Seyfert "changing-look", concretamente con espectros de tipo 1.5 y 1.9. Ya que en nuestro detallado estudio en rayos X no detectamos cambios significativos en la actividad nuclear (la correspondiente luminosidad es estable a lo largo de cinco aõns), concluimos que estos cambios en los espectros ópticos vienen dados por estructuras absorbentes del toro presentes en nuestra LOS hacia la región de líneas anchas presentes cuando la fuente muestra sus espectros 1.9. También discutiremos que es altamente improbable que estas estructuras sean exactamente las mismas que las detectadas en rayos X.

Además, nunca antes se había llevado a cabo un estudio en luz polarizada una galaxia Seyfert "changing-look", a pesar del potencial de este tipo de medidas para entender la geometría de las distribuciones de gas y polvo presentes alrededor del núcleo de los AGN.

Como un análisis independiente y paralelo a ESO 362-G18 que todavía contínua en desarrollo, nos proponemos investigar las capacidades de la herramienta matemática PCA (del inglés, "Principal Component Analysis") para determinar las componentes espectrales de los AGNs a través de un método que no requiera aplicar modelos establecidos. La PCA no solo puede proporcionarnos información acerca de la variabilidad espectral en general, sino también datos acerca de los cambios de flujo medido así como mostrar sensibilidad ante eventos de absorción. Las herramientas desarrolladas a partir de este trabajo serán aplicadas en futuros ánalisis para complementar la tradicional metodología usada en rayos X, fundamentada principalmente en espectroscopía y análisis temporales.

Abstract

The standard Unified Model (UM) of Active Galactic Nuclei, established 30 years ago, has been key to shed light in the taxonomy of such a heterogenous class of objects. Its basic premise is the ubiquitous presence of an obscuring torus around the central engine, so that the observed diversity simply reflects different viewing angles of an axisymmetric geometry. Consequently, type 1 AGNs are observed with a direct view of fast moving material close to the super massive black hole (SMBH), resulting in broad emission lines in their optical/UV spectra, while type-2 AGNs are observed from a more edge-on view, intercepting the obscuring torus that blocks the broad emission line region (BLR) component from our line of sight (LOS). This scheme was consolidated with the discovery of polarized broad emission lines (PBLs), also known as hidden broad-line regions (HBLRs), in the type 2 AGN, hence presenting the same properties as type 1 nuclei in polarized light.

Nowadays, additional ingredients are likely needed to account for some observational facts that are apparently in conflict with the predictions. For instance, the UM predicts the absorbing torus as an homogeneous and uniform structure. There is broad evidence, especially at infrared wavelengths, that the dusty torus is indeed clumpy instead uniform.

The general goal of this thesis is to endorse the current evidence for the clumplyness of the key element of the standard UM from other wavelengths: X-rays, UV and optical. To this end, we will focus on the study of the absorption variability performed by an interesting Seyfert galaxy: ESO 362-G18. This source gets our whole attention because it is usually classified as a type 1 AGN, however a spectrum retrieved from the 6 degree Galaxy Survey (6dFGS) shows the optical spectrum of ESO 362-G18 to lack its broad emission lines. This type 2 spectrum suggests ESO 362-G18 to be a changing look Seyfert galaxy. This rare type of sources represents a violation of the UM and probes that its corresponding classification is not only angle-dependent. Thus, we decided to start a deep multi-wavelength analysis of ESO 362-G18 to get as many complementary views as possible and approach the intriguing nature of this source.

Since this target was known to exhibit a potential X-ray variability, as a first step we decided to carried out a multi-epoch X-ray monitoring (9 observations performed with *Swift*, *XMM-Newton*, *Suzaku* and *Chandra* satellites) to assess its X-ray flux and spectral variability on timescales of months to years. The high-quality observations allow us to decompose the complex X-ray spectrum of ESO 362-G18 into its different components finding among them a X-ray relativistic reflection originated in the innermost regions of the accretion disc. Then, its spectral shape will be distorted by the gravitational effects of the SMBH, what allow us to get a valuable information about the central engine analyzing these distortions. Particularly , we measure a black hole spin $a \geqslant 0.92$ at the 99.99% confidence level, which implies that the SMBH powering ESO 362-G18 is a nearly maximally rotating Kerr black hole. The disc-reflection

emissivity profile is steep, with $q = 4.3^{+0.8}_{-0.6}$, suggesting that the primary source of X-rays (the so called X-ray corona) is compact and centrally concentrated. On the other hand, the inclination between the disc axis and our LOS is measured to be 53° ± 5° via disc reflection modeling of the X-ray spectra. Such high inclination is further supported by different estimates based on virial assumptions as well as on the relationship between black hole mass and stellar velocity dispersion of the SMBH, providing independent support for the disc reflection interpretation of the spectral features seen in the X-ray spectrum.

We also detect a time delay between the primary continuum and the reflected one which may be used to infer the light-crossing distance between the primary X-rays emitting site (the X-ray corona) and the reprocessing site (the inner disc). Thus, we infer that the reprocessing site is located at distances of the order of ~ 7 gravitational radii from the X-ray continuum source (the corona). This strongly supports and confirms beautifully and independently (no spectral modeling is performed to derived the time delays) the presence of relativistic reflection again.

On the other hand, the derived high inclination is consistent with the idea that our LOS is grazing the obscuring torus (which has a typical half-opening angle of the order of 45° or so). If the torus is not homogeneous but clumpy, such high inclination may intercept from time to time some of the clumps of the upper layers of the obscuring torus possibly explaining why ESO 362-G18 exhibits changes of look from type 1 to type 2 in its optical spectra taken only 1 year and 8 months apart. In fact, one observation of our multi-epoch analysis is consistent with be absorbed by a dusty clump belonging to the torus, which increases the column density in approximately two orders of magnitude in timescales lower than two months. This occultation also get us enable to confirm that the X-ray emitting region (comprising both X-ray continuum and soft excess) come from within about 50 gravitational radii from the black hole, supporting the compact nature of the X-ray emission in AGN, conclusion also inferred from the relativistic reflection component.

Such occultation event was not isolated, but a *Swift* monitoring campaign of our target over 2 months, comprising 36 pointed observations, reveals another eclipse event that this time we could follow almost from ingress to egress. This allowed us to infer with good accuracy all the relevant properties of both the X-ray emitting regions (that resulted to be slightly more compact than the upper limit of 50 gravitational radii derived in the multi-epoch analysis) and of the cloud responsible for the eclipse confirming the dynamic and clumpy nature of the X-ray absorbers towards ESO 362-G18.

Our analysis of ESO 362-G18 also includes four low-resolution long slit optical spectra which show the source exhibiting broad Balmer lines in two of the four observations, while these broad lines disappear in the two remaining spectra leading to a changing look classification for the source, between Seyfert 1.5 and Seyfert 1.9. The minimum observed timescale for a change of look is 1 year and 8 months. We do not see any evidence for dramatic changes in the nuclear activity (this is also demonstrated by the stability of the X-ray intrinsic luminosity over few years), so that the most natural explanation for the change of look is that intervening dusty absorbing structures are present into our LOS towards the broad line region at the epochs when the source exhibits a Seyfert 1.9 optical spectrum. Wi will probe that it is unlikely that we are observing exactly the same intervening structures in the optical and X-rays.

Besides, no polarimetric observations of changing look AGN have been performed to date despite the obvious potential of this kind of measurements in the context of understanding the circumnuclear geometry and gas/dust distribution. We will present here the first analysis of a changing look nuclei in optical polarized light.

As a parallel and independent work, which is still in progress, we are exploiting the mathematical tool of the Principal Component Analysis (PCA) as a model-independent way to assess spectral components in the AGN X-ray spectrum. This technique can be used to study not only the X-ray spectral variability in general, but also its flux-dependence as well as its sensitivity to subtle absorption events. The tools developed here will use in the near future for complementing the more traditional X-ray data analysis performed from spectroscopy and timing analysis.

Contents

List of Figures

List of Tables

Acronyms

6dF Six-degree Field. 46, 105–107, 109, 110, 113–117, 121, 122

6dFGS Six-degree Field Galaxy Survey. 103–106, 110

ACIS Advanced Charged Couple Imaging Spectrometer. 55

ADAF advection dominated accretion flow. 23

AGN active galactic nucleus. 1–3, 5, 8, 9, 11–17, 19–22, 24–31, 33, 34, 36, 37, 41, 43–47, 49, 58, 64, 65, 71, 72, 77, 78, 80–83, 85, 89, 99, 101–106, 110, 112–114, 116, 118, 123, 125–127, 130, 131, 133, 134, 137–139, 142, 152, 156, 159, 161, 162, 166, 168, 169, 172–175, 177, 178, 182, 184, 186, 190

ASCA Advance Satellite for Cosmology and Astrophysics. 5, 6

ATHENA+ Advanced Telescope for High ENergy Astrophysics. 6

BAT Burst Alert Telescope. 57

BeppoSAX Beppo X-ray Astronomy Satellite. 5, 6

BI back illuminated. 55

BLR broad line region. 9, 15, 20, 21, 25–27, 29, 38, 44–46, 49, 71, 72, 75–77, 79, 81, 82, 102, 103, 107, 113, 118, 120, 121, 123, 125, 126, 132, 133, 137–140, 142, 143, 169, 174

BLRG broad-line radio galaxy. 12

CCD charge-coupled device. 5, 52, 53, 55, 57, 109, 148, 151, 152, 155, 167

DDT director discretional time. 105, 116

dof degrees of freedom. 62, 64, 66, 68, 89, 90, 92

EFOSC2 ESO Faint Object Spectrograph and Camera v.2. 105, 114–116, 120–122, 144, 167, 169

EMMI ESO Multi-Mode Instrument. 46, 105, 109, 110, 112, 113, 116, 118, 120–123

ENLR extended narrow line region. 50

EPIC European Photon Imaging Camera. 52, 53, 57

ESA European Space Agency. 5, 6, 52

ESO European Southern Observatory. 104, 110, 114, 116, 144, 148, 167

EUV extreme ultraviolet. 2

EW equivalent width. 109

EXOSAT European X-ray Observatory Satellite. 5

FI front illuminated. 55

FORS2 **FO**cal **R**educer and low dispersion **S**pectrograph v.2. 103, 105, 116–118, 120–123, 143, 148, 152, 154–156, 167–169, 171, 174

FOV field of view. 57, 156, 158, 167

FWHM full-width at half maximum. 8–10, 20, 26, 52, 55, 71, 107, 109, 112, 114, 116, 118

GRB gamma-ray burst. 57, 58

HBLR hidden broad line region. 9, 27–29, 127, 175

HETGS High Energy Transmission Grating Spectrometer. 55

HRC High Resolution Camera. 55

HXD Hard X-ray Detector. 55, 60

IFU Integral Field Unit. 105, 110, 122, 123

IR infrared. 21, 23, 24, 41

ISM interstellar medium. 131, 150, 156–159, 161, 162, 164, 166, 169

JAXA Japan Aerospace Exploration Agency. 55

LETGS Low Energy Transmission Grating Spectrometer. 55

LEV log-eigenvalue. 180, 181

LINER Low ionization nuclear emission region. 12

LOS line of view. 9, 11, 27, 32, 33, 38, 44–46, 50, 65, 72, 75, 78–81, 97, 99, 101, 104, 106, 112, 125–127, 131, 132, 134–143, 156, 158, 159, 169, 172–174

MOS Metal Oxide Semi-conductor. 52, 53, 57

NASA National Aeronautics and Space Administration. 6, 57

NHBLR non-hidden broad line region. 9

NIR near infrared. 8

NLR narrow line region. 26, 27, 29, 46, 107, 109, 110, 112, 113, 120, 123, 126

NLRG narrrow-line radio galaxy. 12

NLS1 narrow line Seyfert 1. 185

NTT New Technology Telescope. 46, 71, 109, 167

OM Optical Monitor. 52, 54, 75

OVV optically violent variable. 13

p degree of polarization. 130–133, 136, 137, 140–142, 144, 146–148, 151–156, 158, 159, 161–164, 166–169

PA position angle. 126, 144, 161, 169

PBL polarized broad emission line. 27, 29, 125–127, 133, 137, 139, 142

PC principal component. 178, 181–190

PCA principal component analysis. 48, 174, 177–185, 187–190

PPA polarization position angle. 126, 130–132, 135–137, 141, 142, 144, 146–148, 151–156, 158, 159, 161–164, 166, 167, 169, 174

PSF point spread function. 52

QSO quasi-stellar object. 2, 12, 138

RGS Reflection Grating Spectrometer. 52, 53, 59, 64

RIAF radiation inefficient accretion flow. 23, 29

RXTE Rossi X-ray Timing Explorer. 82

SED spectral energy distribution. 25, 30

SMBH super massive black hole. 2, 3, 6–8, 11, 19, 20, 22–27, 29, 31, 38, 41, 44, 45, 48, 102–104, 175

SN signal-to-noise. 51, 105, 106, 110, 146, 163, 164

SNR signal to noise ratio. 180

SVD Singular Value Decomposition. 179

Sy1 Seyfert 1. 11, 24, 28–31, 33, 35–37, 41, 47, 79, 100, 112, 126, 127, 131–133, 136–140, 142–144, 162, 166, 169, 174, 177

Sy1.5 Seyfert 1.5. 103, 105, 106, 122, 123, 143, 162, 167–169, 173, 174

Sy1.9 Seyfert 1.9. 105, 121, 122, 167–169, 173, 174

Sy2 Seyfert 2. 11, 12, 27–31, 33, 35, 36, 47, 103, 105–107, 121, 125–127, 131–133, 137–139, 142, 175

UM unified model. 23, 27, 28, 30, 31, 37, 45–48, 104, 125, 134

UV ultraviolet. 2, 8, 13, 14, 20–22, 24, 26, 27, 30, 31, 41, 43–45, 47, 54, 57, 75, 76, 79, 80, 82, 83, 94–97, 99, 100, 102–104, 122, 126, 148

UVOT Ultraviolet-Optical Telescope. 57, 58, 75, 82, 94, 102, 122

VLT Very Large Telescope. 143, 148, 154, 167, 171, 174

XIS X-ray Imaging Spectrometer. 55

XRS X-ray Spectrometer. 56

XRT X-ray Telescope. 57, 58, 82, 83, 86, 88

Physical Constants

Electron mass $m_e = 9.10938356 \times 10^{-31}\ kg$

Gravitational constant $G = 6.6742799 \times 10^{-11}\ m^3 kg^{-1} s^{-2}$

Hubble constant $h_0 = 100\ km\ s^{-1} Mpc^{-1}$

Proton mass $m_p = 1.6726219 \times 10^{-27}\ kg = 1836.15\ m_e$

Solar Mass $M_\odot = 1.9891001 \times 10^{30}\ kg$

Solar luminosoty $L_\odot = 3.846 \times 10^{33}\ erg\ s^{-1}$

Speed of Light $c = 2.997\,924\,58 \times 10^{8}\ m\ s^{-1}$

Symbols

a	black hole spin	dimensionless, between 0 and 1
b	galatic latitude	degrees
i	inclination	degrees
p	degree of polarization	%
q	emissivity index	dimensionless
N_H	column density	cm^{-2}
Γ	photon index	dimensionless
ξ	ionization parameter	$erg\ cm\ s^{-1}$

Chapter 1

Introduction

1.1 Brief history and basic concepts about active galactic nuclei

In 1909, E. A. Fath observed, without knowing, the first active galactic nucleus (AGN) at the Lick Observatory. One of the major questions at that time was about the nature of 'spiral nebulae', mainly if those were relatively nearby gaseous objects similar to the Orion nebula, or on the contrary, very distant collections of unresolved stars. Fath tried to test the claim that spirals show a continuous spectrum consistent with a collection of stars, rather than the bright line spectrum characteristic of gaseous nebulae. However in the case of NGC 1068, he observed that the spectrum was composite, showing both bright emission and absorption lines (Fath, 1909). The six bright emission lines were similar to those seen in the spectra of gaseous nebulae. During the following years, several astronomers reported the presence of nuclear emission lines in the spectra of spiral nebulae. For instance, Hubble (1923) discovered two more spirals with star-like nuclei showing a planetary nebula-type spectrum: NGC 4051, and NGC 4151. Thus, the first notably distinct observational characteristic of AGN was the presence of emission lines with widths upwards of $10^3\ km \cdot s^{-1}$ and far in excess of any known class of objects. Nevertheless, the systematic study of galaxies with nuclear emission did not begin until the work by Seyfert (1943), who selected a group of six galaxies with star-like appearing cores to analyze their spectra: NGC 1068, NGC 1275, NGC 3516, NGC 4051, NGC 4151 and NGC 7469. All of them were dominated by high-excitation nuclear emission lines and the two brightest ones, NGC 1068 and NGC 4151, showed all the stronger emission lines typically seen in planetary nebulae. In addition, Seyfert (1943) also noticed that some galaxies showed broad emission lines, while others exhibit only narrow ones. Now, galaxies with high-excitation nuclear emission lines are known as *Seyfert Galaxies* in his honor. The nature of this strong nuclear emission remained a mystery. A proposed explanation was that a large number of stars would produce the observed features.

However, AGNs did not become a focus of interest for astronomers until the development of radio astronomy in the early 1950s with the first radio surveys of the sky: the third Cambridge (3C) catalog (Edge et al., 1959) and its revision 3CR catalog (Bennett, 1962). Allan Sandage of the Mount Wilson and Palomar Observatories and Maarten Schmidt of the California Institute of Technology (Caltech) initiated the search for optical identifications and redshifts of radio galaxies. In 1960, Sandage observed 3C 48 which looked like a 16 mag stellar object with a faint nebulosity on normal photographs. However, its spectra were very confusing exhibiting broad emission lines at unfamiliar wavelengths while its photometry showed the object to be variable and to have an excess of ultraviolet emission. Several other apparently star-like images coincident with radio sources were found to show broad emission lines. Thus, the terms quasi-stellar radio sources (QSRS), quasi-stellar sources (QSS), quasi-stellar objects (QSOs) or quasars were coined, being 3C 48 the first of its class. The true breakthrough in understanding these amazing objects came with Schmidt (1963) and their study of the source 3C 273. They realized that the emission lines seen in the spectrum of this source were actually the hydrogen Balmer-series emission lines and Mgɪɪ λ2798 at the uncommonly large redshift of $z = 0.158$: the strange objects with stellar appearance become distant and bright galaxies. The 3C 48 spectrum was explained with a redshift of $z = 0.37$ and the mystery of the spectrum of quasars was solved. AGNs properties were recognized in the incoming years. Cosmological redshift of QSOs was accepted by the astronomical community (Greenstein & Schmidt, 1964) and the parallel between Seyfert galaxies and quasars suggested a common physical nature. Simultaneously, the idea that the observed concentration of the emission within the central 100 pc of these galaxies would require a mass of $\sim 10^8 M_\odot$ was first presented (Woltjer, 1959). This idea evolved into the possible explanation that in the center of AGNs could lie a black hole which would emit mainly by accretion processes of a surrounding disc of gas (Salpeter, 1964).

Nowadays, the term AGN involves some the most powerful continuous sources of luminosity in the Universe which cannot be attributed directly to normal stellar processes. Such a high luminosity is produced in a very concentrated volume, specifically on sub-parsec scales. Their luminosity is in the range of $10^{40} - 10^{47} erg \cdot s^{-1}$ Fabian (1999), i.e. more than a hundred billion times more powerful than the Sun, and emerging from an unresolved source. Their luminosity is comparable, and can even exceed, to that of their own host galaxies. This prodigious radiation means that active galaxies can be seen over huge distance and are among the most distant objects that have ever been detected. Their emission is spread widely across the whole electromagnetic spectrum, from *gamma*-rays to sub-mm, often peaking in the ultraviolet (UV) or extreme ultraviolet (EUV), but with significant luminosity in the X-ray and infrared bands. This fact separates active galaxies from normal galaxies, as normal galaxies emit most of their energy as a thermal blackbody curve due to stars and glowing gas.

Although there is still much to clarify in the field of AGNs, the most accepted explanation for such release of energy is that it is produced by accretion onto a super massive black hole

(SMBH) (Kormendy, 1988). Since the outward force of radiation pressure must be counterbalanced by the inward forced of gravity, high luminosities imply high masses, otherwise the object will disintegrate (Peterson, 1997). As a result, AGNs must present very high mass density, and it has long been assumed that they consist of a SMBH, whose mass is $> 10^5 M_\odot$, accreting gas and dust at the center of a galaxy (Netzer, 2015). Hence, the deep gravitational potential of the black hole is responsible for the radiatively efficient accretion leading to the extremely high luminosities as well as for the dynamical broadening of the observed lines.

Moreover, the power output of AGN is often variable on timescales of years and sometimes on timescales of days, hours, or even minutes. An object that varies rapidly in time t must be smaller than the light-crossing time of the object, ct (where c is the speed of light) and therefore must be spatially small, otherwise the variation would appear smoothed Fabian (1999). Thus, a SMBH explain not only the large energy output, but also the small size of the emitting regions and the associated short variability timescales of AGN. Within this picture, AGN field of research is currently open to study the physics involved in the accretion phenomenon, to observe and explain their emission throughout their whole electromagnetic spectrum and unravel the distribution in space, the origin, the evolution and the fate of these thrilling objects.

In particular, the X-ray domain has suffered an enormous evolution over recent decades, and is currently one of the key energy ranges for the study the AGN. The more energetic is the radiation coming from the AGN, the closer to the central engine it is emitted, so that X-rays are a tool to probe the vicinity of the SMBH. A great part of this dissertation is focused in X-ray analysis of AGN.

1.2 Beyond the atmosphere: satellites and birth of X-ray astronomy

In late 1895, the german physics Wilhelm Röntgen discovered X-rays quite by accident, while he was analyzing the violet fluorescence of cathode rays. It all began with the experiments of another british scientist, William Crookes, who studied the effects of applying electrical discharges to some gases. Crookes carried out his tests inside vacuum tubes implemented with electrodes, known as *Crookes tubes*. However, he did not go ahead with his experiments. Röntgen carried on investigating these effects and realized that when one of his tubes was placed about 1 meter away for the photographic plate, a green colored fluorescent light could be seen over the screen even when the tube was covered with a black cardboard to filter out any visible light. This strange event led him to deeply analyze what appeared like a new type of radiation, very penetrating but invisible, that he called radiation “X” or unknown. On 22th December 1985, Röntgen asked his wife, Berta, to place her hand over the photographic plate of his improved

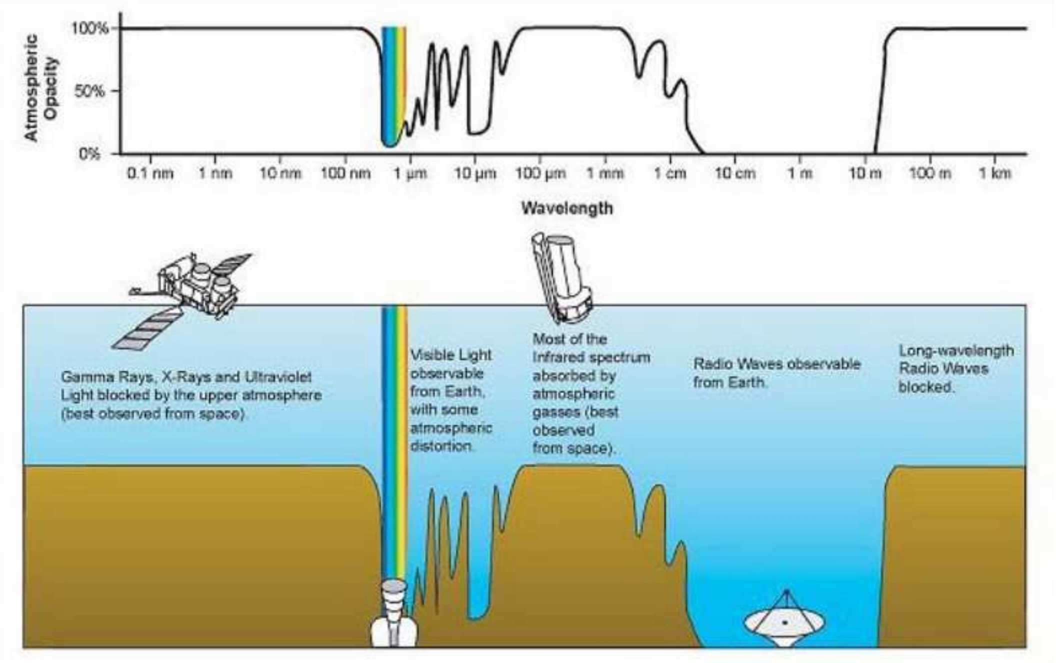

FIGURE 1.1: Electromagnetic opacity of atmosphere. Image credit:
http://gsp.humboldt.edu/olm_2015/Courses/GSP_216_Online/images/atmo-abs.jpg

and upgraded device that needed a person to be handled. By developing the plate, a historic image for science had appeared: the bones of Berta's hand with a ring in her finger, the first radiography of human body. The discovery spread quickly throughout the world and X-rays started to be of very important application in medical and other sciences. Röntgen was awarded the first ever Nobel Prize for Physics in 1901.

Much later, thanks to Röntgen, Riccardo Giacconi would became known as "the father of X-ray astronomy" because of his work whose fruit was nothing more, nothing less, than the discovery of the first cosmic X-ray source. The advance of X-ray astronomy was a challenging task due to a problem of big dimensions: our atmosphere. We can live in our planet because the atmosphere is protecting us from potentially damaging radiation, including of course X-rays. The atmospheric electromagnetic opacity (see fig. 1.1) makes it impossible to detect X-rays from ground-based instruments: it is necessary to fly detectors at high altitudes, for instance using balloons or rockets. X-ray astronomy was born with the launch of the first rocket by the US Naval Research Laboratory in 1948 which allowed the first detection of X-rays coming from the Sun. The following modest rocket supplied with a X-ray detector and launched by the group of Giacconi et al. (1962) at the American Science and Engineering cracked the atmosphere for a few minutes but made possible the detection of extrasolar X-rays for first time: it was the discovery of Scorpius X-1, an X-ray binary which is the strongest apparent source of X-rays in the sky.

A significant breakthrough came with the launch of the *Uhuru* satellite in 1970 (Giacconi et al., 1971), which provided astronomers with the first X-ray catalog of 339 objects detected in the 2-6 keV energy band. The predominant fraction of these sources were found to be compact, mass-exchange, i.e. X-ray binaries, but 15 AGN were also detected. Because of his pioneering contributions to astrophysics Riccardo Giacconi was awarded the Nobel Prize for Physics in 2002.

Through the 1970s, the *Ariel V* satellite established Seyfert galaxies as another class of X-ray objects. The field progressed rapidly, with detectors having larger collecting area, increased spectral coverage and improved spectral resolution in order to give birth to the first true orbiting X-ray telescope, the *Einstein Observatory* (Giacconi et al., 1979): it utilized a concentric array of grazing incidence mirrors to focus keV photons onto its focal plane detector. It revolutionized X-ray astronomy thanks to its capability to create images of extended objects and diffuse emission to detect faint sources. The resulting images vastly improved spatial localization of objects in the sky and the sensitivity experienced a turning point since source and celestial background could be effectively separated. At this point, improved results were pushing more advances in the instrumentation and this feedback remains still today.

By 1980, X-ray astronomy was a major branch of astronomy. The best was yet to come: the European X-ray Observatory Satellite (EXOSAT), Röntgen Satellite (ROSAT), Advance Satellite for Cosmology and Astrophysics (ASCA), and Beppo X-ray Astronomy Satellite (BeppoSAX) satellites would define a new era for X-ray astronomy, providing crucial tests of general relativity and demonstrating that we still knew so little about the contents, structure, physics and evolution of the universe. The X-ray bandwidth, far more energetic than visible light, is about seven times wider in terms of energy range (visible light has a frequency of about 10^{15} Hz while X-rays cover from 10^{16} to 10^{20} Hz). So, one instrument or one satellite cannot cover the entire X-ray regime. EXOSAT, launched by European Space Agency (ESA) in 1983, zoomed on the higher-energy part of the X-ray spectrum and made 1780 observations of a wide variety of objects, including AGN, stellar coronae, cataclysmic variables, white dwarfs, X-ray binaries, clusters of galaxies, and supernova remnants (Taylor et al., 1981). The known X-ray universe was growing. ROSAT, led by German Aerospace Center and launched in 1990, was the first imaging telescope at low X-ray energies to provide high-quality images, improving on those from *Einstein Observatory* (Truemper, 1982). ROSAT expanded the number of known X-ray sources to 125000 and proved to be especially valuable in investigating the gas present between stars and galaxies. *Astro-D*, commonly known as ASCA was launched in 1993 and complemented the ROSAT's imaging capability with spectral observations of X-rays sources of higher energy (Tanaka et al., 1994). ASCA was the first one to employ the so-called *nested gold-coated foil mirrors*, that greatly improved X-ray photon collecting efficiency, and the first mission to use charge-coupled device (CCD), becoming both standard technologies for future missions. It was the first X-ray mission to combine imaging capability with broad band pass, good spectral resolution and a large effective area in order to find the first evidence of the gravitational redshift due to the strong gravitational field around a black hole, the 'broad iron K line'. In 1996, anothe X-ray observatory with Italian-Dutch collaboration was launched: BeppoSAX, working in the broadest range of energy, from 0.1 to 300 keV (Scarsi, 1997). It had moderate imaging capability but was prepared for producing high-quality spectra. One of its key discoveries was that of gamma-ray bursts X-ray emission.

Nowadays, operating X-ray mission provides us with still a better understanding of the amazing X-ray Universe. National Aeronautics and Space Administration (NASA)'s *Chandra X-ray Observatory* (Weisskopf et al., 2003) and the ESA's *XMM-Newton Satellite* (Jansen et al., 2001) are like sister telescopes launched in July and December 1999, respectively. Chandra provides the highest spatial resolution to date and therefore excels in producing images with 0.5 arcsec angular resolution and decoding the structure of extended X-ray sources. XMM-Newton possesses a large mirror surface with an excellent collecting area and sensitivity to deliver faint images and spectra in less time, revealing the components of structures that Chandra sees.

While Chandra and XMM-Newton operate up to 10 keV, the hardest X-rays up to several hundred keV are accessible through *Swift* or *Suzaku*. Since 2004, *Swift* (Burrows et al., 2005) also provide spectacular views of the X-ray Universe performing the first sensitive hard X-ray survey of the sky. At hardest X-ray regime with $E >> 10keV$ grazing incident telescopes would need focal lengths of >> 10 m, i.e. *Wolter-type telescopes*. Instead, *Swift* includes coded masks, similar to pin-hole masks but with a pattern of holes allowing for ~ 50% of the light to reach the detector, achieving an imaging resolution of several arcmin. In 2005, *Suzaku* was launched (Mitsuda et al., 2007), the dramatically improved successor of ASCA. It was designed to perform various types of observational studies of a wide variety of X-ray sources, with higher energy resolution and a higher sensitivity than ever before, over a wider energy range from soft X-rays to gamma-rays (0.4-600 keV). *NuSTAR* (Harrison et al., 2013), launched in 2012, brought focusing optics to high-energy X-rays for the first time implementing long focal length. It gives an observational window between 5 and 80 keV.

The next generation of X-ray observatories is coming in order to achieve further advances and disentangle the mysteries of this energetic world. The most expected spacecraft, Advanced Telescope for High ENergy Astrophysics (ATHENA+) (Barcons et al., 2012) with a focal length of 11.5 m is envisioned to carry out a wide-field imager and a microcalorimeter. It will be launched around 2028 to give answer to e.g. how SMBH do grow and contribute to our Universe.

Then, since 18th June1962, when the first X-ray object outside our solar system was discovered, our understanding of the X-ray universe has grown as a string of X-ray satellites which have revealed exotic objects and energetic events. Yet here we are, 54 years later, with hundreds of thousand X-ray sources detected. Among them are the most exotic phenomena in the universe as SMBH. It takes a lot of energy to make X rays. Black holes are a source of thermal

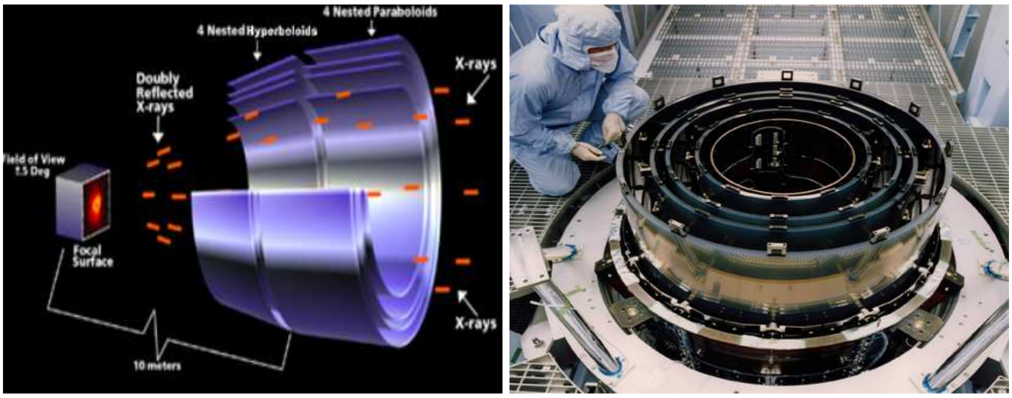

FIGURE 1.2: *Left:* Schematic representation of the X-ray mirrors of *Chandra* observatory. *Right:* Real picture of *Chancra*'s X-ray mirrors. Image credit: .

X-ray emission, pure heat and therefore energy. Gas falling down onto SMBH, attracted by the extreme gravity, is heated up to temperatures of millions of degrees. In this way, astronomers can "see" a black hole thanks to the "commotion" around it despite its invisible nature. That is what makes X-ray astronomy so exciting. The scene is filled with the most explosive and energetic phenomena and it just took a little while for humans to go into to the X-ray universe.

It is worth mentioning that X-ray observatories cannot use the conventional mirrors that we are used to in everyday life, since X-rays would just pass straight through the gaps between the atoms. The reason is that the larger the wavelength of light, the larger its interaction cross-section, and the larger the chance of an interaction i.e. an reflection. Unlike optical light, X-rays have a short wavelength (high energy) and a small interaction cross-section so that they can pass between the atoms of a mirror without interacting with them at all. The solution is to get the incoming X-rays to interact with more atoms and this can be achieved by turning the mirrors edge-on, and so the X-rays are more likely to hit an atom thus bringing the X-rays to a focus point. The X-rays are slipping off the atoms like a stone slipping over water, since an incoming X-ray will see more atoms when the mirror is placed edge on.

Indeed, one of the most complex part of X-ray observatories is the manufacture of the mirrors, since they only can "collect" a tiny fraction of the incoming X-rays leading them to a focus after passing between the different mirrors (see Fig. 1.2). In order to get around this problem, the designers of the *XMM-Newton* observatory placed 58 nested mirrors within each other trying to catch as many X-rays as possible. Whereas, designers of *Chandra* spacecraft opted for only 4 mirrors, but four mirrors so accurately made, exquisitely shaped and aligned nearly parallel to incoming X-rays, that the resulting images are much sharper that the images taken by *XMM-Newton*.

The origin of X-rays from close to the SMBH means that X-ray data offer a chance to study the immediate environments of black holes and the poorly understood accretion process that fuels them, allowing us to test physics in the extreme relativistic regime. Although the X-ray emission is unresolved in images with current instrumentation, timing analysis and spectroscopy allow us to probe these regions indirectly. Gas inflows and outflows near the most central regions inprint specific spectral features. The reprocessing of radiation in the innermost accretion disc makes it possible to reconstruct the geometrical structure and motion of the accreting material on small radii.

1.3 AGN classification

Depending on their multi-wavelength properties, the taxonomy of AGN constitutes a disparate zoo of different names and different spectral, polarization, and variability characteristics. Since the physics underlying their nature was not yet clear, this kind of objects have been historically divided in a huge variety of classes, types and subtypes and nowadays AGNs form a very heterogeneous group, that collectively occupy a vast parameter space. Here, the main classifications of AGN are shortly described.

With respect to radio emission they can be classified as: *radio-loud* and *radio-quiet*. The **radio-loud** objects produce large scale radio jets and lobes of plasma in the vicinity of the SMBH, thus being detected as bright sources in radio band. Otherwise, the weak radio ejection of the **radio-quiet** objects does not show strong radio dominance and radio emission is generally energetically insignificant (Wilson & Colbert, 1995a). A generally accepted quantitative way of knowing if an AGN is radio-loud or radio-quiet is the ratio of radio (5 GHz) to optical (B-band) flux. Thus, roughly 15 – 20% of AGNs are radio-loud with $F_5/F_B \gtrsim 10$ (Kellermann et al., 1989). The capability of an AGN to form powerful relativistic jets, i.e. its radio-loudness, can be related to host galaxy type (Smith et al., 1986) or to black hole mass and spin (Wilson & Colbert, 1995b).

The multi-wavelength study carried out by Sanders et al. (1989) revealed, with few exceptions that the infrared to soft X-ray continuum and optical and ultraviolet emission-line spectra of most radio-loud and radio-quiet AGNs are very similar. Therefore they would be a product of more or less the same mechanisms. Thus, based on the characteristics of their UV , optical and near infrared (NIR) spectra, AGN can be separated into three broad types (Urry & Padovani, 1995, Netzer, 2015):

Type 1: Their spectra are characterized by a bright continuum and the presence of broad emission lines from hot and high velocity gas with a full-width at half maximum (FWHM) of 1000–20000 $km\ s^{-1}$ superimposed to narrower lines (Netzer, 2015). According to the relative intensity of the broad and narrow components of the Balmer lines, several subgroups of

Type 1 sources can be distinguished : type 1.5, type 1.8 or type 1.9, being type 1.5 the ones with the stronger broad component.

Type 2: Their spectra show a weak continuum, which is normally constant in time, and only strong narrow emission lines with a FWHM of 300 – 1000 $km\ s^{-1}$ (Netzer, 2015), which accomplish a ratio of fluxes of $\frac{F_{[OIII]\lambda 5007}}{F_{H\beta}} \sim 10$ (Antonucci, 1993) and show clear indications of photoionization by a non-stellar source. As type 1, they also appear like point sources in X-ray wavelengths at least at high energies, where the continuum emission dominates.

Type 2 AGN can be divided in other two subgroups: those with a hidden broad line region (HBLR) which can only be detected in polarized light and not in common spectroscopy (Miller & Goodrich, 1990, Young et al., 1996), named HBLR AGN, and those where observations in polarized light have failed to reveal the hidden broad emission, so non-hidden broad line region (NHBLR). In some cases, their X-ray emission is unabsorbed, typical of type 1 AGN, indicating a clear view towards the nucleus , but without detected broad lines in the optical. These sources are sometimes known as *true type 2 AGN* or *naked AGN* as they perhaps lack their broad line region (BLR) component (Valencia-S. et al., 2012, Hawkins, 2004). *True type 2 AGN* characteristics will be more detailed in section 1.6.2.

Type 0: This subgroup includes AGNs with extremely weak, sometimes completely undetected emission lines and, ocassionally, continuum variability (Netzer, 2015). Urry & Padovani (1995) related them by a small inclination angle to the line of view (LOS).

Different subgroups of AGN have been defined. Below, the main ones are detailed:

- **Seyfert galaxies**

  Seyfert galaxies are the most common class of AGN that we can observe in the local Universe. Due to their relative proximity, they provide us with the best available spectra and images and allow to study the AGN physical processes in better detail. Taking this into account, it is not surprising that they were the first AGN classified as such.

  They exhibit a low luminosity with $M_B > -21.5 + 5 \log h_0$, established originally by Schmidt & Green (1983) for distinguishing Seyfert galaxies from quasars. Hence, they are seen only nearby, where the host galaxy can be resolved. Photometrically, the surface brightness of their nuclei is high, but they are mainly identified due to the presence of strong, high-ionization emission lines in their spectra. Morphological studies suggest that most, if not all, Seyferts occur in spiral galaxies (Simkin et al., 1980).

  Khachikian & Weedman (1974) realized that there were in reality two broad subclasses of Seyfert galaxies, depending on the presence or absence of broad bases on the permitted emission lines. As noted above, type 1 Seyfert galaxies show two set of emission lines:

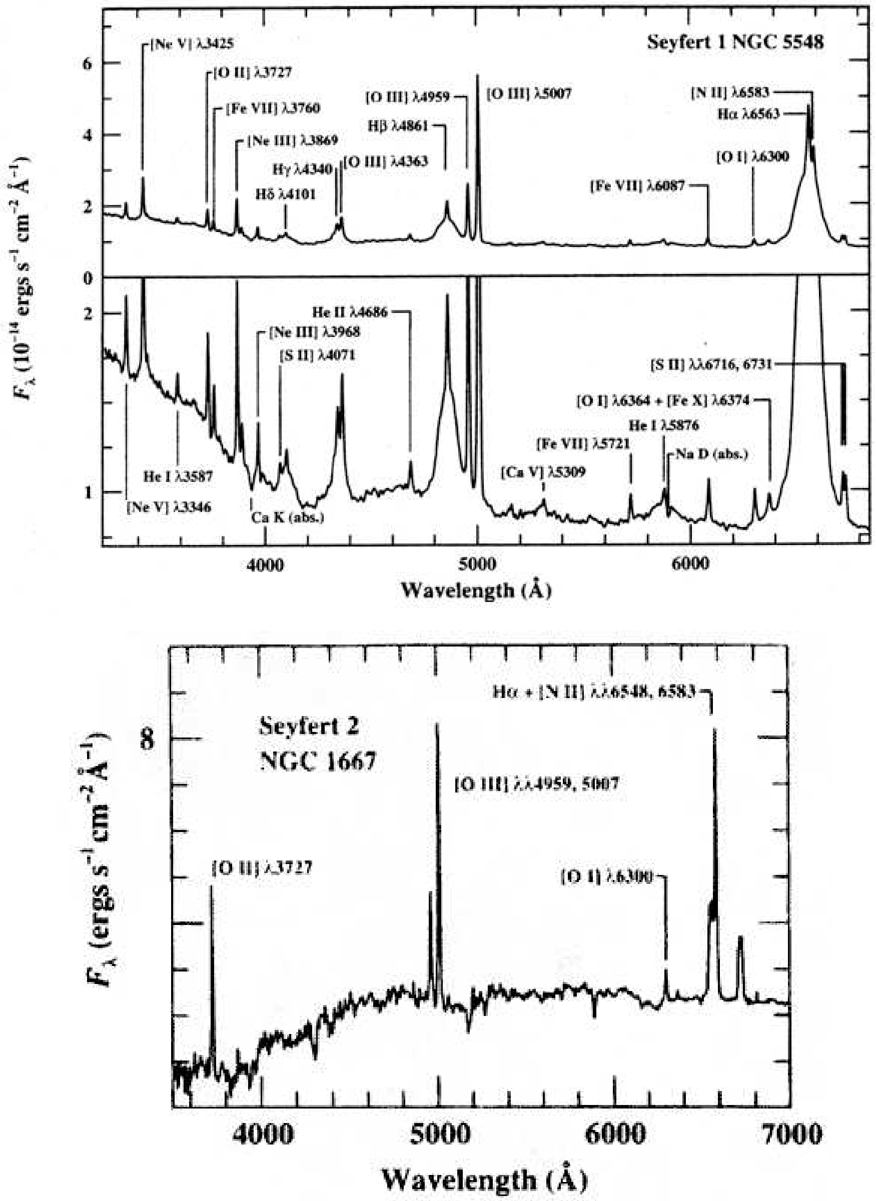

FIGURE 1.3: *Top panel:* Example of a typical Seyfert 1 galaxy, in this case NGC5548, optical spectrum . The prominent broad and narrow emission lines are labeled. The vertical scale is expanded in the lower panel to show the weaker features. The FWHM of the broad components is about 5900 *km* s^{-1}, and the width of the narrow components is about 400 *km* s^{-1}. The strong rise shortward of 4000Å is the long-wavelength end of the "small blue bump" feature which is a blend of Balmer continuum and FeII line emission. *Bottom panel:* The optical spectrum of the Seyfert 2 galaxy NGC1667 is shown with important emission lines identified along some strong absorption lines that arise in the host galaxy rather than the AGN itself . Image credit: http://www.faculty.virginia.edu/ASTR3130/lectures/spectroscopy/spec.html

narrow and broad lines, superposed on one another. Narrow lines come from low-density (electron density $n_e \approx 10^3 - 10^6 cm^{-3}$) ionized gas and show widths corresponding to velocities of several hundred kilometers per second (in non-AGNs objects this means somewhat broad). In contrast, broad lines only appear in the bottom of permitted narrow lines, have widths of up 10^4 $km\ s^{-1}$, and are likely emitted form high-density regions $n_e \gtrsim 10^9 cm^{-3}$ (Peterson, 1997). According to sub-classification mentioned above, in type 1 and 1.5 Seyferts, the broad and narrow components of the lines can be easily seen, in type 1.8 Seyferts, the broad components are weak but nonetheless detectable in $H\alpha$ and $H\beta$, and finally, in type 1.9 Seyferts the broad component can only be detected in the $H\alpha$ line (Osterbrock, 1981). The absence of broad wings in the forbidden emission lines corroborates the fact that that the broad-line emitting gas is of high density as the forbidden transitions do not occur at low densities since they are collisionally suppressed (Peterson, 1997). Forbidden and permitted transitions will be explained in more detail on section 1.4.2.

On the other hand, as mentioned above, the spectra of type 2 Seyfert galaxies only comprise narrow emission lines. Possibly Seyfert 2 (Sy2) nuclei have even extremely weak broad components but too faint too detect against the continuum spectrum of the nucleus (Osterbrock, 1989). Both Seyfert 1 (Sy1) and Sy2 galaxies exhibit weak absorption lines due to late-type giant stars in the host galaxy in addition to the strong emission lines. These absorption lines are weak because the starlight is diluted by the non-stellar continuum (Peterson, 1997). Sy2 galaxies exhibit a fainter emission continuum in the optical than Sy1s because their AGN core is usually less dominant with respect to the surrounding galaxy than in Sy1s. Hence their non-stellar continuum is also usually very weak so that isolating it from the synthetic stellar spectrum coming from the host galaxy becomes a very difficult task. Otherwise, Sy1 galaxies often exhibit a strong continuum which appears to be featureless, i.e. without the characteristic stellar absorption lines.

Up to here, the optical classification of Seyfert galaxies has been discussed. An equivalent distinction between Seyfert types is made in the X-rays, based on the intrinsic absorption measurement in the soft X-ray band, i.e. $E < 5\ keV$. At these energies, intrinsic absorption means the presence of matter close to the SMBH and it is measured as a column density of hydrogen, N_H, in units of atoms per cm^2 in the LOS. In general, Seyfert galaxies which present an intrinsic absorption of $N_H < 10^{22} cm^{-2}$ are classified spectroscopically as Seyfert 1 or 1.2 while those with $N_H > 10^{22} cm^{-2}$ are classified as Seyfert 1.8, 1.9 or 2 (Beckmann & Shrader, 2012). It is likely that the transition between absorbed and unabsorbed sources is smooth and therefore not all Sy1 galaxies exhibit low absorption (Awaki et al., 1991) and not all Sy2 nuclei show intrinsic absorption (Pappa et al., 2001). It should also to be outlined that intrinsic absorption is variable as it can depend on occultation events as it will be discussed in detail in section 2.

Regarding to radio emission, Seyfert galaxies are radio quiet. This dissertation is precisely focused on the study of this subclass of AGN.

- **Quasars (QSOs)**

  They are the most luminous objects in the sky and, therefore, they are also the ones we see far across the Universe. At date of writing, the highest-redshift quasar is detected at $z = 7.085$ (Momjian et al., 2014), which puts these objects at times as early as 800 million years after the Big Bang .

  According to the relation of Schmidt & Green (1983) for Seyfert galaxies, quasars accomplish the complementary one: $M_B < -21.5 + 5 \log h_0$. In fact, they are so luminous that they outshine the light coming from their host galaxies and only the nucleus can be detected. That is the reason why firstly they were confused with star-like objects (Sandage, 1964), hence their name QSOs or quasars to shorten.

  A small minority, $\sim 5 - 10\%$ of quasar are radio-loud (Peterson, 1997) and can also be divided in type 1 and type 2. Their spectra are remarkably similar to those of Seyfert galaxies, except that stellar absorption features are very weak, sometimes undetectable, and narrow lines are usually weaker relatively to broad lines compared to Seyferts.

- **Low ionization nuclear emission regions (LINERs)**

  Low ionization nuclear emission regions (LINERs) constitute the low luminosity end of the AGNs with $L_{bol} \sim 10^{39} - 10^{42} erg\ s^{-1}$ (Ho, 2008). They show faint core luminosities and strong emission lines originating from low-ionization gas. Typical emission line widths are $200 - 400\ kms^{-1}$ and their properties are very similar to those of Sy2 nuclei but, despite their lower luminosity, LINERs have stronger forbidden lines. According to their position at the low luminosity end of the AGN phenomenon, they may be accreting matter with low radiative efficiency or at low rate compared to Seyferts. The ionizing mechanism is still unclear and type 1 and 2 LINERs can also be found.

- **Radio galaxies**

  They are strong radio emitters concentrated in a point-like radio source with, typically, two lobes of radio emission that are often approximately aligned with the jets (Urry & Padovani, 1995). Due to their spectral similarity, radio galaxies can be considered to be the radio-loud Seyferts. According to their optical spectrum, broad-line radio galaxys (BLRGs) and narrow-line radio galaxys (NLRGs) can be defined (Osterbrock, 1989). On the other hand, radio galaxies are preferentially located in elliptical galaxies (Best et al., 2005) rather than spirals, although recently, Singh et al. (2015) have detected four rare double-lobe radio sources hosted in spirals.

- **Blazars**

In the rare cases where one of the jets is directed straight at us, special relativistic beaming strongly enhances the observed jet emission, often diluting and thus making it difficult to observe any other emissions from the AGN. Such objects are known as blazars and are always radio-loud.

There are two subgroups of blazars: optically violent variables (OVVs) and BL Lac Objects. OVVs are extremely variable on short timescales at X-ray, optical and radio wavelengths , e.g. $\Delta m \gtrsim 0.1$ mag. in optical wavelengths within one day. In addition to their large variations in flux, they usually show high polarization, up to a few percent while most AGNs tend to have $\sim 1\%$, which also varies in both magnitude and position angle. Hence their name, OVVs. BL Lac Objects adquired their name from the highly variable star BL Lacertae, since this class, like quasars, also exhibit stellar appearance. They are mainly distinguished from OVVs because of the absence of strong optical emission lines in their spectra. The emission-line features may be intrinsically absent or simply swamped by the additional variable component: in the latter case, emission lines may become visible when the variable component is at a low level. OVVs behave more like standard radio-loud quasars with the addition of a rapidly variable component. In both classes of source, the variable emission is believed to originate in the relativistic jet. Relativistic effects amplify both the luminosity of the jet and the amplitude of variability.

1.4 Radiative processes in active galactic nuclei

Radiation mechanisms hold a outstanding place in astrophysics world since they are our "eyes" to the astrophysical objects of the Universe. Understanding the interaction between photons and particles and between particles or fields is essential in order to understand emission and absorption processes taking place in AGN. Synchrothron emission seems to play a key role in jets. Accretion discs emit UV thermal radiation, being the X-ray emission produced through the inverse Compton effect. Fluorescence is responsible for the main X-ray line profile: Fe $K\alpha$ at 6.4 keV. Some processes emit unpolarized radiation while others issue polarized light, which will become important in this dissertation. Bellow, a overview of these processes is outlined.

1.4.1 Continuum emission processes

Electromagnetic radiation produced in any kind of physical process within the AGN environment cannot travel undisturbed to the observer due to the geometrical anisotropy that characterizes this class of objects . Photons will be scattered on particles, losing or gaining energy. This has important effects on the observed spectrum. Those than can be seen acting in Seyfert galaxies are:

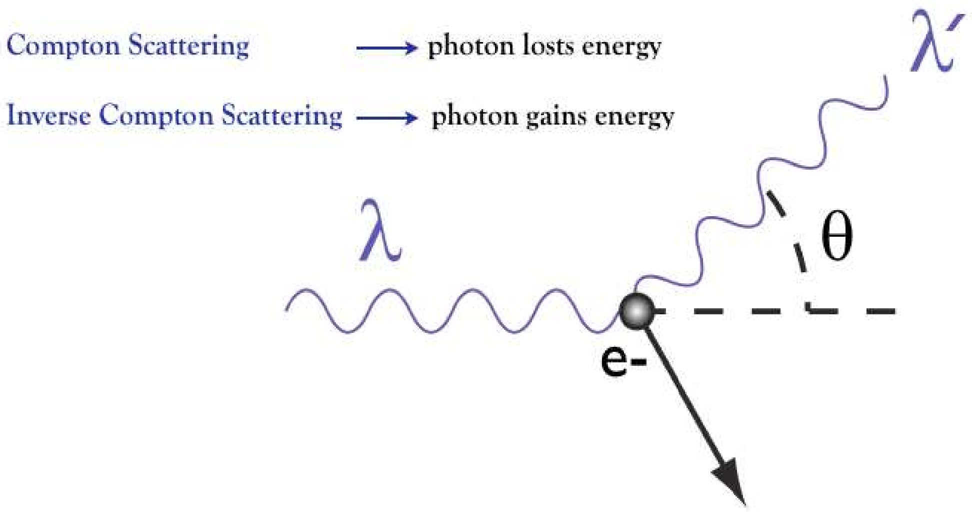

FIGURE 1.4: Graphic description of Compton scattering. Image credit: https://astrobites.org/wp-content/uploads/2012/04/500px-Compton-scattering.png

- **Compton scattering**

  Compton scattering is the inelastic interaction between a high energy photon, i.e relativistic $E \sim mv$, by a charged particle at rest, usually an electron. It results in a decrease in energy (increase in wavelength) of the photon, called *Compton effect*, which becomes important for X-rays and dominates at γ-rays. Part of the energy of the photon is transferred to the recoiling electron. Using the principles of conservation of energy and conservation of momentum, the energy of the scattered photon can be derived in terms of the incident photon energy and the angle through which it is scattered (Rybicki & Lightman, 1979).

- **Inverse Compton scattering**

  The inverse process of scattering, in which a high energy electron transfers part of its energy to a low energy photon, is called *Inverse Compton scattering*. Multiple inverse Compton scattering by hot thermal electrons, i. e. thermal comptonization (Zdziarski et al., 1994), are thought to occur in the accretion disc corona onto the UV photons coming from the disc so the resultant photons acquire X-ray energies. Hence, inverse Compton effect is thought to be responsible for the primary X-ray emission of AGN, being the most important X-ray emission mechanism in radio quiet AGN. The resulting spectrum depend on the luminosity and incoming radiation spectrum, the energy distribution of relativistic electrons, number of scattering events and energy balance between the energy gained by the photons and lost by electrons.

- **Cyclotron and Synchrotron emission**

Radio emission in astrophysical sources is caused by the *cyclotron process* which occurs when charged particles are accelerated in a magnetic field. The electron changes its direction because the magnetic field exerts a force perpendicular to its original direction of motion. If the electron is relativistic, process is renamed as *Synchrotron emission*. The energy of the emitted photons is a function of the electron energy, of the magnetic field strength and of the angle between the electron's path and the magnetic field lines (Rybicki & Lightman, 1979). Unless, the magnetic field is disordered, the resulting radio emission is polarized.

1.4.2 Spectral line radiation

- **Allowed and forbidden lines**

  A distinguishing observational feature of Seyfert galaxies is the presence of narrow, non-variable forbidden emission lines. What means "forbidden" lines in this context? The allowed line transitions are governed by the selection rules of quantum mechanics. The quantum numbers which describe the properties of the electrons and of their configurations in the atom can only change in certain ways during a transition. The transitions "forbidden" by the selections rules are only partially forbidden. A more correct description is to say that the transition probability is small but not zero. Lines resulting from this kind of transitions are known as *forbidden lines* and are normally several orders of magnitude fainter than those from the allowed lines, so that they are normally lost in the noise level of the spectrum. However, special circumstances may lead to the forbidden lines becoming detectable, and sometimes, dominating the spectrum. The interstellar medium, also known as nebular medium, existing in AGNs makes their characteristic spectra to show very strong forbidden emission lines. This arises because some elements of this interstellar medium, composed mainly of gas and dust, present energy levels which have no allowed transitions to the lowest energy (ground state) level. Excited electrons may cascade downwards to such a level and become stuck. In the absence of collisions or other processes to provide alternative paths to the ground state, most of the atoms of that element will eventually make their way into this metastable state. The forbidden transition, whose lifetimes ranges from 10^{-3} s to many years, is then the only way out to the electrons, so that the only observed lines are the forbidden ones (Kitchin, 1991).

  Since the BLR presents high densities, collisions impede forbidden transitions. This is the reason why only permitted broad lines are seen. The forbidden transitions are often symbolized in the literature using two brackets, e.g. [O III] λ5007, while the allowed lines are written without brackets. The numerical value corresponds to the wavelength of the line in angstroms.

- **X-ray fluorescense and Auger process: production of Fe $K\alpha$ line**

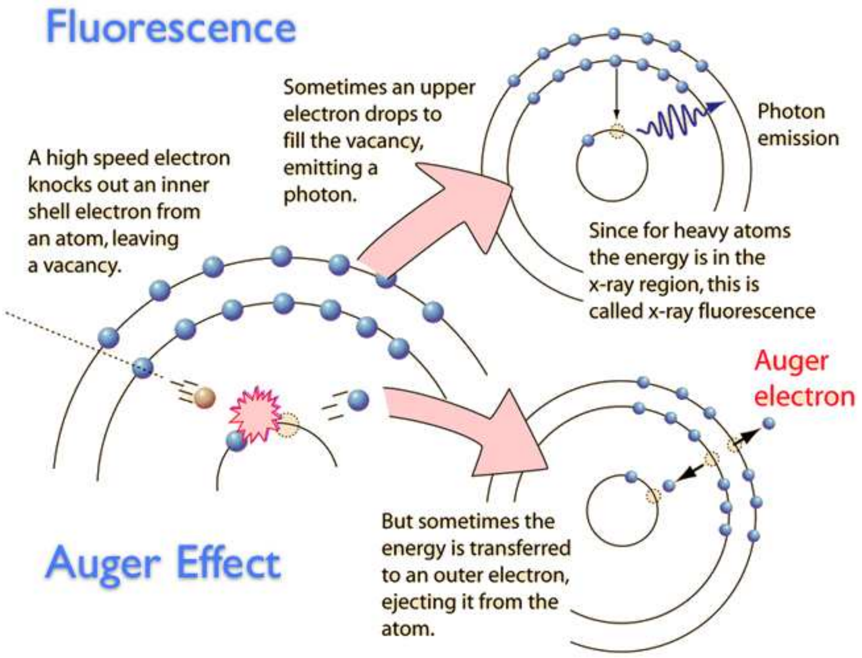

FIGURE 1.5: Graphic description on X-ray fluorescence and Auger effect. Image credit: http://hyperphysics.phy-astr.gsu.edu

In the vicinity of a black hole, an high speed electron or X-ray photon can collide or be absorbed by one of the inner electrons of a multi-electron atom, ion or molecule. One of the outer electrons then drops to fill the vacancy. At this point there are two possible endpoints: *(1)*, the dropping electron can emit another X-ray photon, a process known as *X-ray fluorescence*, or *(2)*, the energy emitted by the dropping electron goes into ejecting one of the outer electrons, the so-called *Auger effect*. Both processes occur in the accretion disc, making the X-ray fluorescence the responsible for the strongest spectral feature in thermal AGNs: the Fe Kα line, which, like all K lines, is the result of an electron dropping from the second orbital shell “L” to innermost “K” shell.

Photoelectric absorption of an X-ray photon by the neutral iron has a threshold of 7.1 keV, i.e., in order to eject one of the two electrons of its K-shell, a photon of energy ≥ 7.1 keV is required. The resulting excited state has 34% probability to decay by fluorescence, releasing 6.4 keV of energy, and 66% probability to suffer an Auger de-excitation, emitting an electron. There are, in fact, two components to the $K\alpha$ line, $K\alpha1$ at 6.404 and $K\alpha2$ at 6.391 keV, which are not separately distinguished in this work because they are unresolved at current X-ray resolution. There is also a $K\beta$ line at 7.06 keV, and a nickel $K\alpha$ line at 7.5 keV is expected (Fabian et al., 2000). For ionized iron, the outer electrons are less effective at screening the inner K shell from the nuclear charge, and the energy of both the photoelectric threshold and the $K\alpha$ line are increased up to 6.9 keV if iron is highly ionized (Antonucci, 2015). Extrapolating the optical depth to bound-free absorption, the area of iron line production in a typical accretion disc should be of 0.1-1% of its

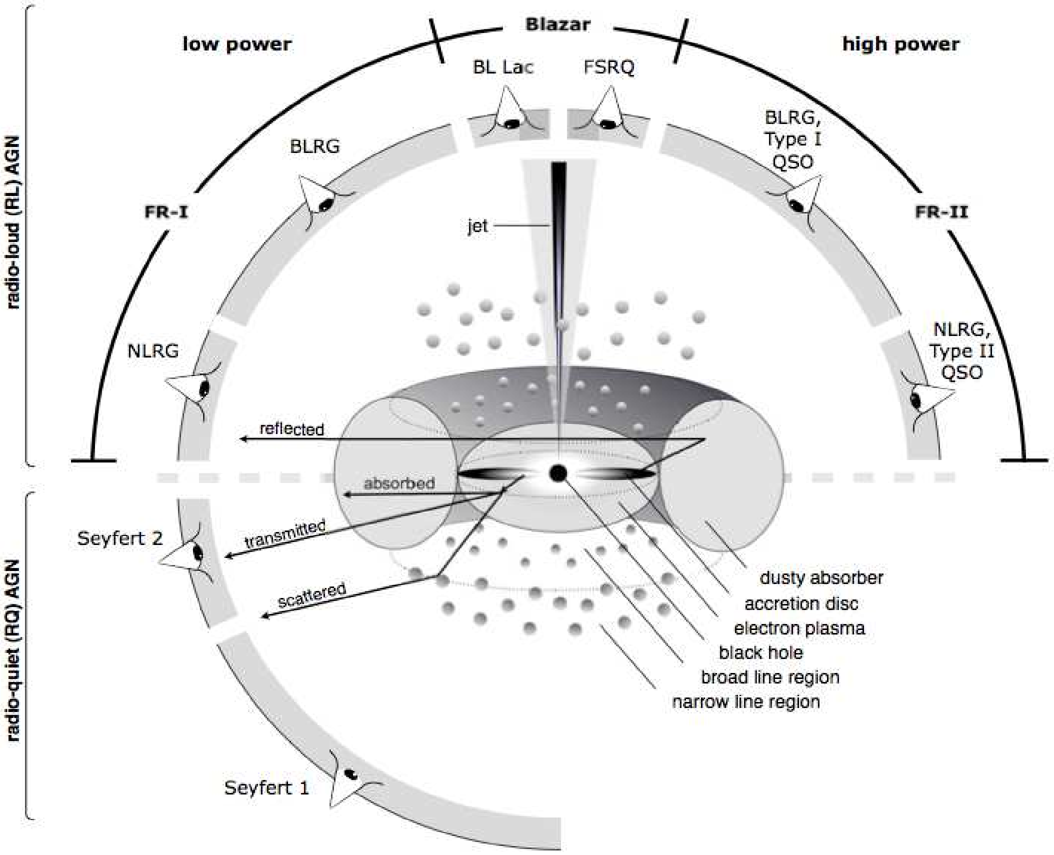

FIGURE 1.6: Physical structure of AGN and unified scheme. Image credit: Beckmann & Shrader (2013)

thickness. It is the ionization state of this thin skin which determines the nature of the iron line.

1.5 Physical structure of active galactic nuclei

AGNs are not only spatially unresolved but also strongly non-spherical. This implies strongly anisotropic radiation patterns which make it difficult to know their detailed physics as it is literally hidden from view, with orientations effects having been the source of much confusion. The prevailing, but not necessarily complete, picture of the physical structure of AGN is illustrated in Fig. 1.6, where the components detailed below can be distinguished.

1.5.1 Supermassive Black Hole

A black hole is a singularity in space-time where a huge amount of mass is compressed into one point. It exhibits such strong gravitational effects that even light is not able to escape. The

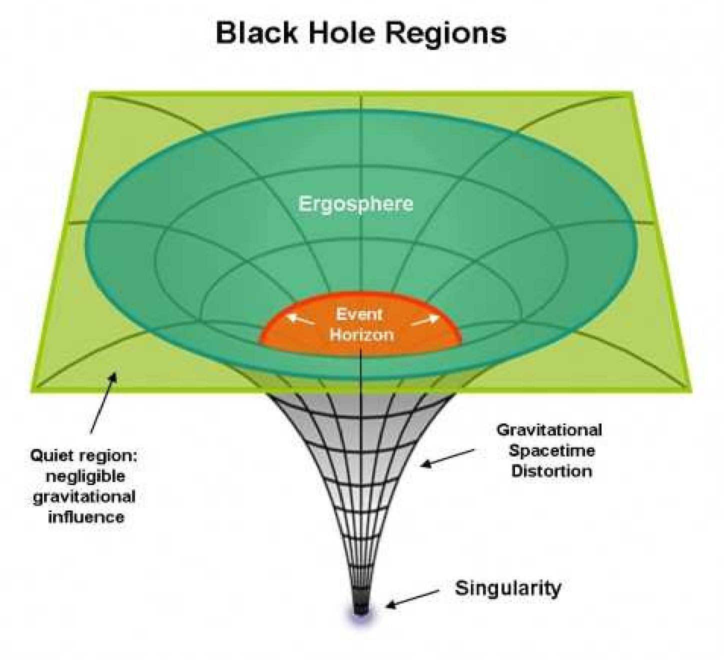

FIGURE 1.7: Graphic description of a general black hole. Image credit: http://www.astronomysource.com/tag/event-horizon-definition/

boundary of this region from which matter and light can fall inward towards the black hole but can never re-emerge is called the *event horizon* (Schwarzschild, 1916). Mathematically, at the event horizon of a non–rotating black hole, the gravitational escape velocity equals the speed of light at the event horizon surface, which occurs at a radius:

$$R_S = 2\frac{GM}{c^2} = 2r_g \tag{1.1}$$

where r_g is known as gravitational radius. R_S was derived by Karl Schwarzschid in 1916, reason why it is known as *Schwarzschid radius* and corresponds to the distance between the singularity and the event horizon. Thus, the event horizon marks the outer boundary of the dark region where the escape velocity is higher than the speed of light. Outside the event horizon, if the black hole is rotating, there is a region, the so-called *ergosphere*, where the black hole drags the surrounding spacetime making it impossible for a particle to be at rest, if seen from a distant observer. However, particles in the ergosphere can escape the black hole if their speed is higher than the appropriate escape velocity, which decreases with distance (see fig. 1.7).

A detailed treatment of the environment of a black hole requires *General Relativity*. However many of the concepts relevant to AGN studies can be formulated from Newtonian approximations or discussed qualitatively without a complete general relativistic treatment.

Since the studies carried out by Lynden-Bell (1969), a SMBH surrounded by a hot accretion disc has been the leading candidate to power the central engine in AGNs . Energy is thought to be generated by gravitational infall to the SMBH of matter, in such a way that the potential energy of this material is converted to radiation and particle outflow in an accretion process.

Although this scenario has long been considered as the explanation for the AGN phenomenon, obtaining unambiguous proof has been difficult. A large amount of optical, infrared, and radio studies have revealed the presence of large masses within small radii that can only plausibly be black holes (Salpeter, 1964). X-ray studies have revealed spectral features from the innermost accretion flow of several Seyfert galaxies: the enormous Doppler shifts and gravitational redshifts of the features showed for the first time the strong gravity near the event horizon (Tanaka et al., 1995). Only in nearby galaxies, spatially resolved kinematics have provided strong evidence for the ubiquity of nuclear black holes (Miyoshi et al., 1995).

- **Accretion basics: Eddington limit**

  Accretion onto a SMBH is governed by two fundamental quantities: *Eddington luminosity*, also referred to as the *Eddington limit*, and *Eddington ratio*. Eddington luminosity is a natural limit to the luminosity that can be radiated by a compact object. This limit arises because the radiation pressure acting on a, say, electron-ion pair must be smaller than the gravitational force that leads to accretion, not to stop the whole accretion-radiation loop. This sets a limit to the maximum possible luminosity of an accreting object.

  $$L \leq \frac{4\pi G c m_p}{\sigma_e} M \approx 1.26 \times 10^{38} \frac{M}{M_\odot}\, erg \cdot s^{-1} \tag{1.2}$$

  Equation 1.2 represents the *Eddington limit*.When the equality is accomplished, it is obtained the *Eddintong luminosity*, L_{Edd}, i.e. the maximum luminosity that a body can achieve when there is balance between the force of radiation acting outward and the gravitational force acting inward:

  $$L_{Edd} \approx 1.26 \times 10^{38} \frac{M}{M_\odot}\, erg \cdot s^{-1} \tag{1.3}$$

  The other fundamental parameter in the accretion process is the *Eddington ratio*, $R_{Edd} = \frac{L_{bol}}{L_{Edd}}$, defined in terms of the bolometric luminosity L_{bol} and L_{Edd}. The Eddington luminosity is reached when $R_{Edd} = 1$.

- **Black Hole Mass**

  Direct kinematic observations of the black hole mass are limited by finite spatial resolution (a typical AGN at redshift 2 would require nanoarcsecond resolution to probe the sphere of influence of the black hole), not to mention that scattered light from the bright central source dilutes any kinematic signal from orbiting material (Woo & Urry, 2002). For these reasons, the need for developing indirect estimations of black holes mass was clear. These estimations can be organized in two different groups. First of them, those assuming that BLR is gravitationally bound by the central black hole potential, so that the black hole mass can be estimated from the orbital radius and the Doppler velocity.

A. Black hole Mass from Virialized Motion:

In classical mechanics, the virial theorem is a link between the average kinetic energy of a system and its average potential energy. When both quantities are balanced, the system is said to be virialized. It is believed that broad-line clouds are virialized (Wandel et al., 1999, Krolik, 2001), so that a direct relation would be:

$$M_{BH} = f\frac{R_{BLR}\, v_{BLR}^2}{G} \tag{1.4}$$

Where f is a scale factor that depends on the geometry of the system. However, radiation pressure and/or magnetic fields may contribute significantly to the dynamics (Krolik, 2001), and outflows or winds could cause the observed line widths to exceed those induced by the black hole potential alone. In these cases the black hole mass calculated from equation 1.4 would be over- estimated.

A1. Reverberation Mapping:

Qualitatively, the observed type 1 AGN spectrum consists of a strong continuum on which are broad emission lines. The continuum emission, particularly towards the UV region of the spectrum, is believed to be due to accretion onto the SMBH. Since the broad lines are produced by photoinoization or excitation from the continuum radiation, variations in the continuum should imply variations in the line emission delayed by a time $\tau = R_{BLR}/c$. Thus, reverberation mapping involves sampling the variability in the continuum and emission line fluxes on time scales expected to be smaller than the light travel time between the central black hole and the broad line clouds. Cross-correlation analysis, combined with a continuum-to-line response function can then be used to infer the size of the broad line region from time delays (Blandford & McKee, 1982, Peterson, 1993).That size, along with dynamical information inferred from the measure lines widths can be used to estimate the black hole mass by applying Eq.1.4.

The broad-line velocity width can be determined in two ways: from the observed spectra or through the mean FWHM derived from the rms spectrum (Peterson, 1988). Although Kaspi et al. (2000) has proved that the two velocity estimates provide similar results, assumptions about the orbital shape and inclination of the broad-line clouds introduce additional uncertainties. The derived black hole masses for a given source can differ by less than a order of magnitude, making reverberation mapping one of the more robust techniques for estimating AGN black hole mass. However it requires many resources, consumes much observing time and is only applicable to type 1 AGNs.

A2. BLR Size-Luminosity Relation:

The distance to BLR or the size of BLR, R_{BLR}, can also be infered from optical luminosity of the continuum throughout the proportionality $R_{BLR} \propto L^{\alpha}$ according to Kaspi et al. (2005). The estimation is usually carried out at $\lambda = 5100$Å, although it is also applicable to X-rays, UV and even infrared (IR) (Shemmer et al., 2004) :

$$M_{BH} = 4.817 \times \left[\frac{\lambda L_{\lambda}}{10^{44} erg\ s^{-1}} \right]^{0.7} FWHM(H_{\beta})^2 \tag{1.5}$$

where $FWHM(H_{\beta})$ corresponds to the full width at half maximum of the broad component in the $H\beta$ emission line. Although this is not the more accurate estimation of black hole mass, it remains important because it is applicable to a relatively high number of AGNs.

B. Black Hole Mass from Stellar Velocity Dispersion:

Second approach to estimate black hole masses is to exploit the close connection seen in nearby galaxies between black hole mass and an observable quantity: the stellar velocity dispersion σ_*. Being nearby, their black hole mass can be determined from spatially resolved kinematics and this correlates with stellar velocity dispersion as $M_{BH} \propto \sigma_*^{\alpha}$ (Ferrarese & Merritt, 2000, Tremaine et al., 2002). Empirically, the slope and scatter of the $M_{BH} - \sigma_*$ relation are still subject to debate, particularly for different types of host galaxies (Greene et al., 2010) and between low and high mass black holes (Greene & Ho, 2004, Greene et al., 2008). In the form of $\log\left(\frac{M_{BH}}{M_{\odot}}\right) = \alpha + \beta \log\left(\frac{\sigma_*}{200\ km\ s^{-1}}\right)$ Xiao et al. (2011) found a zero point of $\alpha = 7.68 \pm 0.08$ and a slope of $\beta = 3.32 \pm 0.22$ for an assumed virial normalization factor of $f = 0.75$. They also found that the galaxy discs with high inclination angles (edge-on systems) show a mild offset from the face-on systems in the $M_{BH} - \sigma_*$ relation, as the rotation of the disc in the edge-on systems may artificially increase the measured σ_*, which introduces a scatter in the relation. In additon, Xiao et al. (2011) confirmed that the narrow emission-line widths can be used as a useful proxy for the stellar velocity dispersion in low-mass AGNs. Further refinements are likely to be presented in the near future as this is a filed of very active research.

- **Black Hole Angular Momentun and Iron Kα Line**

  Since the SMBH is accreting matter form the rotating accretion disc, another fundamental parameter should be its angular momentum, or ‘spin’. It can have important implications on the overall behavior of the system.

In Seyfert galaxies, the Fe Kα line at E = 6.4keV is often found to be very broad and asymmetric. It is believed that such lines arise from the innermost regions of the accretion disk, with mildly-relativistic Doppler shifts and gravitational redshifts combining to produce the line profile. Hence, such a line can provide us with a very powerful tool for assessing black hole rotation, as its profile will be relativistically broadened and asymmetric for fast spinning black holes (Fabian et al., 2000).

1.5.2 Accretion Disc and X-ray Corona

The angular momentum of the matter pulled toward the black hole lead to form a rotationally-flattened structure, the accretion disc. The gravitational potential energy of material flowing through the accretion disk is converted into radiative, i.e. electromagnetic, and kinetic energy, while its angular momentum is lost through viscous or turbulent processes. Nowadays, it is believed that this angular momentum transport is due magnetic and hydrodynamic processes (Balbus & Hawley, 1998). Such an energy transformation glows mainly at UV wavelenghts. However, AGNs are copious X-ray emitters. These X-rays are thought to originate from the innermost regions of an accretion disk around the central SMBH. Since the accretion disk itself is expected to be an optical/UV emitter, the most likely mechanism producing hard X-rays is inverse Compton scattering of these soft photons in a hot and tenuous corona formed by a plasma of hot electrons that sandwiches the accretion disk (Haardt & Maraschi, 1991). Thus, accretion disc and the X-ray corona are coupled. Part of the photons turned to X-ray energies irradiate the accretion disc, which is colder that the hot corona due to its radiative efficiency, in the sense that it radiates locally almost all of the energy absorbed locally. Therefore, the comptonized photons heat up the surface layer of the accretion disc generating a reflection component within the X-ray spectrum (Guilbert & Rees, 1988). This scenario gives a two phases accretion disc: a cool thick accretion disc with $kT < 50\ eV$, and a hot thin corona with $kT \sim 100\ keV$ (Mushotzky et al., 1993), both connected by the described feeedback.

The coronal heating mechanism is not known, but some possibilities are that a portion of the accretion flow is intrinsically hot (Shapiro et al., 1976, Narayan & Yi, 1994) or that magnetic reconnection creates hot flaring regions above the accretion disk (Nayakshin & Melia, 1997, Poutanen & Fabian, 1999). It is believed to be located somewhere along the rotation axis of the SMBH and/or off-axis in the proximity of the inner parts of the accretion disc.

The main features that the accretion disc imprints on an AGN spectrum are:

- **UV-optical spectral observed signatures: Big Blue Bump**

  There is often a distinct bump in the spectrum at optical/UV wavelengths, generically referred to as the big blue bump, that is thought to correspond to thermal radiation from the optically-thick portions of the accretion flow. While the spectra of solar-type stars peak around $\lambda = 500\ nm$, those of O-stars at around $\lambda = 350\ nm$. The blue bump appears at $\lambda = 100-400\ nm$ reaching even shorter wavelengths and peaking at frequencies $\nu = 10^{15} - 10^{16} Hz$. Therefore, this spectral component cannot have its origin in the starlight of the host galaxy and is commonly represented as a positive flux excess relative to an underlying power law continuum which extends from optical wavelengths up to hard X-ray energies. This feature was interpreted as the first observational evidence for the presence of an accretion disc (Malkan & Sargent, 1982).

- **X-ray spectral observed signatures: Fe Kα emission line and Compton Hump**

  The cold and optically-thick matter that constitutes the accretion disc can intercept and reprocess some fraction of the X-ray hard continuum emission imprinting atomic features into the observed spectrum. It is a process of "X-ray reflection" responsible for a broad reflection hump peaking at $\sim$ 30 keV and for the $K\alpha$ iron emission line at 6.4 keV (Reynolds, 1999). These spectral features which will be further described in section 1.7.2.

Thus, accretion disc is a crucial tool for our study of black holes, since they become these invisible objects, which do not emit any type of radiation, in visible. This disc is what we actually observe and from what we are able to infer properties of their central objects. Its structure is optically thick, but geometrically it can be thin , *thin accretion disc*, or thick, *thick accretion disc*.

As noticed, such structures are dominated commonly by radiation, but radiatively inefficient accretion flows can occur when the accretion rate is low, of the order of 1% of R_{Edd}. In this case, the accretion disc has low density, then the cooling time may exceed the inflow time of the gas and the gravitational-to-radiative energy conversion is inefficient because most of the energy is advected into the SMBH. These flows are generally described as advection dominated accretion flow (ADAF) (Narayan & Yi, 1994), or more generally as radiation inefficient accretion flow (RIAF) (Quataert, 2004).

1.5.3 Dusty torus

This central, axisymmetric dusty structure with toroidal geometry is the key element of the unified model (UM), which is described section 1.6. Indeed its opening angle as inferred from near-IR observations is generally in agreement with the observed type 2 / type 1 ratio (e.g. Maiolino & Rieke (1995) in Seyfert galaxies). Early evidence for its existence was also obtained from near-IR studies, which revealed the presence of very hot dust, close to the sublimation temperature, in the nuclei of Sy1 galaxies (e.g. Storchi-Bergmann et al. (1992)). Thus, it is considered to present a column density which is large enough, $\sim 10^{25} cm^{-2}$, to completely obscure the central source in some directions whit presents low densities, $\sim 10^3 - 10^6 cm^{-3}$. It presents a variable size between 1-100 pc and is located at 1-10 pc from the nucleus. The torus surrounds the accretion disc, which in turn, as said above, surrounds the SMBH (Netzer, 2013). Its inner radius is considered to be coincident with the dust sublimation radius, which is located at sub-parsec scales in Seyfert galaxies (Bianchi et al., 2012). Extensive reverberation observational campaigns have confirmed the expected luminosity dependence of the sublimation radius $\propto L^{1/2}$ (Suganuma et al., 2006).

The torus structure is not clear yet and many efforts are investing to clarify this question. Firstly, it was proposed as a homogeneous or smooth absorbing toroidal structure (Pier & Krolik, 1992). However, observations did not match the models and new models, as a clumpy torus (Nenkova et al., 2008a) or a two-phased medium including a clump and inter-clump material (Stalevski et al., 2012) are currently preferred as they better describe the observations.

The torus is filled by gas which, at the innermost radii of the torus, is partially ionized by the central source. Hence strong X- ray lines are produced, in particular iron $K\alpha$ lines. Due to the large column densities, this part reflects and scatters the incident X-ray continuum radiation as well as the optical/UV emission from the hot corona and the accretion disc respectively. Deeper in, the torus contains dusty molecular gas which is optically thick, and whose signatures are observed at infrared wavelengths (González-Martín et al., 2015). Only hard X-ray radiation can penetrate it, and even those photons are limited to a few Compton depths Awaki et al. (1991).

Apart from the ubiquitous X-ray, UV and optical absorption and reflection, other remarkable features related to the dusty torus are:

- **Ionization cones**

  The unobscured radiation coming from the central source reaches the gas in the galaxy causing heating and ionization. As a result the narrow emision lines are detected. A torus like geometry surrounding the central source acts as “collimator” of this ionized gas forming two ionization cones, one each side of accretion disk (Pogge, 1988).

- **Dust boundary**

  The maximum temperature that a dust grain can resist before it evaporates is known as *dust sublimation temperature*, T_{sub} and it depends on grain size and composition and the local flux. In AGN context, a *mean sublimation radius*, R_{sub},i.e. the minimum radius where a grain of certain size and composition can survive the local radiation field, is estimated from the AGN luminosity (Barvainis, 1987, Netzer, 2013). Thereby, R_{sub} coincides with the inner boundary of the dusty torus and two distinct regions of high velocity gas near the SMBH can be differentiated from R_{sub} matching with observations: dust-free gas with strong emission lines within R_{sub}, known as BLR, and dusty gas with weaker emission lines outside it (Netzer & Laor, 1993).

- **Variable infrared emission**

  As dust reemits the absorbed radiation at infrared wavelengths, a broad infrared spectral energy distribution (SED) is detected with a luminosity proportional to the number of absorbed photons. This radiation can be reemitted isotropically, or anisotropically, depending on the optical depth and exact geometry. Since radiation emitted by the central source is varying in time, it results in a time-dependent incident flux on the inner torus walls, and a time dependent infrared emission by the dust.

1.5.4 Broad Line Region

The so-called *broad line region*, BLR, is formed by high density and dust-free gas clouds moving rapidly with roughly Keplerian velocities at a luminosity dependent distance of 0.01-1 pc in the gravitational potential of the SMBH (Netzer, 2015). The BLR clouds are assumed to be in photoionization equilibrium, that is, the rate of photoionization is balanced by the rate of recombination. This can expressed in terms of a *ionization parameter* ξ which describes that balance between the ionization rate as driven by the incident photon flux and the rate of recombination which is directly dependent on the density n. Typical values for the BLR are $\log \xi \sim 1.5$ and $n \sim 4 \times 10^9 cm^{-3}$ (Kwan & Krolik, 1981).

Strong optical and ultraviolet emission lines are produced as a result of the excitation caused by the radiation emitted from the accretion onto the SMBH: the *broad lines*, the broadening being due to the high velocities of the gas. The most prominent of these lines are the hydrogen Balmer serie lines $H\alpha$ $\lambda\lambda$6563, $H\beta$ λ4861 and $H\gamma$ λ4340, hydrogen $Ly\alpha$ λ1216, and also common are the lines of ions Mg II λ2798, [C III] λ1909 and C IV λ1549.

Individual clouds, depending on their size, present their front side, that one facing the central engine, highly ionized. Depending on their column densities, they will be less ionized or mostly neutral on the back side. Thus, the front side emits high ionization lines while the back side emits low ionization lines. This basic geometrical scenario can be assessed observationally with the reverberation mapping technique (Beckmann & Shrader, 2012).

1.5.5 Narrow Line Region

The narrow line region (NLR) consists of lower density and slower moving ionized clouds of gas extending from just outside the torus to hundreds and even thousand of parsecs along the general direction of the opening of the torus (ionization cones). Most of this gas contains dust.

The presence of narrower and lower ionization forbidden emission lines was indicative of a spatially distinct component from which the broad high ionization lines emanate. The lack of observable flux variability led to the conclusion that this region was much larger and kinematically separated from that of the broad lines. It is well-established that the NLR gas is photoionized by the UV-X-ray continuum radiation emitted by the central source.

The FWHM of the narrow emission lines is typically $\sim 400 - 500\ km\ s^{-1}$, an order of magnitude less than typical BLR line widths. Forbidden lines, like oxygen, magnesium, neon and sulfur imply gas densities of $\sim 10^5 - 10^5 cm^{-3}$ as compared to densities of $\sim 10^9 cm^{-3}$ or greater inferred for the BLR (Beckmann & Shrader, 2012). The size of the NLR is thought to scale with the luminosity in some of the prominent forbidden lines. For instance, Bennert et al. (2004) found that the NLR size obeys the relation $R_{NLR} \propto L^{\alpha}_{OIII}$, where L_{OIII} is the luminosity in the O III λ5007 line and $\alpha = 0.55(0.32)$ respectively for type 1 and type 2 AGN.

1.5.6 Relativistic Jets

Outflows of energetic particles occur along the poles of the disk and torus, escaping and forming collimated radio-emitting jets, sometimes giant radio sources when the host galaxy is an elliptical, but forming only very weak radio sources when the host is a gas-rich spiral. The plasma in the jets, at least on the smallest scales, streams outward at very high velocities, beaming radiation relativistically in the forward direction along, in some cases, distances of $10^5 - 10^6\ pc$ (Urry & Padovani, 1995).

The primary physical mechanisms initiating, accelerating and collimating these jets remains an enigma still far from clear in many regards. Reynolds & Nowak (2003) suggested that they can be launched from the inner accretion disk or ergosphere of the SMBH and can be accelerated/collimated by hydromagnetic processes. But the nature of these radio-loud AGN features - their remarkable energetics, enormous size and phenomenology- is a crucial open question yet to be solved by modern astrophysics.

1.6 Unified Model

As already pointed out in section 1.3, the term AGN includes a large variety of sub-types according to their multi-wavelength properties, that collectively occupy a vast parameter space. Many effort have been focused over the years to define the AGN phenomenon according its observational characteristics, but the battery of different characteristics was growing more and more. In the current understanding, the effort is renewed so that this disparate zoo can be explained by the simplest possible model. This is the key idea behind the Unification Scheme or Unified Model (UM) (Antonucci, 1993, Urry & Padovani, 1995, Elitzur, 2012), whose basic premise is the ubiquitous presence of the obscuring torus on scales of 1-100 pc around the central engine, so that the observed diversity simply reflects different viewing angles of such an axisymmetric geometry. In other words, all AGN are the same, and the differences among them can be primarily associated with the different orientations, being the optically and geometrically thick torus responsible for the line of sight viewing angle dependency.

Thus, the first prediction of placing such a simple geometrical structure around the central SMBH and the accretion disc, is a dependence of the obscuring column on inclination to the LOS, where inclination is measured relative to symmetry axis of the system. Consequently, type-1 AGNs are observed with a direct view of fast moving material close to the supermassive black hole, resulting in broad emission lines in their optical/UV spectra, while type-2 AGNs are observed from a more edge-on view, intercepting the obscuring torus that blocks the BLR component from our line of sight. As the NLR lies further away from the central SMBH, than the BLR, the former is still observable despite the obscuring torus.

The second prediction is based in the fact that electromagnetic radiation reflected off dust grains and electrons is polarized with angle and percentage polarization which depend on wavelength and geometry of the scattering region or regions. In other words, although the BLR is hidden by obscuring material as in the case of type 2 AGN, the light of the BLR can escape in directions where no material hinders the view to the central engine ant its surroundings. If then the BLR emission hits, for instance, electrons, it can be scattered into the LOS and still reach us. Indeed, the UM arose with the discovery three decades ago of polarized broad emission lines (PBLs), also known as HBLR, in the type-2 AGN –more specifically Sy2 galaxy– NGC 1068 by Miller & Antonucci (1983) and Antonucci & Miller (1985) using spectropolarimetry. Although the direct view of the active nucleus is blocked by the torus in Sy2 galaxies, radiation escapes from the nucleus in conical beams aligned with the poles of the torus. Thus, some of this radiation is scattered towards us, i.e. scattering material acts like a mirror which enable us to look behind the absorbing matter. As a result, Sy2 galaxies may exhibit the spectroscopic properties of Sy1 nuclei in polarized light.

In conclusion, UM explains the large differences in appearance of AGN throughout two interceding parameters: the torus inclination and source luminosity. This causes different absorption effects intrinsic to the innermost regions of the AGN, as well as geometrical effects regarding the beaming of the emission. There are two versions of UM, that for radio-quiet AGN and another one for radio-loud AGN in which jets are intervening. A schematic representation can be seen in fig. 1.6. Since the focus of this study are Seyfert galaxies, radio unification is out of scope of this work.

1.6.1 X-ray unification scheme for Seyfert galaxies

Regarding specifically X-rays, Sy2 galaxies should display very similar properties to Sy1 galaxies but with additional absorption from the torus. Thus, Sy2s are expected to possess accretion disc reflection spectra as do Sy1s. However, because the central engine of Sy2s is heavily absorbed, additional X-ray spectral components become relatively more important, depending sensitively on the amount of absorption (Beckmann & Shrader, 2012).

For Sy2s with relatively low absorbing column densities ($N_H \lesssim 10^{22} cm^{-2}$), the central engine emission can penetrate the absorbing material at energies above a few keV. Consequently, in these cases, Sy2s can exhibit broad iron lines at 6.4 keV (Iwasawa et al., 1996, Turner et al., 1998). As in Sy1 nuclei, these broad lines are thought to originate from the inner regions of the accretion disc. Even though, the reflection hump can be observationally challenging to detect against the absorbed spectrum, this also seems to be present as expected in at least some sources (Weaver et al., 1998).

In high absorption Seyfert 2 systems ($N_H \gtrsim 10^{24} cm^{-2}$) , the central engine emission is completely blocked by the Compton thick absorber. In these cases, a very flat continuum with a large equivalent width ($\sim$ 1 keV) narrow iron line are inprinted in the corresponding spectra. This is interpreted as being an almost pure reflection spectrum possibly from the illuminated inner edges of the torus (Reynolds et al., 1994, Matt et al., 1996). The fluorescence lines from low-Z elements can also been seen in these reflection dominated cases.

1.6.2 Exceptions to unification model

Since the very beginning, the UM has been extremely successful. There have been plenty of other examples of HBLR seen in reflected light, also in nearly all types of AGNs. However, additional ingredients are needed to account for some observational facts that are apparently in conflict with the predictions.

Recent observations of large AGN samples, and more detailed information about specific sources warn that the unification scheme requires modifications. There are real differences between various sub-groups, beyond the dependence on luminosity and torus inclination. This can be due to the nature of the central power-source, e.g. a RIAF instead of high efficiency accretion flow, and the fact that some AGNs lack one or more of the main components, e.g. their BLR or their NLR. Also, the scientific community are currently involved to investigate if evolution the SMBH, directly tied to the host galaxy evolution, or the nature of the circumnuclear obscuring torus (as already noticed in section 1.5.3), could impact on the main characteristics of different types of AGNs (Netzer, 2015).

Numerous investigations have tried to explain the differences in the geometry or physical properties of the circumnuclear absorber. E.g. Ramos Almeida et al. (2011) concluded that the dusty torus have a larger covering factor, a lower optical depth and is more clumpy in Sy2 than in Sy1 galaxies.

One of the most remarkable open questions related to Seyfert galaxies is why some Sy2s do not show any observational signs of PBL. Tran (2001, 2003) and Moran et al. (2001) reported that only 30 – 50% of Sy2 galaxies show HBLRs. The non-detection of HBLRs is by no means a certain confirmation that a given type-2 AGN lacks its BLR, because it may simply indicate that no adequate scattering medium is present. However, in recent years, a new class of AGN, classified as type-2 by optical spectroscopy, has been identified: *true or real Seyfert 2 galaxies* (e.g. Heckman et al. (1995)). They also exhibit some characteristic behaviour typical of type-1 AGN such as, for instance, short timescale variability and/or lack of X-ray obscuration and, at the same time, are observationally found to accrete at low Eddington rates (Shu et al., 2007, Wu et al., 2011). This is in agreement with theoretical models which predict that the BLR disappears below a certain critical value of accretion rate and/or luminosity (Elitzur & Ho, 2009, Trump et al., 2011). If the BLR cannot form in weakly accreting AGN, some of the observed type-2 AGN would be so independently of the viewing angle. Therefore, true Sy2 galaxies are thought to lack their BLR not only observationally (due to orientation) but also physically. In last decade, a significant number of such true Sy2s with low accretion rates has been claimed in the literature (Panessa et al., 2009, Shi et al., 2010). This might also be the explanation of why *BL Lac objects* the weakest blazar, do not show any emission lines. However, some candidates to true Sy2 galaxies as GNS 069 (Miniutti et al., 2013) or 2XMM J123103.2+110648 (Terashima et al., 2012) show high accretion rates, which seem to contradict the generally accepted explanation that the true Sy2 phenomenon is associated with very low luminosity/accretion rates. Further investigations in this class of object are needed to shed light on the study if its nature and still much effort is required to explain the whole appearances of the AGN phenomenon within the unification scheme. Is the UM needing further adjustment and dependence on other parameters than only orientation and radio-loudness? Or, maybe are the many different classes of AGNs intrinsically distinct? Precisely, this dissertation will be focused on aspects which violate the standard UM.

1.7 Typical spectrum of Seyfert galaxies

By definition, emission from a black hole does not resemble that from an ensemble of normal stars. It has a different broadband spectral shape, i. e. SED, a very high luminosity density and a very time variability properties. Roughly speaking, the broadband spectrum of an AGN can be represented by a power law in X-ray, UV and optical ranges:

$$L_\lambda = C\lambda^\Gamma \tag{1.6}$$

where Γ is know as *photon index* and is, typically, $\Gamma = 1 - 2$ for AGN (Osterbrock, 1989). But, let us analyze in detail the UV-optical and X-ray spectral properties separatelu, since each band provide us with very different information about the AGN phenomenon.

1.7.1 UV/optical spectrum

In the modern era of astronomy, with observations ranging 16 decades in frequency, the identification of an object as an AGN still often comes from its optical properties, as already noticed in section 1.3. Optical spectroscopy is the main AGN classification tool and redshifts, and hence distances, are measured from this domain.

As noted above, the optical emission can be represented by an approximate power-law dependence in wavelength plus (often) a *big blue bump* component believed to be of thermal emission origin (Shields, 1978, Malkan & Sargent, 1982). This property gets AGNs to appear "bluer" than non-active galaxies. In addition to this continuum emission, the spectrum exhibits the showy presence of superimposed broad and narrow emission lines. Besides, an integrated stellar continuum plus absorption-line spectrum of a normal galaxy is also detected. All these signatures can be detected in Fig. 1.3.

The UV/optical emission continuum is very strong in Sy1 galaxies, often so much stronger that the integrated stellar absorption-line spectrum is nearly invisible (Osterbrock, 1989). In typical Sy2s this emission is much fainter and, in many cases, it can be detected only by careful analysis of the observed continuum, as one would expect from UM. Thus, the additional unabsorbed light coming from the nucleus makes a typical Sy1 more luminous (before correcting from any intrinsic absorption) than a typical Sy2.

1.7.2 X-ray spectrum

As already discussed in section 1.5.2, it is widely accepted that the accretion disc surrounding the SMBH produces a thermal UV continuum. This continuum acts as UV seed photons field that will be up-scattered to higher energies by relativistic electrons in the hot corona above the accretion disc throughout inverse Compton scattering, producing the X-ray continuum (Haardt & Maraschi, 1991). Thus, a substantial amount of the power in AGNs is thought to be emitted as X-rays from the accretion disc corona and the study of these X-rays should provide information about the immediate environment of the SMBH. At the same time, the circumnuclear torus will

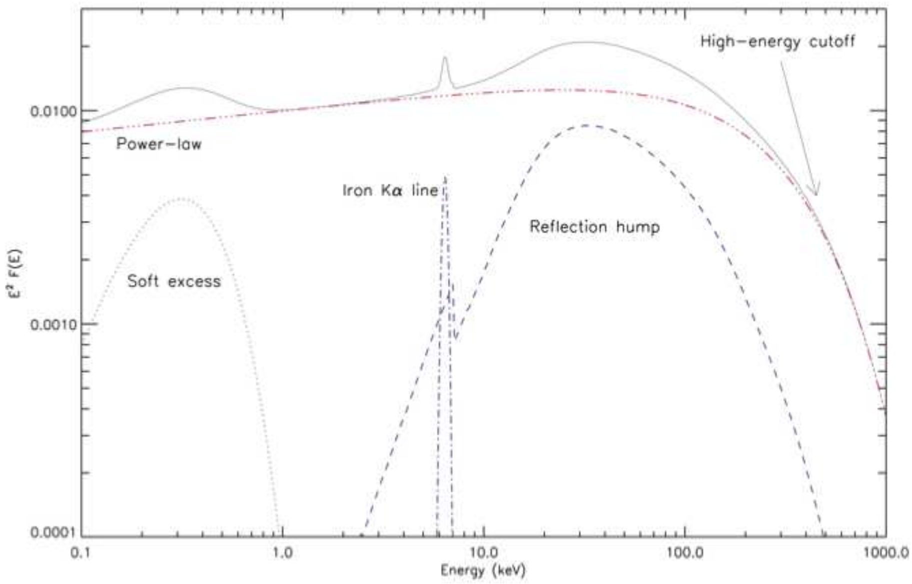

FIGURE 1.8: General components of a typical AGN spectrum. The solid lines represents a prototype of unabsorbed AGN. Image credits: Ricci (2011).

be responsible for a column density dependent X-ray absorption. The typical components of the X-ray spectrum of AGNs are discussed below:

(*i*) *Power law*: Thermal Comptonization in the X-ray corona reprocess the UV photons coming from the accretion disc giving rise to a (primary) X-ray continuum emission. This intrinsic spectrum can be well described by a single power law with a photon index $\Gamma \sim 2$ up to several hundresds of keV (Nandra & Pounds, 1994, Risaliti, 2002, Cappi et al., 2006). Since the relativistic electrons have a finite energy, the resulting inverse Compton scattering will have a high-energy cut-off as photons cannot be scattered up to higher energies than those of the electron population (Madejski et al., 1995, Guainazzi et al., 1999, Nicastro et al., 2000). The shape of the continuum spectrum above a few tens of keV is only poorly determined due to the lack of sensitive observations at those energies, while it is well known that the exponential cut-off must be around 50-500 keV (Gilli et al., 2007).

(*ii*) *Fe Kα emission line and the reflection Compton hump*: As noted in section 1.5.2 the two-phase accretion disc generates a (secondary/processed) X-ray reflection spectrum. This assumption can be easily understood by considering a hard X-ray continuum (of power law shape) illuminating a semi-infinite slab of cold gas. In this context, ‘cold’ means that metal atoms are essentially neutral, but H and He are mostly ionized. Then, a hard X-ray photon penetrating in the slab can suffer three different interactions: (1) Compton scattering by free or bound electrons, (2) photoelectric absorption followed by fluorescent line emission and (3) photoelectric absorption followed by Auger de-excitation. Therefore, the hard X-ray photon can be (1) scattered out the slab with a lower energy than the incident one, (2) reprocessed into a flourescent line photon which escapes the slab, or destroyed by a Auger de-excitation implicating the emission of a new electron (Krolik & Kallman, 1987, Matt et al., 1991, Fabian et al., 2000). All these processes are included in the Monte Carlo simulation carried out by Reynolds (1996) shown in figure 1.9, where two remarkable characteristics should catch our attention: a broad-hump shape and a set of well defined emission lines. Photoelectric absorption exhibit a energy dependence such soft X-ray photons are mostly absorbed, whereas hard photons are rarely absorbed and tend to Compton scatter back out of the slab. This cold reflection shapes the showy hump at hard X-rays, peaking around 20-30 keV (see Fig. 1.9 and 1.8), where reflection efficiency reaches its maximum (Piro et al., 1990), although its shape and its strength depend on the geometry, chemical composition, and orientation to the LOS.

Then, the emission line spectrum results mainly from fluorescent $K\alpha$ lines of the most abundant metals, being the iron $K\alpha$ line at 6.4 keV the strongest one. The line profile can be used to examine the movement and gravitational field at the location where the reflection takes place. Intrinsically the fluorescence lines should be narrow. However, the lines are often broad if originating from the surface of the central accretion disc, and/or narrow and if due to X-ray illuminating of the cold gas in the innermost regions of the torus.

This reflection component is superposed on the direct primary continuum (power-law) flattening it above 10keV (as the reflection hump starts to emerge) and allowing the strong Fe $K\alpha$ line to arise. For solar or cosmic abundances and a plane-parallel slab geometry, the expected equivalent width of the line is 150-200 eV (George & Fabian, 1991).

(*iv*) *Soft excess:* Another recurrent X-ray feature is a "soft excess" below 1-2 keV discovered by Singh et al. (1985) and (Arnaud et al., 1985). While Sy2 galaxies are generally highly absorbed, the absence of absorption allows us to see a soft X-ray emission in excess of the extrapolation of the hard X-ray continuum in many Sy1 nuclei below 1 keV. It cannot be resolved into a series of emission lines with gratings, although there are some discrete emission/absorption features superimposed on it. Its origin is still under debate although it looks like an apparent continuum component, but it is at far too high a temperature to be simply the high energy tail of the accretion disc emission. Three models have been proposed to justify its origin: *(1)* an additional Comptonization component (Dewangan et al., 2007), *(2)* an additional ionized reflection (Crummy et al., 2006) and *(3)* a complex or ionized absorption Done et al. (2007).

(*v*) *Warm absorbers:* Soft X-ray absorption by ionized gas in our LOS, i. e. the so-called *warm absorbers*, was first discovered by Halpern (1984), against the *cold or neutral absorbers* provided by the torus at extended distances. Since then, evidence of warm absorption has been detected in about half of Sy1 galaxies with column densities up to

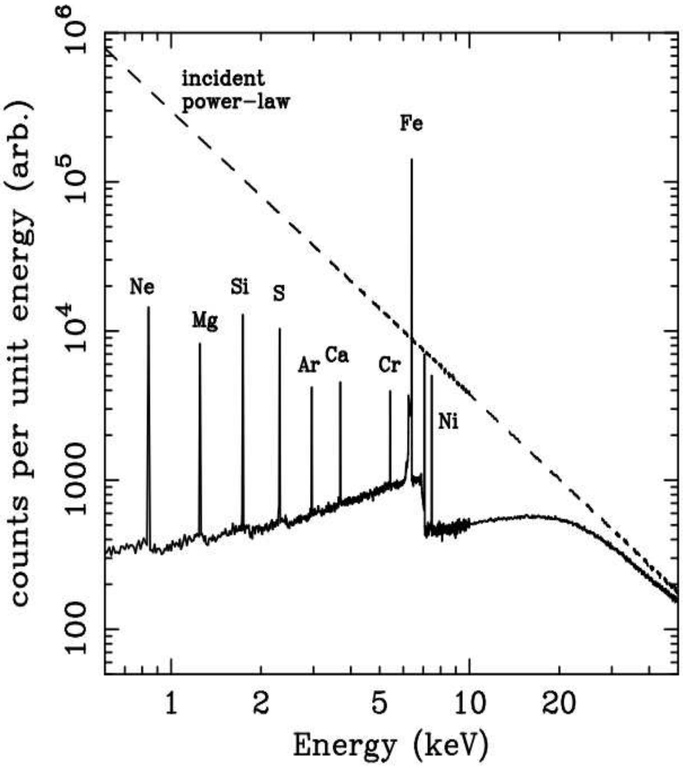

FIGURE 1.9: *X-ray reflection from an illuminated slab* - Monte Carlo simulation carried out by Reynolds (1996) representing the X-ray reflection from an illuminated slab. Dashed line shows the incident continuum and solid line shows the the reflected spectrum integrated over all angles.

$N_H \sim 10^{23} cm^{-2}$(Reynolds, 1997) and now we know that they are photo-ionized by the primary X-ray continuum and also known to vary. A warm absorber inprints over the spectrum both absorption and re-emission lines. There is some evidence for its origin as a wind from the dusty torus envisaged in unification models for Seyfert galaxies (Blustin et al., 2005), but cases in which an origin from the accretion disc seems to be preferred do also exist (Krongold et al., 2007).

To sum up, the general observed X-ray spectrum of unabsorbed Seyfert galaxies consists of the primary continuum with its corresponding cut-off at high energies, and a reflection component with signatures of photoelectric absorption, iron fluorescence and Compton scattering inprinted over a broadband spectrum. In addition, cold and warm absorption can also appear while a soft excess is observed in some cases.

1.7.2.1 Absorption

All components described above are schematically represented in Fig. 1.8, where an unabsorbed (type 1) prototype AGN is pictured as a solid line. Nonetheless, we can also encounter moderately obscured AGN, i.e. *Compton-thin sources* and strongly absorbed (type 2) AGN, i.e. *Compton-thick sources*. The distinction between absorbed and unabsorbed could be establish approximately around $N_H \sim 10^{21} - 10^{22} cm^{-2}$ but this is always a arbitrary diving line. In Fig. 1.10 it is shown how a typical X-ray spectrum is affected by different column densities, from an unabsorbed case (i.e type 1) to an opposite Compton-thick case (i.e type 2), passing through Compton-thin states. At energies above 10 keV absorption will have very little effect on the X-ray emission, unless $N_H \gtrsim 10^2 5 cm^{-2}$

Absorption only affects components that are not associated to extended emission on scales larger than the absorber's. Therefore, emission due to scattering on kpc scales or emission lines arising from star formation or gas photoionized by the AGN (green components in Fig. 1.10) will remain unaffected even for absorption at the torus scale, as well as the the reflection of the power law continuum by distant gas (red components in the same Fig.). In the cases of absorbed AGN these components became observable since they are no longer buried below the continuum level as in unabsorbed AGNs. Thus, a typical very absorbed AGN will exhibit a strong Fe line arising from distant reflection and different emission lines in the soft X-ray band while the common spectrum of an unabsorbed AGN will be dominated by the X-ray power law continuum.

A scheme of how absorption affects the different emitting regions is show in Fig. 1.12. The primary X-ray continuum is represented as solid blue arrows. As shown in that same figure, the accretion disc is not the only reflector able to produce a X-ray reflection, the torus itself is Compton-thick and therefore act as such. Both reflection contributions can be distinguished since the spectral line profiles arising from the center of the accretion disc will be altered by special and general relativistic effects (Fabian & Miniutti, 2005).

As discussed above, there is evidence for the presence of warm gas surrounding the central nucleus, the so-called *warm absorbers*. This photo-ionized gas is detected thanks to its contribution to the total spectrum in absorption. These effects are displayed on Fig. 1.11, where two different warm absorbers, one of low ionization and the another one highly ionized, are superimposed over the unabsorbed example shown on upper-left panel of Fig. 1.10.

In Sy1 galaxies, the continuum level is not absorbed and the the constant emission components from extended regions are diluted and generally not observable whereas, in Sy2 galaxies, the primary continuum is heavily absorbed by the large column densities of the torus, so that the large scale environment of the AGN becomes detectable via emission lines, scattering and reflection components. On the contrary, the warm absorption is easier to detect in Sy1 nuclei

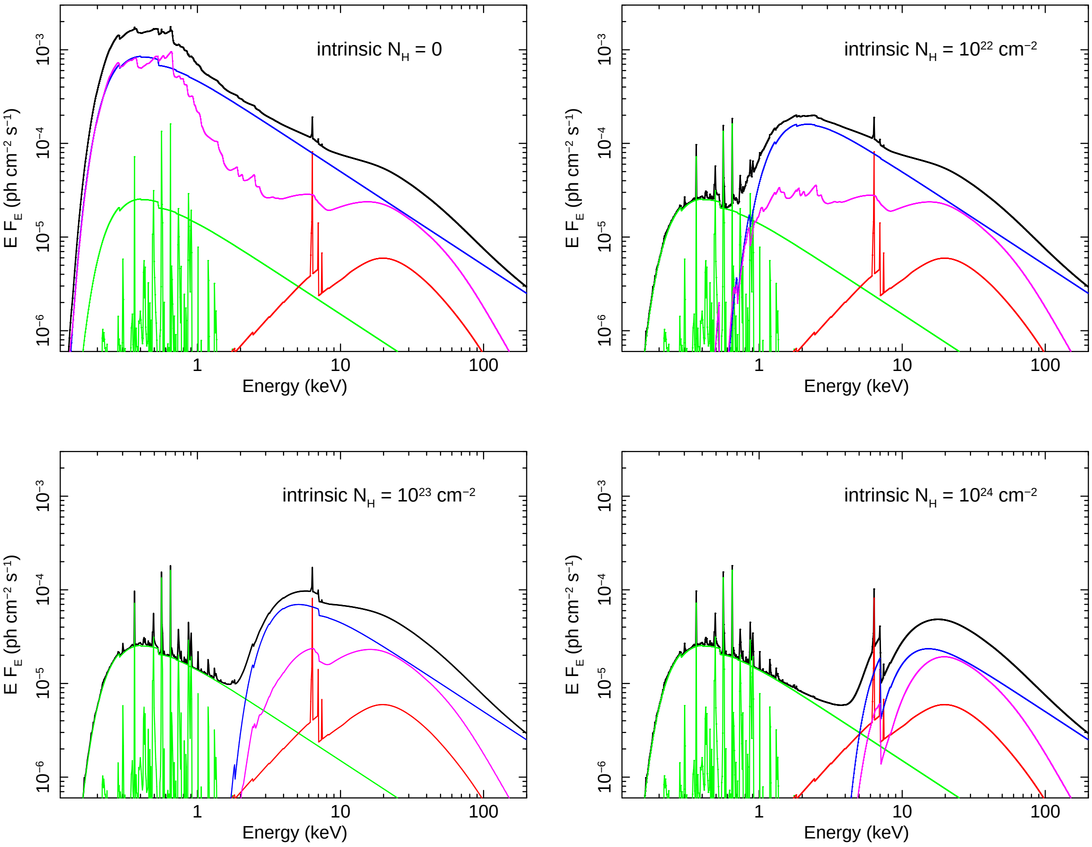

Figure 1.10: Absorption effects on typical X-ray spectral components. An increasing intrinsic column density is applied to a general unabsorbed X-ray model (top left panel) up to get to a Compton-thick state ($N_H = 10^{24} cm^{-2}$). The intrinsic absorption applied in each case is indicated on the upper-right corner of the corresponding plot. Black lines represent the total spectral model. Blue component coincides with the power law X-ray primary continuum. Green shows the extended emission caused by distant scattering (green power law) and also emission lines arising from photoionized gas or star-forming regions. Red represents the reflected X-ray continuum by distant neutral gas. Finally, magenta displays the X-ray reflected continuum by the accretion disc. High velocities and strong gravitational effects distorts the resulting spectrum.

due to precisely the higher level of continuum. Thus, the (generally outflowing) ionized gas gives rise to absorption lines that can be used to derive the column density, ionization state and outflowing velocity of the warm absorber. The general results points out to rather compact locations for the warm absorbers and place them at distances of the inner torus or closer. Therefore they do not have an effect upon the extended emission and, on the contrary, they influence the compact emission (nuclear continuum and disc reflection).

1.7.2.2 Spectral X-ray absorption variability: softest X-ray bands

When the absorbing column density is $N_H > 1.5 \times 10^{24} cm^{-2}$, it becomes optically thick to Compton scattering giving rise to the so-called *Compton-thick sources* (Awaki et al., 1991, Matt

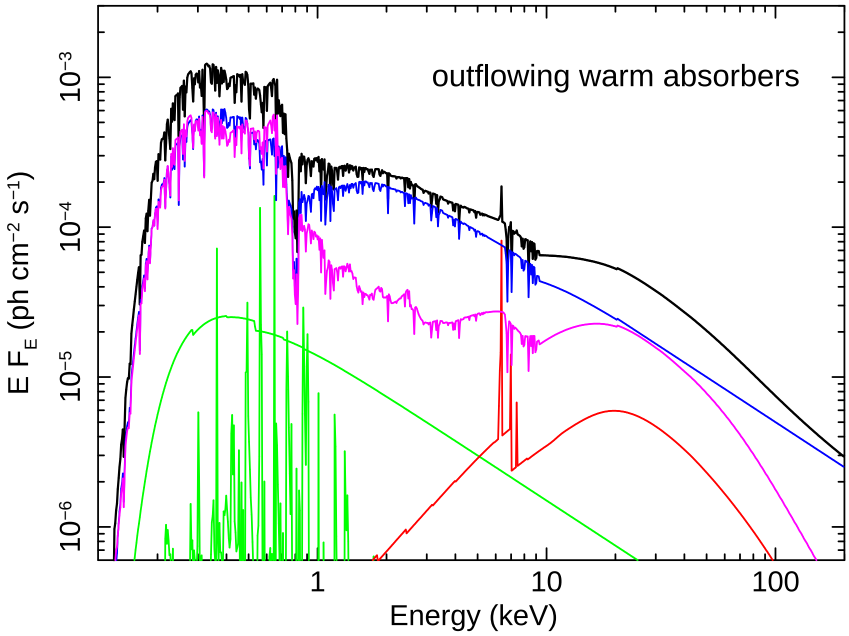

FIGURE 1.11: Here it is shown how two warm absorbers, one with low and another one wit high ionization, affect the typical X-ray spectrum of an AGN (upper-left panel of Fig. 1.10).

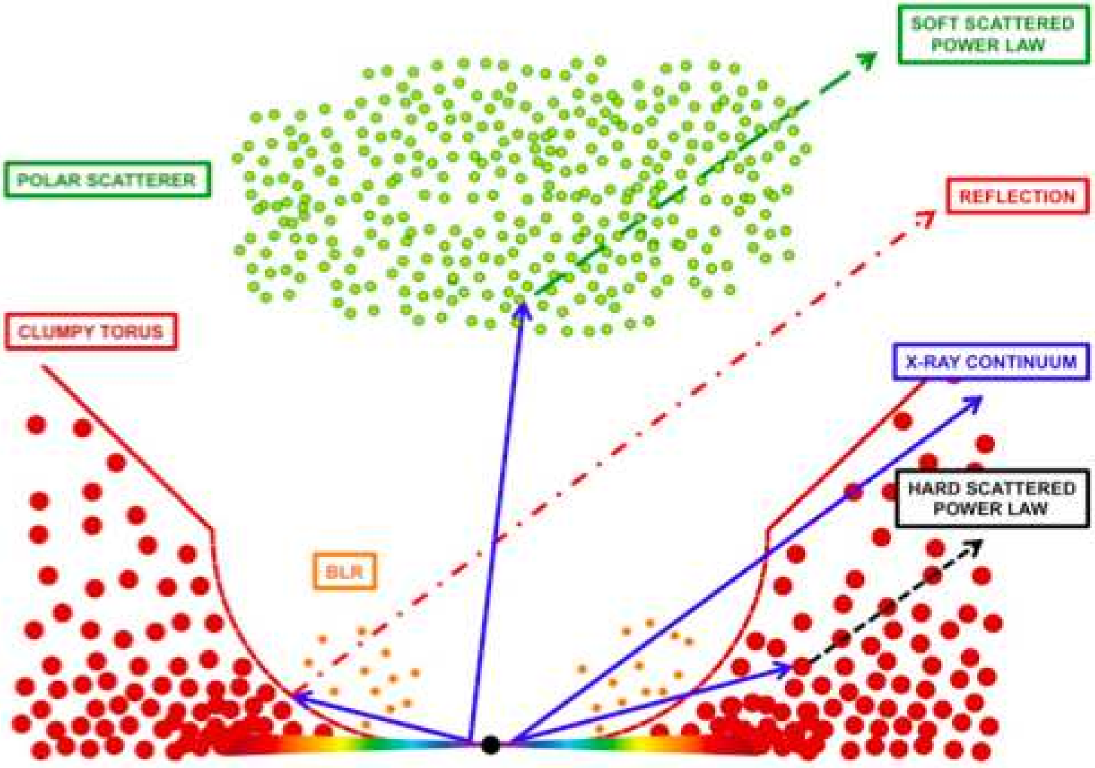

FIGURE 1.12: Scheme representing one of the possible schemes describing the geometry of the innermost AGN regions. Image credits: Miniutti et al. (2014).

et al., 1993). Their direct component is completely absorbed below 10 keV (i.e. *hard X-rays* while the 0.1-2 keV range is commonly designed as *soft X-rays*). However, the nuclear radiation can be still Compton reflected by the cold obscuring torus or scattered by free electrons in a highly ionized warm gas. If these media extend outside the absorbing torus, then signatures of the X-ray nuclear activity are observable via the reflected/scattered continuum.

On the other hand, if the column density is between $21 < \log N_H < 24$, the AGN is classified as a *Compton-thin source* (Gilli et al., 2007). However, Risaliti et al. (2002) analyzed a sample of 25 Sy2 galaxies and found that 90% of them showed significant variations of their absorption column density. This is another fact that forces to assume some clumpiness in the torus model for the absorber. One of the most prominent of those “changing look” AGN is the Seyfert 1.8 NGC 1365, which changes from a Compton-thick to Compton-thin absorber and back on a monthly timescale, while the X-ray reflection spectrum does not vary (Risaliti et al., 2005).

1.7.2.3 Fe $K\alpha$ emission line and its implications: relativistic effects

As expected by UM, Sy1 nuclei appear to be the clearest evidence of X-ray reflection (Nandra et al., 1990, Nandra & Pounds, 1994), and it is precisely in these objects where the Fe $K\alpha$ line is found broader and asymmetric, with an extensive red wing (Fabian et al., 2000, Fabian & Miniutti, 2005), despite being emitted locally as symmetric and intrinsically narrow. Such a broad and asymmetric shape is expected if X-ray reflection occurs in the inner regions of an accretion disc, since only in the neighborhood of a black hole, strong Doppler shifts and gravitational redshifts combine to produce an extensive low-energy wing and a sharp truncation of the line at high-energies (Fabian et al., 1989). In that case, besides Newtonian distortions, special and general effects shape the line profile as shown in Fig. 1.13. In a non-relativistic case, each radius of the disc will produce a symmetric double-peaked line profile. The two peaks correspond to emission from material on both the approaching (blueshifted) and receding (redshifted) sides of the disc (top panel of Fig. 1.13). Closer to the black hole, orbital velocities of the disc become mildly relativistic and, consequently, the blue peak is intensified (second panel). Moreover, the transverse Doppler effect shifts the contribution of each radius to a lower energy. In the innermost vicinity of the black hole, where gravity becomes so strong, gravitational redshifts cause the displacement of the entire line profile (third panel). Adding the line emission from all radii of the relativistic disc results in a asymmetric and highly broadened line profile (bottom panel). Since relativistic beaming and gravitational light bending effects depends on the angle of LOS, the disc inclination will determine the maximum energy at which the line can be seen.

Thus, the Fe $K\alpha$ line profile has the extraordinary potential of revealing the dynamics of the innermost accretion flow in SMBH. In addition, the line profile for a non-rotating Schwarzschild

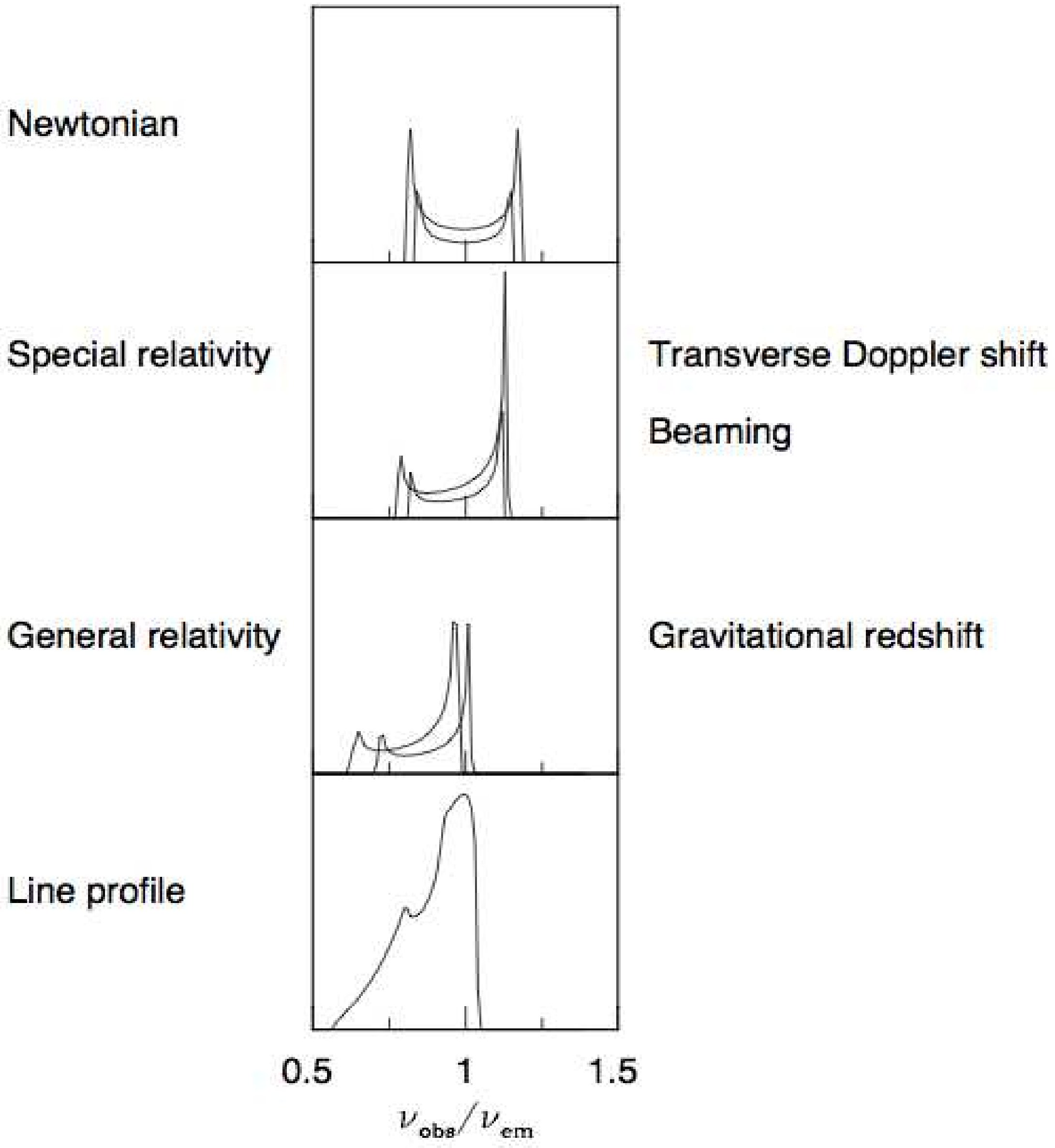

FIGURE 1.13: The asymmetric and broad profile of the Fe $K\alpha$ emission lines is the result of the interplay of Doppler and transverse Doppler shifts, relativistic beaming and gravitational redshift as shown in the three panels that are separated according to their velocity/gravity regime. Image credits: Fabian et al. (2000).

case will look different from the case of a spinning black in which a Kerr metric has to be considered (Laor, 1991, Martocchia et al., 2000). In this way, the relativistic broad Fe line also represents a unique tool from X-rays observations to probe the strong gravity regime of General Relativity in a way unaccessible to other wavelengths. The disconcerting spectral variability seen in some sources can be understood by considering strong gravitational bending of the radiation emanating close to a rotating Kerr black hole.

Moreover, the line will vary as a function of the geometry of the accretion disc (primarily

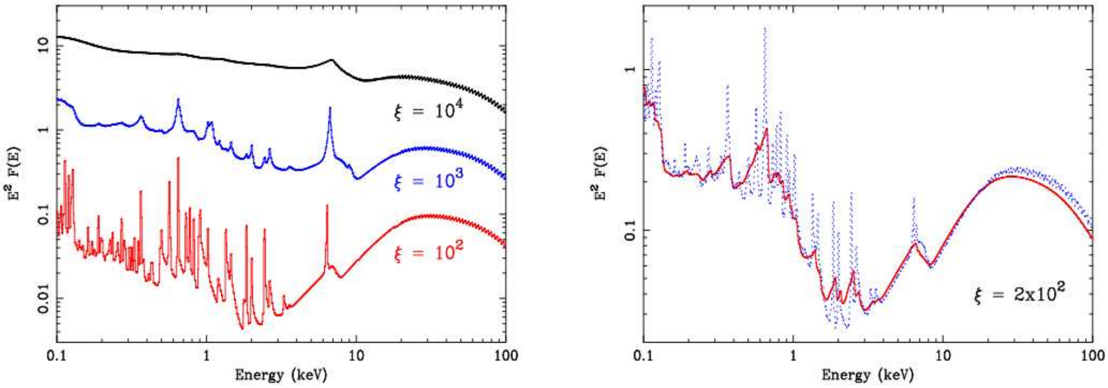

FIGURE 1.14: X-ray reflection model for three different values of ξ (left panel) and taking into account the relativistic effect (right panel). See text for details. Image credits: Fabian & Miniutti (2005).

the solid angle subtended by the reflecting matter as seen by the X-ray source), the elemental abundances of the reflecting matter, the inclination angle at which the reflecting surface is viewed and the ionization state of the surface layers of the disk among others (Tanaka et al., 1995, Miniutti et al., 2004, Miniutti & Fabian, 2006).

On the other hand, XMM-Newton and Chandra spacecrafts have revealed narrow Fe $K\alpha$ emission lines on bright Seyfert galaxies (Yaqoob & Padmanabhan, 2004, Nandra, 2006). Such unresolved Fe lines are most likely emitted by a reflector located at some distance from the central nucleus, as the outermost accretion disc and/or even more distant matter such as the torus or the BLR clouds.

1.7.2.4 Ionization

Until here, we have considered a simplification of the accretion disc (or to be more precise its external layers). The real situation is likely more complicated than the assumed slab of uniform density gas where hydrogen and helium are fully ionized, but all the metals are neutral. A further approach to reach a more representative model is to take into account thermal and ionization equilibrium. The ionization parameter, ξ, is defined as the ratio between the isotropic total illuminating flux and the corresponding hydrogen number density of the gas. Ross & Fabian (2005) developed a successful model which assumes the illuminated radiation to have an exponential cut-off power law form with high-energy cut-off fixed at 300 keV and variable photon index Γ between 1 and 3. They computed results for ξ ranging from 1 to 10^4 $erg\ cm\ s^{-1}$. The local temperature and fractional ionization of the gas are computed self-consistently by solving the equations of thermal and ionization equilibrium and C, N, O, Ne, Mg, Si, S, and Fe ions. The Fe abundance can be variable. The X-ray reflection spectra produced by this code for three different values of ξ, keeping the remaining parameters constant, are shown in the left panel of Fig. 1.14. The effect of the ionization over the spectrum is clear and even more remarkable on the emission lines. For the higher parameter of ionization, $\xi = 10^4$ $erg\ cm\ s^{-1}$ (top black spectrum), the surface layer is very highly ionized and the only noticeable line is a highly Compton-broadened Fe $K\alpha$ line, while the overall spectral shape closely resembles that of the illuminating continuum. For the intermediate value shown of $\xi = 10^3$ $erg\ cm\ s^{-1}$ (blue spectrum), the $K\alpha$ lines from the lighter elements begin to emerge in the 0.3-3 keV and the Fe line becomes dominated by the Fe XXV intercombination line. The lowest value of the ionization parameter, $\xi = 10^2$ $erg\ cm\ s^{-1}$ (red spectrum), gives way to emission lines features below 3 keV over a largely absorbed continuum and the residual Compton broadening of the emission disappears. In conclusion, the less ionization, the more density of emission lines and the more visible absorption. The right panel of the same figure represents the relativistic effect over the reflection spectrum keeping the lowest ionization parameter shown, $\xi = 10^2$ $erg\ cm\ s^{-1}$. The blue version model corresponds to the X-ray reflection spectrum in the absence of any relativistic effect, whereas the red one shows the relativistically-blurred version of the same model keeping fixed its parameters. The sharp emission features are broadened by the relativistic effects described in the former subsection 1.7.2.3. However, the Fe line remains clearly visible thanks to its strength, isolation, and location on a region of the X-ray spectrum relatively free from absorption. This fact adds another advantage to the valuable mine of knowledge that the Fe $K\alpha$ emission line is able to provide.

1.8 AGN variability

From the very beginning, one of the defining characteristics of AGNs was their variable emission over the whole electromagnetic spectrum. These variations do not appear to be periodic and exhibit variable amplitude whereas the mechanism for producing them is not totally clear yet (Nandra, 2001).

The first hint of AGN variability was found in quasars. Smith & Hoffleit (1963) and Matthews & Sandage (1963) proved significant variations ($\geq$ 0.1 mag) in the optical brightness of these objects on time scales as short as days. The detection of variability in quasars within days represented a landmark since it implied that the size of the emitting region must be also the order of lights days (1 tl-day= 2.6×10^{15} cm). If a source varies coherently the entire emitting region must be causally connected, then the maximum size for the emitting source must be directly related to the light-travel time (Peterson, 2001). Therefore, the variability time scale translates into an upper limit to the ratio between the size of the emitting region and the velocity at which the changes propagate. That means that variability is a powerful tool to probe physical properties of the innermost unresolved regions of AGNs and give rise to the question of how so much energy can be produced in a region that is about the size of the Solar System for typical

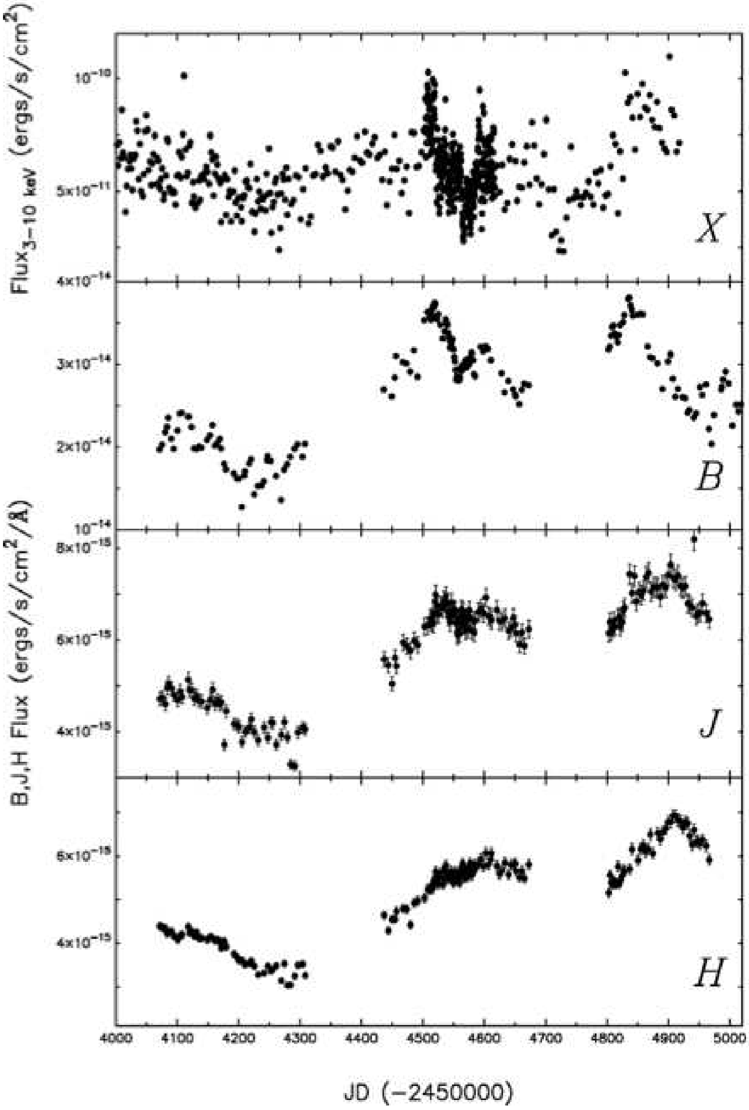

FIGURE 1.15: *Continuum variability of Seyfert 1 galaxy NGC 3787 at X-ray, optical and IR wavelengths* - The variability on long time scales is well correlated among the different bands although the corresponding amplitude is decreasing with larger wavelengths. Short time scale variability is clearly more significant in X-ray band and decays with longer wavelengths. Image credits: Lira et al. (2010)

black hole mass. Indeed, the original arguments for the existence of SMBHs in AGNs arose from size constraints determined throughout variability together with mass constraints derived from the Eddington limit.

Multi-wavelength light curves are used to study the physical and geometrical connections between the different regions around the central engine. The early accepted scenario for the interplay of these emitting regions is that variability is driven by the emission from the X-ray corona (Krolik et al., 1991, Collier et al., 1999, Cackett et al., 2007). In general, continuum variability of AGN is color-dependent: the blue bands show higher variability amplitude than

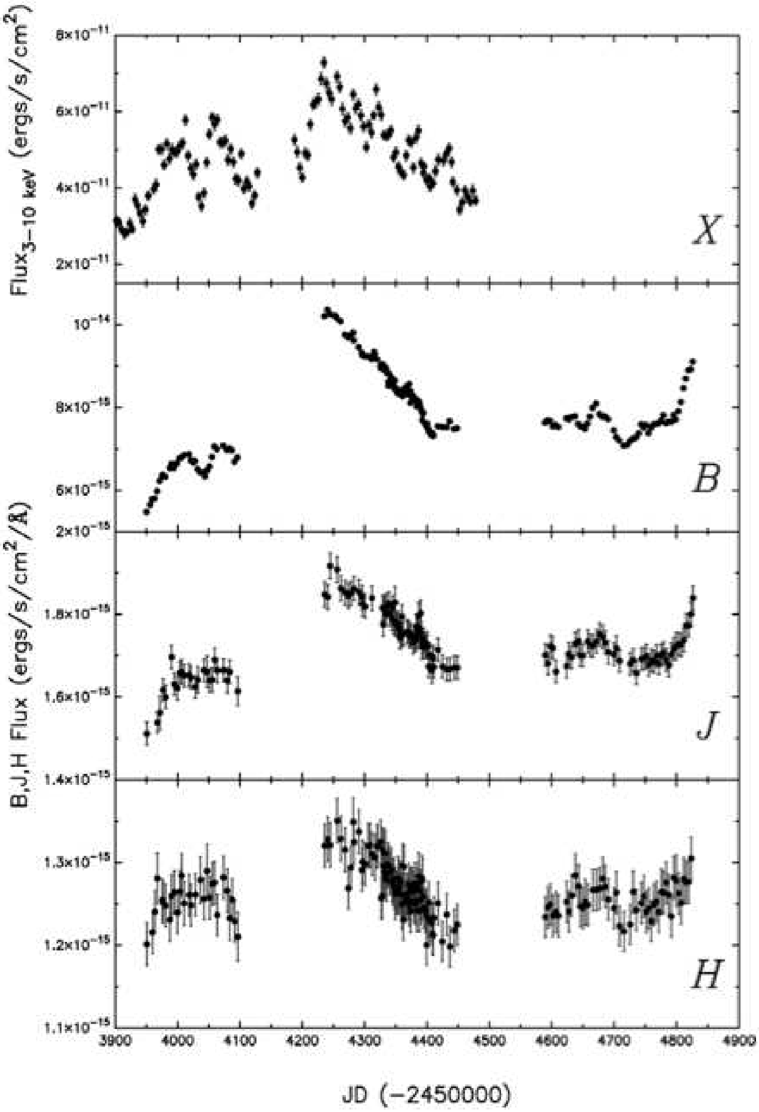

FIGURE 1.16: *Continuum variability of the nearby quasar MR 2251-178 at X-ray, optical and IR wavelengths* - X-ray band presents the largest amplitude variations over time scales of days to weeks. However the optical wavelengths show larger amplitudes of variation over time scales of months to years . Image credits: Lira et al. (2010)

the red bands. This is consistent with the statement that the optical continuum represents predominantly thermal emission from the accretion disc and longer wavelength emission arise from larger radii where the disc is cooler. The outer, larger and cold disc is thought to respond more slowly than the inner, compact and hot regions. Indeed, the response of dust in IR wavelengths lags variation of the UV flux. However, coordinate multi-wavelength monitoring campaigns are not always consistent with this picture (Beckmann & Shrader, 2012). For instance, Lira et al. (2011) carried out a 3-year X-ray and optical-IR monitoring of both the Sy1 galaxy NGC 3787 and the nearby quasar MR 2251-178. Their results for NGC 3787 are shown In Fig. 1.15. The variability is well correlated among the different bands on long time scales while the corresponding amplitude is decreasing towards the bottom of the figure with less energetic bands.

At the same time, the short time scale variability is clearly more significant in X-ray band and it decreases with longer wavelengths. Their results for MR 2251-178 (see Fig. 1.16) show that X-rays present the largest amplitude variations over time scales of days to weeks but optical wavelengths show larger amplitudes of variation over time scales of months to years. These results are not compatible with the idea of X-ray reprocessing driving all this observed variability. Lira et al. (2011) could reproduce the overall variability of MR 2251-178 by models invoking both variable accretion rates and X-ray reprocessing.

On the other hand, delays between variations of, for example, continuum and emission-line spectral components together with the involved time scale, provide essential information on the locations and properties of those components. In fact, this is the basis of the *reverberation mapping* technique as already discussed in section 1.5.1.

1.8.1 UV/optical variability

Similarly, the origin of the the UV/optical variability of AGN is still not clear and there are also three main possible pictures that can explain the phenomena, which are not mutually exclusive and can coexist (McHardy et al., 2016):

(*i*) It can be result from reprocessing of X-ray emission by the accretion disc and the hot corona. This should lead to measurable time delays between the optical and X-ray light curves (Beckmann & Shrader, 2012). UV/optical variations will lag behind the X-ray variations by the light travel time between the two emission regions. This time is of the order of a few hours in a typical AGN.

(*ii*) It can be due to intrinsic variability of the thermal emission from the disc. If UV/optical photons are the seed photons for the X-ray emission, throughout inverse Compton scattering within the X-ray corona, then the X-ray variations are produced by seed photon variations and therefore the X-ray emission will lag behind the UV/optical variations by the light travel time between the two emitting region, so a few hours again.

(*iii*) If UV/optical variability is a product of inwardly propagating accretion rate variations, these variations will propagate at the viscous disc and will affect the X-ray emission region (Arévalo & Uttley, 2006). As a result the X-ray variations will lag the UV/optical varations by some years.

Therefore, neither the relationship between UV/optical variability and X-ray variability is clear. In general, strong X-ray/UV or X-ray/optical correlations, with short lags of less than a day, have been observed on short time scales (weeks - months) (Uttley et al., 2003, Arévalo et al., 2009). However, these same studies show poorer correlations on longer timescales (months -

years): often the long-term UV/optical variability is not reproduced by the X-ray variations, suggesting that UV/optical variability is dominated by different processes depending on the timescale involved (intrinsic variability on long timescales and reprocessing on short ones).

1.8.2 X-ray variability

The rapid X-ray variability of AGN is thought to originate in the innermost region of the accretion flow what reinforces the presence of SMBHs since it implies very compact emitting sources. Among the spectral X-ray emission components, the soft excess and the power law are variable. The medium energy power-law component in general varies in intensity with very little change of the spectral index (Ulrich et al., 1997). In some well-observed AGN, the flux variations are accompanied by a softening of the spectrum with increasing intensity, see e.g. Mushotzky et al. (1993).

As already discussed, X-ray flux and spectral variability can also be due to absorption by the circumnuclear, clumpy torus or by clouds of the BLR. In this context the variability time scale will provide us with relevant information about the absorber. Long time scale absorption variability are usually associated to transits of dusty absorbing clouds in our LOS, proving the clumpy nature of the dusty torus at relatively large radii, e.g. Rivers et al. (2011), Agís-González et al. (2014). On the contrary, short time scale absorption variability (from hours to days) suggests absorbing clouds placed at shorter radii, probably belonging to the BLR, e.g. Risaliti et al. (2009), Sanfrutos et al. (2013). Let us discuss briefly both cases.

- **X-ray absorption variability within the sublimation radius: sub-parsec scales**

  The evidence for gas absorption within the sublimation radius comes mostly from X-ray observations and the most direct way to probe the presence of such gas component is through X-ray absorption variability measurements. As noticed, column density variations are often observed in Seyfert galaxies (e.g. Risaliti et al. (2002)), which means that the X-ray absorber must be clumpy. In some cases, the involved timescales are so short that the clumpy absorber can only be located at sub-parsec distances from the central source. In particular, in the case of NGC 1365, *Chandra*, *XMM-Newton* and *Suzaku* observations revealed extreme spectral changes, from Compton-thin ($N_H \sim 10^{23} cm^{-2}$) to reflection-dominated ($N_H > 10^{24} cm^{-2}$) states on time scales ranging from a couple of days to $\sim$ 10 hours (Matt et al., 2003, Risaliti et al., 2005, Bianchi et al., 2012). Such rapid events imply absorbing clouds with velocities $v > 10^3 km\ s^{-1}$ and placed at distances of the order of $\sim 10^4$ gravitational radii from the SMBH. Assuming that these clouds are homogeneous with a constant column density, and that they are moving across the LOS with Keplerian velocity, their physical size and density are estimated to be of the order of $10^{13} cm$ and $10^{10} - 10^{11} cm^{-3}$, respectively. All these derived parameters are consistent with BLR clouds, strongly suggesting that the variable X-ray absorber seen in NGC 1365 and other similar sources and the clouds responsible for broad emission lines in the optical/UV are one and the same.

High signal-to-noise data of X-ray "eclipse" can provide further information on the geometrical and physical structure of the clouds (e.g. Maiolino et al. (2010), Risaliti et al. (2011)). X-ray absorption variability within the sublimation radius will be further discussed in Chapter 3.

- **X-ray absorption variability from the pc-scale torus**

  While X-ray absorption variability studies have reported exquisite information on the structure of the absorbing medium on scales of the BLR, the same kind of analysis is difficult to perform on the parsec scale absorber because the time scale for variation is much longer and hence difficult to detect the absorption events. However, there exits some registered cases, e.g. Marinucci et al. (2013), Miniutti et al. (2014), which points towards a clumpy torus origin (Nenkova et al., 2008a,b). X-ray absorption variability conducted by the pc-scale torus will further discussed in Chapter 2.

1.9 Motivation and structure of this thesis

The main motivation behind this work is to significantly contribute to the refinement of the UM of AGN, namely the basic idea that all AGN are intrinsically the same (apart from some physical distinction based for example on the ability, or lack of it, of launching collimated relativistic jets), and that their widely different observational properties can be understood, to first order, in terms of LOS orientation with respect to an ubiquitous toroidal, circumnuclear obscuring structure: the dusty molecular torus (see section 1.6). Several pieces of observational evidences accumulated since its formulation have provided support to this scheme. The success of this general unification model has been extraordinary and allowed us, in the past 30 years or so, to clarify and unify in a common framework the often remarkably different observational phenomenology of Active Galactic Nuclei.

However, in the past few years, outliers have emerged challenging the UM and calling for some modifications of the general scheme. Another of the most remarkable cases is that of the so-called changing look AGN, namely the cases of AGN whose optical spectral properties are seen to change from one classification to another of the course of time: some AGN are seen to change from a type 1 classification in the optical (i.e. optical spectra with broad permitted emission lines as well as narrow permitted and forbidden lines) to a type 2 classification (only narrow lines). In the general unification scheme, type 1 nuclei are those offering a clear view of both the extended NLR and the compact BLR, i.e. sources in which our LOS does not intercept the obscuring circumnuclear torus. Obviously, type 2 nuclei are those in which our LOS towards the BLR is instead obscured, so that optical spectra only reveal narrow lines (as well as a typically fainter and non-variable nuclear continuum). As a consequence, the only plausible explanation within the UM scheme for changing look AGN would be that a standard type 1 nucleus exhibits a type 2 optical spectrum if the nucleus has switched off, i.e. only if no ionizing continuum is available anymore to illuminate the gas responsible for the emission of the broad lines leaving, as a relic, only narrow emission lines that are produced in such extended regions that their response to the nuclear continuum drop is much slower (on typical timescales of hundreds of years or more).

On the other hand, X-ray observations of AGN have revealed that X-ray absorption towards the nuclear continuum often varies on timescales ranging from days (or even hours) to months and years. As X-ray absorption generally also obeys to the Unification scheme, i.e. type 2 nuclei are much more heavily absorbed in the X-rays than type 1 sources, the X-ray absorption variability may be thought of as a sign that the Unification Model is not dynamic enough to represent the real situation.

In order to study and contribute to this field, we focus here our attention on one particular Seyfert galaxy, ESO 362-G18. The reason is that historical optical spectra (from Six-degree Field Galaxy Survey (6dFGS) in January 2003 and from ESO Multi-Mode Instrument (EMMI) in September 2004) indicated that ESO 362-G18 is indeed a member of the changing look AGN class, as the 2003 6dF spectrum only shows narrow emission lines, while the EMMI@New Technology Telescope (NTT) one clearly exhibits strong broad H_α and H_β emission lines as well. We then decided to study this Seyfert galaxy in all possible detail, retrieving all available observations in the optical as well as in the X-rays and proposing for new observations at both wavelengths in order to probe the largest possible range of timescales, as well as to obtain totally new information on the source (as it is the case for our polarimetric observations).

Such changes of look suggest ESO 362-G18 to be a potential candidate to exhibits a remarkable intrinsic variability which can allow us, on one hand, to put physical constraints on the circumnuclear gas and dust both at sub-pc scales and at lager scales of the AGN from X-ray variability , and, on other hand to test the basis of the UM model in optical wavelengths with appear to be a Seyfert galaxy whose optical spectra change of appearance between Sy1 and Sy2.

Thus, at X-ray energies we decided to explore minor timescales presenting a proposal of a new long observation of the source with the aim of look for variability within a day, together with a linked monitoring of the source along 15 days to follow its mood in timescales of several days. Besides, with the aim of deepening in the apparent change of state in the optical band we also decided to observe the source again to find out which state is showing ESO 362-G18 this time. Then, we started a multi-wavelength study from X-ray to optical bands. We will

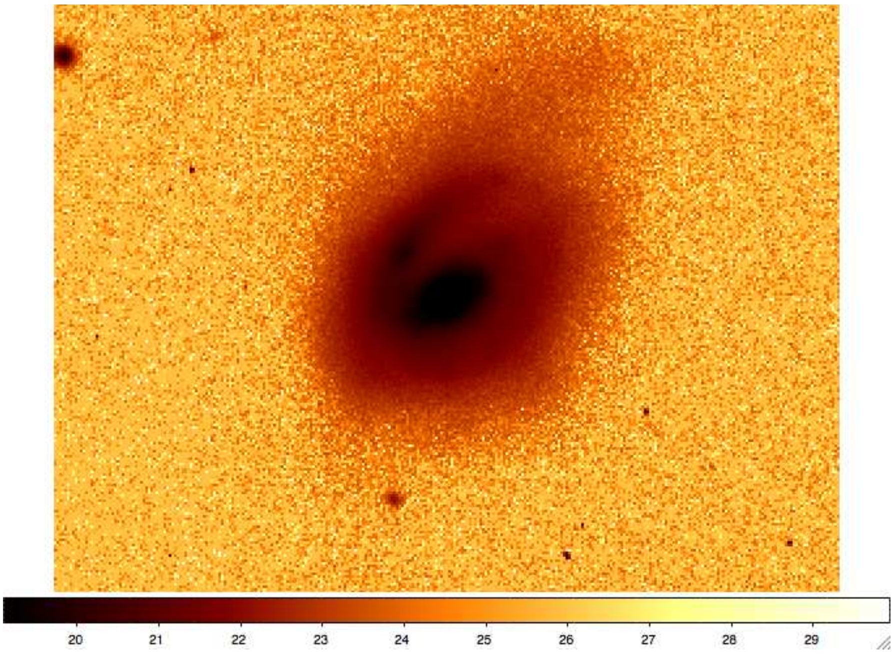

Figure 1.17: Optical image of ESO 362-G18 at 5500Å, the source that we are going to further discuss along this dissertation. Image credits: Hunt et al. (1999)

complement our own observations carrying out a profound search for archive data , where also take advantage of optical telescopes on board some spacecraft to analyze UV data.

Hence, this thesis addresses the following main issues:

(1) Study the X-ray variability of our target in order to assess the functioning of the AGN at sub-parsec scales and get constraints to its physical properties. Can we probe the cause of variability?

(2) Go in depth into the issue of a Seyfert galaxy showing changes of state in its optical spectra. How can we explain this violations of the UM?

Answering the above questions is the main objective of this thesis, which outlines as follows.

In chapter 2, a exhaustive X-ray analysis of the target ESO 362-G18 is carried out on timescales which range from days to years. This study allow us to assess the spectral components of the source establishing a model to define the behavior of the source along the observed epochs. This model get us enable to derive physical parameters of the SMBH and study its environment until torus scales.

In chapter 3, we demonstrate that the former absorption event is not isolate catching our target under a X-ray eclipse event, almost from ingress to egress, which allow us to explore shorter variability timescales and probe the model derived in last chapter.

In chapter 4, we analyzed different optical low and medium resolution spectra of our source that probe ESO 362-G18 as a changing look Seyfert galaxy, fact in concordance with results obtained in chapter 2 and 3.

In chapter 5, we perform a study of our source in polarized light in order to disentangle its apparently changing nature. It is the first study carried out of a changing look Seyfert galaxy using polarimetry to assess its properties.

As complementary study, we also include an appendix where we exploit the mathematical tool called principal component analysis (PCA) to perform a spectral-timing analysis with this technique and assess the energy-dependent X-ray flux variability. The final goal of this ongoing work will be to verify the interpretation derived in chapter 2 but in a model independent way and also obtain a method to be used routinely in future data analysis of X-ray analysis complementing the information that can be derived from traditional spectroscopy and timing analysis.

Chapter 2

A multi-epoch X-ray analysis of the Seyfert 1.5 galaxy ESO 362-G18

This chapter is devoted to a detailed multi-epoch X-ray analysis, performed between November 2005 and June 2010, of the z=0.012 Seyfert galaxy ESO 362-G018, also known as MGC 5-13-17, classified as Seyfert 1.5 by Bennert et al. (2006a). The main goal of this study is to study the X-ray variability exhibited by the source on both long and short time scales. For this purpose, we look for the best-fitting model which describe the variability of the source according to the physics of AGN. Besides determining the cause of the observed variability, our study allow us to derived key parameters the size of the X-ray emitting(s) region(s) and the black hole spin. This chapter is adapted from Agís-González et al. (2014).

2.1 Introduction

In recent years, several examples of X-ray absorption variability in AGN have been reported on relatively short timescales ranging from hours to days, e.g. NGC 4388, Elvis et al. (2004); NGC 4151, Puccetti et al. (2007); NGC 1365, Risaliti et al. (2005, 2007, 2009) and Maiolino et al. (2010); NGC 7582, Bianchi et al. (2009); Mrk 766, Risaliti et al. (2011); SWIFT J2127.4+5654 Sanfrutos et al. (2013). The data are generally consistent with absorption by neutral/low–ionization clouds with typical column density of $10^{22} - 10^{24}$ cm^{-2}, number density of $10^{9} - 10^{11}$ cm^{-3}, and velocity of few times 10^{3} km s^{-1} which suggests to identify the variable X-ray absorber with broad line region BLR clouds. In the best studied cases, occultation events have been followed almost entirely from ingress to egress enabling, e.g. Risaliti et al. (2007, 2009) with NGC 1365 and Sanfrutos et al. (2013) in SWIFT J2127.4+5654, to infer that the X-ray source is compact, and confined within $5 - 10\ r_g$ around the central black hole.

X-ray absorption variability is also seen on longer timescales. These events are obviously more difficult to detect, as the longer timescale ideally requires long and continuous X-ray monitoring campaigns. In the few cases reported so far (e.g. Cen A, Rivers et al. (2011); NGC 4507, Marinucci et al. (2013); ESO 323–G77,Miniutti et al. (2014)) absorption on timescales of a few months can be attributed to clouds with typical column density of $10^{22} - 10^{23}$ cm^{-2} and number density of $10^7 - 10^8$ cm^{-3}, which points towards a clumpy torus origin (Nenkova et al., 2008a,b).

The X-ray luminosity of ESO 362-G18 from a *ROSAT* observation in the early 90s is $\sim 4 \times 10^{41}$ erg s^{-1} in the 0.1-2.4 keV band, much lower than that required to model the extended narrow line region (ENLR) properties, while Fraquelli et al. (2000) detected a ENLR in ESO 362-G018. This suggests that the ROSAT observation may have been affected by X-ray absorption, with different soft X-ray fluxes into our LOS and into that of the ENLR. Subsequent observations with *Swift* and *XMM–Newton* confirm that X-ray absorption variability is present towards the X-ray emitting region of ESO 362-G18, and that the soft X-ray luminosity during unabsorbed states is much higher than that derived by *ROSAT*. In fact, ESO 362–G18 transits from an unobscured state with soft X-ray luminosity of $L_{0.5-2} \sim$ few $\times\, 10^{42}$ erg s^{-1} observed with *Swift* to a highly absorbed state with one order of magnitude lower soft luminosity observed with *XMM–Newton* about 2 months later (Winter et al., 2008).

We have monitored ESO 362–G18 in 2010 with six new observations to study in greater detail the absorption variability towards the X-ray emitting region. To that end, we focus on the general X-ray spectral shape of the source as well as on X-ray absorption variability.

2.2 X-ray Observations and instrumentation

Our dedicated X-ray monitoring of ESO 362-G018 comprises one long exposure (53 ks) taken with *XMM-Newton* Satellite on January 2010 and 5 shorter exposures (10ks) performed with Chandra spacecraft within 15 days between 2010-05-18 and 2010-06-03. Moreover, we consider 3 previous observations of ESO 362-G18 performed with the *Swift*, *XMM-Newton* and *Suzaku* X-ray observatories in 2005, 2006 and 2008 respectively. The first 2 observations were performed only $\sim$ 2 months apart (2005-11-26 and 2006-01-28), and the third was performed about 2.2 years later. The most important details of the observations involved in this work are given in Table 2.1.

Below, we will introduce very briefly each one of the four X-ray observatories and their instruments used for this campaign.

Table 2.1: Details of the performed X-ray observations. The last two columns refer to the X–ray counts collected in a soft and hard energy band. The soft band is the 0.3-2 keV for the *Swift*, XMM 1 and XMM 2 observation, and the 0.5–2 keV for the *Suzaku* and the five *Chandra* observations. The hard band lower limit is set at 2 keV, while the upper bound is 10 keV except for the *Swift* and the five *Chandra* observations, where we use data up to 8.5 keV and 7.5 keV respectively because of SN limitations.

Obs.	Obs. ID	Obs. date	Net exp.	$F_{0.5-2}$	F_{2-10}	Soft counts	Hard counts
Swift	00035234002	2005-11-26	7	3.9 ± 0.1	13.5 ± 0.4	1.7	1.0
XMM 1	0312190701	2006-01-28	8	0.66 ± 0.01	3.7 ± 0.1	4.3	2.1
Suzaku	703013010	2008-04-11	41	27.2 ± 0.1	33.2 ± 0.1	127.4	76.4
XMM 2	0610180101	2010-01-29	53	2.86 ± 0.02	9.58 ± 0.04	107.8	43.6
Chandra 1	11608	2010-05-18	10	2.67 ± 0.05	10.5 ± 0.2	6.5	3.9
Chandra 2	11609	2010-05-19	10	4.29 ± 0.06	13.3 ± 0.2	10.4	5.1
Chandra 3	11610	2010-05-21	10	2.11 ± 0.04	6.5 ± 0.2	5.3	2.5
Chandra 4	11611	2010-05-25	10	10.2 ± 0.1	19.9 ± 0.2	24.0	8.6
Chandra 5	11612	2010-06-03	10	6.55 ± 0.07	14.9 ± 0.2	15.2	5.8

The net exposure (fourth column) is in units of ks. Observed fluxes in the 0.5–2 keV (fifth column) and 2–10 keV bands (sixth column) are given in units of 10^{-12} erg s^{-1} cm^{-2}. The soft and hard X–ray counts (last two columns) are in units of 10^{3} photons.

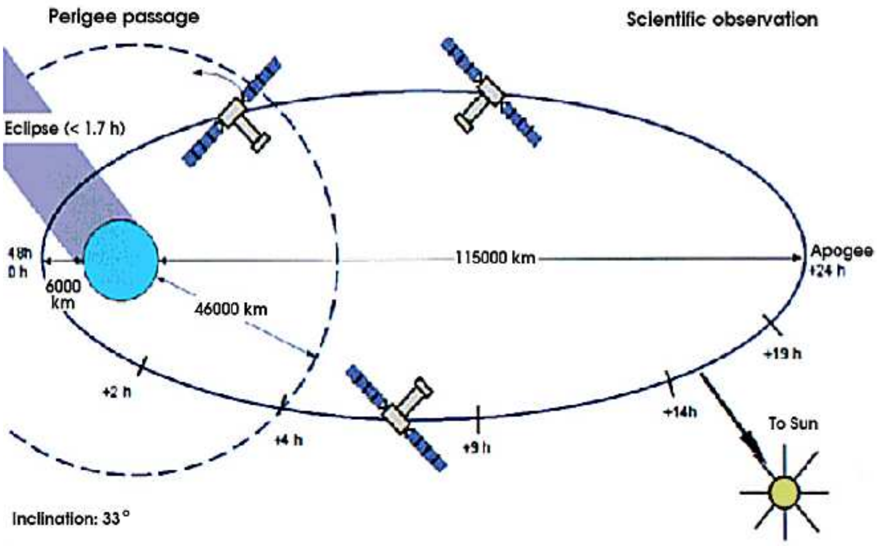

Figure 2.1: Schematic representation of *XMM-Newton*'s orbit . Image credit: http://xmm-tools.cosmos.esa.int/external/xmm_user_support/documentation/uhb/orbit.html.

FIGURE 2.2: *Left:* EPIC-MOS camera. The central CCD is at the focal point on the optical axis of the telescope while the outer six are stepped towards the mirror by 4.5 mm to simulate approximately the focal plane curvature, and improve the focus for off-axis sources. *Right:* EPIC-pn camera presents four individual quadrants, each having three pn-CCD subunits with a format 200 × 64 pixels which are operated in parallel. Image credit: http://www.cosmos.esa.int/web/xmm-newton/technical-details-epic.

2.2.1 XMM- Newton

The X-ray Multi-Mirror Mission *XMM-Newton* was launched by ESA on December 10th 1999. With 10 meters of length and 4 tonnes of weight, it is the biggest science satellite ever built by ESA. It carries on board three advanced X-ray telescopes with an unprecedented effective area along with an optical monitor, the first one on board of an X-ray mission. Its orbit is highly elliptical, traveling at nearly one third of the distance to the moon what enables long interrupted exposures (see Fig. 2.1). In addition, its large collecting area provide us with highly sensitive observations. A key aspect of the design of *XMM-Newton* is that it presents six co-aligned instruments: the European Photon Imaging Camera (EPIC) including the EPIC-pn (Turner et al., 2001) and two EPIC-Metal Oxide Semi-conductor (MOS) (Strüder et al., 2001) imaging detectors, two Reflection Grating Spectrometer (RGS) (den Herder et al., 2001) readout cameras and the Optical Monitor (OM) telescope (Mason et al., 2001) (see Fig. 2.3).

The EPIC cameras were created to exploit the full design range of the X-ray mirrors, they are sensitive in the 0.1-15 keV range in a field of view of 30 arcmin. They give us a spectral resolution of $E/\Delta E \sim 20-50$ whereas their spatial resolution is enough to resolve the mirror performance of 6 arcsec FWHM of point spread function (PSF). All EPIC CCDs operate in photon counting mode with a fixed, mode dependent frame read-out frequency in order to produce the *event lists*, (see section 1.2). Due to the intrinsic energy resolution of the pixels, it is possible to achieve simultaneous imaging and non-dispersive spectroscopy.

Two of X-ray telescopes are equipped with EPIC-MOS CCD arrays, the third uses pn CCDs, so it is referred as EPIC-pn camera. The types of EPIC differ in some major aspects, mainly in their geometries (see Fig. 2.2) and readout times. Both EPIC-MOS cameras consist

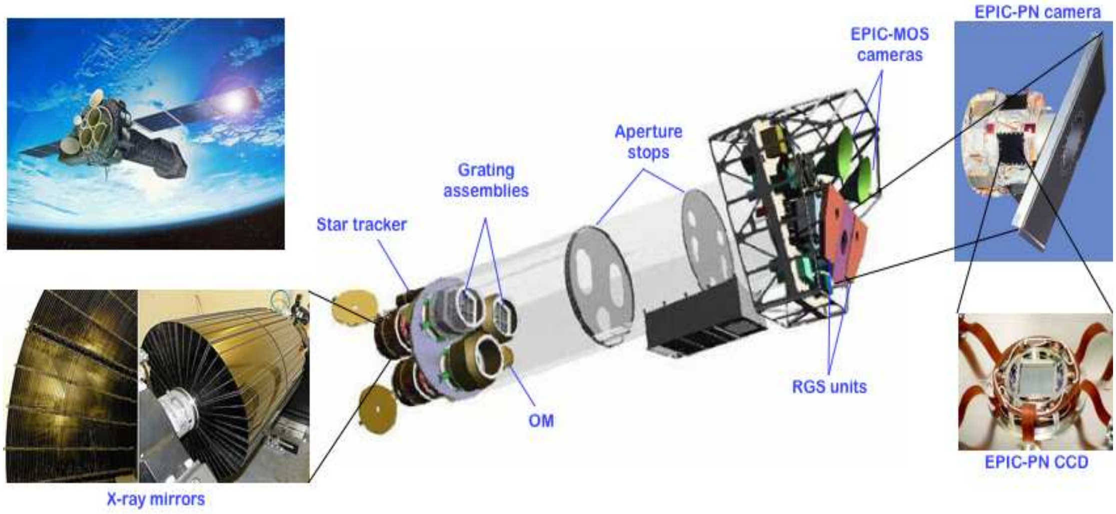

FIGURE 2.3: Reperesentation of *XMM-Newton* spacecraft along with its instruments and X-ray mirrors. The Image credit: http://www.esa.int/Our_Activities/Operations/XMM-Newton_operations.

of seven CCDs, with each CCD made up of 600 × 600 pixels, one pixel covering 1.1 x 1.1 arcsec on the field of view. They are essentially two 2.5 Mpx digital X-ray cameras. The EPIC-pn camera is of a different design, it presents a spatially uniform detector quality over the entire field of view realized by the monolithic fabrication of twelve 3 × 1 cm pn-CCDs of 64 × 200 pixels on a single wafer. Each CCD has a pixel size of 4.4”. Moreover, the pn camera can be operated with very high time resolution down to 0.03 ms in the timing mode and 0.007 ms in the burst mode. However, the absolute timing accuracy is determined by the process that correlates the on-board time to the universal time. The accuracy of the absolute and relative timing reconstruction in the EPIC-pn camera is regularly monitored through observations of the Crab Pulsar, e.g Martin-Carrillo et al. (2012). Due to their major qualities, we will work mainly with pn data, although checking their consistency with MOS data.

Among the science instruments of *XMM-Newton*, RGS is the most appropriate for high spectral resolution X-ray spectroscopy within the energy range 0.33-2.5 keV, i.e. 5-38 Å. That range has a particularly high density of X-ray emission lines including the K-shell transitions and He-like triplets of light elements, such as C, N, O, Ne, Mg and Si; and the L-shell transitions of heavier elements like Fe and Ni; offering thus a large number of diagnostic tools to investigate the physical conditions and chemical composition of the emitting material. Two of the three X-ray telescopes are equipped with RGS units: RGS1 and RGS2, with a dispersion slowly varying function of dispersion angle, being equal to approximately 8.3 and 12.7 mm $Å^{-1}$ at 15 Å in first and second order, respectively.

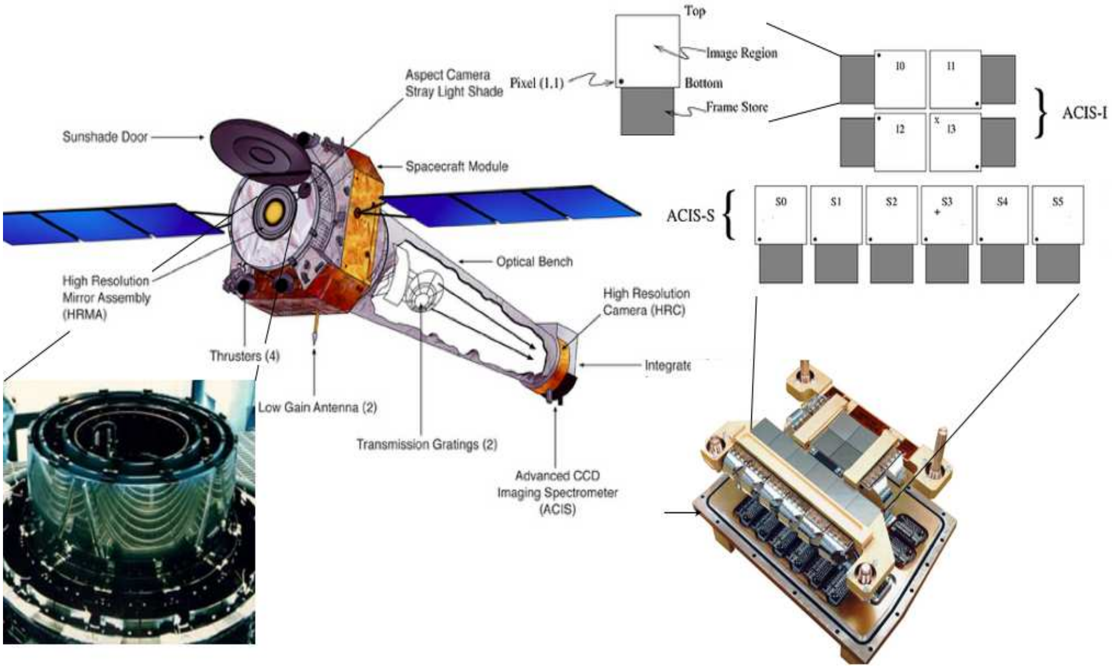

FIGURE 2.4: Reperesentation of the *Chandra* X-ray observatory along with its accurate X-ray mirrors and details of ACIS instrument. The Image credit: http://www.chandra.si.edu/blog/node/500.

The OM is co-aligned with the X-ray telescopes providing simultaneous optical/UV/X-rays observations. It consist of a Ritchey-Chretien telescope which feeds a compact image-intensified photon counting detector. Despite its 30 cm, it is a powerful instrument because of the absence of atmospheric extinction, diffraction and background. It has three optical and three UV filters over the 180-600 nm range and provides us with images of the central part of the X-ray field of view with a resolution of 1 arcsec (depending on instrument configuration), low-resolution spectra and high time-resolution photometry. Due to the extreme sensitivity of the detector, the OM is well suited for observations of faint sources in photometry. By contrast, very bright sources would cause irreversible damage in the detector. The safety limit is $m_V < 7.4$ mag for an A0 star. Therefore, OM can not be used with targets exceeding this boundary.

2.2.2 Chandra

The *Chandra* X-ray Observatory was developed and launched on July 23^{th} 1999 by NASA through the Space Shuttle Columbia. Similarly to the *XMM-Newton* satellite, the observatory was boosted to a high Earth elliptical orbit to allow uninterrupted exposures of 55 hours. Its X-ray telescope is the most sophisticated built to date, and it consists of four pairs of cylindrical mirrors with diameters between 0.69-1.4 m (see Fig. 1.2). The alignment of these mirrors is extremely accurate, with a precision up to 1.3 μm (or about one fiftieth the width of a human hair). The successful completion of that high resolution mirror assembly was one of the major accomplishments in the development of *Chandra*. On the contrary, the X-ray mirrors of *XMM-Newton* are not so accurate, although it possesses 58 (as opposed to just 4) pairs of cylinder in order to increase the collector capability of X-ray photons, as already discussed in section 1.2.

The incoming X-rays on *Chandra* are led by the mirrors onto two of the four instruments: the High Resolution Camera (HRC) (Murray & HRC Team, 1999), and the Advanced Charged Couple Imaging Spectrometer (ACIS) (Garmire et al., 2003). These focal plane instruments take the most of the high-quality images formed by the accurate mirrors providing the number, position, energy and time of arrival of the X-ray counts. There are two additional instruments dedicated to high resolution spectroscopy: High Energy Transmission Grating Spectrometer (HETGS) (Drake, 2002) and Low Energy Transmission Grating Spectrometer (LETGS) (Dewey, 2003), which provide detailed information about the X-ray energies. Each spectrometer is activated by swinging an assembly into position behind the mirrors according the energy of each incoming photon (see Fig. 2.4).

In this work we have exploited the ACIS instrument which consists of ten CCDs divided in two arrays, ACIS-I and ACIS-S (see FIg. 2.4). Two CCDs are back illuminated (BI) while eight are front illuminated (FI). It allows for spectroscopy within the 0.2-10 keV energy range and imaging with a pixel size of 0.5 arcsec. The main capability of ACIS is that it makes exquisite high angular resolution images and, at the same, can measure the energy and arrival time of each incoming X-ray, adding spectral capabilities to its excellent spatial resolution of *Chandra* around $1 - 2$ arcsec.

2.2.3 Suzaku

Suzaku, previously called Astro-E2, was launched on July 10^{th} 2005 by the Japan Aerospace Exploration Agency (JAXA) in collaboration with US and Japanese institutes and ended its operations in September 2015. This observatory performs astronomical observations using two instruments: X-ray Imaging Spectrometer (XIS) (Matsumoto et al., 2005) and Hard X-ray Detector (HXD) (Kawaharada et al., 2004) (see figure 2.5). XIS consist of four sets of X-ray CCD cameras operating in the standard X-ray band within the 0.1-15 keV range (alhough, effectively, the 0.5-10 keV range is the optimal). Each one of them presents 1024×1024 pixels and covers a region of $18' \times 18'$ on the sky combined with an X-ray telescope. One XIS uses BI CCDs, and the other three are equipped with FI CCDs. The BI CCD presents a higher quantum efficiency than the FI CCDs below 2 keV, while the FI CCDs are more sensitive to X-rays above 5 keV. Both types of devices have nearly the same energy resolution, FWHM$\sim$ 130 eV at 6 keV. HXD works in the wide energy band of 10-700 keV. It consists of a combination of the GSO well-type phoswich counters ($>$ 50 keV) and the silicon PIN diodes ($<$ 50 keV). The GSO emits optical light when they absorb X/gamma-ray photons. The optical photons are detected by

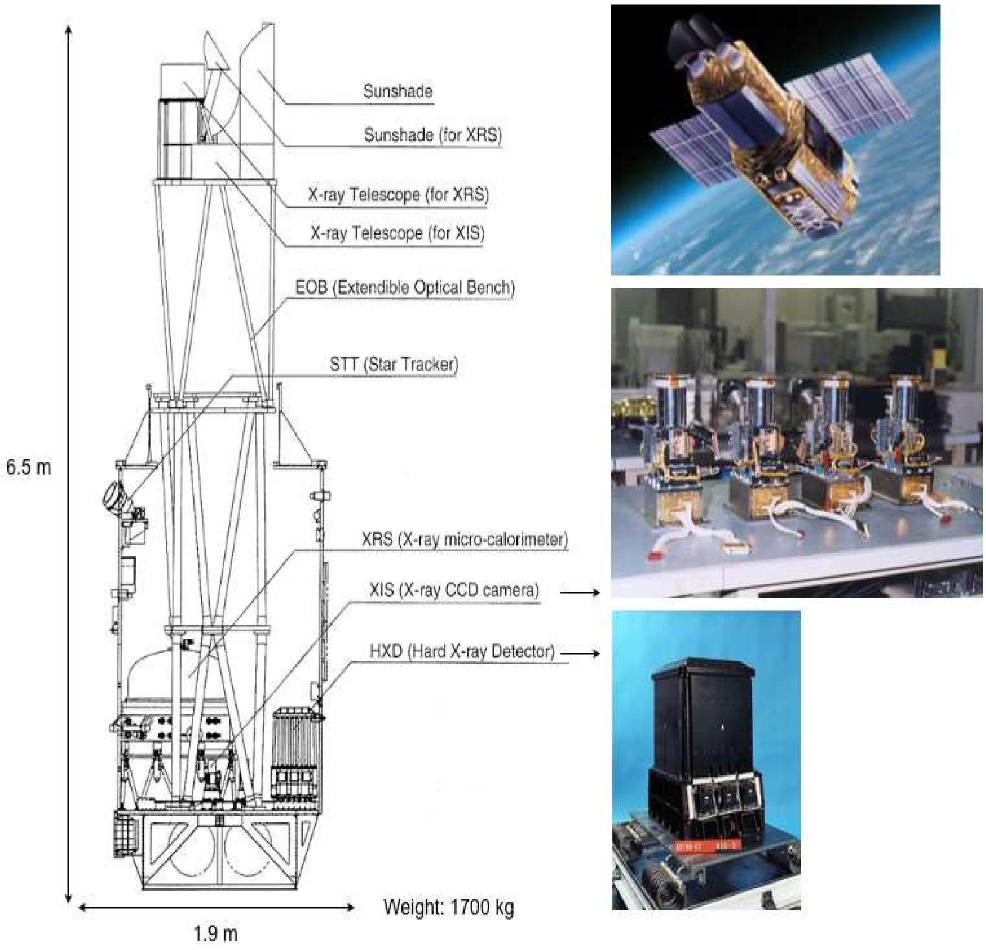

FIGURE 2.5: Reperesentation of the *Suzaku* satellite together with its operative instruments. Image credit: http://www.isas.jaxa.jp/e/enterp/missions/suzaku/.

photo-multiplier attached to the bottom of each well-detector, and signals are read through the pre-amplifiers. On the other hand, on the GSO crystal there exist two layers of the PIN diodes sensitive to X-rays between 10-50 keV. That functioning gives such a low background that the sensitivity is higher than any past missions in the hard X-ray band.

Suzaku also carried on board what would be a new type X-ray Spectrometer (XRS) designed to achieve, for the first time, both high-resolution, in order to see much finer details in the spectrum, and high-throughput, in order to measure a very large percentage of photons. Unfortunately, nineteen days after its launch, a cryogen loss made XRS no longer able to perform the planned science.

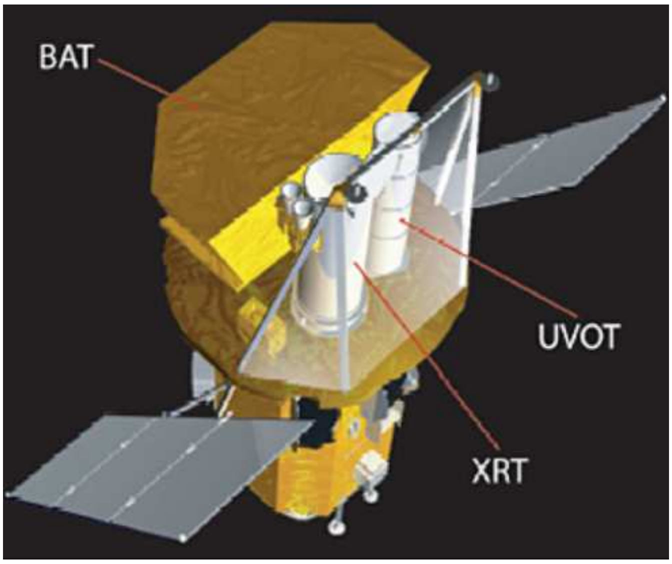

FIGURE 2.6: Reperesentation of the *Swift* spacecraft where its three instruments are indicated. Image credit: http://www.nasa.gov/mission_pages/swift/spacecraft/.

2.2.4 Swift

The main scientific objective of NASA's *Swift* spacecraft, launched on November 20th 2004, is to study the phenomenon of the gamma-ray bursts (GRBs) and their afterglows along the different wavelengths of the electromagnetic spectrum that they embrace: gamma-rays, X-rays, UV and visible. For this aim to be achieved, *Swift* carries three instrument: Burst Alert Telescope (BAT) (Barthelmy & Swift/BAT Instrument Team, 2004), X-ray Telescope (XRT) (Hill et al., 2004) and Ultraviolet-Optical Telescope (UVOT) (Roming et al., 2004) (see Fig. 2.6). *Swift*'s multiwavelength observations are completely simultaneous. BAT is a wide-field of view (FOV), coded-aperture instrument with a CdZnTe detector plane operating over the 15-150 keV energy rang. It detects and locates the bursts with an accuracy of 1-4 arcmin within 20 sec after the start of the event. Immediately, it begins an autonomous spacecraft slew to point XRT and UVOT, which have co-aligned FOVs, towadrs the target. XRT uses a excellent mirror set and an improved XMM/EPIC MOS CCD detector in order to provide us with a sensitive broad-band (0.2-10 keV) X-ray imager with an effective area of 110 cm^2 at 1.5 keV, a FOV of 23.6×23.6 arcmin and a angular resolution of 18 arcsec. It produces images, spectra and light curves working in an auto-exposure mode, which adjusts the CCD readout according to the count rate automatically. UVOT is a Ritchey-Chretien telescope with advance CCD detectors which operate in either a photon-timing or an imaging mode while providing sub-arcsecond resolution. It possesses a filter wheel accommodating broadband UV and visual filters for photometric studies including determination of photometric redshifts. UV and visual grisms for low-resolution spectroscopy are also available in the filter wheel.

While *Swift* is not carrying out observations of new GRB, its telescopes perform pre-programmed observations, which include long-term follow-up of GRBs and but also of other sorts objects. Thus, in our analysis of ESO 362-G18 we will make use of XRT and UVOT.

2.3 Reduction of the data

The data from the missions and detectors described above have been reduced as standard using the dedicated software SAS v12.01 (*XMM–Newton*), CIAO v4.4 (*Chandra*), and HEASOFT v6.11 (*Swift* and *Suzaku*). Epoch- and position-dependent ancillary responses and redistribution matrices have been generated for each data set. Source products have been extracted from circular regions centered on the source, and background products have been generated from nearby source-free regions. For simplicity, we only consider here EPIC pn spectra from *XMM–Newton*, although we have checked their consistency with the MOS data. As for the *Suzaku* data, we merge the spectra from the front-illuminated CCD detectors XIS0 and XIS3 using the FTOOL ADDASCASPEC to obtain one single front-illuminated CCD spectrum of the source. The resulting spectrum from the front–illuminated detectors is consistent with that from the back–illuminated XIS1 detector, although only the former is used here for simplicity. We also make use of the PIN data from the Suzaku HXD, which have been reduced with the dedicated FTOOL HXDGSOXBPI. The source flux obtained from the PIN detector is about 25 per cent of the background below 40 keV. Our *Chandra* observations were performed in continuous-clock mode to minimize pile-up and the resulting spectra are indeed pile–up free. Hereafter, when needed to convert fluxes into luminosities, we adopt a cosmology with $H_0 = 70$ km s^{-1} Mpc^{-1}, $\Omega_\Lambda = 0.73$, and $\Omega_M = 0.27$. Quoted uncertainties refer to the 90 per cent confidence level for one interesting parameter unless otherwise stated.

2.4 X-ray variability

In this section, we will explain in detail how we determined the best-fitting model that better describe the spectral shape and the variability exhibited by our target along the nine available observations. We always search for the simpler model, i.e minor number of free parameters, keeping the consistency with the typical X-ray spectrum of AGN.

As the five *Chandra* observations are part of a two-week monitoring campaign, we shall treat them separately from the others to investigate any short-timescale spectral variability in detail (see Section 2.4.5). In order to first define a global X-ray spectral model to be used

Table 2.2: The soft X–ray emission lines detected in the RGS spectrum of the XMM 2 observation. Line energies are given in keV, and intensities are reported in units of 10^{-5} ph s^{-1} cm^{-2}.

Line ID	Lab. Energy	Observable	Measurements
N VII Lyα	0.500	Energy	0.49 ± 0.02
		Intensity	1.3 ± 0.6
O VII Lyα	0.561 (f)	Energy	0.561 ± 0.001
		Intensity	4.6 ± 1.0
	0.569 (i)	Energy	0.569 ± 0.002
		Intensity	1.2 ± 0.7
	0.574 (r)	Energy	0.575 ± 0.002
		Intensity	$0.7^{+1.0}_{-0.5}$
O VIII Lyα	0.654	Energy	0.653 ± 0.002
		Intensity	1.3 ± 0.5

to study the spectral variability of ESO 362-G18, we start our analysis from the two highest-quality observations of our campaign, namely the *Suzaku* and the XMM 2 observations which provide, by far, the largest number of X-ray counts (see Table 2.1).

2.4.1 The high-resolution RGS data from the XMM 2 observation

As a first step, we examine the high-resolution spectrum from the RGS on board of *XMM–Newton* during the XMM 2 observation[1]. We fit the RGS data with a simple blackbody plus power law and Galactic absorption model ($N_H = 1.75 \times 10^{20}$ cm^{-2}, Kalberla et al. (2005)) which is adequate for the continuum. Several soft X-ray narrow emission lines are visually clear. We then add a series of Gaussian emission lines, as required by the data. We detect five soft X-ray emission lines corresponding to N VII and O VIII Lyα, and to the O VII triplet. The properties of the detected lines are reported in Table 2.2. In Fig. 2.7 it is shown the most relevant portion of the RGS 1 spectrum together with the best-fitting model and the identification of the N VII, O VII (actually a triplet), and O VIII emission lines. The dominance of the forbidden O VII Lyα line at 0.561 keV strongly suggests emission by photo–ionized gas, e.g. Porquet & Dubau (2000). All subsequent spectral models include the emission lines of Table 2.2 with energy fixed at the laboratory value, and with normalization allowed to vary only within the uncertainties derived from the RGS analysis.

---

[1] The RGS data during the XMM 1 observation have poor quality due to the short exposure (~ 8 ks) and relatively low soft X-ray flux ($F_{0.5-2} \sim 6.4 \times 10^{-13}$ erg s^{-1} cm^{-2}). On the other hand, the RGS data during the longer and higher-flux XMM 2 observation are of good enough quality to be used.

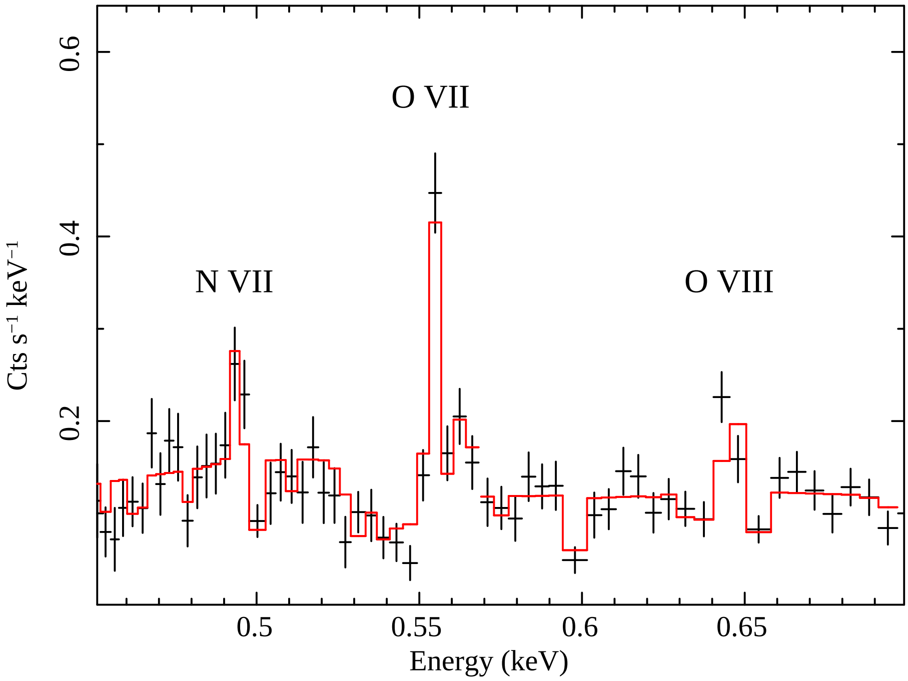

FIGURE 2.7: The RGS 1 spectrum obtained during the XMM 2 observation is shown together with the best–fitting model. The most important emission lines are labeled for reference (the O VII line being in fact a triplet). Data have been rebinned for visual clarity.

2.4.2 The high-quality *Suzaku* and XMM 2 observations

The X-ray spectra from the two high-quality observations (*Suzaku* and XMM 2) are shown in the upper panel of Fig. 2.8. In order to show the general spectral shape of the two observations, we fit a power law plus Galactic absorption model in the 1–4 keV and 7–10 keV bands, i.e. ignoring the soft and Fe K bands, as well as the *Suzaku* HXD data above 10 keV. The resulting data-to-model ratios are shown in the middle panel of Fig. 2.8. A soft excess with similar spectral shape is detected in both observations. Both spectra also exhibit broad residuals in the Fe K band, and the HXD/PIN data suggest that a hard X-ray excess is present above 10 keV. Note, however, that while the best-fitting photon index from the (higher flux) *Suzaku* observation is in line with the typical spectral slope of unobscured AGN ($\Gamma \simeq 2.0$, e.g. Piconcelli et al. (2005)), the XMM 2 observation is extremely hard with $\Gamma \simeq 1.3$, possibly signaling that some extra component is needed in the hard band.

We then consider a global spectral model for both observations initially including:

(*i*) a power law continuum,

(*ii*) a distant reflection component (we use the PEXMON model in XSPEC),

(*iii*) all soft X-ray emission lines of Table 2.2 and

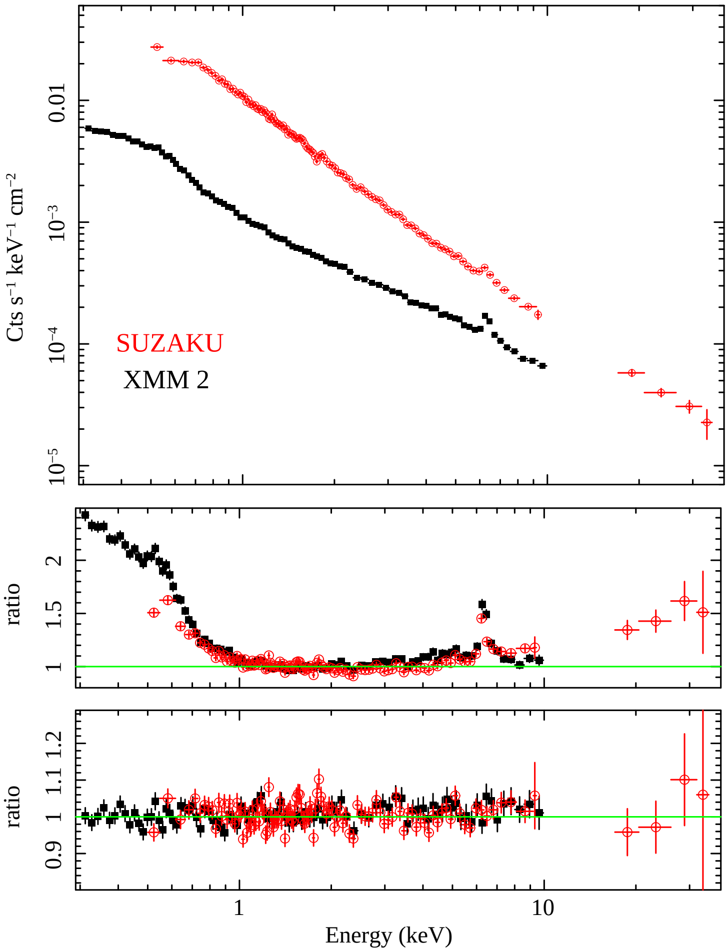

FIGURE 2.8: In the upper panel, we show the high–quality data from the *Suzaku* (upper red open circles) and XMM 2 (lower, filled squares) observations. The two spectra are normalized to the different detector effective area to show the real spectral shape. In the middle panel, we show the data-to-model ratios obtained by fitting a power law absorbed by the Galactic column density in the 1-4 keV and 7-10 keV band (i.e. ignoring the soft excess, Fe K band, and hard X-ray data above 10 keV). This shows that both observations are characterized by a soft excess and broad residuals in the Fe K band, while HXD/PIN data suggest the presence of a hard X-ray excess. In the lower panel, we show our final, best-fitting model, see text for details.

(*iv*) a relativistic disc-reflection component which may account for the soft excess, and for the positive residuals in the Fe K band (and in the HXD/PIN).

The latter is modeled with the Ross & Fabian (2005) partially ionized reflection model reflionx[2] which is convolved with the KERRCONV relativistic kernel (Brenneman & Reynolds, 2006) to account for any relativistic effects. The soft X-ray emission lines and the distant reflection component are forced to be the same in both spectra, as these components are not expected to vary.

---

[2] We extend their original grid to include values of the ionization parameter down to ξ = 0.01 erg s^{-1} cm and photon indices down to $\Gamma = 1.5$.

The fit is relatively good with $\chi^2 = 3040$ for 2580 degrees of freedom (dof) ($\chi^2_r ed = 1.18$). The description of the data improves by adding a rather typical warm absorber (we use the ZXIPCF model in XSPEC). As the column density of the warm absorber is consistent with being the same in the two observations, we force a common $N_{\rm H}$ in both data sets. We obtain a significant improvement to $\chi^2 = 2880$ for 2577 dof ($\chi^2_{red} = 1.12$) with a common column density of $\simeq 10^{21}$ cm^{-2} and $\log \xi \simeq 2.4$ ($\simeq 2.0$) for the *Suzaku* (XMM 2) observation. Although the fit is now acceptable, the XMM 2 data are not well reproduced with systematic positive residuals in the 2-6 keV band. Moreover, the resulting spectral shape for that observation is still rather flat ($\Gamma \simeq 1.5 - 1.6$) when compared with the typical value for unobscured AGN ($<\Gamma> \sim 1.9$, Piconcelli et al. (2005)).

We then consider the possible presence of absorption by including a neutral absorber affecting both the power law and disc-reflection components. For the sake of generality, we allow it to partially cover the X-ray source. The fit improves dramatically by $\Delta\chi^2 = -137$ for 4 more free parameters ($\chi^2 = 2743$ for 2573 dof, $\chi^2_{red} = 1.07$). In fact, the *Suzaku* spectrum is consistent with being unabsorbed (with covering fraction ≤ 0.1). Hence, the improvement is only due to a better description of the XMM 2 spectrum which requires a neutral absorber with column density $N_{\rm H} \simeq 10^{22}$ cm^{-2} and covering fraction $C_{\rm f} \simeq 0.4$. The photon index during the XMM 2 observation is now $\Gamma \simeq 1.8$, broadly consistent with a standard spectral slope. Replacing the disc-reflection component with a phenomenological blackbody (or disc blackbody) model to account for the soft excess results in a much worse statistical description of the data ($\chi^2 = 2938$ for 2576 dof, $\chi^2_{red} = 1.14$), strongly indicating that the disc-reflection model is the best description for the soft excess. Therefore, our best-fitting model for the two observations of highest quality comprises:

(*i*) a power law continuum,

(*ii*) a distant reflection component (PEXMON model in XSPEC),

(*iii*) all soft X-ray emission lines of Table 2.2,

(*iv*) a relativistic disc-reflection component (KERRCONV convolved with REFLIONX),

(*v*) a warm absorbed required by both observations and

(*vi*) a neutral absorbed required by *XMM 2* observation.

Let us discuss here results on the relativistic parameters associated with the disc-reflection component, namely the black hole spin a, emissivity index q, and disc inclination i. The error contour for the black hole spin is shown in the upper panel of Fig. 2.9. We measure a black hole spin of $a \geq 0.92$ at the 99.99 per cent confidence level, and of ≥ 0.98 at the 90 per cent one. Hence, the accreting black hole powering ESO 362–G18 is a very rapidly spinning Kerr

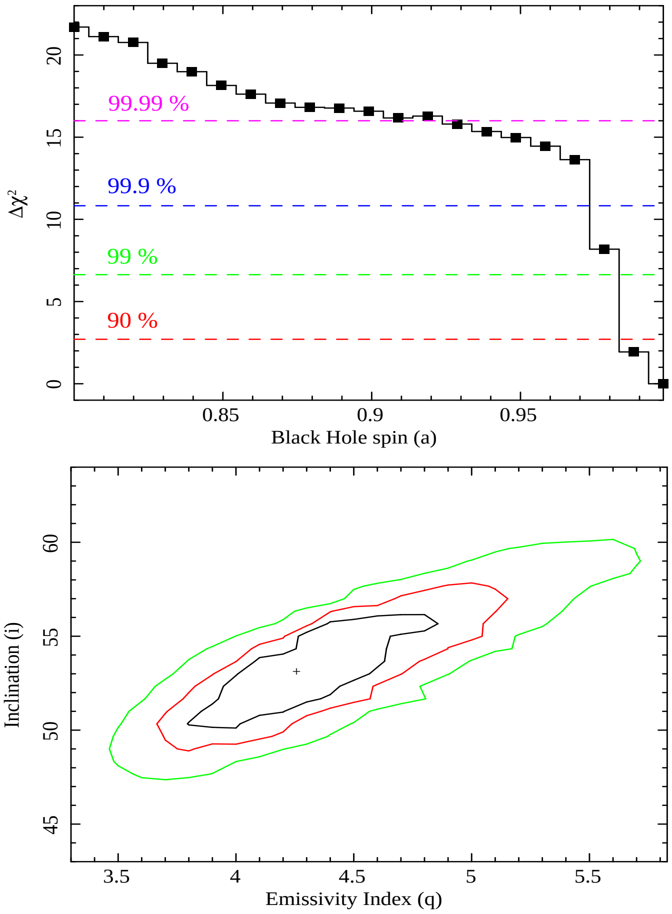

FIGURE 2.9: *Left panel:* it is shown the error contour for the black hole spin in ESO 362-G18, as obtained from the disc reflection model applied to the two high-quality observations (*Suzaku* and XMM 2). The contour has been obtained allowing all other model parameters to vary. The horizontal dashed lines are, from bottom to top, the 90, 99, 99.9, and 99.99 per cent confidence levels. Values of $a \leq 0.8$ always give $\Delta\chi^2 \geq 22$, and are not shown for visual clarity. *Right panel:*we show the 68, 90, and 99 per cent confidence level contours for the disc-reflection emissivity index and for the disc inclination. The contours have been obtained allowing all other parameters to vary.

black hole, consistent with being maximally spinning ($a = 0.998$). The contours plot for the disc-reflection emissivity index (q) and for the disc inclination (i) is shown in the lower panel of the same Figure and indicates that $q = 4.3^{+0.8}_{-0.6}$ and $i = 53° \pm 5°$ (90 per cent confidence level for the two interesting parameters).

2.4.3 Joint fits to the *Swift*, *Suzaku* and the two *XMM–Newton* spectra

Having found a good global spectral model for the two highest-quality observations of our campaign, we use the model to perform a simultaneous analysis of the first four X-ray observations of Table 2.1, namely to the *Swift*, XMM 1, *Suzaku*, and XMM 2 observations. We defer the analysis of the five *Chandra* monitoring observations to Section 2.4.5, since they represent a time scale of days and in this section we are treating time scales from months to years .

The X-ray spectrum of ESO 362-G18 from the first four observation observations is shown in the upper panel of Fig. 2.10 together with the best-fitting models. Remarkable spectral variability is present with a general steeper-when-brighter behavior. Moreover the (lowest flux) XMM 1 observation appears to have a distinct spectral shape. The visually larger narrow Fe line equivalent width suggests that the hard X-ray continuum is significantly depressed during the XMM 1 observation, either because of an intrinsic low flux state or because of absorption.

We proceed by performing a joint fit to the four observations with the same model discussed above. The warm absorber ionization is unconstrained during the *Swift* and XMM 1 observations. We then fix this parameter to that obtained during the higher quality XMM 2 observation which, according to our best-fitting model, has a similar intrinsic luminosity. We force the warm absorber column density to be the same in all observations, as in the analysis of the high–quality *Suzaku* and XMM 2 observations. The joint fit is excellent with $\chi^2 = 3140$ for 2933 dof ($\chi^2_{red} = 1.07$). The most remarkable result is that the lowest-flux XMM 1 observation appears to be heavily absorbed by a column density of $\simeq 10^{23}$ cm^{-2} covering about 80 per cent of the X-ray source. Removing the absorber from the XMM 1 model, i.e. attempting to explain the XMM 1 spectral shape with no intrinsic absorption (beside the warm absorber), yields to a disc-reflection dominated model but results in a poorer statistical description($\chi^2 = 3162$ for 2936 dof, $\chi^2_{red} = 1.08$). Moreover, the photon index is too flat to be realistic ($\Gamma \sim 1.5$). We conclude that the spectral shape during the XMM 1 observation is driven by cold absorption rather than by an extremely low intrinsic flux.

Still some residuals are seen at $\sim$ 0.9 keV during the lowest flux XMM 1 observation. Adding a further soft (unresolved) X-ray emission line at 0.904 keV (corresponding to Ne ɪx Ly) yields $\Delta\chi^2 = -34$ for 1 more free parameter (the line intensity is consistent with the RGS spectrum of the XMM 2 observation, and it is included with the same intensity in all observations, as is the case for all other unresolved soft X-ray emission lines, see Table 2.2). The soft X-ray emission lines we include in our model are most likely associated with emission from extended gas that is photoionized by the AGN. The same gas may also be associated with a soft scattered component, as ubiquitously seen in the X-ray spectra of heavily absorbed AGN (e.g. Bianchi et al. (2005)). We test this scenario by adding to our model a soft power law that is only absorbed by the Galactic column density. Its normalization is the same in all spectra, as this component is not expected to vary (see Fig. 1.12). The fit does not improve ($\Delta\chi^2 = -3$ for 2 more free parameters). We measure a a photon index $\Gamma \simeq 2.4$ and a scattered 0.5-2 keV luminosity of $\sim 10^{41}$ erg s^{-1}. This component is overwhelmed by the X-ray continuum, and thus negligible, in all observations except the lowest-flux XMM 1 observation. For consistency with the typical soft X-ray spectrum of heavily obscured AGN, we keep this component in our best-fitting spectral model although, as mentioned, it is not formally required by the data. Therefore, until now, our best-fitting model comprises:

(*i*) a power law continuum,

(*ii*) a distant reflection component (PEXMON model in XSPEC),

(*iii*) all soft X-ray emission lines of Table 2.2,

(*iv*) a relativistic disc-reflection component (KERRCONV convolved with REFLIONX),

(*v*) a warm absorbed required by both observations,

(*vi*) a neutral absorbed required by *XMM 2* observation and

(*vii*) a soft power law only absorbed by the Galaxy which gives account of the ubiquitous extended gas photoionized by the AGN, associated with a soft scattered component and probably responsible for the detected soft X-ray emission lines .

We conclude that most of the spectral variability seen in the upper panel of Fig. 2.10 is due to a variable cold absorber changing in both column density and covering fraction, although photon index variability is also detected with $\Delta\Gamma \sim 0.2 - 0.3$. The most important absorption variability event is detected during the XMM 1 observation which requires a much higher level of X-ray absorption than any other observation and, in particular, than the *Swift* observation which was performed only 63 days earlier. We measure a column density of $\simeq 10^{23}$ cm^{-2} covering $\simeq$ 80 per cent of the X-ray emitting regions during the XMM 1 observation. Such a column density is at least one order of magnitude higher than that measured during any other observation.

2.4.4 A hard scattered component

As discussed extensively by Miniutti et al. (2014), the inclusion of a hard scattered component describes very well the absorbed X-ray states of another source which exhibits extreme X-ray absorption variability, namely ESO 323-G77. A hard scattered component is likely present in all cases where absorption is due to a clumpy rather than homogeneous structure. This is because our LOS is absorbed by a specific clump (cloud), but the X-ray continuum in different directions intercepts different clumps which re-direct part of it into our LOS via scattering (see Fig. 1.12). The presence of a hard scattered component has also been suggested in other absorbed AGN such as NGC 3227 (Lamer et al., 2003) and NGC 7582 (Piconcelli et al., 2007). Both sources exhibit variable X-ray absorption, most likely associated with clumpy absorbers, in line with

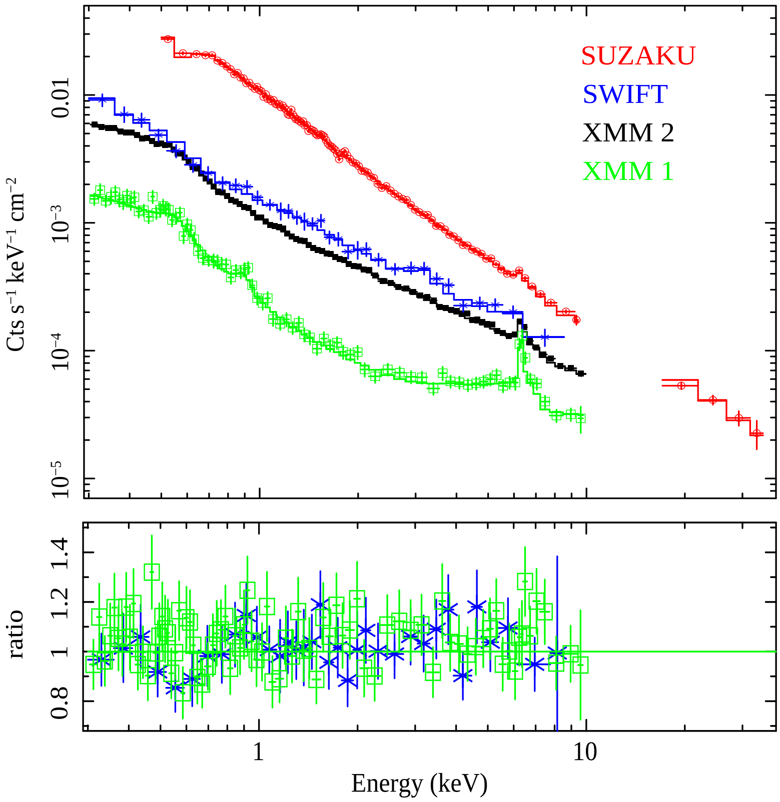

FIGURE 2.10: In the upper panel, we show the data and best-fitting models for the first four observations of our campaign (see Table 2.1). From top to bottom, we show the *Suzaku*, *Swift*, XMM 2, and XMM 1 data. In the lower panel, we show the best–fitting data–to–model ratios for the *Swift* and XMM 1 observations. The corresponding plot for the *Suzaku* and XMM 2 observations has already been shown in the lower panel of Fig. 2.8, and it is not reproduced here for visual clarity.)

the scattering interpretation outlined above. The X-ray absorption variability ESO 362-G18 strongly suggests that this is the case here as well.

In order to check for the presence of a hard scattered component in ESO 362-G18, we use the same phenomenological model used by (Miniutti et al., 2014) for the case of ESO 323-G77. Thus, we include an additional absorbed power law with the same (observation-dependent) photon index and normalization as the intrinsic nuclear continuum, we allow the column density towards this component to be different than that affecting the nuclear continuum (but the same in all observations), and we multiply the model by a constant allowed to vary between 0 and 1 which represents the hard scattering fraction. The statistical description of the data improves significantly by $\Delta\chi^2 = -28$ for 2 more free parameters for a final result of $\chi^2 = 3075$ for 2928 dof ($\chi^2_{red} = 1.05$). The hard scattered component is absorbed by a column density of $\sim 2-3\times10^{22}$ cm^{-2}, and its scattering fraction is ~ 12 per cent. Note that this component is significantly detected only during the most heavily absorbed XMM 1 observation (as expected,see the discussion Miniutti et al. (2014)). The inclusion of that component induces a higher column density and covering fraction during the XMM 1 observation, while not affecting any other parameter. We now measure a column density of $\sim 3-4\times10^{23}$ cm^{-2}, consistent with a full coverage of the X–ray emitting region with covering fraction $C_{\rm f} \geq 0.94$ during the XMM 1 observation. Note that, as our phenomenological description of the hard scattered component is likely only a rough approximation of the true spectral shape, these values are likely affected by larger uncertainties than the quoted statistical ones.

Re-running the error contours on the relativistic parameters (see Fig. 2.9) gives identical results. This is expected since the relativistic parameters are best constrained from the highest-quality X-ray spectra that are unaffected by the inclusion of the hard scattered component. The final best-fitting results are reported in Table 2.3 and a summary and brief discussion of the main results is presented in Section 2.5. The data-to-model ratios for the *Swift* and XMM 1 observations are shown in the lower panel of Fig. 2.10 (see Fig. 2.8 for the *Suzaku* and XMM 2 observations).

So finally, our definitive best-fitting model comprise:

(*i*) a power law continuum,

(*ii*) a distant reflection component (PEXMON model in XSPEC),

(*iii*) all soft X-ray emission lines of Table 2.2,

(*iv*) a relativistic disc-reflection component (KERRCONV convolved with REFLIONX),

(*v*) a warm absorbed required by both observations,

(*vi*) a neutral absorbed required by *XMM 2* observation,

(*vii*) a soft power law associated with a soft scattered component and

(*viii*) a hard scattered component associated to clumpy absorbers.

2.4.5 The two weeks *Chandra* monitoring campaign

We consider here a joint fit to the five *Chandra* monitoring observations performed between 2010-05-18 to 2010-06-03 using the same X-ray spectral model described above. We fix the parameters associated with the soft X-ray emission lines, the distant reflection component, and the soft and hard scattered components to the values derived from the analysis discussed above, as the *Chandra* data have typically lower spectral quality, and because these components are not expected to vary. The relativistic parameters affecting the disc reflection component are also fixed to the best-fitting values obtained from the analysis of the first four observations, as the *Chandra* data cannot constrain them any better. As before, we force the warm absorber column density to be the same in all observations, while the ionization parameter is free to

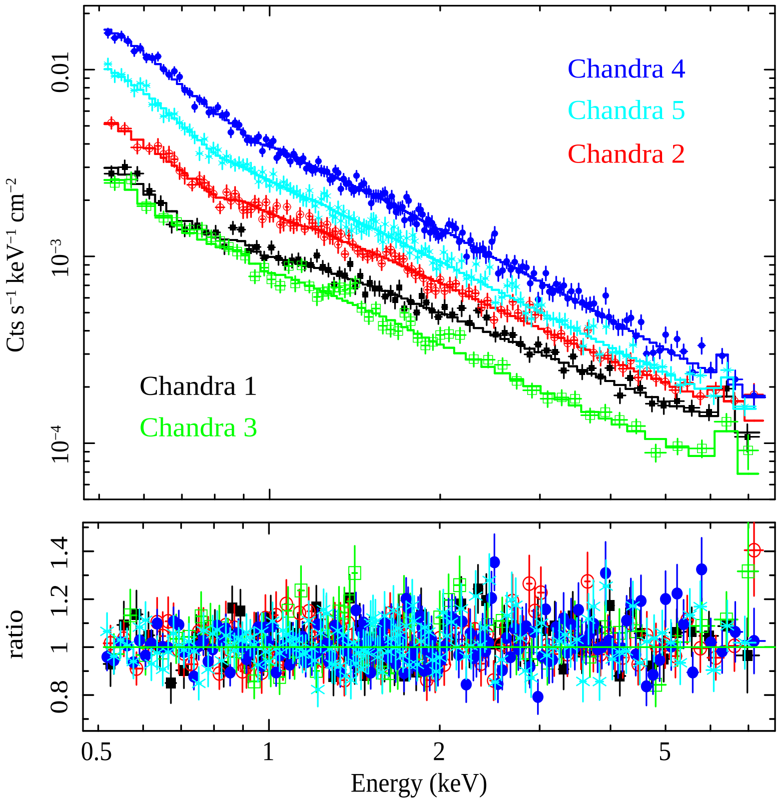

FIGURE 2.11: In the upper panel, we show the data and best-fitting models for the five *Chandra* monitoring observations performed within 15 days from 2010-05-18 to 2010-06-03. In the lower panel, we show the best-fitting data-to-model ratios resulting from the joint fit to the five data sets.

vary independently. As for the neutral partial covering absorber, the column density is initially free to vary independently. However, as N_{H} turns out to be consistent with being the same in all *Chandra* observations, we force it to have the same value in all data sets, so that the cold absorber is only allowed to vary in covering fraction.

We reach a good statistical description of the five *Chandra* monitoring observations with a final result of $\chi^2 = 1248$ for 1218 dof ($\chi^2_{red=1.02}$). The spectra, best-fitting models, and final data-to-model ratios for the joint fit to the five data sets are shown in Fig. 2.11. The observed spectral variability can be explained by a combination of photon index variability ($\Delta\Gamma \simeq 0.3$, although with large errors) and by moderate changes in the covering fraction of a cold absorber with column density of $\simeq 8 \times 10^{21}$ cm^{-2}. Our best-fitting results are reported in Table 2.3 and discussed in Section 2.5.

TABLE 2.3: Best-fitting parameters for the multi-epoch analysis. The constant continuum components (upper part of the Table) comprise the soft and hard scattered power law as well as the distant reflection component. $L^{(\mathrm{ss})}_{0.5-2}$ is the luminosity of the soft scattered (ss) component, comprising contributions from the soft scattered power law and from all unresolved soft X–ray emission lines. $N_{\mathrm{H}}^{(\mathrm{hs})}$ and $f^{(\mathrm{hs})}$ are the column density towards the hard scattered component and its scattering fraction. The superscript $^{(\mathrm{XMM2})}$ means that the parameter is tied to that during the XMM 2 observation. Luminosities are unabsorbed and given in units of 10^{42} erg s^{-1}; column densities are given in units of 10^{22} cm^{-2}; the ionization parameter is given in units of erg cm s^{-1}.

Constant continuum components and common relativistic parameters								
	Soft scattering		Hard scattering		Distant reflection	Disc–reflection relativistic parameters		
	$\Gamma^{(\mathrm{ss})}$	$L^{(\mathrm{ss})}_{0.5-2}$	$N_{\mathrm{H}}^{(\mathrm{hs})}$	$f^{(\mathrm{hs})}$	$L^{(\mathrm{ref})}_{2-10}$	a	q	i
	2.4 ± 0.1	0.12 ± 0.05	2.5 ± 1.6	$0.12^{+0.08}_{-0.06}$	0.32 ± 0.09	≥ 0.98	$4.3^{+0.8}_{-0.6}$	53 ± 5
Variable components								
Obs.	Cold absorber		Warm absorber		Continuum		Disc–reflection	
	$N_{\mathrm{H}}^{(\mathrm{cold})}$	$C_{\mathrm{f}}^{(\mathrm{cold})}$	$N_{\mathrm{H}}^{(\mathrm{ion})}$	$\log\xi$	Γ	$L^{(\mathrm{nuc})}_{2-10}$	$\xi^{(\mathrm{ref})}$	$L^{(\mathrm{ref})}_{2-10}$
Swift	0.5 ± 0.4	0.5 ± 0.3	0.15 ± 0.04	$2.0^{(\mathrm{XMM2})}$	2.0 ± 0.4	2.0 ± 0.3	≤ 25	≤ 2.0
XMM 1	35 ± 8	≥ 0.94	”	$2.0^{(\mathrm{XMM2})}$	1.90 ± 0.09	2.3 ± 0.2	≤ 32	$0.9^{+0.5}_{-0.7}$
Suzaku	–	≤ 0.1	”	2.4 ± 0.2	2.12 ± 0.03	8.35 ± 0.08	16 ± 12	1.9 ± 0.2
XMM 2	1.3 ± 0.2	0.42 ± 0.04	”	2.0 ± 0.3	1.80 ± 0.04	1.95 ± 0.06	≤ 8	0.9 ± 0.1
χ^2/dof = 3075/2928								
Chandra 1	0.8 ± 0.2	0.6 ± 0.1	0.20 ± 0.08	2.0 ± 1.1	1.7 ± 0.2	2.3 ± 0.2	≤ 26	0.7 ± 0.5
Chandra 2	”	0.4 ± 0.1	”	1.9 ± 0.6	1.8 ± 0.2	3.1 ± 0.1	≤ 25	0.9 ± 0.4
Chandra 3	”	0.5 ± 0.2	”	2.5 ± 1.3	1.8 ± 0.3	1.2 ± 0.4	≤ 35	≤ 1.6
Chandra 4	”	0.48 ± 0.06	”	2.5 ± 0.4	2.1 ± 0.1	4.9 ± 0.1	7 ± 6	1.3 ± 0.3
Chandra 5	”	0.4 ± 0.1	”	2.1 ± 0.4	2.0 ± 0.1	3.4 ± 0.1	≤ 19	1.1 ± 0.2
χ^2/dof = 1248/1218								

2.5 Summary of the multi-epoch spectral analysis

The relevant best-fitting parameters of our multi-epoch spectral analysis are reported in Table 2.3. The parameters associated with the soft emission lines, the soft/hard scattering components, the distant reflector, and the disc-reflection relativistic kernel are the same in all observations. They are reported in the upper part of the Table. As mentioned, these parameters have been fixed in the joint analysis of the *Chandra* observations, so that the reported values and errors are drawn from the joint fit to the *Swift*, XMM 1, *Suzaku*, and XMM 2 observations.

A disc-reflection component is detected in all observations, except the *Swift* and *Chandra* 3 ones, where only upper limits are obtained. This is likely because of the relatively low spectral quality of these observations (see Table 2.1). The relativistic parameters are best constrained from the highest-quality spectra (*Suzaku* and XMM 2) and suggest that ESO 362-G18 is powered by a very rapidly spinning Kerr black hole (with spin $a \geq 0.98$ at the 90 per cent confidence level). The observer inclination with respect to the disc axis is also very well constrained ($i \sim 53^\circ$). The disc ionization state is rather low, and we are only able to obtain upper limits on the ionization parameter, except during the highest flux *Suzaku* and *Chandra* 4 observations.

The intrinsic photon index Γ is variable and it appears to be steeper during the highest flux observations (*Suzaku* and *Chandra 4*), consistent with a steeper-when-brighter behaviour. After checking that the data allow us to do so, the warm absorber column density is forced to be the same during the first four and during the subsequent five observations. The final results indicate that the warm absorber column density is in fact likely constant during the whole 2005-2010 campaign with $N_\mathrm{H} \simeq 1-2\times10^{21}$ cm^{-2}. On the other hand, the warm absorber ionization is marginally variable and roughly consistent with responding to the intrinsic variability although the relatively large errors do not allow us to investigate its variability in detail.

A neutral, partially covering absorber is detected in all observations but the *Suzaku* one, which appears to be unabsorbed. The absorber is variable, and the X-ray spectrum of ESO 362-G18 changes from unabsorbed or only mildly absorbed states (e.g. during the *Swift* and *Suzaku* observation) to highly absorbed ones (the XMM 1 observation), going also through states with intermediate levels of absorption (the remaining XMM 2 and *Chandra* observations). The most remarkable absorption variability event is that occurring over the 63 days separating the mildly absorbed *Swift* observation ($N_\mathrm{H} \sim 5\times10^{21}$ cm^{-2} and $C_\mathrm{f} \simeq 0.5$) and the heavily absorbed XMM 1 one ($N_\mathrm{H} \simeq 3-4\times10^{23}$ cm^{-2} and $C_\mathrm{f} \geq 0.94$).

2.6 The black hole mass and further, independent constraints on the system inclination

Along this section we will derive estimations for the black hole mass of ESO 362-G18 following the methods discussed on section 1.5.1. It will allow us to reinforces our disc-reflection interpretation.

Garcia-Rissmann et al. (2005) measure the stellar velocity dispersion of ESO 362-G18 from the Calcium triplet obtaining $\sigma_* = 130 \pm 4$ km s^{-1} (we consider the average value and standard deviation of their two measurements). As already noticed, the black hole mass can be estimated from the $M_{\rm BH} - \sigma_*$ relation (e.g. Merritt & Ferrarese (2001), Tremaine et al. (2002)). Using the $M_{\rm BH} - \sigma_*$ relationship as obtained by Xiao et al. (2011) (see section 1.5.1), we estimate a black hole mass of $M_{\rm BH} = (0.8 - 1.7) \times 10^7\ M_\odot$. However, in order to include the spread and not only the statistical uncertainties on the best-fitting $M_{\rm BH} - \sigma_*$ relation, we prefer to consider the sample of reverberation-mapped AGN from Woo et al. (2010) that have stellar velocity dispersion consistent with that of ESO 362-G18, and to assign to our AGN the black hole mass range that can be derived from this sub-sample. With this prescription, we obtain a larger mass range of $M_{\rm BH} = (0.7 - 7.2) \times 10^7\ M_\odot$.

Since our source is a type 1 AGN, another estimate of the black hole mass can be obtained by combining the observed optical luminosity with the H_β broad emission line FWHM by using, e.g. the relationship from Park et al. (2012):

$$M_{\rm BH} = A \left(\frac{\rm FWHM_{H_\beta}}{10^3\ \rm km\ s^{-1}} \right)^{1.666} \left(\frac{\lambda L_{5100}}{10^{44}\ \rm erg\ s^{-1}} \right)^{0.518} \tag{2.1}$$

where $A = 10^{6.985}\ M_\odot$. Bennert et al. (2006a) report a H_β FWHM= 5240 ± 500 km s^{-1} from the optical spectrum obtained at the NTT on 2004-09-17. They also measure a nuclear 5100 Å luminosity of $\sim 4.1 \times 10^{43}$ erg s^{-1}. By using Eq. 2.1, we then have $M_{\rm BH} = (0.8 - 8.1) \times 10^8\ M_\odot$, which appears to be inconsistent (and much higher) than that derived from the stellar velocity dispersion.

However, Eq. 2.1 assumes an average virial coefficient $\log f = 0.72$, as derived by Woo et al. (2010). In fact, f is likely source-dependent, and depends on the unknown BLR geometry. If we assume a disc-like BLR geometry, the virial relationship can be expressed in terms of line FWHM as:

$$M_{\rm BH} = \frac{R_{\rm BLR} FWHM^2_{H_\beta}}{4 \sin^2 iG} \tag{2.2}$$

where i is the inclination between the LOS and the angular momentum of the disc-like BLR, whose direction is likely parallel to that of the accretion flow angular momentum. $R_{\rm BLR}$ can be estimated from the Bentz et al. (2009) R_{BLR}-luminosity relationship which, for the given 5100 Å luminosity gives $R_{\rm BLR} \sim 5.2 \times 10^{16}$ cm. Our disc-reflection model provides information on the system inclination, namely $i = 53^\circ \pm 5^\circ$. Inserting $R_{\rm BLR}$ and i into the virial relationship leads to a black hole mass estimate of $M_{\rm BH} = (4.5 \pm 1.5) \times 10^7 \ M_\odot$, which is now totally consistent with the mass estimated from the stellar velocity dispersion. Notice that, in order for the black hole mass estimates from σ_* and from the virial assumption to be consistent with each other, one must have $\sin^2 i \geq 0.46$. In other words, under the assumption of a disc-like BLR geometry, $i \geq 43^\circ$. This provides further, independent support to the relatively high inclination we derive from the X-ray spectral analysis with the disc-reflection model. Hereafter, we assume that $M_{\rm BH} = (4.5 \pm 1.5) \times 10^7 \ M_\odot$ and we refer to $M_{\rm best} = 4.5 \times 10^7 \ M_\odot$.

2.7 Looking for a reverberation time lag

An inescapable consequence of interpreting the soft X-ray excess as partially ionized X-ray reflection off the inner accretion disc is that relatively short time delays are expected between X-ray energy bands dominated by the intrinsic power law, and bands dominated by disc-reflection (i.e. the soft excess). Such lags have been indeed discovered in the Narrow Line Seyfert 1 galaxy 1H 0707-495 (Fabian et al., 2009), where the variability in the spectral band dominated by reflection from the accretion disc is found to lag behind that in the spectral band corresponding to primary X-ray emission by tens to hundreds of seconds (Zoghbi et al., 2010). Subsequently, these lags have been discovered in many other AGNs (Emmanoulopoulos et al., 2011, de Marco et al., 2011, De Marco et al., 2013, Kara et al., 2013b,a, Cackett et al., 2013, Fabian et al., 2013). Measuring these time lags implies measuring the light travel time between the source and reflector and allows us to probe scales as small as 10 light-seconds in AGN. This interpretation has then been proved thanks to the detection of very similar Fe K lags in some sources (Zoghbi et al., 2012, Kara et al., 2013c, Zoghbi et al., 2013). However a few authors disagree this most accepted picture and consider the detected soft lags spurious and thus physically meaningless (Miller et al., 2010, Legg et al., 2012).

The base supporting the study of the timing properties is the concept of coherence. The coherence of two light curves is a measure of how correlated they are, or how much of one light curve can be predicted from the other, which implies the Fourier transforms of the two light curves under study (for a further discussion about the mathematical development see e.g Nowak et al. (1999), Vaughan et al. (2003), Zoghbi et al. (2010), Wilkins & Fabian (2013)). The coherence takes a value of 1 if the two light curves are perfectly coherent and the coherence

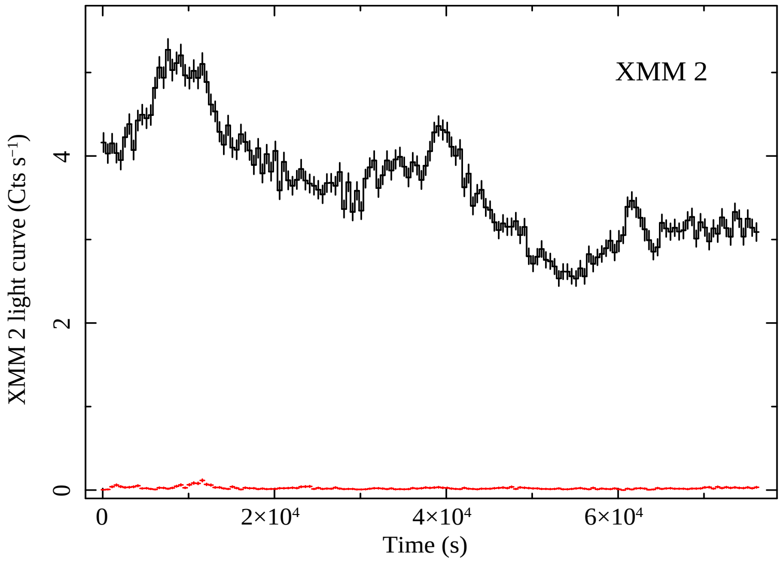

FIGURE 2.12: The broadband, 0.3–10 keV EPIC-pn light curve of ESO 362–G18 during the XMM 2 observation is shown with a bin size of 500 s. The corresponding background light curve is also shown for comparison.

can be translated into time lags between 2 light curves representing two different energy bands. According to Nowak et al. (1999), the time lag can be calculated as:

$$\tau(f) = \frac{\phi(f)}{2\pi f} = \frac{arg[C(f)]}{2\pi f} \tag{2.3}$$

where $C(f)$ is the cross spectrum between the Fourier transforms of both soft and hard light curves and $arg[C(f)]$ is the argument of the complex number $C(f)$. Following this calculation and sign convention, a negative time lag indicates that the variability in the soft energy band is lagging behind that in the hard energy band, as it would be expected if the hard band is dominated by an X-ray continuum which is subsequently reflected off the accretion disc and this reflection dominates the soft band.

ESO 362-G18 is X-ray variable during the long XMM 2 observation, and the broadband 0.3-10 keV light curve is shown in Fig. 2.12. The X-ray variability is of sufficiently high amplitude that lags between different energy bands can in principle be computed. To compute the lag-frequency spectrum, we select energy bands that, according to our best-fitting spectral model, are dominated by disc-reflection (0.3-0.6 keV) and by the intrinsic power law continuum (0.8-3 keV) respectively. In Fig. 2.13, we show the lag-frequency spectrum of ESO 362-G18 between the two selected energy bands, where negative (soft) lags mean that the soft band lags the hard one. We measure a soft lag of $|\tau| = 658 \pm 342$ s at $\nu \sim 1.7 \times 10^{-4}$ Hz. The errors in the lag were calculated following equation (16) Nowak et al. (1999). A similar lag is consistent to be present in the wide $0.4 - 7 \times 10^{-4}$ Hz frequency band. For $M_{\rm BH} = M_{\rm best}$, and assuming that

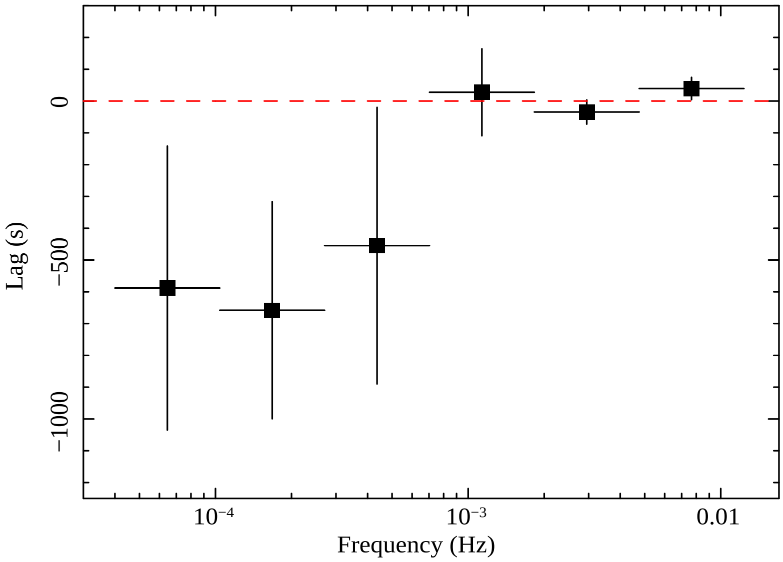

FIGURE 2.13: The lag-frequency spectrum of ESO 362-G18 between the 0.3-0.6 keV and the 0.8-3 keV bands. The lag is defined such that negative values mean that the softer (soft-excess-dominated) band lags the harder (likely continuum-dominated) one.

soft lags are related to the light-crossing-time between primary and reprocessed X-ray emission components (i.e. the power law continuum and the soft excess), the observed soft lag translates into a distance of (3.0 ± 1.5) r_g between the continuum and soft excess emission sites.

However these calculations assume that the light curves of the directly observed continuum and reflected emission can be measured directly. This is not true since light curves are obtained in spectral bands that are only dominated by either the continuum emission (the hard band at 0.8-3 keV) or the reflection from the accretion disc (the soft band at 0.3-0.6 keV). Therefore, the measured time lag is diluted as the selected reflection includes promptly arriving photons from the continuum and the continuum includes late-arriving photons from the reflection (Wilkins & Fabian, 2013). The effects of this dilution can be taken into account by using the developed best-fitting model. Integrating the number of photons detected from both components over both energy bands, the fraction of the reflection and power law components in the two selected bands can be computed. The remaining spectral components are assumed to be constant and therefore not to contribute the lag.

Following the same arguments of Wilkins & Fabian (2013), we infer an intrinsic lag of ~ 1600 s, corresponding to a distance of $\sim 7\ r_g$ between the continuum and reflection emitting regions.

2.8 Origin of the variable absorber and constraints on the X–ray emitting region(s) size

The main result of our X-ray absorption variability monitoring is that ESO 362-G18 transits from a mildly absorbed state with $N_{\rm H} \simeq 5 \times 10^{21}$ cm^{-2} and $C_{\rm f} \simeq 0.5$ as observed during the *Swift* observation, to a highly absorbed state with $N_{\rm H} \simeq 3-4 \times 10^{23}$ cm^{-2} and $C_{\rm f} \geq 0.94$ during the XMM 1 observation performed 63 days later.

The observed X-ray absorption variability is most likely due to one absorber clump (cloud) crossing our LOS during the XMM 1 observation. A clumpy absorber may be directly identified with the clumpy obscuring torus (Nenkova et al., 2008a, Rivers et al., 2011, Miniutti et al., 2014). Another possibility is that the variable absorber is related to BLR clouds (Lamer et al., 2003, Elvis et al., 2004, Risaliti et al., 2005, 2007, 2009, Sanfrutos et al., 2013, Miniutti et al., 2014). Although the BLR and clumpy torus are likely part of the same continuous obscuring structure (Elitzur & Shlosman, 2006), they can be physically distinguished by their dust content. The BLR is dust-free, which locates the BLR within the dust-sublimation radius. The same radius is instead generally considered as representative of the inner edge of the clumpy torus. To gain some insight on the location and origin of the variable absorber, we consider UV data of ESO 362-G18 with the goal of distinguishing between dust-free and dust-rich absorption during the XMM 1 observation.

If the $3-4 \times 10^{23}$ cm^{-2} absorber affecting the XMM 1 observation is associated with the dusty clumpy torus, the UV emission from ESO 362-G18 may also be affected, provided that the absorber covers a sufficiently high fraction of the UV-emitting region (likely the accretion disc). On the other hand, if the absorber is dust–free (e.g. the BLR clouds), no significant effect is expected in the UV. Reliable optical and UV fluxes can be obtained from the UVOT and OM telescopes on board *Swift* and *XMM-Newton* during the mildly absorbed (hereafter *"unabsorbed"* for simplicity) *Swift* and XMM 2 observations as well as during the absorbed XMM 1 one. The resulting optical/UV flux densities are given in Table 2.4.

The U and W1 fluxes are nearly consistent with being constant in all observations. On the other hand, the M2 flux is nearly the same during the unabsorbed *Swift* and XMM 2 observation, but ~ 30 per cent lower during the X-ray absorbed XMM 1 observation. The same is true for the W2 flux, which is ~ 40 per cent lower during the X-ray absorbed XMM 1 observation than during the unabsorbed *Swift* one (no data were collected in W2 during the XMM 2 observation). It is worth pointing out that the UV intrinsic variability is an unlikely explanation for the observed variability in the M2 and W2 filters because the intrinsic X-ray luminosity is higher during the X–ray absorbed XMM 1 observation than during the two X-ray unabsorbed ones.

TABLE 2.4: Flux densities in the UVW2 UVM2, UVW1, and U filters during the *Swift* and XMM 2 (X–ray unabsorbed) observations, and the XMM 1 (X–ray absorbed) one. Results are given in units of 10^{-15} erg cm^{-2} s^{-1} Å^{-1}.

Filter	Swift[a] (unabsorbed)	XMM 1[b] (absorbed)	XMM 2[b] (unabsorbed)
UVW2	13.5 ± 0.6	7.9 ± 0.4	–
UVM2	12.2 ± 0.4	8.5 ± 0.4	12.4 ± 0.5
UVW1	11.8 ± 0.7	10.6 ± 0.5	9.9 ± 0.5
U	10.0 ± 0.5	10.7 ± 0.5	8.8 ± 0.4

[a] The *Swift* UVOT filters are centered at 1928 Å (UVW2), 2246 Å (UVM2), 2600 Å (UVW1), and 3465 Å (U);
[b] The *XMM–Newton* OM filters are centered at 2025 Å (UVW2), 2250 Å (UVM2), 2825 Å (UVW1), and 3450 Å (U).

The most natural interpretation of the observed UV variability is then that the UV-emission in the shorter wavelength M2 and W2 filters is affected by absorption (as are the X-rays) during the XMM 1 observation, while it is not during the two X-ray unabsorbed ones. By comparing the UV flux during absorbed/unabsorbed observations, and assuming that total coverage would completely block the UV emission, we infer that the absorber covers ~ 30 (~ 40) per cent of the UV-emitting region in the M2 (W2) filter. In summary, the UV data are consistent with a dusty absorber covering about 30-40 per cent of the UV emitting region during the X-ray absorbed XMM 1 observation. This strongly suggests to identify the absorber with one clump (or cloud) of the clumpy dusty torus, rather than with a BLR cloud.

As the UV are only partially covered during the XMM 1 observation with $C_{\mathrm{f,\,UV}} \sim 0.3-0.4$, while the X-rays are fully covered with $C_{\mathrm{f,\,X}} \sim 1$, the X-ray emitting region must be significantly smaller in size than the UV emitting region. This is not highly surprising, and it is in line with the mounting evidence from e.g. microlensing results that X-rays originate in more compact, centrally concentrated regions of the accretion flow than optical/UV (e.g. Morgan et al. (2008), Chartas et al. (2009), Dai et al. (2010), Morgan et al. (2012), Mosquera et al. (2013)). Further constraints on the X-ray emitting region size can be obtained from the X-ray absorption variability itself. As the X-ray emitting region is consistent with being fully covered during the XMM 1 observation ($C_{\mathrm{f}} \geq 0.94$), one has $D_{\mathrm{X}} \leq D_{\mathrm{c}}$, where D_{X} and D_{c} are the assumed linear sizes of the X-ray emitting region and of the obscuring cloud respectively. On the other hand, $D_{\mathrm{X}} = \Delta T v_{\mathrm{c}}$, where v_{c} is the absorbing cloud velocity and $\Delta T \leq 63$ days is the time it takes to transit from an unobscured to a fully covered spectral state[3].

As discussed above, the UV data strongly suggest to identify the absorbing structure with one cloud of the clumpy, dusty torus. Hence, v_{c} is lower than the Keplerian velocity at the dust

---

[3] Although the *Swift* observation is mildly absorbed, we consider it to be unobscured because the two N_{H} during the *Swift* and XMM 1 observation differ by nearly two orders of magnitude, making it highly unlikely that the same structure was obscuring partially the *Swift* observation as well.

sublimation radius $R_{\text{dust}} \sim 0.4 L_{\text{Bol},45}^{0.5}$ pc (Nenkova et al., 2008a). The (averaged) bolometric luminosity of ESO 362-G18 can be estimated from the 2–10 keV luminosity assuming a X-ray bolometric correction k_{2-10}. We use here the total (rather than the power law) averaged and unabsorbed 2-10 keV luminosity $L_{2-10}^{(\text{tot})} \sim 5.1 \times 10^{42}$ erg s^{-1}, as material at R_{dust} sees all contributions. As for the X-ray bolometric correction, we assume $k_{2-10} = 25$ (Vasudevan et al., 2009), which gives $L_{\text{Bol}} = 1.3 \times 10^{44}$ erg s^{-1} (i.e. an Eddington ratio of $L_{\text{Bol}}/L_{\text{Edd}} \simeq 0.02$ for a black hole mass of $M_{\text{BH}} = M_{\text{best}} = 4.5 \times 10^{7}\ M_{\odot}$). From the estimated L_{Bol} we have that $R_{\text{dust}} \sim 0.14$ pc. Assuming Keplerian motion of the clumpy torus clouds, one has that $v_{\text{c}} \leq 1180$ km s^{-1} for $M_{\text{BH}} = M_{\text{best}}$.

Substituting the upper limit on v_{c} (as well as $\Delta T \leq 63$ days) into $D_{\text{X}} = \Delta T v_{\text{c}}$ gives $D_{\text{X}} \leq 6.4{\times}10^{14}$ cm. This corresponds to $D_{\text{X}} \leq 96\, r_g\ M_{\text{best}}/M_{\text{BH}}$, so that X–rays come from radii within $D_{\text{X}}/2 = 48\, r_g\ M_{\text{best}}/M_{\text{BH}}$ from the central, accreting black hole under the natural assumption of axial symmetry. This is consistent not only with microlensing results (e.g. Mosquera et al. (2013) and references therein), but also with measurements of the X-ray emitting size coming from other, better monitored X-ray occultation events which imply $D_{\text{X}} \leq 10-20\, r_g$ (e.g. Risaliti et al. (2007, 2009), Sanfrutos et al. (2013)). A simple sketch of the envisaged geometry and time-evolution is shown in Fig. 2.14.

The upper limit on D_{X} also represents a lower limit on D_{c}. By combining this with the maximum observed column density, we infer that the cloud number density is $n_{\text{c}} \leq 6.7 \times 10^{8}$ cm^{-3}. Such a density is lower than that required for BLR clouds ($\geq 10^{9}$ cm^{-3}), supporting our identification of the variable absorber with one clumpy torus cloud.

2.9 Discussion

The multi-epoch X-ray observations ESO 362–G18 reveal that the AGN is generally mildly absorbed by both partially ionized and neutral/low-ionization gas. While the warm absorber properties do not change significantly during our monitoring, the neutral absorber exhibits remarkable spectral variability with one observation (XMM 1) being highly significantly more absorbed than all others.

While unabsorbed, the X-ray spectrum is characterized by a strong soft excess, typical of the X-ray spectra of type 1 AGN. A broad feature is also seen at Fe K energies, and the *Suzaku* data from the HXD also suggest a hard X-ray excess around 20-30 keV. All features are highly reminiscent of a reflection component off the inner accretion disc, whose spectral shape is distorted by relativistic effects. Using data from two the two highest-quality, relatively unabsorbed observations *Suzaku* and XMM 2, we show that the X-ray spectrum is indeed best-described by a power law continuum affected by warm absorption, a reflection component from distant matter

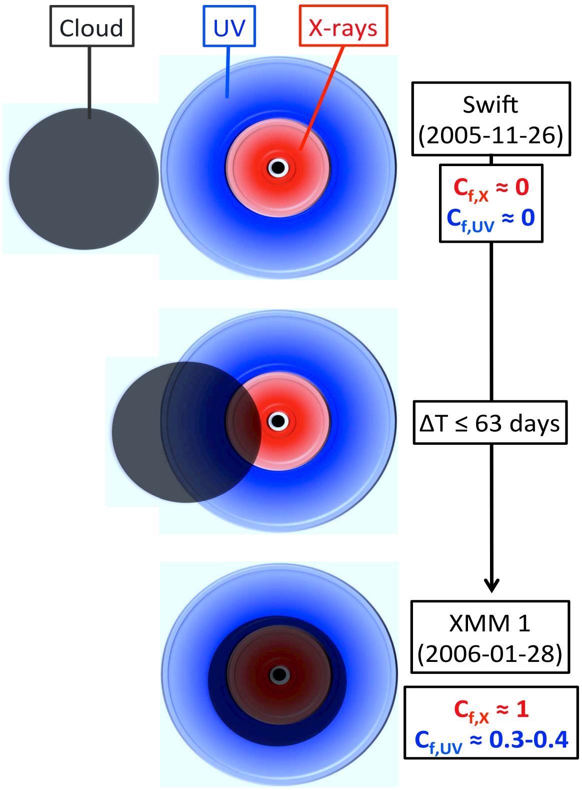

FIGURE 2.14: A simple sketch of the possible system geometry as a function of time during the transition between the unabsorbed *Swift* and the heavily absorbed XMM 1 observation. We show the larger and blue UV-emitting region, the smaller and red X-ray one, and the absorbing cloud (dark gray). The figure is not to scale for visual clarity. The time-evolution proceeds from top to bottom. The upper panel is representative of the unabsorbed *Swift* observation. The lower panel represents the likely geometry during the absorbed XMM 1 observation performed 63 days later, when the UV-emitting region is partially covered ($C_{\mathrm{f,\ UV}} \sim 0.3 - 0.4$) by the dusty absorbing cloud, while the X-ray-emitting region is fully covered ($C_{\mathrm{f,\ X}} \sim 1$). An intermediate situation where both the UV and X-ray-emitting regions are partially covered is shown in the middle panel.

(comprising an unresolved Fe emission line) and, most importantly, a relativistically distorted disc–reflection spectrum originating in the inner accretion flow. The detection of an X-ray reverberation lag between the continuum-dominated and soft-excess-dominated bands supports our spectral model and suggests that the continuum and reprocessing sites are separated by $\sim 7\ r_g$. From our disc-reflection model, we infer that the black hole powering the AGN in ESO 362-G18 is a rapidly spinning Kerr black hole, and we measure a black hole spin $a \geq 0.92$ at the 99.99 per cent (statistical) confidence level. The disc-reflection emissivity profile is steep, with $q = 4.3^{+0.8}_{-0.6}$, and the inclination i between the disc axis and our LOS is $53° \pm 5°$. Such a relatively high inclination implies that our LOS may intercept the classical obscuring torus of AGN unification schemes whose half-opening angle is typically assumed to be of the order of 45°.

Indeed, we observe X-ray absorption variability during our campaign, pointing to a clumpy structure of the absorber. All observations but one are consistent with being unabsorbed, or mildly absorbed. The absorbed observation XMM 1 is characterized by a column density of $\sim 3-4\times10^{23}$ cm^{-2} and a covering fraction of $C_\mathrm{f} \geq 0.94$. On the other hand, the prev ous *Swift* observation performed only 63 days earlier is consistent with a typical mildly absorbed state, with a neutral column density about two orders of magnitude lower. UV variability between the absorbed XMM 1 and the unabsorbed *Swift* and XMM 2 observations strongly suggests that absorption is due to a dusty cloud of the clumpy torus transiting the LOS during the (only) heavily obscured observation of our monitoring campaign.

It is worth pointing out that, in our best-fitting spectral model, the absorber is applied to both the power law continuum and the disc-reflection component with the same covering fraction in each observation. We now perform a simple check of this assumption. We select the two most heavily absorbed observations (namely the XMM 1 and XMM 2 ones). Our best-fitting model, obtained by assuming the same covering fraction towards the two spectral components in each observation, results in $\chi^2 = 1634$ for 1579 dof. We then allow the covering fraction towards the power law and the disc-reflection component to be different. We reach a similar statistical quality ($\chi^2 = 1631$ for 1577 dof), and the covering fraction towards the two components is consistent with being the same during each observation. This means that any constraint that can be obtained on the size of the X-ray emitting region is valid for both spectral components.

The relatively short X-ray absorption variability timescale of $\sim$ 2 months between the *Swift* and XMM 1 observations enables us to constrain the X-ray emitting-region size to $D_\mathrm{X} \leq 96\ r_g$, i.e. assuming the natural axial symmetry, $D_\mathrm{X}/2 = R_\mathrm{X} \leq 48\ r_g$. As absorption affects both the power law continuum (X-ray corona) and soft excess (disc-reflection, according to our decomposition), R_X has to be associated with the outer boundary of the largest of the two emitting sites. The resulting compact nature of the soft excess emitting-region is fully consistent with our interpretation in terms of disc-reflection as, according to our model (and the steep emissivity profile), the bulk of the X-ray reflection flux originates from radii within $\sim 10\ r_g$. As the X-ray source is consistent with being fully covered during the XMM 1 observation, the cloud linear size must be larger (or at most equal) to the X-ray source size. By combining this result with the observed column density we infer a cloud density of $n_\mathrm{c} \leq 6.7\times10^{8}$ cm^{-3}. Such a density is lower than that typically required for BLR clouds, supporting our identification of the variable absorber with one cloud of the dusty, clumpy torus.

2.10 Summary and outcomes of this chapter

From the analysis described in this chapter, we can conclude that ESO 362-G18 generally exhibits the typical X-ray spectrum of a Sy1 galaxy comprising a power law representing the primary X-ray continuum, warm absorption by partially ionized gas, a narrow iron emission line and its reflection continuum. Moreover, a highly significant soft X-ray excess is detected below $\sim$ 1 keV and, at the same time, a neutral absorber partially covering the X-ray emission is also required by the data in most observations. The soft excess is very well described by a relativistically distorted X-ray disc-reflection component. The disc-reflection component also accounts for broad residuals in the iron K band and above 10 keV. From our best-fitting reflection model, we infer that the accreting black hole powering the AGN in ESO 362–G18 is a very rapidly spinning Kerr black hole with spin $a \geq 0.92$ at the 99.99 per cent confidence level and system inclination of $\sim 53°$.

As for the neutral partially covering absorber, ESO 362–G18 is typically only mildly absorbed. However, the absorber is variable (in both column density and covering fraction). In particular, one observation is heavily absorbed by a cold column density of $\sim 3-4 \times 10^{23}$ cm^{-2}, consistent with a full coverage of the X–ray emission. The heavily absorbed observation was performed only $\sim$ 2 months after a mildly absorbed one (with nearly two orders of magnitude lower column density). Clear UV variability between the heavily absorbed observation and the others strongly suggests to identify the variable absorber with a dusty cloud of the clumpy torus transiting the LOS during the (only) heavily obscured observation. The $\sim$ 2 months absorption variability timescale enables us to constrain the X-ray emitting region to be confined within $\sim$ 50 gravitational radii from the central black hole. Such result holds not only for the X-ray corona responsible for the power law continuum emission, but also for the soft X-ray excess which then originates from radii that are fully consistent with a disc-reflection interpretation. The detection of a $\sim$ 650 s, time delay possibly corresponding to $\sim$ 1600 s the intrinsic one, between energy bands that are dominated by the continuum and the soft excess respectively also supports the reflection interpretation for the soft excess.

In addition, ESO 362-G18 is characterized by an averaged bolometric luminosity of 1.3×10^{44} erg s^{-1} which, considering our best-estimate for the black hole mass of 4.5×10^{7} $M_{\odot}$, translates into an Eddington ratio of 0.02. Also the derived high inclination of $\sim 53°$ is expected to intercept, at least at times, the atmosphere of the obscuring torus which is generally thought to have an half-opening angle of $\sim 45°$. This is consistent with the X-ray and UV results which enable us to identify the variable absorber with the clumpy, dusty torus.

Chapter 3

Further X-ray monitoring of ESO 362-G18: tracking a eclipse event

In this chapter we report the detection of an eclipse event taking place in ESO 362-G18. A supernova explosion dated on 2010 November and placed 20” from the nucleus of ESO 362-G18, resulted in a monitoring of our target during more than two months. The available 36 observations allow us to study in detail the evolution of the X-ray absorption variability on shorter time scales than in our analysis described in the previous chapter. Besides detecting a clear eclipse of the X-ray emitting region, it gave us an opportunity for verifying and reinforcing the conclusions obtained in Agís-González et al. (2014) (hereafter Paper I). This work will is part of a planned future publication.

3.1 Introduction

As mentioned in previous chapters, occultation events are rather common in AGN. One of the most showy cases is that of the Seyfert galaxy NGC 1365 reported by Risaliti et al. (2007). They caught the source in an occultation event of the central X-ray source with extreme spectral variability, transiting from a Compton-thin state to another one dominated by reflection and back to Compton-thin again in a time scale of only four days. They interpreted this event as a Compton-thick cloud crossing our LOS, and they were able to estimate an upper limit to the X-ray source of size of $10^{14} cm$ whereas derived a cloud-source distance less than $10^{16} cm$. Thus, they proved the theoretical predictions on the extremely compact size of the central X-ray emitting region on the one hand, and they demonstrated that the gas Compton-thick circumnuclear gas responsible for the occultation is located at a distance consistent with the scale of the BLR on the other hand.

Maiolino et al. (2010) went in depth into the properties of BLR clouds. They analyzed a 300 ks *Suzaku* observation of NGC 1365 and found variations of the column density and the covering fraction during the occultation. They inferred that the intercepted BLR clump is far from having a spherical geometry (as sometimes assumed) and, instead, propose a comet-like structure, i.e a cloud comprising a dense head ($n \sim 10^{11} cm^{-3}$) and an expanding dissolving tail longer than $\sim 10^{13} cm$. They suggest that the cometary shape ma be a common feature if BLR clouds in general, but it is difficult to recognize observationally. This structure could be originated by shocks and hydrodynamical instabilities generated in turn by the supersonic motion of the BLR clouds into the intra-cloud medium. On the other hand, the presence and structure of "cometary" clouds adds possible solutions for long-standing problems in modeling the BLR. Maiolino et al. (2010) also estimate that the cloud head loses a significant fraction of its mass through the cometary tail, which is expected to cause the total cloud destruction within a few months, which implies that the BLR region must be continuously replenished with gas clouds, possibly from the accretion disk. Such scenario would solve the problem of the long-term stability of BLR clouds, for which a convincing solution has not been found yet (Bianchi et al., 2012).

Markowitz et al. (2014) carried out a deep analysis of multitime-scale X-ray-absorption variability, looking for discrete absorption events in nearby type 1 and Compton-thin type 2 AGN within the vast archive of Rossi X-ray Timing Explorer (RXTE). They detected 12 eclipse events in 8 objects, with durations of hours to months. In seven of these objects, the occultations are caused by clouds whose derived parameters are consistent with being located at the outer BLR or at the inner regions of the torus. The remaining object, NGC 3783 was found to exhibit a double peak in its hardness ratio light curve, suggesting two eclipses separated by only 11 days. After proving that other different scenarios physically probable do not fit with the data, the authors conclude that double peak is likely due to two connected clumps belonging to a same same cloud that is being tidally distorted or sheared.

Here we report results from a monitoring campaign of ESO 362-G18 with *Swift* observatory, which yields 36 observations within 2 months and 8 days. These data allow us a further study on the X-ray variability of this source where we prove that such variability is clearly driven by remarkable absorption which triggers a eclipse event.

3.2 The *Swift* monitoring campaign

Swift monitored ESO 362-G18 between 2010 November 15 and 2011 January 23 with a total of 36 short exposures to follow the optical/UV decay of the Supernova SN2010jr that was first detected on 2010 November 12 about 20″ from the nucleus. The observation ID, date, and net X-ray exposure for the XRT instrument are reported in Table 3.1 for all monitoring observations. UVOT was operated simultaneously to the XRT observations hterefore each XRT exposure is complemented with optical/UV data in most of the available filters from V (centered at ~ 5468 Å) to UVW2 (~ 1928 Å). We are interested here only in the central AGN, and we have extracted optical/UV products taking care of excluding SN2010jr from both source and background regions using a circular region of 5″ radius for the source, and an annulus with inner (outer) radii of 5″ (10″). As for XRT data, we extract source products from a circular region with a radius of ~ 47″, and the background is estimated from nearby source-free circular regions. SN2010jr lies within the X-ray source region. However, we check that, even during the first monitoring observation corresponding to the epoch when SN2010jr was at its brightest level, the X-ray flux contribution is negligible, and nuclear X-ray spectra obtained with and without the excision of a circular region with 5″ radius centered on SN2010jr do not exhibit any significant difference.

3.3 Summary of previous X–ray observations of ESO 362–G18

To briefly remind the reader, ESO 362-G18 has been observed several times in X-rays in the past few years. In our previous work on the source (Paper I), we report results from the detailed analysis of *Swift* (1 observation), *Suzaku* (1), *XMM* (2), and *Chandra* (5) observations obtained between November 2005 and June 2010. The main results of our analysis can be summarized as follows: ESO 362-G18 is, typically, a mildly absorbed AGN whose most relevant X-ray continuum components are an X-ray power law with a stable photon index of $\Gamma \sim 2.0$ and a partially ionized relativistic reflection component off the accretion disc. The latter component implies a disc inclination of $\sim 53^\circ$, a relatively steep emissivity profile with $q \sim 4.3$ (where the reflection emissivity is defined as $\epsilon(r) \propto r^{-q}$), and an inner radius consistent with the innermost stable circular orbit for a maximally spinning Kerr black hole. The relativistic reflection component accounts very well for a clear soft X-ray excess and broad Fe line, as well as for a hard X-ray excess seen in the *Suzaku* data above 10 keV. A (mild) neutral column density of $\sim 10^{22}$ cm^{-2} with covering fraction of ~ 0.5 always partially covers the above continuum components. A weak warm absorber is also present.

However, one of the available X-ray observations (performed on January 2006 with *XMM–Newton*) caught ESO 362–G18 in a highly absorbed state with an additional column density of $\sim 3.5 \times 10^{23}$ cm^{-2} consistent with full coverage of the X-ray continuum components. The event was interpreted as the transient eclipse of the X-ray nuclear emitting regions (X-ray continuum and disc reflection) by a cloud of the dusty clumpy torus.

The analysis of the 9 previous X-ray observations allowed us to derive a detailed spectral model for ESO 362-G18 in its typical mildly absorbed X-ray state. Besides the absorbed continuum components mentioned above, the model comprises a soft power law associated with distant scattered suffered by the primary X-ray continuum and absorbed by the Galactic column density only, as well as a series of soft Gaussian emission lines that are (both) typically detected

TABLE 3.1: Log of the X-ray observations used in this work. We report the *Swift* observation ID, the observation date, and the net exposure in the XRT detector in seconds.

Obs. ID	Date	Net exposure (s)
00031868001	2010-11-15	1970
00031868002	2010-11-16	2605
00031868003	2010-11-17	2392
00031868004	2010-11-18	1950
00031868005	2010-11-19	2008
00031868006	2010-11-21	2100
00031868007	2010-11-22	2100
00031868008	2010-11-23	2410
00031868009	2010-11-24	2365
00031868010	2010-11-25	2100
00031868011	2010-11-26	2615
00031868012	2010-11-27	2080
00031868013	2010-11-28	2021
00031868014	2010-11-29	2032
00031868015	2010-11-30	1533
00031868016	2010-12-02	1821
00031868017	2010-12-06	697
00031868018	2010-12-10	3874
00031868019	2010-12-12	4388
00031868020	2010-12-14	4308
00031868021	2010-12-16	3988
00031868022	2010-12-18	4338
00031868023	2010-12-20	88
00031868024	2010-12-22	4023
00031868025	2010-12-24	4250
00031868026	2010-12-27	4006
00031868027	2010-12-30	4088
00031868028	2011-01-02	4028
00031868029	2011-01-05	1303
00040311001	2011-01-07	1244
00031868030	2011-01-08	4218
00031868031	2011-01-12	1983
00031868032	2011-01-15	3961
00031868033	2011-01-18	4310
00031868034	2011-01-21	4365
00040311002	2011-01-23	1026

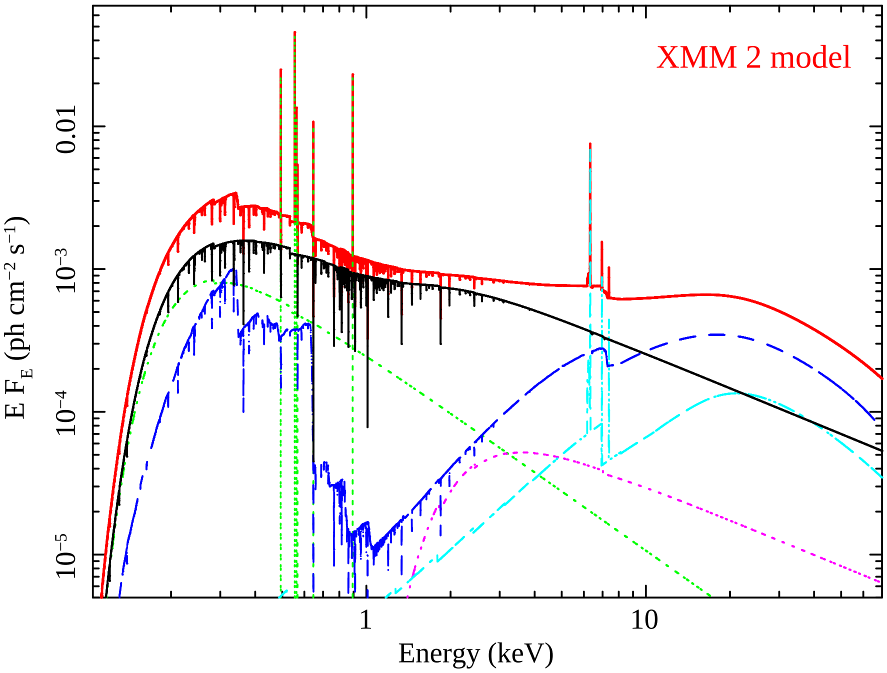

Figure 3.1: Best-fitting model for the highest quality previous *XMM-Newton* observation of ESO 362-G18 from Paper I. The observation was performed on 2010 January 29 and caught the source in a typical, mildly absorbed X-ray state. The overall model is shown as the upper red solid line together with all spectral components. The black solid line is the intrinsic power law, affected by both warm and cold (partially covering) absorption. The disc-reflection component is the dashed dark-blue line, while the dash-dotted light-blue line represents the distant reflection component. Dotted lines show the scattered components, comprising a soft scattered power law plus emission lines (green), and an absorbed, hard scattered component (magenta) that has a luminosity of ~ 12% that of the intrinsic continuum. Note that the latter component has a negligible contribution in this observation, and that it is significantly detected only at epochs where the hard X-ray continuum is more heavily obscured.

in the X-ray spectrum of AGN whenever the soft X-ray flux drops (either intrinsically or due to absorption, as in typical Seyfert 2 galaxies). Our model also comprises a standard, distant neutral reflection component carrying a narrow Fe emission line at 6.4 keV (again, as ubiquitously observed in the X-ray spectra of AGN) and a hard scattered power law component that we associate with scattering off the dusty clumpy torus. The latter component is only significantly detected in heavily absorbed states (see also our work on ESO 323-G77, Miniutti et al. (2014) and Sanfrutos et al. (2016)) and it is consistent with having the same scattering fraction at all epochs. The overall spectral model is shown as reference in Fig. 3.1, adapted from Paper I.

3.4 X–ray spectral variability of ESO 362–G18

In the upper panel of Fig. 3.2, we show the 4-7 keV X-ray light curve of ESO 362-G18 during the whole *Swift* monitoring campaign. The source is clearly variable in the X-ray band in a time scale as short as two days. AGN variability is, typically, either intrinsic or driven by X-ray absorption variability (Elvis et al., 2004, Risaliti et al., 2005, Sanfrutos et al., 2013). We choose the 4-7 keV band in order to minimize the latter effect, so that the light curve shows the best possible approximation to the intrinsic X-ray flux variability of ESO 362-G18 during the ~ 2 months of the monitoring campaign.

A soft (0.3-0.6 keV) light curve of ESO 362-G18 is shown in the middle panel. In soft bands the absorption effects are usually more noticeable and indeed the source show even higher amplitudes. In order to search for any spectral variability during the monitoring campaign, we produce a hard-to-soft ratio (H/S) between the hard 4-7 keV and the soft 0.3-0.6 keV bands. This is shown in the lower panel of the same figure. Clear H/S variability is seen during the first ~ 30 days, while H/S remains approximately constant thereafter, despite significant 4-7 keV flux variability. To increase the signal-to-noise and reduce the uncertainties (especially in the lower panel of Fig. 3.2) we combine each three consecutive *Swift* observations, obtaining 12 new *Swift* XRT exposures. The resulting binned 4-7 keV light curve is shown in the upper panel of Fig. 3.3. In the lower panel of the same figure, we show the corresponding H/S ratio between the 4-7 keV and the 0.3-0.6 keV light curves.

Thus, Fig. 3.3 confirms the H/S variability during the initial $\sim 30-35$ days. It may be associated either with genuine spectral variations intrinsic to the source, or with absorption variability mostly affecting one of the two bands (normally the soft one). In general, the X-ray continuum slope is a function of X-ray flux, with steeper continua associated with higher flux states. As can be seen in both Fig. 3.2 and Fig. 3.3, significant hard X-ray flux variability is present throughout the monitoring campaign, but H/S only varies significantly during the first half. This suggests that the H/S variability is not driven by spectral variability associated with intrinsic X-ray flux fluctuations, but rather to an external transient event, possibly absorption variability, occurring during the first half of the monitoring campaign.

In order to understand the origin of the H/S variability, we extract two different spectra. One is representative of the highest possible H/S epoch, and it is obtained by combining the two highest H/S data points (filled red circles in the lower panel of Fig. 3.3), corresponding to six individual *Swift* observations for a total exposure of 12.4 ks. The other, is obtained by combining the last three data points of the same figure (blue empty circles) and it is representative of an epoch during which H/S is constant, as well as much lower than during the high-H/S epoch. Its total net exposure if 26.4 ks, and the spectrum is obtained by combining 9 individual *Swift* observations. For simplicity, we refer to the two spectra as the high H/S and low H/S respectively.

We start our analysis with the low H/S spectrum. As it is approximately constant, the spectrum is likely representative of the typical spectral shape of ESO 362-G18. Although the quality of the spectrum is not very high (slightly less than 20000 counts are gathered in the 0.3-8.5 keV band), we define our spectral model making use of our previous work on ESO 362–G18

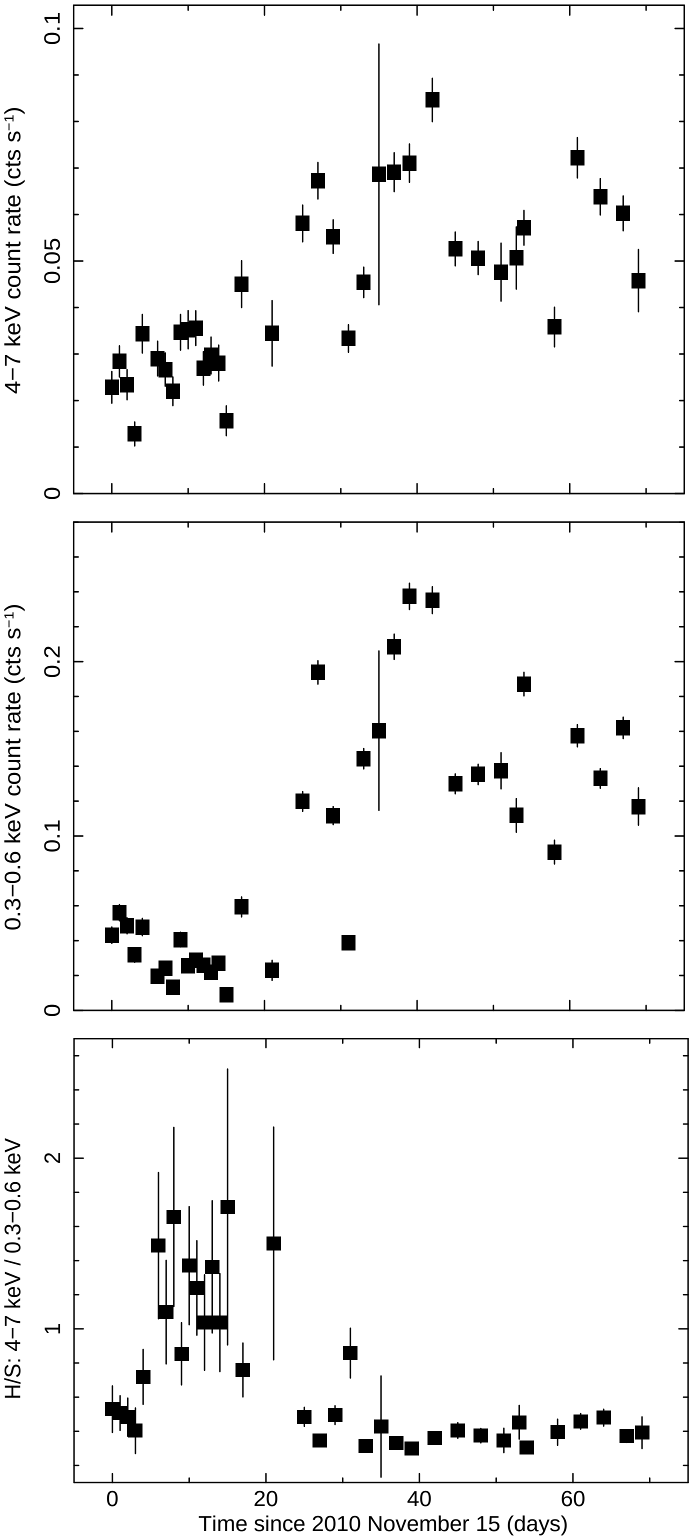

FIGURE 3.2: The 4-7 keV light curve during the *Swift* monitoring campaign is shown in the upper panel. The 0.3-0.6 keV light curve is shown in the middle panel, and the hard-to-soft ratio H/S between the 4-7 keV and the 0.3-0.6 keV bands is plotted in the lower panel. Each data point is obtained from one individual *Swift* observation. Time is shown in days since the first observation on 2010–11–15

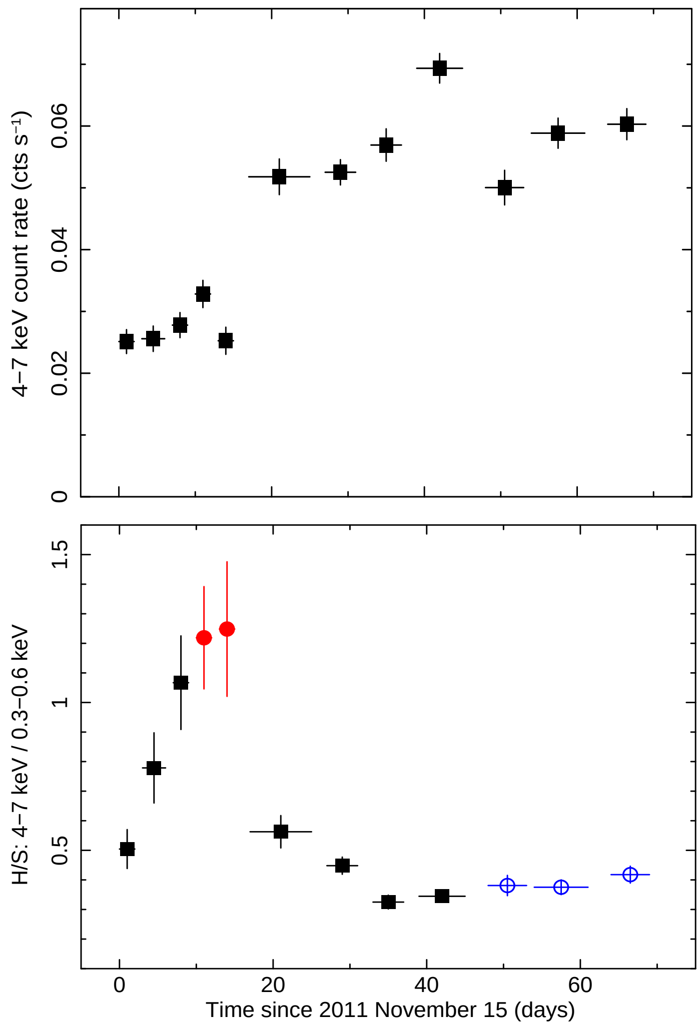

FIGURE 3.3: A binned version of the upper and lower panels Fig. 3.2. Each data point is obtained by combining three consecutive *Swift* observations. Filled (red in the on–line version) and open (blue) circles represent the time intervals used to extract the high and low H/S spectra respectively, see text for details.

(Paper I), as detailed in Section 3.3. Due to the relatively low quality of the *Swift* XRT data (in comparison with much longer previous exposures with *XMM–Newton*, *Suzaku*, and *Chandra*), the spectrum could be described by simpler and more phenomenological spectral models, but the derived spectral parameters would not be consistent with the analysis of previous higher quality X-ray observations of the source (for instance, considering a simple absorbed power law plus blackbody model results in a flat photon index of Γ 1.6). For this reason, we prefer to consider a more complex, but also more physical model which can describe well not only the *Swift* data, but also all previous X-ray observations of ESO 362-G18.

The adopted spectral model comprises a power law continuum, its distant and relativistic reflection components, a series of soft Gaussian emission lines plus a soft power law accounting for extended emission and scattering, and a hard, absorbed scattered power law. The overall spectral model is absorbed by the Galactic column density (1.75×10^{20} cm^{-2}, see Kalberla et al. (2005)). A layer of partially covering neutral gas with $\simeq 10^{22}$ cm^{-2} and covering fraction of the order of 50 % affects only the nuclear components (power law continuum and disc reflection component) that are also affected by a weak warm absorber (see Section 3.3 and Chapter 2).

We apply this model to the low H/S spectrum, fixing as many parameters as possible to those derived from the much higher quality X-ray data presented in Paper I. The parameters that are fixed include all those associated with emission from extended components (scattered and soft X-ray emission lines), the distant reflection component carrying the narrow Fe emission line, the warm absorber parameters, as well as all the relativistic parameters affecting the disc reflection component (black hole spin, disc inclination and emissivity profile that are all fixed to their best-fitting values reported in Paper I). In summary, our final spectral model is characterized by the following 6 free parameters: [(*i*)] the intrinsic power law continuum photon index and normalization, [(*ii*)] the relativistic reflection ionization state and normalization and [(*iii*)] the column density and covering fraction of the neutral absorber. As mentioned, the overall spectral model is discussed in Paper I, Chapter 2 and Section 3.3, and it is shown in Fig. 3.1.

The model provides a fair description of the low H/S spectrum with $\chi^2 = 381$ for 361 dof ($\chi^2_{red} = 1.05$). The neutral absorber has a column density of $1.5 \pm 0.6 \times 10^{22}$ cm^{-2} and a covering fraction of 0.5 ± 0.1, consistent with that derived in Paper I from much higher quality *XMM-Newton* and *Chandra* data during typical mildly absorbed states. The AGN X-ray continuum has a photon index of $\Gamma = 2.1 \pm 0.1$, again consistent with previous X-ray observations of ESO 362-G18. The relativistic reflection component presents an ionization parameter of 40 ± 30 erg cm s^{-1}, and a 2-10 keV luminosity of $\sim 7.76 \times 10^{41}$ erg s^{-1}, while the intrinsic X-ray continuum has a 2-10 keV luminosity of 4.36×10^{42} erg s^{-1}. We consider that this spectral model provides an adequate description of the low H/S spectrum which, by comparing the resulting parameters with those obtained from previous X-ray observations of the source, appears to represent a typical, mildly absorbed X–ray state of ESO 362-G18.

The low H/S spectrum and best-fitting model are shown in the top panel of Fig. 3.4. In the same Figure, we also show the high H/S spectrum together with the same spectral model rescaled to approximately match the 4-7 keV data of the high H/S spectrum. The spectral shape above 4 keV is very similar, but the high H/S spectrum is characterized by a large deficit of soft X-ray photons. Thus, the most likely explanation for this spectral shape is that the high H/S spectrum is affected by extra absorption with respect to the low H/S one, like the similar event observed on 2006 January 28 with *XMM-Newton*. During that observation ESO 362-G18 was heavily absorbed, while a *Swift* observation two months earlier caught the source in the typical mildly absorbed state, i.e. the event occurred on a timescale of the order of 2 months. In that case, the *XMM-Newton* data were interpreted as a transient occultation of ESO 362-G18 by a cloud of the dusty clumpy torus (see Chapter 2) and the *XMM–Newton* heavily absorbed spectrum could be very well reproduced by the typical spectral model discussed in Section 3.3 (and used above for the low H/S spectrum) with the addition of an extra layer of absorbing gas (in the sense that the column density of the neutral absorber was allowed to vary along the observations). It is therefore natural to look for a similar solution for the high H/S state observed during the *Swift* monitoring campaign.

We then proceed by fitting simultaneously the low and high H/S spectra using the same baseline spectral model (as defined above for the low H/S spectrum), adding an extra absorption component. We consider neutral absorption at the redshift of the galaxy and, for the sake of generality, we allow the neutral absorber to only partially cover the X-ray continuum components. The only parameters that are allowed to be different between the two spectra are the same than we keep free to try the spectral shape of the low H/S data : (*i*) the nuclear power law photon index and normalization, (*ii*) the extra absorption column density and covering fraction and (*iii*) the disc reflection ionization and normalization. However, after a few tests, the photon indices in the two spectra appear to be consistent with each other, and we then force the same Γ at both epochs to reduce further the number of free parameters. As the extra absorber is not required by the low H/S data, we also force the same column density in the two spectra to obtain an upper limit on the covering fraction during the low H/S interval. The simultaneous fit of the low and high H/S spectra is acceptable with $\chi^2 = 463$ for 441 dof ($\chi^2_{red} = 1.05$).

The absorber covering fraction in the low H/S state is $C_f \leq 0.13$. On the other hand, the high H/S state requires extra absorption with $N_H = 4.2 \pm 1.5 \times 10^{22}$ cm^{-2} and $C_f = 0.83 \pm 0.04$. Replacing the extra absorber with an ionized one (with column density and ionization forced to be the same at the two epochs for simplicity) further improves the fit and we reach a final best-fitting model of $\chi^2 = 455$ for 440 dof. Allowing for a different ionization at the two epochs does not provide any further statistically significant improvement. The low H/S spectrum is still unabsorbed with $C_f \leq 0.15$, while the high H/S is affected by a partially ionized absorber with column density $N_H = 5.0 \pm 1.5 \times 10^{22}$ cm^{-2}, ionization $\log \xi = 1.0 \pm 0.4$ and covering fraction $C_f = 0.88 \pm 0.03$. The data and best–fitting models are shown in the middle panel of Fig. 3.4, and the resulting residuals for the two spectra are shown in the lower panel of the same Figure.

3.4.1 Time-resolved spectral analysis

Having found a good description for the low and high H/S spectra, we then proceed with a time-resolved spectral analysis of the whole *Swift* campaign. We consider the simultaneous analysis of all 12 spectra corresponding to the data points shown in Fig. 3.3. All spectra are considered in the 0.3-7 keV band, except the last five that have enough spectral quality to be used up to 8.5 keV. We use exactly the same model as above. Guided by the previous analysis, we force the photon index to be the same at all epochs (we have checked a posteriori that leaving

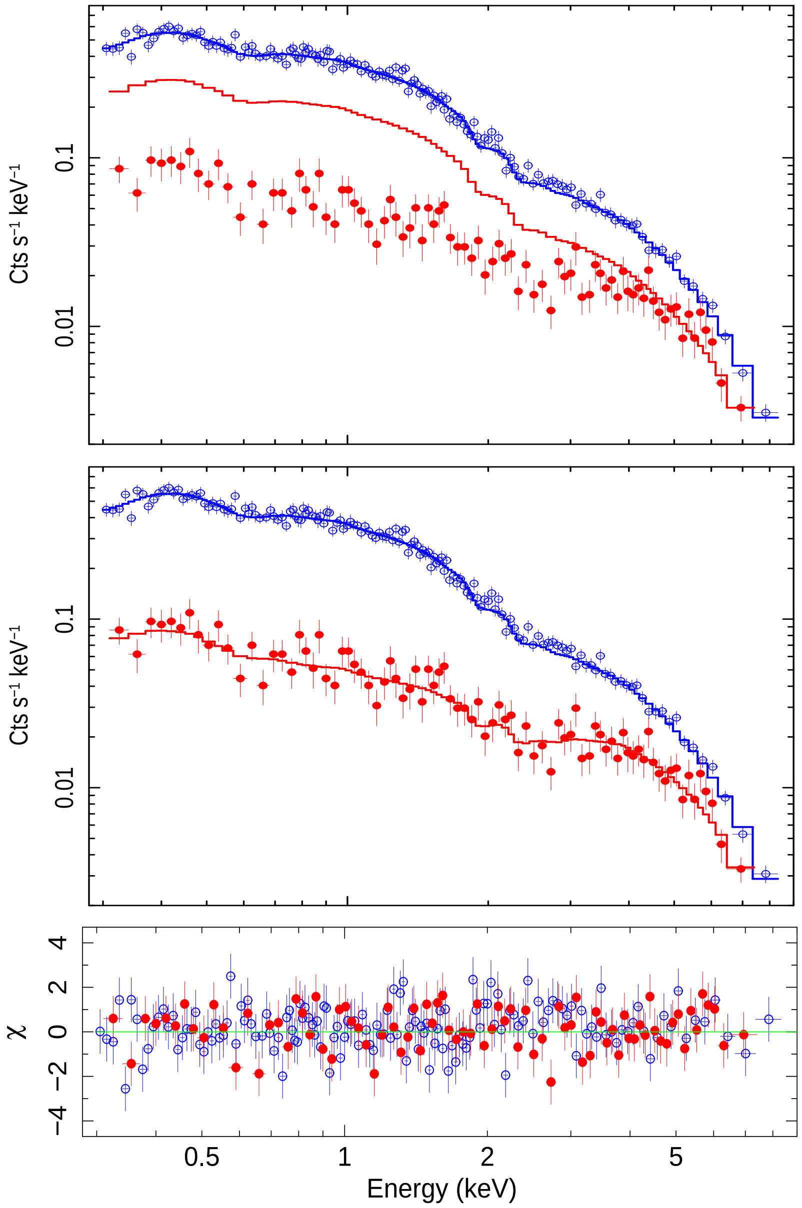

Figure 3.4: *Upper panel:* we show the low H/S spectrum (empty blue circles) together with the high H/S spectrum (filled red circles). The top (blue) solid line represents the best-fitting model for the low H/S spectrum. The bottom (red) solid line is the same model rescaled to match the 4–7 keV data of the high H/S spectrum. *Middle panel:* same as above, but the bottom solid red line is now the best–fitting model for the high H/S spectrum. The model differs from that of the low H/S spectrum only for a layer of partially covering ionized gas. *Lower panel:* The best-fitting residuals ($\sqrt{\chi^2}$ in each channel) for the low and high H/S best-fitting models (shown in the middle panel above).

the photon index free to vary does not improve the fit). In order to describe any evolution of the absorber properties, we first consider the simplest possible model in which the column density and ionization are always the same, and only the covering fraction is allowed to vary during the *Swift* monitoring. We assume at first that the absorber covers, at each epoch, with the same covering fraction both nuclear continuum components (intrinsic power law and disc reflection). In summary the only parameters that are allowed to vary independently in the 12 spectra are the continuum normalization, the disc reflection ionization and normalization, and the covering fraction of the extra ionized absorber. Its column density and ionization, as well as the continuum photon index and the overall neutral absorber parameters are allowed to vary but they are forced to be the same at all epochs.

The model describes the data well, and we reach a $\chi^2 = 1849$ for a total of 1764 dof ($\chi^2_{\rm r} \simeq 1.05$). The extra ionized absorber is statistically required (i.e. its covering fraction is different from zero at the 90 per cent level at least) in the first 7 spectra only (the first 7 data points in Fig. 3.3). The (common) column density and ionization are $\rm N_H = 4.8 \pm 1.1 \times 10^{22}\ cm^{-2}$ and $\log \xi = 1.0 \pm 0.3$ respectively. In principle, if the absorber density and location are constant, the absorber ionization should be variable and proportional to the intrinsic X-ray flux. If the ionization state of the absorber is let free to vary independently in the 12 spectra, no improvement is obtained. This is probably because all ionization best-fitting values are within the range allowed by the previous fit (a factor 4 in total), while the maximum intrinsic flux variability during the campaign is a factor of ~ 3.5 between the 5th and 9th spectrum, see upper panel of Fig. 3.3). The same lack of statistically significant improvement occurs when the column density is free to vary independently in the 12 spectra. The most important parameter is the (variable) covering fraction of the extra ionized absorber. Its evolution across the whole monitoring period is shown in the upper panel of Fig. 3.5. The evolution is very smooth and, in fact, it can be well described by a Gaussian centered at 12.0 ± 0.6 days with $\sigma = 8.1 \pm 0.6$ days since the beginning of the monitoring campaign. Such smooth Gaussian evolution of the covering fraction implies that the X-ray emitting region experiences a transient occultation event by an absorbing structure of similar size as the X-ray emitting region, and that the event is followed almost completely from ingress to egress during the *Swift* monitoring campaign.

We then consider the possibility that the covering fraction towards the power law X-ray continuum and that towards the disc reflection component might be different. In other words we look for a solution in which the emitting regions of the two components (namely the X-ray corona and the reflecting accretion disc) are spatially distinct (in size and/or location). The statistical quality of the fit is basically the same, and we obtain $\chi^2 = 1834$ for 1752 dof ($\chi^2_{red} \simeq 1.05$) to be compared with $\chi^2 = 1849$ for 1764 dof ($\chi^2_{red} \simeq 1.05$) of the model in which the covering fraction towards the two components is the same at any given epoch. As the two fits are statistically equivalent, we shall not draw any strong conclusion from the latter attempt. It is however interesting to compare the evolution of the covering fraction towards the two

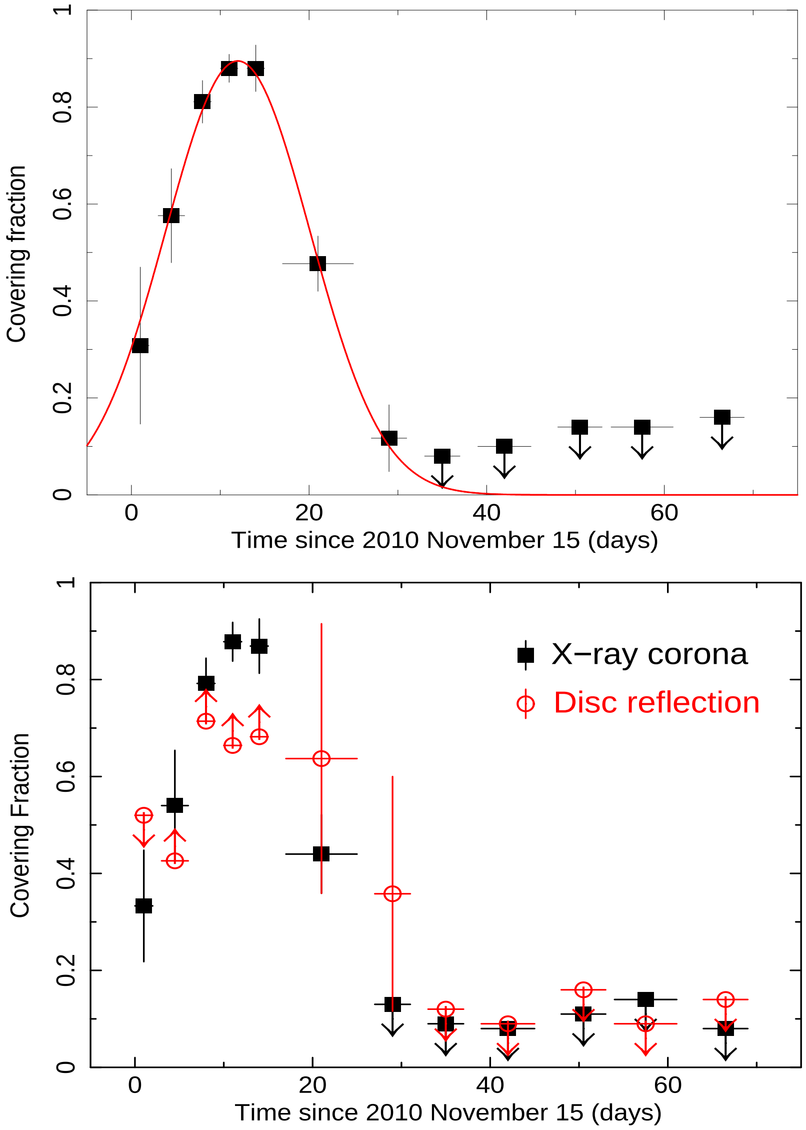

Figure 3.5: The covering fraction evolution during the *Swift* monitoring campaign. In the **upper panel** we show the evolution under the assumption that the covering fraction towards the X–ray power law continuum (physically, the X–ray corona) and the disc reflection component is the same at any given epoch. We also show a simple Gaussian fit to the covering fraction evolution. The best–fitting centroid is at 12.0 ± 0.6 days since 2010 November 15. In the **lower panel** we show the evolution of the covering fractions towards the two continuum components (X–ray corona and disc reflection) when they are allowed to be different at any given epoch, possibly reflecting a different spatial distribution of the two emitting region.

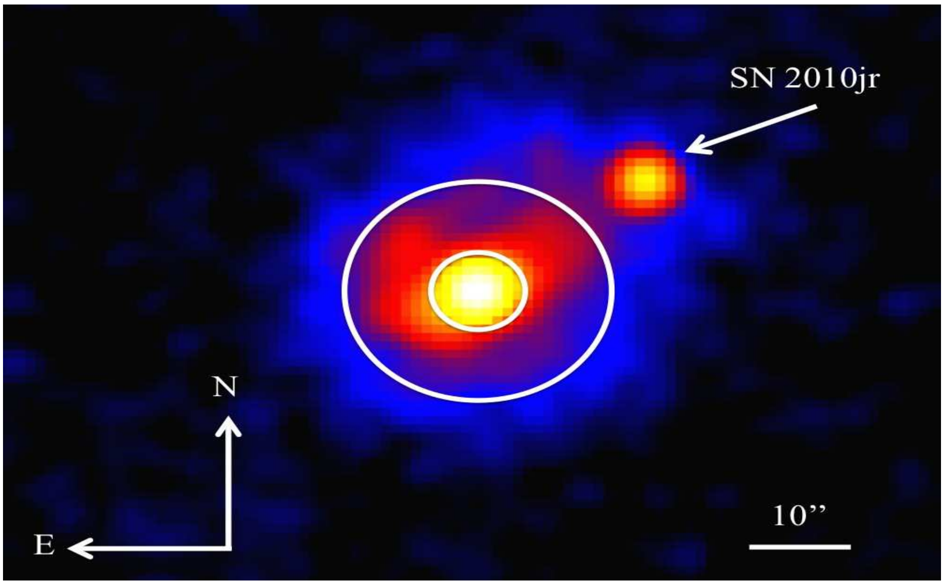

FIGURE 3.6: The UVOT image of ESO 362-G18 in the M2 filter during the first monitoring observation on 2010–11–15. The supernova SN 2010jr is clearly seen. We show the source (inner circle) and background (outer annulus) extraction regions used for the optical/UV photometry.

components in order to see whether the derived values show any trend. The evolution of the two covering fractions is shown in the lower panel of Fig. 3.5. At all epochs, the two covering fractions are consistent with each other within the errors. The covering fraction toward the disc reflection component is more loosely constrained than that towards the X-ray corona.

3.4.2 UV variability

The UVOT telescope on board the *Swift* mission provides simultaneous ultraviolet and optical coverage in the $\sim 1700-6000$Å band. During the *Swift* monitoring of SN201jr (which was the trigger for the *Swift* campaign), the 36 observations were complemented with optical and UV data using filters V (central wavelength at 5468 Å), B (4392 Å), U (3465 Å), UVW1 (2600 Å), UVM2 (2246 Å), and UVW2 (1928 Å). The galaxy is well detected in all filters and the supernova SN2010jr is clearly visible in most images. In Fig. 3.6 we show the UVOT image of ESO 362-G18 in the UVM2 filter during the first observation of the monitoring campaign (on 2010 NOvember 15), where the UV flux from SN2010jr is the highest. As we are only interested in the optical/UV photometry of the nucleus, we extract UVOT products in an inner circle of 5 arcseconds in radius, considering an outer annulus with inner (outer) raddi of 5′′ (10′′) as background region. As can be seen in Fig. 3.6, our selection makes the contribution of SN2010jr totally neglibile, so that our final UVOT products are not affected by the supernova flux.

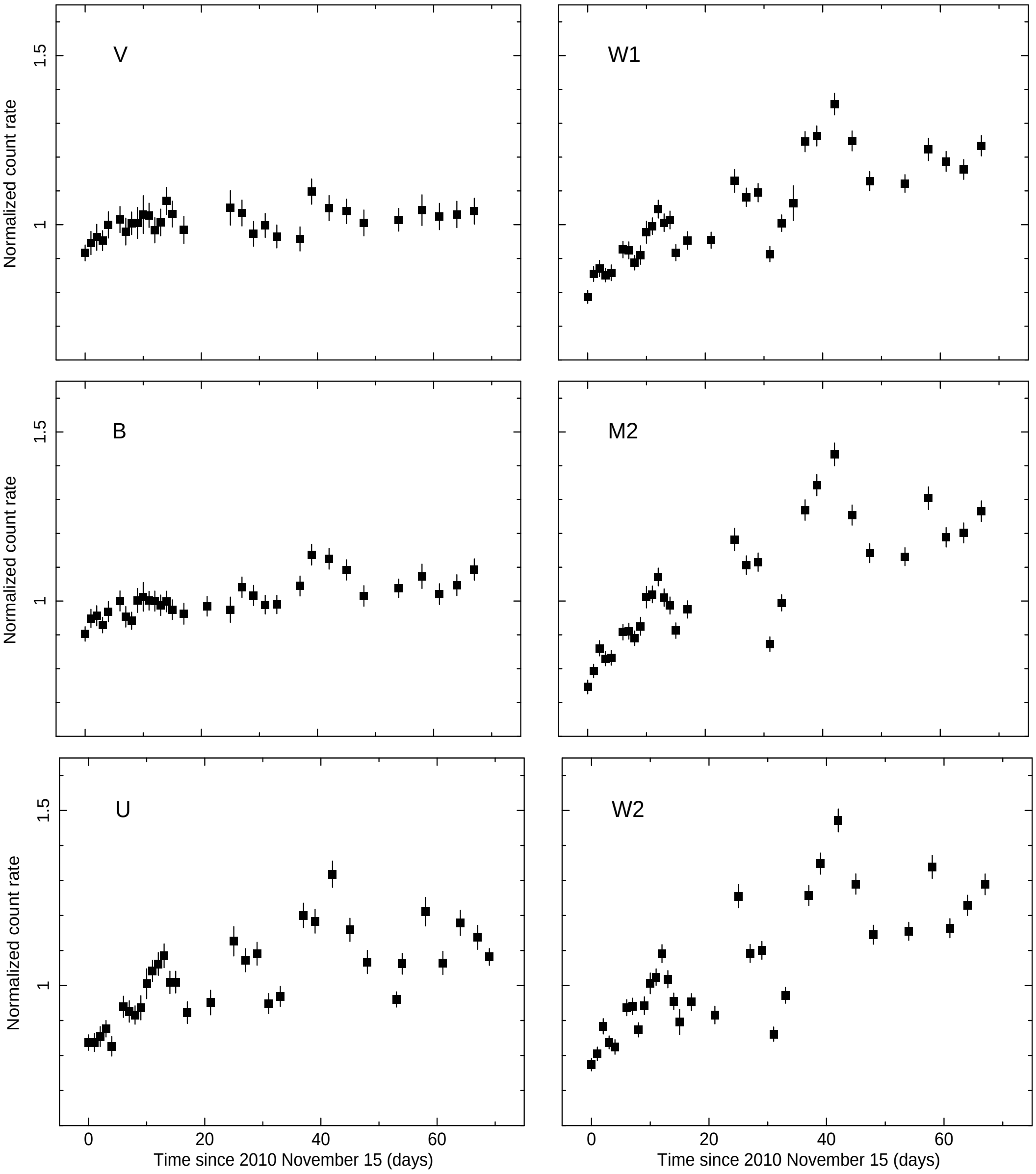

FIGURE 3.7: The UVOT count rates in the optical filters V, B, U (left) and in the UV filters W1, M2, and W2 (right). To ease comparison, the light curve in each filter has been normalized to its mean value. The y-axis scale is the same in all panels.

Fig. 3.7 show the optical and UV light curves in all filters. In all panels we show the background subtracted count rate normalized to its mean value to ease comparison between the different light curves. ESO 362-G18 is variable in all filters, with increasing amplitude from long to short wavelengths, from a few per cent variability in filter V during the whole monitoring, to more than 100 per cent at the shortest available wavelength (W2). The variability amplitude is even higher in the X-rays, as can be seen in Fig. 3.2. The overall long term trend is of an increase of optical/UV flux, matching closely the similar behavior seen in the X-rays. The longer wavelengths (V and B filters) are likely affected by the galaxy flux, which might explain their lower variability amplitude, and we do not discuss them any more here.

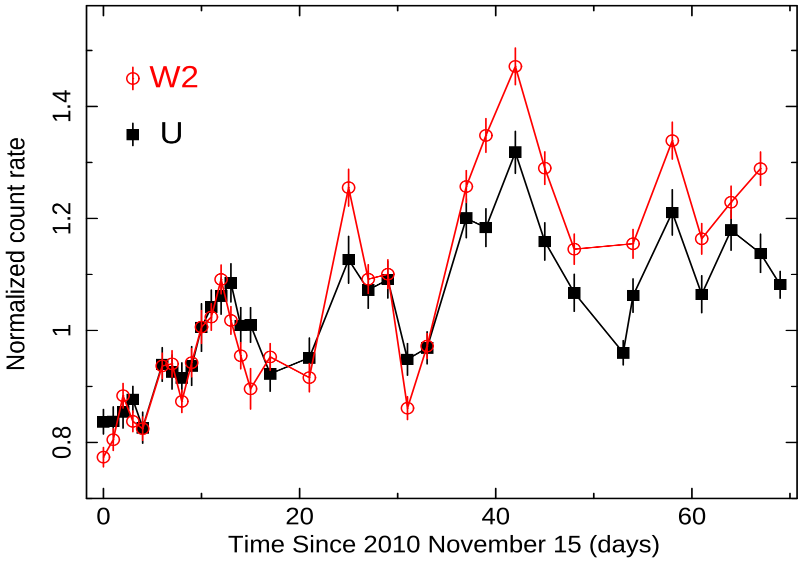

FIGURE 3.8: The U (filled squares, black) and W2 (open circles, red in the on–line version) normalized light curves are shown in the same panel to ease he comparison between optical and UV variability properties.

Here we are interested in understanding whether part of the optical/UV variability could absorption-induced, as it is the case in the X-rays. Assuming that the optical and UV emission are due to the thermal accretion disc emission (plus reprocessing, if any), the optical flux should originate in more extended regions than the UV that, in turn, should originate in more extended regions than the X-rays. Hence, any absorption-induced variability should be associated with (*i*) increasingly longer timescales and (*ii*) increasingly smaller covering fractions going from short to long wavelengths (X-rays to optical). Optical and UV light curves should then show a different behavior if part of their variability is indeed absorption-induced.

In Fig. 3.8 we show a comparison between an optical (U) and an UV (W2) light curve (in both cases we show the normalized count rate). The two light curves are very well correlated and, besides the higher variability amplitude in the W2 filter, the only significant difference appears to occur during the first significant optical/UV flare. There appears to be a time delay of the order of 1 days between the leading W2 and lagging U light curves between causing the W2 flux to drop faster than the U flux between 12 days and 15 days. This apparent time delay does not occur in the other three optical/UV flares around 25 days, 42 days, and 58 days. Although the difference between U and W2 light curves occurs close to the epoch at which X-ray absorption is maximal (12 days) it is difficult to interpret this behavior securely in terms of optical (or, most likely, UV) absorption. This is because if the faster UV drop was due to absorption, we would expect to see much longer timescales, as the UV emitting region is expected to be much more extended than the X-rays. The only plausible explanation might be that a significant part of the UV (W2) flux originates in a region as compact as the X-ray emitting region and that it is only the flux from that compact region that is affected. In principle this may be a viable explanation, as the X-ray reflection spectrum off the accretion disc can extend naturally to the UV due to a non-zero ionization state.

However, besides this difference, we do not see a clear trend of absorption-induced variability in the comparison between optical and UV light curves. This may be because:

(*i*) the covering fraction towards the corresponding emitting regions is too low to have a significant effect on the optical/UV fluxes, and/or

(*ii*) the timescales for absorption-induce variability are too large to have a significant impact across the monitoring campaign, and/or

(*iii*) the absorber that affects the X–rays is dust–free so that its impact in the optical and UV is only minor.

3.5 Absorber properties and X–ray emitting region size

The intrinsic (i.e. the power law continuum only) and unabsorbed 2-10 keV luminosity of ESO 362-G18 averaged over the occultation event (first 30 days of the monitoring) is $\simeq 2.7 \times 10^{42}$ erg s^{-1}. As in the former chapter, considering a standard bolometric correction of a factor $k_{2-10\ keV} = 25$ (Vasudevan et al., 2009), the bolometric luminosity is estimated to be $\simeq 6.75 \times 10^{43}$ erg s^{-1}. As discussed in section 2.6, the black hole mass is of the order of $4.5 \times 10^7\ M_{\odot}$, so that the Eddington ratio for ESO 362-G18 during the first 30 days of the *Swift* monitoring camapign is $L_{\rm bol}/L_{\rm Edd} \simeq 0.012$. The dust-sublimation radius during that epoch is $R_{\rm dust} \simeq 0.4 L_{\rm bol,45}^{1/2} \simeq 0.104$ pc $= 3.2 \times 10^{17}$ cm (Barvainis, 1987).

Let us consider the simplest possible geometry for the occultation event. We consider a uniform X-ray emitting region of linear size $D_{\rm s}$ and an obscuring cloud of linear size $D_{\rm c}$. The cloud has uniform column density $N_{\rm H}$, so that its number density $n_{\rm c}$ is simply defined as $n_{\rm c} = N_{\rm H}/D_{\rm c}$. It should be noticed that, in order to accomplish the former assumption, the cloud cannot present a spherical geometry because a sphere cannot keep a constant column density towards all directions parallel to our LOS. Instead, the rough approximation of considering a cube, whose face-on is perpendicular to our LOS, give rise to a constant column density along our LOS. Besides, we consider that the cloud motion is dominated by gravity, i.e. the cloud orbits the central black hole with a velocity $v_{\rm c} = (GM_{\rm BH}/R_{\rm c})^{1/2}$ where $M_{\rm BH}$ is the black hole mass and $R_{\rm c}$ is the cloud radial distance from the center. This very crude approximation of the real geometrical structure will enable us to constrain the physical parameters of the absorber as well as to derive an estimate of the X-ray emitting region size.

Let us consider two possible geometries for the occultation event:

(*i*) the source size $D_{\rm s}$ is slightly larger than the cloud size $D_{\rm c}$, or

(*ii*) the source is smaller than the cloud, but the occultation is mis-aligned, so that it is possible that the X-ray emitting region is never fully covered.

These two possibilities have different consequences for the covering fraction overall evolution, and they can actually be distinguished. Let us define as $\Delta T_{\rm Max}$ the time interval during which the X-ray emitting region is maximally covered, and as $\Delta T_{\rm Part}$ the time interval during which the covering fraction decreases (or increases). From the upper panel of Fig. 3.5 it is clear that $\Delta T_{\rm Max} < \Delta T_{\rm Part}$. In fact, the covering fraction evolution implies that $\Delta T_{\rm Max} \leq 6$ days while $\Delta T_{\rm Part} = 15 - 21$ days.

We then consider the two possibilities mentioned above. If $D_{\rm c} < D_{\rm s}$ (see upper panel of Fig. 3.9), we have that:

$$v_{\rm c} = \frac{D_{\rm c}}{\Delta T_{\rm Part}} = \frac{D_{\rm s} - D_{\rm c}}{\Delta T_{\rm Max}} \quad \text{, so that} \quad \frac{D_{\rm s}}{D_{\rm c}} = 1 + \frac{\Delta T_{\rm Max}}{\Delta T_{\rm Part}} \tag{3.1}$$

which is consistent with the initial assumption of $D_{\rm c} < D_{\rm s}$.

On the other hand, if $D_{\rm c} > D_{\rm s}$ (see bottom panel of Fig. 3.9), then:

$$v_{\rm c} = \frac{D_{\rm c}}{\Delta T_{\rm Max}} = \frac{D_{\rm s}}{\Delta T_{\rm Part}} \quad \text{, so that} \quad D_{\rm c} = D_{\rm s}\frac{\Delta T_{\rm Max}}{\Delta T_{\rm Part}} \tag{3.2}$$

which can never be consistent with the initial assumption of $D_{\rm c} > D_{\rm s}$ because $\frac{\Delta T_{\rm Max}}{\Delta T_{\rm Part}} < 1$. We then conclude that the occultation we observe is characterized by $D_{\rm c} < D_{\rm s}$ and, using the observed value of $C_{\rm f,max} \geq 0.83$ we have that $0.81 D_{\rm s} \leq D_{\rm c} \leq D_{\rm s}$, since the covering fraction is defined as the ratio between the projected areas of the source and the cloud, $C_f = \frac{D_C^2}{D_S^2}$.

We can now derive the properties of the absorbing cloud. We first consider the definition of the ionization parameter $\xi_{\rm c} = \frac{L_{\rm ion}}{n_{\rm c} R_{\rm c}^2}$, where $L_{\rm ion}$ is the ionizing luminosity betwee 1 and 1000 Rydberg. In our case, we estimate $L_{\rm ion} \simeq 5.06 \times 10^{43}$ erg s^{-1}. Using our best-fitting results for the cloud ionization parameter $\log \xi_{\rm c} = 1.0 \pm 0.3$, we have that $n_{\rm c} R_{\rm c}^2 = [0.25 - 1.00] \times 10^{43}$ cm^{-1}.

On the other hand, the cloud velocity is defined as $v_{\rm c} = \sqrt{\frac{G M_{\rm BH}}{R_{\rm c}}}$ and, as mentioned above, we also have $v_{\rm c} = \frac{D_{\rm c}}{\Delta T_{\rm Part}} = \frac{N_{\rm H}}{n_{\rm c} \Delta T_{\rm Part}}$. By combining both relationships, we obtain $R_{\rm c} n_{\rm c}^{-2} = [2.9 - 14.0]$ cm^7. Using the previous result of $n_{\rm c} R_{\rm c}^2 = [0.25 - 1.00] \times 10^{43}$ cm^{-1}, we can solve for $n_{\rm c}$ and $R_{\rm c}$, and derive $n_{\rm c} = [1.05 - 2.6] \times 10^8$ cm^{-3} and $R_{\rm c} = [1.5 - 2.0] \times 10^{17}$ cm where lower densities and larger radii are associated with smaller column densities and viceversa. The derived $R_{\rm c}$ places the absorber just within the dust sublimation radius $R_{\rm dust} \simeq 3.2 \times 10^{17}$ cm

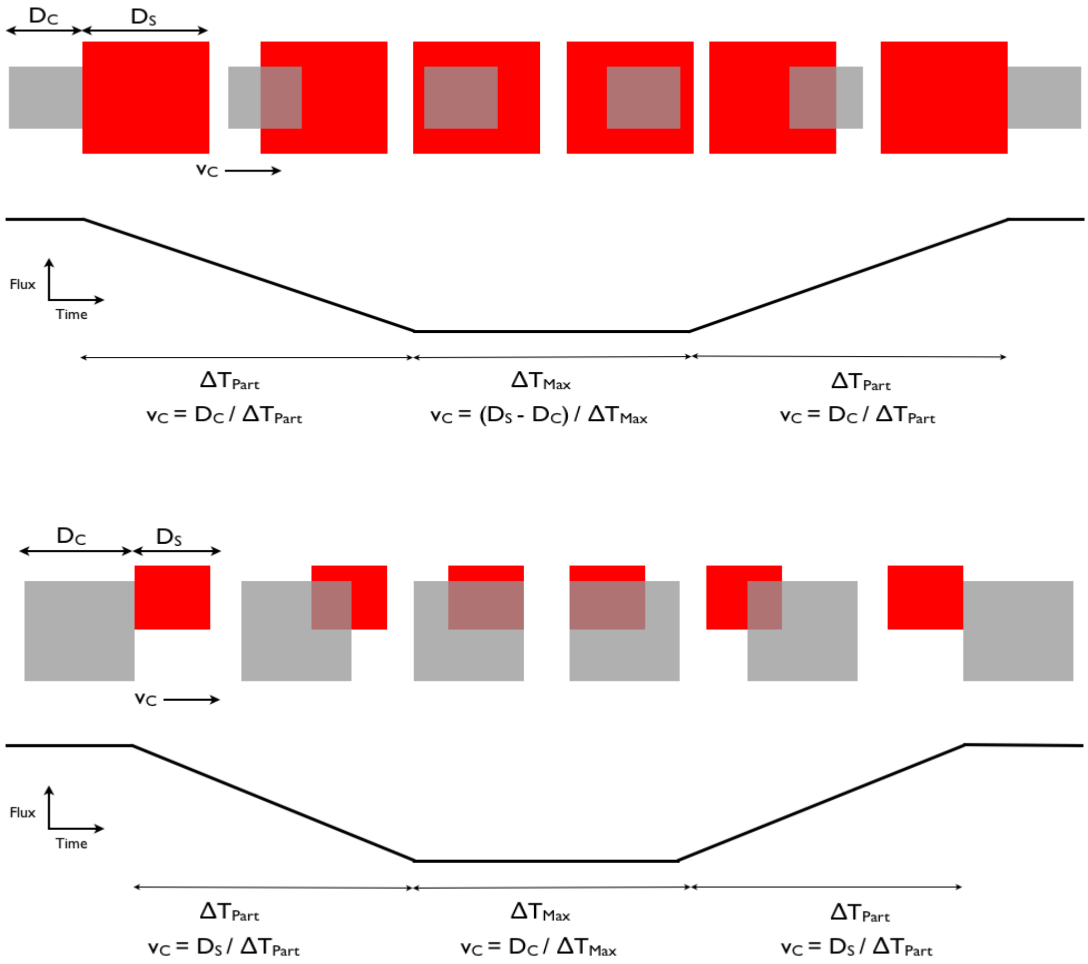

FIGURE 3.9: Sketch of the possible relative sizes of the cloud and the source (see text for details).

which may explain why no clear signs of absorption–induced variability is seen in the optical and UV lught curves (see Fig. 3.7 and Fig. 3.8), because the absence of dust.

As $D_{\rm c} = \frac{N_{\rm H}}{n_{\rm c}}$, taking into account that high densities correspond to high $N_{\rm H}$ values, we have $D_{\rm c} = [2.3–3.5]\times 10^{14}$ cm. For the adopted black hole mass, this corresponds to $D_{\rm c} = [34–53]\ r_g$. Since, $0.81 D_{\rm s} \leq D_{\rm c} \leq D_{\rm s}$, the X-ray emitting region size is $D_{\rm s} = [34-65]\ r_g$. Assuming the natural axial symmetry, the outer radius of the X-ray emitting region is then constrained in the range between 17 r_g and 33 r_g, demonstrating the compact nature of the X-ray emission in AGN.

3.6 Discussion

We report the detection of an X-ray occultation event in ESO 362–G18 during a ~ 2 months *Swift* monitoring campaign, originally motivated by the follow-up of supernova SN2010jr. A mildly ionized absorber with $\log \xi \sim 1.0$ and column density $N_{\rm H} \sim 5 \times 10^{22}\ cm^{-2}$ crosses our LOS to the AGN X-ray emitting region during the first ~ 35 days of the campaign. The X-ray data suggest that the ionization and column density of the absorber remain approximately constant across the occultation event. The X-ray emitting region is maximally covered with covering fraction $C_{\mathrm{f}} \sim 0.88$ during 6 days at most. The covering fraction evolution shown in the upper panel of Fig. 3.5, coupled with derived ionization and column density, enables us to estimate the properties of the absorber. Assuming a cloud with uniform column density, linear size D_{c}, and motion dominated by gravity, we derived the cloud location $R_{\mathrm{c}} = 1.75 \pm 0.25 \times 10^{17}$ cm, corresponding to a cloud velocity $v_{\mathrm{c}} = 1.85 \pm 0.15 \times 10^{3}$ km s^{-1}. The cloud location suggest that the absorber lies just within the dust sublimation radius ($R_{\mathrm{dust}} \simeq 3.2 \times 10^{17}$ cm for ESO 362-G18 during the occultation) which may be the reason why no clear absorption-induced variability is seen in the optical and UV (Fig. 3.7 and Fig. 3.8). The cloud number density is estimated to be in the range $n_{\mathrm{c}} = [1.05 - 2.6] \times 10^{8}$ cm^{-3}, and its linear size is $D_{\mathrm{c}} = 2.9 \pm 0.6 \times 10^{14}$ cm $= 49.5 \pm 15.5\ r_g$. From the maximum covering fraction observed during the occultation event, one has that the X-ray emitting region linear size D_{s} (we assume uniform emission within the region) is related to the cloud size D_{c} by $0.81 D_{\mathrm{s}} \leq D_{\mathrm{c}} < D_{\mathrm{s}}$. Assuming the natural axial symmetry for the X-ray emitting region, we conclude that the outer radius of the X-ray emitting region is constrained in the range between 17 r_g and 33 r_g. This demonstrates the compact nature of the X-ray emitting region. As shown in the lower panel of Fig. 3.5, the quality of the X-ray data is insufficient to distinguish the evolution of the covering fraction towards the nuclear intrinsic continuum (the X-ray corona) and the disc reflection component. Hence, the limits on the outer radius we derive above apply to both the power law continuum and the disc reflection component.

In the adopted spectral model, we have included a disc reflection component. However, as mentioned, at the level of quality of the *Swift* data, disc reflection simply models the soft X-ray excess that is seen in ESO 36-G18 as well in most Sy1 galaxies in the X-rays. Indeed, if we use a simple power law plus blackbody model to reproduce the X-ray continuum, we find a similarly good description of the spectral evolution of ESO 362-G18 and an extra ionized absorption with variable covering fraction is still required to model the spectral variability across the monitoring campaign. The absorber has now a column density of $5.2 \times 1.4 \times 10^{22}$ cm^{-2} and ionization $\log \xi = 0.9 \pm 0.3$. The (common) photon index is flat with $\Gamma = 1.6 \pm 0.1$ vs. $\Gamma \sim 2.1$ derived from the disc- reflection interpretation. The covering fraction evolution using this very simple spectral model as baseline is shown in Fig. 3.10 and is very similar to the evolution shown in the upper panel of Fig. 3.5 with the only difference being that the maximum covering fraction is slightly lower, most likely reflecting the much flatter X-ray photon index. As for the previous model, we can not distinguish the evolution of the covering fraction towards the X-ray corona and the soft X-ray excess (here simply described with a thermal model), so that the two emitting regions are consistent with similar location and size. For the simple power law plus blackbody phenomenological model, we repeat the calculations performed above, and we derive a cloud size of $D_{\mathrm{c}} = [1.4 - 3.5] \times 10^{14}$ cm $= [21 - 53]\ r_g$, in very good agreement with the result

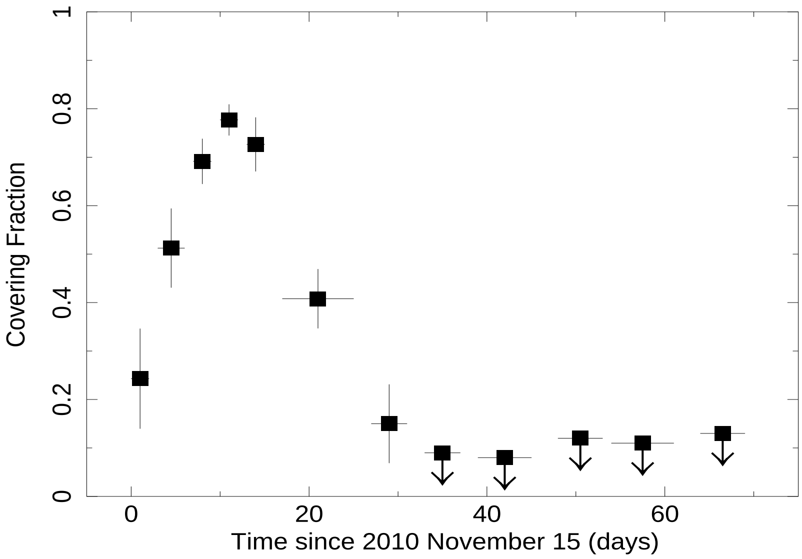

FIGURE 3.10: The covering fraction evolution during the *Swift* monitoring campaign when a phenomenological absorbed power law plus blackbody model is used as baseline. The blackbody reproduces the soft X–ray excess that was previously accounted for by the disc reflection component in the more physically–motivated model used so far. The evolution is very similar qualitatively to that shown in the upper panel of Fig. 3.5 demonstrating that the overall shape of the evolution is not driven by a specific adopted spectral model.

obtained with the more complex and physically–motivated model ($D_{\rm c}$ = [2.3 – 3.5] × 10^{14} cm = [34 – 53] r_g). As the maximum covering frction is now $C_{\rm f}$ = [0.74 – 0.79], the source size is $D_{\rm s}$ = [38 – 61] r_g. Assuming axial symmetry, we conclude that the outer radius of the X-ray emitting region is constrained in the range between 19 r_g and 30.5 r_g. This applies to both the nuclear power law and to the soft X-ray excess components, and the derived size is fully consistent with that obtained using the complex spectral model including disc reflection (outer radius between 17 r_g and 33 r_g). This demonstrates that the soft X-ray excess in ESO 362-G18 has a compact origin. Coupling this results with the spectral analysis of high quality data presented in Chapter 2 and Paper I, where a disc reflection component was necessary to model no only the soft excess but also a broad emission feature at Fe energies, and a hard X-ray excess around 20–30 keV, our analysis suggests to identify the soft X-ray excess, an almost ubiquitous spectral component in the X-ray spectra of AGN, with the contribution of a partially ionized reflection component off the inner accretion disc.

We are aware that the rough estimation of considering the column density of the absorber as constant along our LOS is not consistent with the conclusions of the works cited in the brief introduction of this chapter, e.g. Maiolino et al. (2010) or Markowitz et al. (2014)., where the clouds causing the occultation events are not homogenous in density. However, the quality of our data is not enough to reach these details of the absorber.

3.7 Summary and outcomes of this chapter

The main results of the work described in this chapter can be summarized as follows:

1. The model derived in our previous work for this same target ESO 362-G18 (see Paper 1 or Chapter 2), is consistent with these new data although here the quality of the data is not enough to resolve the finest features detected in that scenario, as for example, those associated to the disc reflection interpretation of the soft excess, or the narrow, soft X-ray emission lines.

2. As in our previous analysis of ESO 362-G18, the variability exhibited here by the source is driven by absorption. However, this *Swift* monitoring campaign provide us with the opportunity of studying an eclipse event almost completely from ingress to egress.

3. While in Chapter 2 the absorber was identified with a neutral cloud of the clumpy torus, here the absorber appears to be ionized by the AGN and it is located just within the dust sublimation radius. However, the derived velocity and density are still low to be consistent with a clump of the BLR and we suggest it to belong to the inter-material placed between the R_{dust} and the SMBH.

4. As in Chapter 2, the absorber affects both the reflection component and the X-ray continuum equally (even if we model the soft excess with a phenomenological black body), therefore, both the soft excess and the X-ray primary source have a compact origin.

5. According the UVOT data, the occultation event does not affect to the optical/UV emission, probably because the absorber is dust-free.

These conclusions make ESO 362-G018 a relative good candidate to study absorption evolution in AGN and the compactness of the X-ray emitting region(s). Then, it is interesting to go on observing this target with the aim of deepening our understanding in these lines of AGN research.

Chapter 4

ESO 362-G18 as a changing look Seyfert galaxy: optical view

In this chapter we investigate historical and new optical spectroscopic data with the goal of understanding whether the absorption variation detected at X-ray energies in ESO 362-G18 also imprints their signature at lower energies. As already discussed, our target is usually classified as a Seyfert 1.5 (Sy1.5) galaxy, e.g. Mulchaey et al. (1996a), Fraquelli et al. (2000), Bennert et al. (2006a), Winter et al. (2008). However, Parisi et al. (2009) retrieved a spectrum of this source belonging to the 6dFGS which does not show the broad lines mandatory to classify the source as type 1 since it only exhibits narrow lines, i.e. the typical spectral signature of a Sy2 galaxy. Indeed, Parisi et al. (2009) classified ESO 362-G18 as a naked, or true, Sy2 galaxy. Here we will report the differences among available archive data and a new granted observation (performed with **FO**cal **R**educer and low dispersion **S**pectrograph v.2 (FORS2)) in order to study and try to explain the disappearance/appearance of the broad emission lines in ESO 362-G18. This results, along with those derived in the next chapter, will be published in Agís-González et. al (2017) (in prep.).

4.1 Introduction

As already discussed, AGN are associated with accretion of gas onto the central SMBHs. The accretion disc, feeding the black hole, generates continuum photons that photoionize and excite the gaseous region of the BLR located light-days to light-weeks away from the black hole (Koay et al., 2016). This region is responsible for the characteristic broad emission lines of velocity widths $v \gtrsim 1000\ km\ s^{-1}$ induced by the keplerian motion around hole and observed in the optical/UV spectra of type 1 AGN. On the other hand, the photoionization of lower velocity gas at distances of hundreds of parsecs, by photons also coming from the accretion disc, produces the narrow emission lines showing $v \lesssim 1000\ km\ s^{-1}$ present in both type 1 and 2 AGN. The absence of broad lines in type 2 AGN is explained by the presence of the absorbing dusty torus, the key element of the UM (see section 1.6). However, there exits well documented cases of rare events where the source transits from type 1 to type 2 state , or vice versa, i.e. its broad lines disappear or appear in its optical/UV spectrum, e.g. in Seyfert galaxies, NGC 3516 (Collin-Souffrin et al., 1973), NGC 7306 (Tohline & Osterbrock, 1976), NGC 4151 (Penston & Perez, 1984), Fairall 9 (Kollatschny & Fricke, 1985), Mrr 1018 (Cohen et al., 1986), Mrk 993 (Tran et al., 1992), NGC 1097 (Storchi-Bergmann et al., 1993), NGC 7582 (Aretxaga et al., 1999), NGC 2617 (Shappee et al., 2014) or Mrk 590 (Denney et al., 2014), and the quasars SDSS J015957.64+003310.5 (LaMassa et al., 2015) or SDSS J101152.98+544206.4 (Runnoe et al., 2016).

Astronomers have suggested two possible potential causes for this exceptional changes in optical spectra of AGN:

(*i*) The AGN activity depends on the availability of gas to fuel the black hole. The mechanisms by which cold gas is transported from the galaxy disc at kpc scales to hundreds of pc scales, and further down into the inner few parsecs to trigger AGN activity determine the efficiency at which the black hole is fuelled (Alexander & Hickox, 2012). Then, large changes in the accretion onto the SMBH can be responsible for these changing looks, either creating or disrupting the broad line region. Moreover, it is tought that below a given critical accretion rate (or luminosity), no broad line regions can be formed nor sustained over a long time, so that sources below that critical limit would always be type 2 objects (Nicastro, 2000, Elitzur et al., 2014, Runnoe et al., 2016).

(*ii*) On the other hand, when the inclination of the source is such that our LOS intercept the upper or lower edge of the torus, relative rapid changes in the observed flux can occur when obscuring clouds belonging to the torus move to allow, or block, a clear view of the central region of the AGN (e.g. Goodrich (1989), Leighly et al. (2015)). In this configuration, the disappearance of broad emission lines can be explained by a dusty absorption event. In the previous Chapters we have shown that ESO 362-G18 presents a very favorable inclination for this scenario and, at the same time, we detected remarkable absorption events, one of which driven by the dusty torus which induces a column density variation of nearly two orders of magnitude.

In this chapter, we first consider 6dFGS and EMMI@NTT observations with the aim of establishing the cause of the disappearance of the broad Balmer emission lines in the 6dF spectrum. Then, within the European Southern Observatory (ESO) archive, we discover another spectropolarimetric observation performed with EFOSC@3.6m that show ESO 362-G18 as a

Sy2 or Seyfert 1.9 (Sy1.9) once more. Studying changing look AGN in polarized light can provide us with further information about the possible scenarios and we shall discuss about it in the next Chapter. Besides, we have obtained new polarimetric observations of ESO 362-G018 through a director discretional time (DDT) program at FORS2@VLT. In the total spectrum derived from these new data, our target shows again its showy broad lines clearly. In summary, we will analyze four observations, two of them showing ESO 362-G018 as Sy1.5, and the remaining ones displaying Sy1.9-like spectra, which allow us to characterize the changes suffered by the broad Balmer lines in ESO 362-G18. The observations are dated on 2003-01-30 (Six-degree Field (6dF)), 2004-09-18 (EMMI), 2006-09-21 (ESO Faint Object Spectrograph and Camera v.1 (EFOSC1)) and 2016-03-30 (FORS2). We will study them in chronological order.

4.2 6dFGS data: Seyfert 1.9 look

In this section we present the already analyzed 6dF spectrum of ESO 362-G18 and develop our own study in order to compare the different available spectra.

4.2.1 Data and instrumentation: 6dF multi-fibre spectrograph

The 6dFGS (Jones et al., 2004) is a large-scale redshift combined with peculiar velocity survey over almost the entire southern sky of our nearby Universe reaching $z \approx 0.15$. Its final redshift release is reported by Jones et al. (2009) and reaches limit magnitudes of $(H, J, r_F, b_J) = (13.05, 13.75, 15.6, 16.75)$. Its 136.304 spectra have yielded 110.256 new extragalactic redshifts and a new catalogue of 125.071 galaxies. Survey data, including images, spectra, photometry and redshifts were collected between 2001 and 2006 and are available through the 6dFGS Online Database (http://www-wfau.roe.ac.uk/6dFGS/).

The 6dFGS is performed with the 6dF multifibre spectrograph, an instrument that uses optical Integral Field Unit (IFU) fibres and robotic positioning technology which enables the UK Schmidt Telescope to record 150 simultaneous spectra. Spectra are obtained in two observations using separate V and R gratings, that together give $R \sim 1000$ over at least $4000 - 7500$Å and SN ~ 10 per pixel (Jones et al., 2004).

4.2.2 Previous work

As noted before, the 6dF sepctrum of ESO 362-G18 was analyzed by Parisi et al. (2009). Since it presents narrow H_α and H_β lines in emission, [O iii] forbidden emission line, as well as Caii H + K ans G absorption bands, they classify the source as Sy2 being aware that ESO 362-G018 was previously classified as Sy1.5 galaxy (e.g Mulchaey et al. (1996a), Fraquelli et al. (2000), Bennert et al. (2006a), Winter et al. (2008)). Besides, they also derives a very low reddening $E(B-V)_{AGN} = 0.036$ consistent with their Swift/XRT analysis which reveals a spectrum without intrinsic absorption. Parisi et al. (2009) reinforce this conclusion performing a diagnostic tool developed by Malizia et al. (2007) in order to evaluate absorption as Compton thin or thick. However they advise that the quality of the used X-ray data is quite low and future deep X-ray observations are needed (possibly together with < 10 keV) to assess the nature of ESO 362-G18 safely. Indeed, X-ray absorption variability reported by ourselves in Agís-González et al. (2014) and in Chapter 2 and 3 with high quality X-ray data are not consistent with the scenario derived by Parisi et al. (2009).

The absence of broad emission lines in the optical spectrum and, at the same time, the absence of intrinsic absorption on both X-ray and optical wavelengths led Parisi et al. (2009) to classify ESO 362-G18 as a true Sy2 galaxy (Bianchi et al., 2008).

4.2.3 Spectral analysis

The releases of the 6dFGS provide already reduced spectra. Nevertheless, because the aim of the survey did not required it, the data are not calibrated in flux. We carried out a flux calibration using the measured simultaneous b_J and r_F magnitudes contained in Jones et al. (2009) by IDL procedures courtesy of Parisi et al. (2009). We do not correct the spectrum for starlight contamination (Ho et al., 1993, 1997) because of its limited SN and spectral resolution, but this is not affecting our results and conclusions.

With the aim of providing an estimation of the local absorption of our source at the different epochs, all spectra were dereddened applying a correction for the Galactic absorption along the LOS. For this purpose, we made use of the extinction law by Cardelli et al. (1989) and the value for the galactic extinction calculated by Schlegel et al. (1998) and listed in NED as $E(B-V)_{GAL} = 0.017$. Then, we estimate the color excess $E(B-V)_{AGN}$ local to the AGN host through the relation from Osterbrock (1989), which compares the intrinsic line ratio:

$$E(B-V) = A \cdot log\left(\frac{H_\alpha/H_\beta}{(H_\alpha/H_\beta)_0}\right) \tag{4.1}$$

where A is a constant which depends on the extinction law and its value for Cardelli's law corresponds to 2.21, H_α/H_β is the galactic Balmer decrement and $(H_\alpha/H_\beta)_0$ is the intrinsic ratio, 2.86. Thus, for 6dF data we obtain $E(B-V)_{AGN} = 0.11 \pm 0.10$, which is consistent with the low very extinction derived by Parisi et al. (2009) $E(B-V)_{AGN} = 0.036$.

TABLE 4.1: Lines parameters together with statistical errors computed from fits with Gaussian functions on 6dF data. In order to calculate FWHMs we have taken into account the instrumental broadening, which, according to Campbell et al. (2014) the average $FWHM_{ins}$ for the fibres of 6dF is ∼ 140 $km \cdot s^{-1}$. The lines belonging to the same multiplet are forced to have the same value of their gaussian sigma, while the broad component of H_α has its center tied to that of the corresponding narrow component. The flux units are $\cdot 10^{-15} erg\ cm^{-2} s^{-1}$. F_{dered} is the reddening-corrected flux and the corresponding correction was carried out for the intervening Galactic absorption $E(B-V)_{Gal} = 0.017$ according to Schlegel et al. (1998) and through Cardielli's law. F_{dered}/H_β is the galactic reddening-corrected narrow emission line intensity ratio relative to H_β.

	FWHM ($km \cdot s^{-1}$)	EW (Å)	F_{dered} ($\cdot 10^{-15} erg\ cm^{-2} s^{-1}$)	F_{dered}/H_β
		NARROW LINES		
$H_\beta\ \lambda4861$	265 ± 60	1.09 ± 0.28	62.18 ± 5.40	1
$[O\ III]\lambda4959$	582 ± 15	3.01 ± 0.36	209.18 ± 9.72	3.36
$[O\ III]\lambda5007$	576 ± 15	10.45 ± 0.58	373.91 ± 13.12	6.01
$[O\ I]\lambda6300$	252 ± 64	1.14 ± 0.34	32.33 ± 9.17	0.52
$[N\ II]\lambda6459$	381 ± 37	1.57 ± 0.39	40.78 ± 9.34	0.66
$H_\alpha\ \lambda6563$	299 ± 17	7.73 ± 0.93	199.44 ± 12.76	3.21
$[N\ II]\lambda6583$	378 ± 37	4.38 ± 0.60	111.96 ± 12.45	1.80
$[S\ II]\lambda6716$	462 ± 40	3.93 ± 0.56	94.81 ± 10.92	1.52
$[S\ II]\lambda6731$	460 ± 40	2.15 ± 0.40	51.50 ± 5.78	0.83
		BROAD LINES		
H$\alpha\ \lambda6563$	3138 ± 746	4.44 ± 2.44	95.64 ± 50.09	-

Since the former expression does not account for radiative transfer, we are assumed that the dust is outside the NLR, or the BLR, and not mixed with gas contained in them. However, this method remains the only practical and an extended solution for finding at least an estimate of the amount of dust obscuring both the NLR and BLR, suited to compare different extinctions in the same source (see e.g. Heard & Gaskell (2016) and references therein).

In order to carry out fits to the narrow lines of this spectrum with Sy2 appearance, we used single gaussians. Nevertheless, a broad component in H$_\alpha$ was found to improve the fit (see Fig. 4.1 and Table 4.1). On the contrary, the spectral shape around H_β makes impossible to fit a broad component for this Balmer line. The results derived through these fits are shown in Table 4.1. We adopted the following notation for the gaussian function:

$$f(\lambda) = A \cdot e^{\frac{(\lambda-c)^2}{2\sigma^2}} + m \cdot \lambda + b, \tag{4.2}$$

where A is the amplitude of the Gaussian, c its corresponding center, σ its width, and m and b account for the lineal continuum (since we select a short range of wavelengths). Thus, the emission lines belonging to the same multiplet are forced to have the same σ, i.e [O III], [N II] and [S II], while the centers of the broad and narrow components of H_α and H_β, if detected, are

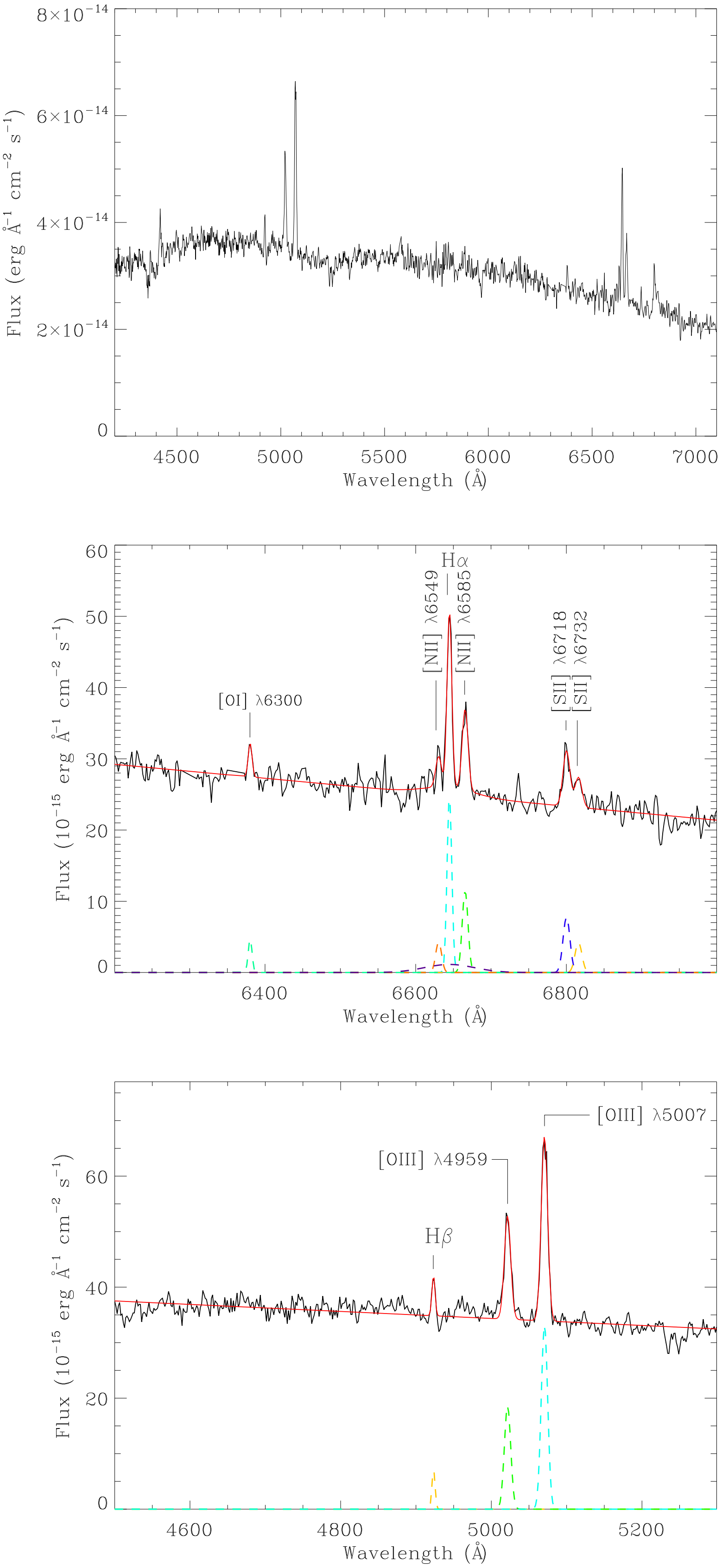

FIGURE 4.1: Calibrated spectrum and Balmer lines fits for 6dF data. *Upper panel:* 6dF calibrated spectrum of ESO 362-G18. *Middle panel and Bottom panel:* Fit performed for the emission lines around H_α. A broad component for H_α is detected. *Bottom panel:* Gaussian fits for H_β and the [O III] doublet.

also obliged to present the same value. Then, from the Gaussian parameters we derived the flux ($\sqrt{2\pi}A \cdot \sigma$), the FWHM ($2.355 \cdot \sigma$) and the equivalent width (EW) $\left(\frac{line\ flux}{m \cdot c+b}\right)$ for each emission line. The statistical errors are computed by propagation over the indicated expressions. We also took into account the instumental FWHM, $FWHM_{ins}$, in such a way that the tabulated value is $FWHM = \sqrt{FWHM_{obs}^2 - FWHM_{ins}^2}$. Campbell et al. (2014) found that the average $FWHM_{ins}$ for all fibres of 6dF along the visible range is 140 $km \cdot s^{-1}$ and we also assume this quantity. All emission lines are resolved.

4.3 EMMI data: Seyfert 1 look

In this section, we develop the same analysis carried out for 6dF spectrum in Section 4.2. This will allow us to compare, analyze and explain the differences between the obtained results.

4.3.1 Data and instrumentation: EMMI

EMMI works on the visible range, between 300 and 1000 nm, in four different observation modes: wide-field imaging, low-resolution multi-object or long-slit grism spectroscopy, medium-resolution long-slit grating spectroscopy and echelle spectroscopy. It was mounted at an adaptor-rotator at the Nasmyth B focus of the NTT, but was decommissionned in March of 2008.

EMMI is divided in two “arms” defined by optical elements: the blue arm which gather light whose wavelength ranges from 300 to 500 nm, and the red arm that delivers products from 400 to 1000 nm. The EMMI spectra of ESO 362-G18 used here were performed in medium-resolution long-slit grating spectroscopy mode. For our purpose of examining the broad components of H_α and H_β Balmer, we are only interested on red arm data and in this case the observations were made in the spectral range 4540-7060Å. The corresponding CCD has a image size of 2048 × 4096 pixels and each pixel is 15×15 μm with a pixel scale of 0.166”. The data were taken in a photometric night with a typical seeing of 0.5-1” and using a slit of width 1”.

4.3.2 Previous work

The EMMI data used here were previously analyzed by Bennert et al. (2006a). As the NLR of our target is spatially resolved, they extract information on the NLR properties by performing spatially resolved spectroscopy. As already showed by Mulchaey et al. (1996b), ESO 362-G18 exhibits [O III] extended emission along the host galaxy radio axis and ground-based images reveal a symmetrically distributed emission. Also Fraquelli et al. (2000) carried out an extensive spectroscopic study confirming that the nuclear continuum ionizes the gas in the disc along $PA = 158°$ out to 17”, giving rise to a cone-shaped region observed in [O III]. Both groups of authors classified ESO 362-G18 as type 1 AGN.

Bennert et al. (2006a), through diagnostic diagrams, find that not all of the gas in the extended NLR is of high ionization, confirming the result reported by Mulchaey et al. (1996b), but while Fraquelli et al. (2000) attribute emission out to $\sim 17''$ from the nucleus to the extended NLR, Bennert et al. (2006a) show that only the central $\pm 3''$ region is ionized by the central engine.

4.3.3 Data reduction and spectral analysis

Unlike 6dFGS, in this case we have access to the raw fits files of ESO 362-G18 through ESO archive portal. Standard reduction including bias subtraction, flat-field correction, and cosmic-ray rejection was performed using IRAF v2.14. Wavelength calibration was achieved using lamp spectra acquired in the same observation night and the spectra were rebinned to a scale of 1.58 Å/ px. Flux calibration was performed using corresponding observations of the standard star LT1788. The extinction caused by the atmosphere at La Silla Observatory was also corrected through the measurements provided by ESO. There were two available spectra with 1500 s of exposure time that we combined in order to increase the SN ratio.

Since our main purpose is to compare the available spectra of our AGN performed with different instruments, we must take care about the area from which the spectra are extracted. This is specially important if the NLR of the AGN is resolved as in this case, because in a larger area we are including a bigger fraction of the NLR, and therefore more flux. Unfortunately, the 6dF spectrum was performed with IFU fibres of 5.7” of diameter, so the long-slit of 1” of width used with EMMI makes it impossible to achieve similar “collecting” areas. Thus, the narrow emission lines will predictably change their flux (per unit of time) from 6dF to EMMI, being higher in 6dF data since this spectrum is extracted from a higher area containing larger fraction of the NLR.

We decided to extract our definitive EMMI spectrum from the three central pixel rows containing the highest flux along the spatial direction. In this way, we obtain a reasonable flux with minimum contribution form the host galaxy. At the same time, this is also a region analyzed by Bennert et al. (2006a) and it allows us to compare results. The extracted spectrum is shown in the upper panel of Fig. 4.2. There are no signs of strong underlying Balmer absorption lines and it seems clear that the AGN continuum and the broad and narrow emission lines dominate the spectrum, as usual in type 1 AGNs, so that a starlight correction is not strictly necessary for our purposes.

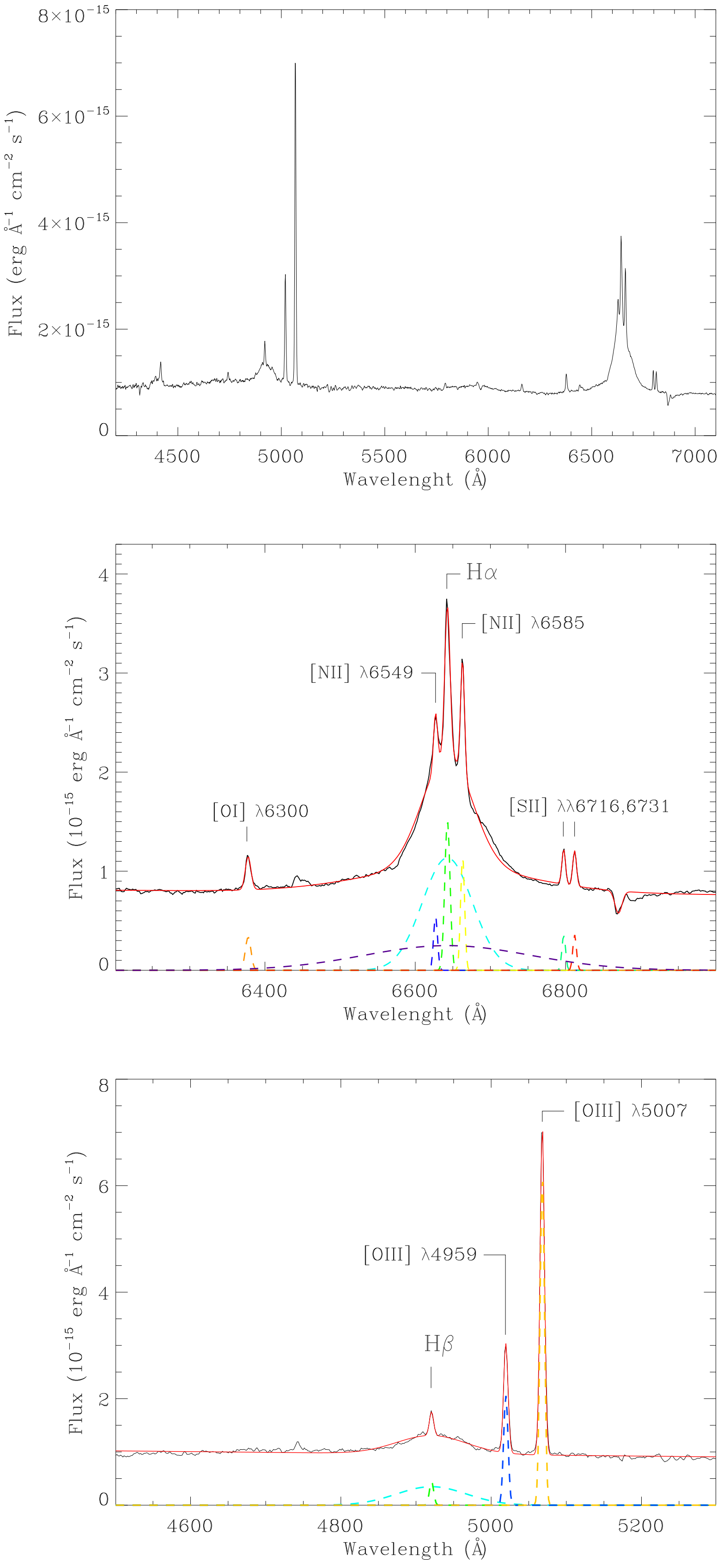

FIGURE 4.2: Calibrated spectrum and Balmer line fits for EMMI data. *Upper panel:* EMMI calibrated spectrum of ESO 362-G18. *Middle panel:* Fit performed for the emission lines around H_α. We disentangle two broad components (see text for details) *Bottom panel:* Fits for H_β and [O III] doublet. A broad component is clearly detected also in H_β.

TABLE 4.2: Lines parameters together with statistical errors computed from fits with Gaussian functions on EMMI data. In order to derive FWHM the instrumental broadening has been taken into account. We assume $FWHM_{ins} = 250\ km \cdot s^{-1}$ as derived by (Bennert et al., 2006a) for a slit width of 1”. Accordingly, [N II] and [S II] doublets are not resolved by EMMI. The lines belonging to the same multiplet are forced to have the same value of Gaussian width, while the broad components have their centers tied to those of the corresponding narrow components. F_{dered} is the reddening-corrected flux and the corresponding correction was carried out for the intervening Galactic absorption, $E(B-V)_{Gal} = 0.017$, according to Schlegel et al. (1998) and through Cardielli’s law. F_{dered}/H_β is the reddening-corrected narrow emission line intensity ratio relative to Hβ.

	FWHM ($km \cdot s^{-1}$)	EW (Å)	F_{dered} ($\cdot 10^{-15} erg\ cm^{-2} s^{-1}$)	F_{dered}/H_β
		NARROW LINES		
Hβ λ4861	321 ± 39	3.28 ± 0.98	3.33 ± 0.42	1
$[OIII]\lambda$4959	334 ± 3	16.10 ± 1.51	16.12 ± 0.25	4.84
$[OIII]\lambda$5007	329 ± 3	48.83 ± 3.58	48.49 ± 1.27	14.56
$[O\ I]\lambda$6300	334 ± 32	3.95 ± 1.52	7.70 ± 0.75	2.31
$[N\ II]\lambda$6549	131 ± 8	4.66 ± 1.00	3.80 ± 0.21	1.14
Hα λ6563	278 ± 8	17.04 ± 2.06	13.87 ± 0.39	4.17
$[N\ II]\lambda$6583	128 ± 8	9.85 ± 1.30	8.00 ± 0.29	2.40
$[S\ II]\lambda$6716	40 ± 16	2.78 ± 0.86	2.24 ± 0.21	0.67
$[S\ II]\lambda$6731	37 ± 16	2.82 ± 2.86	2.26 ± 0.21	0.68
		BROAD LINES		
Hβ λ4861	6662 ± 224	42.09 ± 11.60	42.74 ± 5.98	-
Hα λ6563	3524 ± 59	120.67 ± 11.49	98.25 ± 2.29	-
Hα gauss 2	11790 ± 564	88.43 ± 9.55	71.99 ± 5.36	-

Because of the Sy1 spectral shape, during the fitting procedure we had to account for the additional broad emission lines underlying the permitted emission of the NLR. In doing so, a second Gaussian, a broad one, is added to fit the permitted broad line profile. Nevertheless, we found that the use of two Gaussians was not sufficient to fit the broad wings of H$_\alpha$. A third broader Gaussian was added generating an improved fit. This fitting method to broad components of H$_\alpha$ and H$_\beta$ lines was also adopted by other authors, e.g. Reynolds et al. (1997), Sulentic et al. (2002), Bennert et al. (2006a). Because emission line profiles represent LOS integrations of several kinematic components, even for narrow lines, considerable profile structure is measured at enough resolution (Vrtilek & Carleton, 1985, Schulz & Henkel, 2003). Another alternative is to try a Lorentz profile in order to account for the broader wings, however (Sulentic et al., 2002) realized a systematic study of the broad H_β lines in several AGN subtypes and concluded that $FWHM \lesssim 4000\ km\ s^{-1}$ are well fitted by a Lorentz function while $FWHM \gtrsim 4000\ km\ s^{-1}$ are better reproduced with two broad gaussian components. This is actually what we see in our data, and we used three Gaussian (one broad, another “very broad” and the last one narrow) profiles to fit the H_α emission line, two gaussians (one broad, one narrrow) for H_β and single gaussians for the remaining narrow lines. It is worth to mention that the sigma of the broad gaussian (and not the “very broad”) fitted to H_α is totally consistent with that derived for 6dF data. Then, it is likely that we are observing the same component.

The obtained results are displayed in Fig 4.2, where we clearly show that broad and narrow lines are very well disentangled as reported in Table 4.2. The correction of the instrumental broadening was applied following the value derived by Bennert et al. (2006a) for the used slit of width 1”, $FWHM_{ins} \sim 250\ km \cdot s^{-1}$.

Here the galactic reddening correction of the data provides us with a intrinsic extinction of $E(B-V)_{NLR} = 0.36 \pm 0.12$ towards the NLR, following Eq. 4.2. This value is approximately twice as high as that derived for the 6dF spectrum $E(B-V) = 0.11 \pm 0.10$, although the two values are almost consistent with each other within the errors. As already noticed, here we are not able to compare the same flux fraction from the NLR. In the 6dF spectrum we are likely collecting spectral data from most of NLR, while the EMMI data, collected with a 1” slit, do not allow us to extract the same area of our source. Hence the extinctions towards the NLR are difficult to compare directly.

On the contrary, the unresolved subpc-scale BLR is for sure entirely contained in both observations. This enables us to compare the extinction suffered by the broad emission lines and determine changes of dust absorption on the smaller BLR scale between the different observation. If we apply Eq. 4.2 to the ratio of the EMMI broad Balmer lines (taking into account the two fitted components for broad $H\alpha$ in order to consider the whole detected BLR), we derive $E(B-V)_{BLR} = 0.32 \pm 0.05$. If we assume that the observed extinction towards the BLR includes the intrinsic extinction suffered by both the BLR and NLR (Heard & Gaskell, 2016). i.e

$$E(B-V)^{obs}_{BLR} = E(B-V)^{int}_{BLR} + E(B-V)^{int}_{NLR} \tag{4.3}$$

we can conclude that the intrinsic extinction suffered by the BLR is $E(B-V)^{int}_{BLR} \sim 0$, since we have calculated $E(B-V)^{int}_{NLR} = 0.36 \pm 0.12$ which is the order of the derived $E(B-V)^{obs}_{BLR} = 0.32 \pm 0.05$. Hence a dust free view of the BLR during the EMMI observation is implied by the data.

It should be mentioned that inside the BLR the Balmer decrement H_α/H_β could be influenced by other many factors than the reddening, for instance the temperature, see e.g. Gaskell (2015). These authors compare a wide range of properties of low-redshift blue AGNs and find that the only difference among them is the internal reddening. Hence, they derived a mean Balmer decrement for the BLR of $\sim 2.72 \pm 0.04$. For the sake of generality, here we keep considering the standard Balmer decrement of 2.86 even for the broad lines, but we have checked that using the decrement derived by Gaskell (2015) we would obtain $E(B-V)_{BLR} \sim 0.36$, a value consistent with our calculations.

TABLE 4.3: Lines parameters together with statistical errors computed from fits with Gaussian functions on EFOSC1 data. In order to compute FWHM, the instrumental broadening has been estimated from the FWHM of the AGN since during the observing night the seeing was $\sim 0.8''$, narrower than the used slit . We derives a instrumental broadening of $\sim$ 460Å. The lines belonging to the same multiplet are forced to have the same value of their gaussian sigma, while the broad component of H_α has its center tied to that of the corresponding narrow component. F_{dered} is the reddening-corrected flux and the corresponding correction was carried out for the intervening Galactic absorption $E(B-V)_{Gal} = 0.017$ according to Schlegel et al. (1998) and through Cardielli's law. F_{dered}/H_β is the reddening-corrected narrow emission line intensity ratio relative to H_β.

	FWHM ($km \cdot s^{-1}$)	EW (counts)	F_{dered}/H_β
	NARROW LINES		
H_β λ4861	229 ± 38	4.72 ± 0.70	1
$[O\,III]\lambda$4959	391 ± 14	7.79 ± 0.43	1.22 ± 1.68
$[O\,III]\lambda$5007	382 ± 14	14.68 ± 0.90	3.13 ± 4.33
$[O\,I]\lambda$6300	176 ± 145	0.97 ± 0.47	4.65 ± 6.50
$[N\,II]\lambda$6459	181 ± 70	2.96 ± 0.43	0.73 ± 1.01
H_α λ6563	184 ± 10	21.18 ± 2.13	4.55 ± 6.28
$[N\,II]\lambda$6583	175 ± 21	9.51 ± 0.87	2.11 ± 2.91
$[S\,II]\lambda$6716	197 ± 24	5.95 ± 0.63	1.18 ± 1.63
$[S\,II]\lambda$6731	194 ± 24	4.18 ± 0.50	0.83 ± 1.15
	BROAD LINES		
Hα λ6563	3509 ± 58	11.22 ± 1.86	-

4.4 EFOSC1 data: Seyfert 1.9 look

In this section we discuss spectropolarimetric observations obtained from the ESO archive and performed with EFOSC1. A further study in polarized light will be developed in the next chapter. Here we only consider the total spectrum in order to analyze changes in the broad emission lines. It must be noted that data in polarized light do not need to be flux-calibrated (since it measures differences in flux between two spectra polarized orthogonally), therefore standard stars are not routinely observed and such data were not available, so we were not able to carry out a reliable flux calibration.

A brief description of EFOSC1, as well as the data reduction, will be given also in the next chapter devoted to polarimetry. There is nothing published about this data.

4.4.1 Spectral analysis

According to the spectrum provided by EFOSC1, the broad component of the H$_\beta$ emission line in ESO 362-G18 seems to disappear again leading to a typical spectrum of a Seyfert 1.9 galaxy (see Fig. 4.3) with similar appearance to the 6dF data (see Fig. 4.1). Indeed, a slight underlying broad

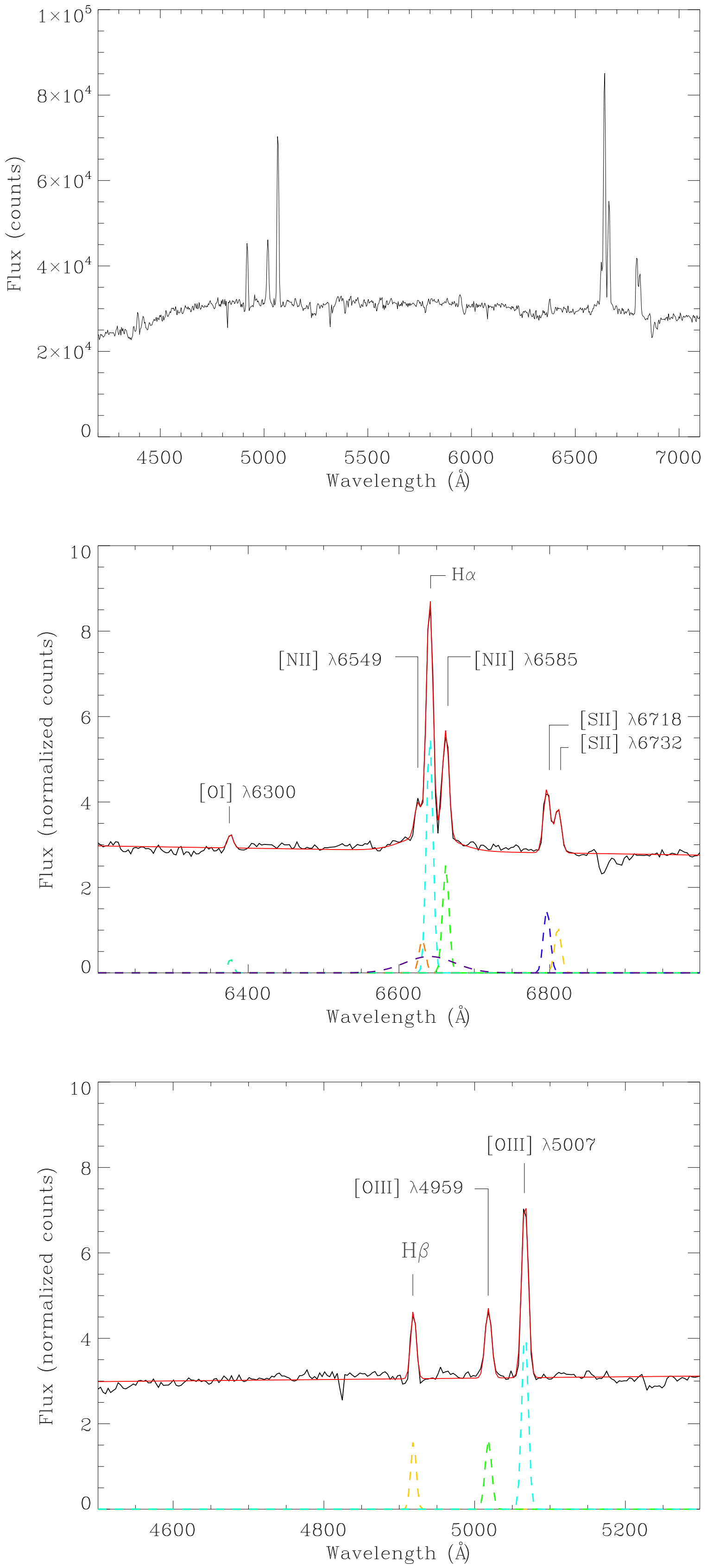

Figure 4.3: Spectrum and Balmer lines fits for EFOSC1 data. *Upper panel:* EFOSC1 calibrated spectrum of ESO 362-G18 (note that flux calibration is not performed). *Middle panel:* Fit performed for the emission lines around H_α. As in the case of 6dF spectrum, we detect a broad component (see text for details) *Bottom panel:* Fit for H_β and [O iii] doublet.

component for the H_α line with its gaussian sigma fixed to those broad components of 6dF and EMMI data (in both cases the sigma is consistent) was also required to obtain a reduced $\chi^2_{red} \sim 1$. We fixed the centroid of [N II]λ6549 since it appears to be buried in the H_α profile. The peculiar continuum shape around Hβ may suggest that absorption is distorting the continuum spectral shape there. We could not derive a reliable upper limit on the putative broad Hβ component. The situation is then similar to that seen in the 6dF data, with only a narrow Hβ emission line confidently detected, and with no broad component pointing towards a Sy1.9 classification. The results delivered by our fitting procedures are recored in Table 4.3.

The instrumental broadening was determined from the FWHM of the AGN since during the observing night the seeing measured was $\sim 0.8''$, narrower than the used Wollmask (equivalent to a slit width of $\sim 1.5''$). Then, the spectral resolution will be determined by the sky and not by the slit width. Taking into account that for grism Gr 4 $FWHM_{resolution} = 13.65$Å for a slit width of 1”, we derived the $FWHM_{ins} = 13.65 * 0.8/1.5 = 7.28$Å. Assuming the $\lambda_{central}$ of the grism for the whole spectral range we obtain $\sim 460\ km \cdot s^{-1}$.

The reddening correction for the intervening Galactic absorption provide us with a $E(B-V)_{NLR} = 0.39 \pm 0.09$., which is totally consistent with that derived for EMMI data.

4.5 FORS2 data: Seyfert 1.5 look

As in the previous section, here we consider of the total spectrum derived from the polarimetric observations granted to us through a ESO DDT program with FORS2 in order to study the spectral broad lines of ESO 362-G18. The analysis in polarized light is deferred the next chapter.

4.5.1 Spectral analysis

In this new spectrum we found ESO 362-G18 to show clearly its broad lines again (see Fig. 4.4). Here, both lines of the [N II] doublet are buried in the H_α profile, so we fixed the centroid of both lines to those derived from EMMI data. The results obtained through our fitting procedures are shown in Table 4.4.

As in EFOSC1 case, the seeing during the observing night was narrower ($\sim 0.7''$) than the slit width ($\sim 1.2''$). Then, the spectral resolution will be determined by the sky and not by the slit width. Taking into account that for grism 300V $frac\lambda\Delta\lambda = 440$ for a slit width of 1”, we derived the $FWHM_{ins} = 440/0.7 = 628.5$Å. Assuming the $\lambda_{central}$ of the grism for the whole spectral range we obtain $\sim 480\ km \cdot s^{-1}$.

The reddening correction for the intervening Galactic absorption allows us to derive a $E(B-V)_{NLR} = 0.78 \pm 0.12$, much higher than in other available observations, but again, this

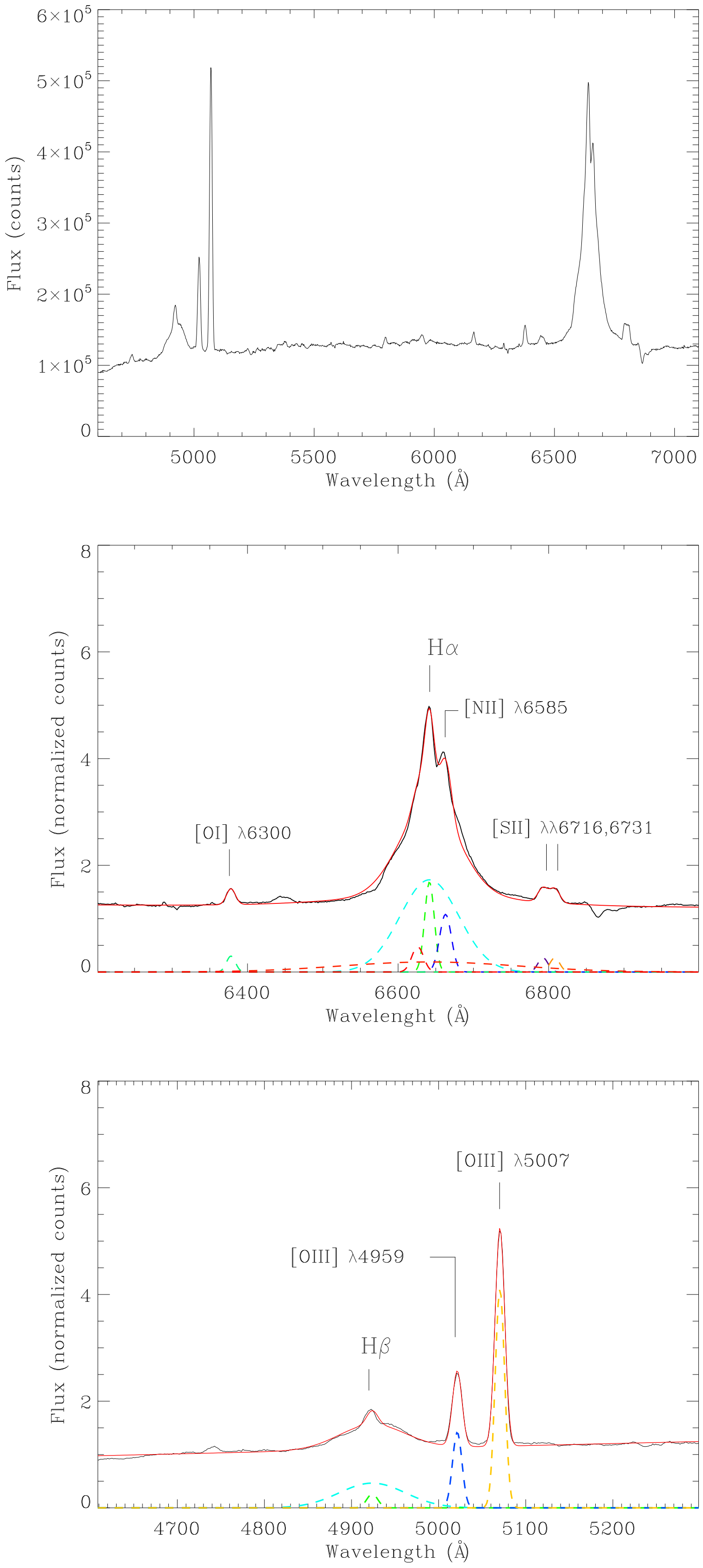

Figure 4.4: Spectrum and Balmer lines fits for FORS2 data. *Upper panel:* FORS2 spectrum of ESO 362-G18 (calibration flux in not carried out). *Middle panel:* Fit performed for the emission lines around H_α. As in the case of 6dF spectrum, we detect a broad component (see text for details) *Bottom panel:* Fit for H_β and [O iii] doublet.

TABLE 4.4: Lines parameters together with statistical errors computed from fits to Gaussian functions on FORS2 data. In order to derive FWHM, the instrumental broadening has been estimated from the FWHM of the AGN since during the observing night the seeing was ~ 0.7″, narrower than the used slit . We obtain a instrumental broadening of ~ 480Å. The lines belonging to the same multiplet are forced to have the same value of their gaussian sigma, while the broad component of H_α has its center tied to that of the corresponding narrow component. F_{dered} is the reddening-corrected flux and the corresponding correction was carried out for the intervening Galactic absorption $E(B-V)_{Gal} = 0.017$ according to Schlegel et al. (1998) and through Cardielli's law. F_{dered}/H_β is the reddening-corrected narrow emission line intensity ratio relative to H_β.

	FWHM ($km \cdot s^{-1}$)	EW (counts)	F_{dered}/H_β
NARROW LINES			
H_β λ4861	773 ± 94	3.78 ± 1.46	1
$[O\,III]\lambda$4959	598 ± 4	17.02 ± 1.76	4.67 ± 2.52
$[O\,III]\lambda$5007	589 ± 4	48.42 ± 3.47	13.48 ± 7.29
$[O\,I]\lambda$6300	452 ± 86	3.58 ± 0.32	1.05 ± 0.60
$[N\,II]\lambda$6459	685 ± 40	7.54 ± 1.19	2.28 ± 1.26
H_α λ6563	482 ± 20	21.91 ± 1.99	6.44 ± 3.49
$[N\,II]\lambda$6583	679 ± 39	17.22 ± 1.79	5.11 ± 2.78
$[S\,II]\lambda$6716	491 ± 84	3.61 ± 0.72	1.05 ± 0.60
$[S\,II]\lambda$6731	489 ± 84	3.58 ± 0.77	1.04 ± 0.59
BROAD LINES			
Hβ λ4861	5443 ± 140	40.29 ± 14.72	-
Hα λ6563	4130 ± 118	137.24 ± 12.38	-
Hα λ6563	12444 ± 1859	44.74 ± 11.02	-

does not posses a lot of meaning since the narrow line regions changes among the different observations because of the different "collecting area". However, as already noted, we can compare the observable extinction in the BLR which in this case appear to be $E(B-V)_{NLR} = 0.57 \pm 0.07$. This value is approximately twice than that obtained for EMMI data. Moreover, according to Eq. 4.3, we computed the intrinsic extinction towards the BLR obtaining $E(B-V)^{ins}_{BLR} \sim 0.20$. We will discuss this absorption change along the next section where a detailed comparison of the four spectra will be performed.

4.6 Comparison among the different observations

The optical lines are a useful tool of diagnosis for comparing different observations of AGNs and getting valuable information. H_α and H_β act as reddening indicator, [O III] λ5007 emission line is sensitive to changes of temperature while the ratio [S II] λ6716 /[S II] λ6731 is affected by changes in the electron density (Bennert et al., 2006b). Unfortunately, as already mentioned, we are not able to take the whole advantage of this great tool for comparing our observations since different regions of the NLR are contained in the various data sets. However, the unresolved

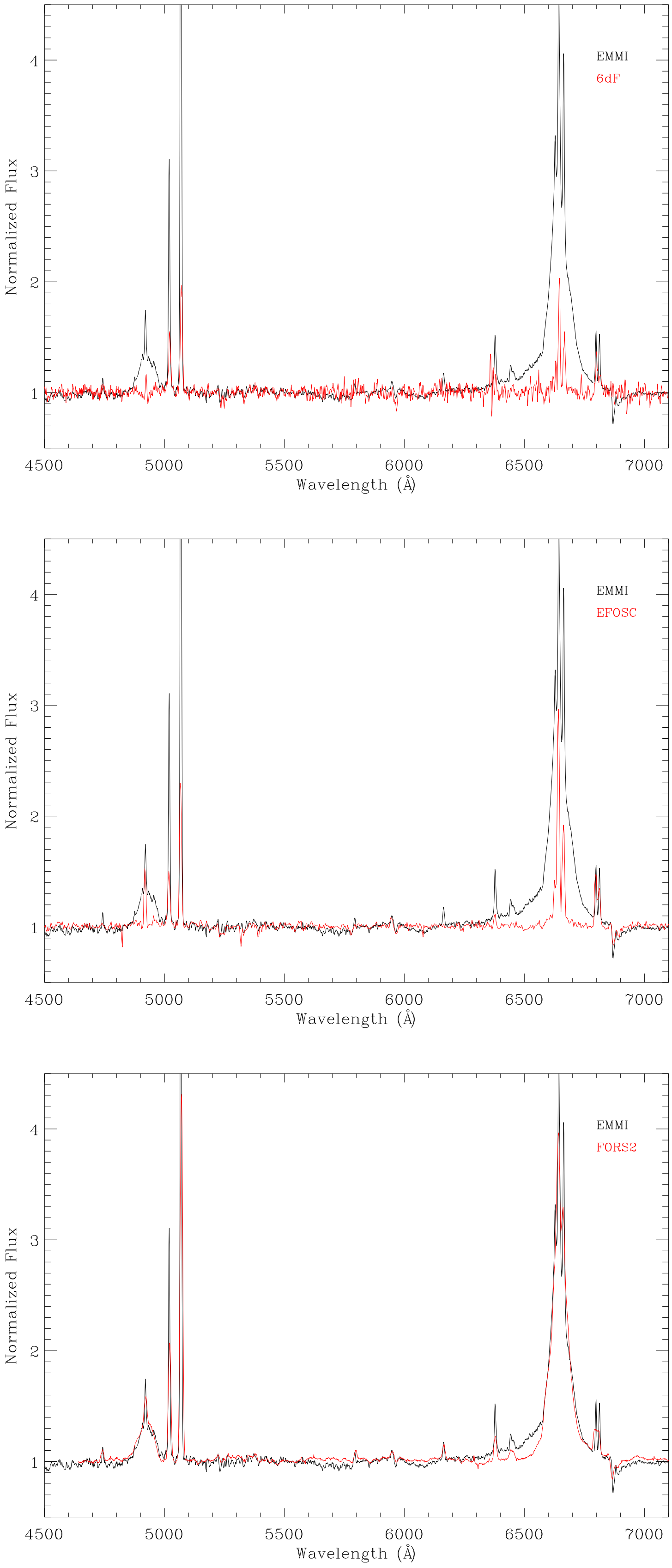

Figure 4.5: Normalized optical spectra comparing the different optical spectra of ESO 362-G18 using the EMMI observation as reference. Data are labeled on the upper right corner (see text for details about comparison).

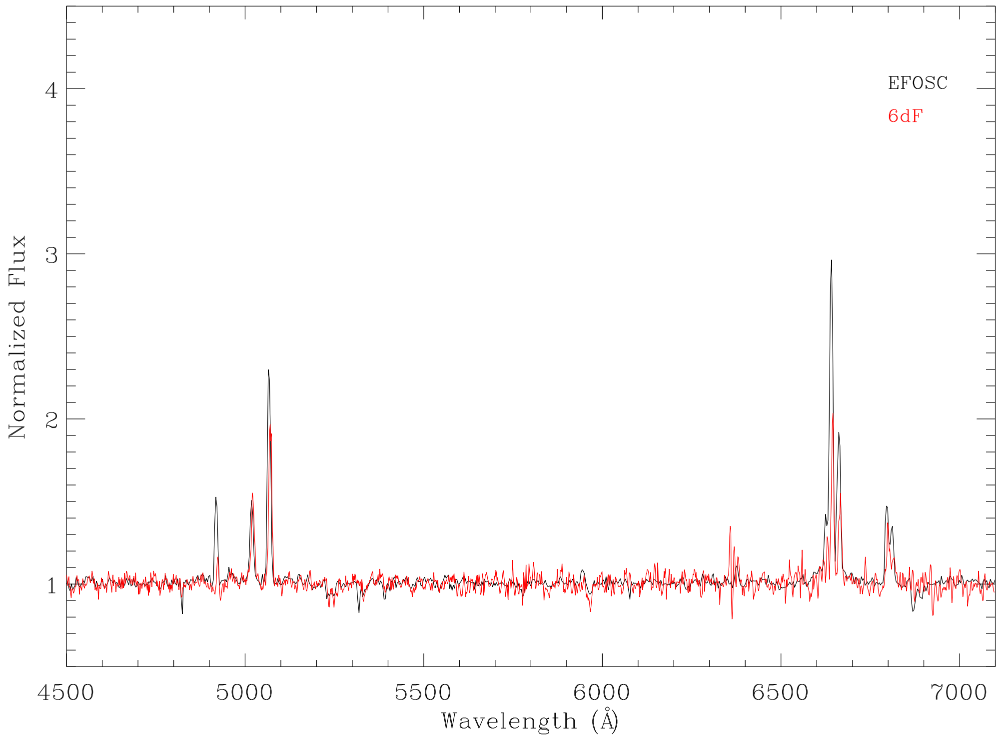

FIGURE 4.6: Normalized optical type 1.9 spectra of ESO 362-G18.

BLR is indeed entirely present in all observations, hence what we can do is to compare the broad emission lines to measure carefully their changes between the available data (see Table 4.5).

In general, we can assume the relation between optical extinction and hydrogen column density in our Galaxy to be the one same that in ESO 362-G18. (Güver & Özel, 2009) measured the column density of 22 supernova through their high energy resolution X-ray spectra and derived the relation:

$$N_H\,(cm^{-2}) = (6.86 \pm 0.27) \times 10^{21} E(B-V)\,(mag) \tag{4.4}$$

This relation gives a column density of $N_{H_{BLR}}^{EMMI} = (2.20 \pm 0.27) \times 10^{21} cm^{-2}$ for EMMI data and $N_{H_{BLR}}^{FORS2} = (3.91 \pm 0.28) \times 10^{21} cm^{-2}$ for FORS2 observations during which the source had a typical type 1 spectrum. Hence, from 2004-09-18 (EMMI data) to 2016-03-30 (FORS2) we detect an increment of the column density of about $\sim 2 \times 10^{21} cm^{-2}$ towards the broad line region of ESO 362-G18. On the other hand, the spectrum obtained on 2006-09-21 (2 years apart from EMMI observation) lacks a clear Hβ broad component. This suggests that during EFOSC1 observation the absorption could be much higher, partially blocking the BLR and leading to the disappearance of the broad Hβ Balmer line on the spectrum of ESO 362-G18.

We have also tried to fit broad gaussians on the base of the narrow H_β lines of both Sy2 spectra with the aim of establishing an upper limit on the detection of the broad components in order to derive a lower limit on the BLR extinction at epochs when the source is a Sy1.9 in the optical. Unfortunately, the spectral shape in the vicinity of H_β, as already mentioned, seems to suffer a drop of flux and we did not achieve a meaningful fit of a broad gaussian, so that no reliable upper limits on its flux could be measured.

For a clear comparison of the four presented observations the continuum-normalized spectra are displayed in Fig. 4.5 keeping EMMI data as reference. The changing look nature of ESO 362-G18 is reinforced in this Figure. The 6dF spectrum has the lowest quality, and it would be possible that broad lines (especially the Hβ one) are lost within the continuum (upper panel of Fig. 4.5) also because the bigger aperture of the IFU fibres respect to long-slit spectroscopy. However, the higher quality long-slit EFOSC1 spectrum (see middle panel of Fig. 4.5) has much higher quality and looks extremely similar to the 6dF one, which strongly suggests that the lack of broad Hβ emission is a real and common feature at the two epochs. If we compare the normalized Sy1.9 spectrum (see Fig. 4.6), we found a really good match between the spectral features, not only regarding the slight detected broad component of H_alpha, but also with respect to the continuum shape around Hβ perhaps suggesting absorption.

The total disappearance of broad the H_β component is unambiguous while a weak broad H_α component remains, as showed by the performed fitting procedures which delivered a consistent Gaussian FWHM pointing towards a 1.9 classification of the source during the 6dF and EFOSC1 epochs.

The bottom panel of the Fig. 4.5 shows that some difference in the blue wing of the broad Hα profile is present when the source is detected as a type 1 AGN. A broader base, possibly blueshifted, seems to be present in the EMMI data, while it has disappeared at the epoch of the FORS2 observation. The peculiar shape of the Hα wing may be associated with an outflow that is only present in the EMMI data. We would tend to disregard extra absorption in the FORS2 observation as the two data sets exhibit remarkably similar broad Hβ line profiles.

4.7 Discussion

According to the X-rays absorption events detected on ESO 362-G18 in this dissertation - an absorption event consistent with being performed by a clump of the dusty torus (Chapter 2) and the eclipse event tracked almost from ingress to egress (Chapter 3) - along with the change of absorption found in this Chapter towards the BLR between EMMI and FORS2 data where the column density increases $\sim 2{\times}10^{21} cm^{-2}$, suggest that the changing looks exhibited by our target are probably driven by dust absorption variability. Besides, having a look at Table 4.5 and at the

TABLE 4.5: Log of the optical observations analyzed in this chapter. 6dF intstrument uses IFU fibres with a diamater of 5.7”. EMMI data is rebinned to a spectral resolution of is 037”/px and the used slit had a width of 1”. We extracted the spectrum form the three central pixel rows, so the corresponding“collecting area” is 1”x1.11”. On the order hand the spectropolarimetric observations performed with EFOSC1 and FORS2 were obtained with stripped masks of width 1.2” and 1.5” respectively.

	6dF	EMMI	EFOSC	FORS2
Look	Sy1.9	Sy1.5	Sy1.9	Sy1.5
Date	2003-01-30	2004-09-18	2006-09-21	2016-03-30
Technique	IFU (5.7”)	Long Slit (1”)	Stripped mask (1.2”)	Stripped mask (1.5”)
$E(B-V)_{NLR}$	0.11 ± 010	0.36 ± 0.12	0.39 ± 0.09	0.78 ± 0.12
$E(B-V)_{BLR}$	-	0.32 ± 0.05	-	0.57 ± 0.07

dates corresponding to each observation we can derived that these look changes took place in time scales lower than 1 year and 8 months.

It is worth to mention that the absorbed XMM1 observation deeply analyzed in Chapter 2 was taken 1 year and 4 months after EMMI data and 8 months before the EFOSC1 spectrum. According to UVOT data, that absorption event was also extended to UV wavelengths. Although the computed observed X-ray column density is probably much higher than that causing the optical spectral differences, we can speculate that perhaps during XMM1 observation, ESO 362-G18 was being involved in the starting of an important absorption due to a cometary shape cloud of the dusty torus with initial high column density (the cloud compact and dense core) and a much more extended, lower column density tail which would conclude with the disappearance of the broad Balmer lines 8 months later. Although, admittedly, our data cannot confirm this picture which remains a simple speculation.

On the other hand, the possibility that the broad lines of ESO 362-G18 disappear due to changes on the accretion rate of the central black hole is at odds with the rough constant intrinsic 2-10 keV X-ray luminosity computed from our best-fitting spectral model on Chapter 2, which is around $\sim 2-3\times10^{42}\ erg\cdot s^{-1}$ with a few excursions. Those intrinsic variations do not seem to be sufficient to induce dramatic optical spectral changes in the broad emission lines of a Seyfert galaxy.

4.8 Summary and outcomes of this chapter

Along this chapter we have carried out a detailed study of four different optical spectra of ESO 362-G18 which show the changing look nature of our target. We have modeled the emission lines along the four epochs through multi-gaussian fits which account for different velocity components of the Balmer lines.

Unfortunately, each analyzed spectrum was observed within different programs with diverse aims, different instruments and, even, different spectroscopy techniques, i.e IFU, spectropolarimetry or long slit spectroscopy of medium resolution. This implies that each spectrum gather different sections of our AGN which present an extended NLR whose emission is confirmed by, e.g. Mulchaey et al. (1996b), Fraquelli et al. (2000) or Bennert et al. (2006a). Consequently, different fractions of the NLR are present in each spectrum and this prevented us to compare the narrow emission lines among the different epochs. However, we are still able to assess changes of the unresolved BLR, which will be always entirely contained in all spectra. H_α/H_β ratios, reddening indicators par excellence, of the broad components can provide us with changes of absorption towards the BLR. Indeed, we found that between the Sy1.5 spectra (EMMI and FORS2) the column density increases by $\sim 2\times10^{21}cm^{-2}$. We would also have liked to determine an upper limit to the extinction during the Seyfert 1.9 states in order to assess the changes of column densities. However, whereas a slight broad H_α component is unambiguously detected in both observations during type 1.9 states, we were unable to derive a reliable upper limit on the putative broad H_β component. This is due to the peculiar flux drop in the continuum level around Hβ in both observations, perhaps suggesting by itself some extra absorption.

In summary, we can conclude that the most probable scenario for the changes of look performed by ESO 362-G18 is that driven by dust absorption variability, precisely, due to the several reported events where the column density towards the inner regions of the AGN changes remarkably. Moreover, as shown in Chapter 2, 9 X-ray observations of high spectral quality covering a period of several years showed that ESO 362-G18 does not show dramatic intrinsic luminosity variations that may explain the optical changing-look phenomenon which is then most likely associated with variability of a dusty clumpy absorber capable of obscuring transiently our view towards the broad Balmer line emitting region.

There are few studies of changing-look AGN analyzing in detail optical spectra. One of the them is the recent work of McElroy et al. (2016). These authors find Mrk 1018 to change from a Sy1 configuration to a Sy1.9 classification after 30 years exhibiting its type 1 spectrum. However, they suggest that the change is due to an intrinsic drop in flux from the accretion disk. In our case, the lower timescales also support the interpretation of a dust absorption picture.

Chapter 5

ESO 362-G18 as a changing look Seyfert galaxy: polarimetric view

The purpose of this chapter is to investigate the changing look nature of ESO 362-G18 in the context of observations in polarized light. Within the AGN picture, this allows to infer information about their unresolved components, as e.g. BLR. Here, we make use of polarimetric observations to enhance our view of the changing look Seyfert galaxy ESO 362–G18 whose optical and X-ray properties have been discussed in the previous chapters.

5.1 Polarimetry: a powerful tool

From common astronomical spectral observations we can obtain valuable information: measurements of intensity, either per unit of time, or wavelength, or both. Through polarimetry, we can measure something more: how the electric field vector oscillates. Electric field oscillations are perturbed by any mechanism or element that breaks the symmetry in the radiative source, for instance, scattering by particles or dust, the influence of a magnetic field or the presence of geometrical structures which collimate he radiation. Thus, polarization arises every time one of these elements is interposed between the source and the observer. Consequently, we will be able to study the geometry of the nucleus immediate surroundings, even though it is well below the spatial resolution of the telescope. In the AGN context, polarization provides a unique way to reconstruct the structure and kinematics of that scattering media, and becomes an alternative and very powerful remote sensing tool for the study of the inner regions out of the direct LOS.

As noted in section 1.6, spectropolarimetry has played a key role in the development of the current UM of AGN (Antonucci, 1993). The presence of PBL, in Sy2 galaxies is due to scattering of BLR light escaping from the AGN, whose direct view is blocked by the circumnuclear torus. In the simplest picture, light coming from the BLR and central continuum source emerges in bipolar radiation cones which illuminate the gas outside the torus, giving rise to, e.g., the emission from the NLR. Free electrons and/or dust associated with the NLR scatter some of the light into our LOS. Depending on the geometry of the medium, light becomes polarized and observations in polarized light offer the opportunity to study the geometry of the scatterer(s).

Antonucci & Miller (1985) proposed that the optical polarized flux spectrum of NGC 1068 could be explained as scattering by free electrons above the poles of the torus. Their proposal has been thereafter confirmed by modeling free electrons and dust in a conical region along the poles of the torus successfully explaining the observed optical and UV polarization of that source (Miller et al., 1991, Young et al., 1995). Then, imaging polarimetry of this same Seyfert galaxy has revealed a bipolar scattering region exhibiting a centro-symmetric polarization pattern, consistent with illumination from a hidden central source (Capetti et al., 1995, Packham et al., 1997, Simpson et al., 2002). This basic polar scattering picture seems to be generally valid for PBL Sy2 nuclei.

Since scattered light has an electric vector **E** position angle (PA) perpendicular to the *scattering plane* (the plane containing the incident and scattered ray), in principle, this **E** vector is thought to be perpendicular to the scattering cone axis of the AGN. This axis is typically defined by the rotation axis of the accretion disc and hence coincident with the radio source, the torus, and the disc symmetry axes. Consequently, the scattering cones will be co-aligned with this system axis and scattered light will be polarized with its **E** vector perpendicular to it (Smith et al., 2002). Observations of PBL Sy2 galaxies support this scenario, where the scattered light in the illumination cone of the torus almost always shows a optical polarization position angle (PPA), θ, perpendicular to the projected radio source axis (Antonucci, 1983, Brindle et al., 1990). Generally Sy2 galaxies meet this condition of *polar scattering*, but in contrast, the optical polarization properties of most Sy1 galaxies are not consistent with this view. Several studies have found that θ is more often aligned with the system axis in these objects (Antonucci, 1983, Martel, 1996). This implies that at least some of the scattered light emerging from the nucleus must follow a different path to that in Sy2 galaxies and suggests that the simplest unification geometry including only one single polar scattering‘ ‘mirror” is incomplete. An additional source of polarized light is then required in Sy1, which provides a different scattering geometry. Moreover, such secondary “mirror” must be blocked from view in Sy2. According to these observational results, Goodrich & Miller (1994) suggested that a number of spectral polarization characteristics commonly exhibited by Sy1 galaxies are best explained by a model in which broad Balmer line emission originates in a rotating disc and is scattered by material in the equatorial plane of the disc. This model predicts that the average PPA, or θ, of the broad Hα line and that of the continuum, are aligned with the rotation axis of the line-emitting disc, and therefore with the system axis. In this way, these authors could account for the *equatorial scattering* which is observed in the majority of Sy1 galaxies.

However, the picture becomes even more complicated, as several Sy1 galaxies show optical polarization orthogonal to their radio source axes. Smith et al. (2002) and Smith et al. (2004) identified a number of Sy1 galaxies whose polarization spectra are very similar to those of Sy2 galaxies in which PBLs, also known as HBLR, are detected. Therefore, although equatorial scattering seems to explain the optical polarization in most Sy1, there exist evidence that polar scattering does not only occur in Sy2 galaxies, as would be expected in the standard unification scheme, but actually dominates over equatorial scattering in some Sy1 cases. These objects are of particular interest in the context of the unification scheme, since they appear to have scattering geometries similar to Sy2 galaxies, despite exhibiting Sy1 spectra in total light.

Smith et al. (2004) used a two-component scattering code in order to demosntrate that the inclination of the system axis to the LOS cannot, by itself, govern which component, polar or equatorial scattering, dominates. Instead, they argued that polar-scattering Sy1 are objects in which the LOS to the nucleus passes through the upper layers of the torus and estimate the amount of extinction needed for the polar scattering region to dominate the observed polarization. They found that $A_V = 1 - 4$ mag is enough to suppress polarized light from the equatorial scattering region, while keeping the broad wings of the Balmer lines visible. Thus, Smith et al. (2004) report that the range in polarization properties observed among Seyfert galaxies can be broadly understood in terms of an orientation sequence consistent with the unification scheme. Polar-scattered Sy1 galaxies represent the transition between unobscured (the majority of Sy1) and obscured (type 2) Seyfert galaxies.

5.2 Polarization parameters

Before discussing the physical picture that emerges from polarization studies of AGN, it is necessary to introduce the basic concepts and parameters of polarimetry. The polarization state of a radiation beam is determined by the state of oscillation of its electric field, i.e. the direction of the electric field and how that direction varies in time and space. Let us consider a monochromatic wave which is totally polarized. Total polarization means that the tip of the associated electric field vector draws an ellipse in a time t in every fixed plane perpendicular to the propagation direction. According to Maxwell's equations (del Toro Iniesta, 2004). This is the so-called polarization ellipse (see figure 5.1), whih is defined by three constant quantities, its major and minor semi-axes, a and b, (expressed in non dimensional units and measured in the rotated $\epsilon - \mu$ coordinate system of the ellipse), and the tilt angle, θ. a and b give the projected amplitudes E_{0y} and E_{0x}, that are also constant. The polarization ellipse remains fixed as the polarized beam propagates.

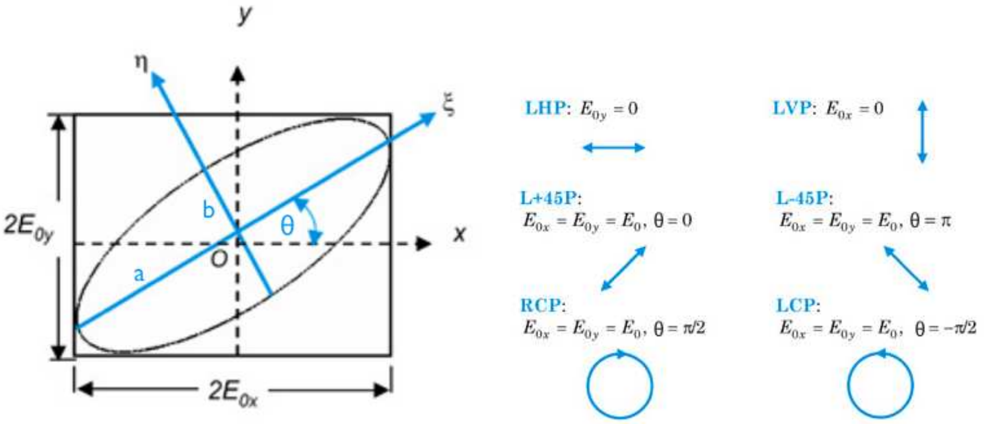

FIGURE 5.1: Polarization ellipse and its degenerated states. Image credit: https://spie.org/publications/fg05_p07-09_polarization_ellipse.

In general, the field is elliptically polarized, but there are several combinations of amplitudes and tilt angle that give rise to degenerate polarization states as specified in Fig. 5.1, in turn, producing:

(*i*) *Linearly polarized light*, whose degenerate states can be horizontal/vertical (LHP/LVP) or ±45° polarized. The total linear polarization is defined by the direction of maximum polarization.

(*ii*) *Circularly polarized light*, composed by right/left degenerate states (RCP/LCP). One of the two directions will dominate the total circular polarization.

In each polarization state (elliptical, linear, circular), the associated electric field draws its corresponding geometry in every fixed plane perpendicular to the propagation direction (see Fig. 5.2). Therefore, the degenerate states of the polarization ellipse describe special polarization states which in turn can be described through the specification of four independent quantities: the Stokes parameters I, Q, U and V (Stokes, 1852). Their definitions require the preliminary choice of a reference direction in the plane perpendicular to the direction of propagation of the radiation (Landi Degl'Innocenti et al., 2007). In astronomical observations, the reference direction can be thought of as a great circle in the celestial sphere passing through the observed object. The choice of this great circle is arbitrary, but in night-time astronomy, it has become customary to choose the reference direction as the celestial meridian passing through the observed object.

The first Stokes parameter, I, describes the total intensity of the optical beam; the second parameter, Q, describes the preponderance of linear polarization contained in the plane perpendicular to the direction of propagation over linear polarization parallel to that plane of reference; the third parameter, U, describes the preponderance of linear polarization with an inclination of 45° to the plane of reference over linear polarization with an inclination of −45° and, finally,

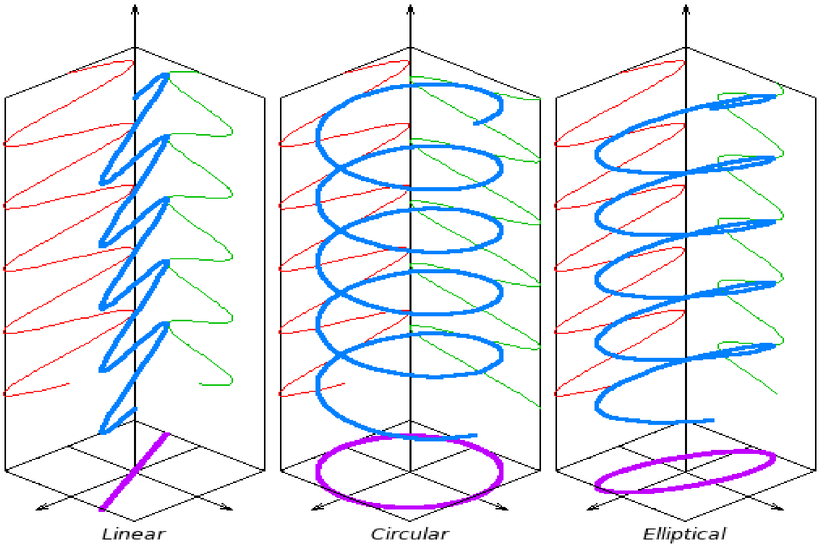

FIGURE 5.2: Schematic representation of the different polarization states. Image credit: http://ganymede.nmsu.edu/tharriso/ast536/ast536week07.html .

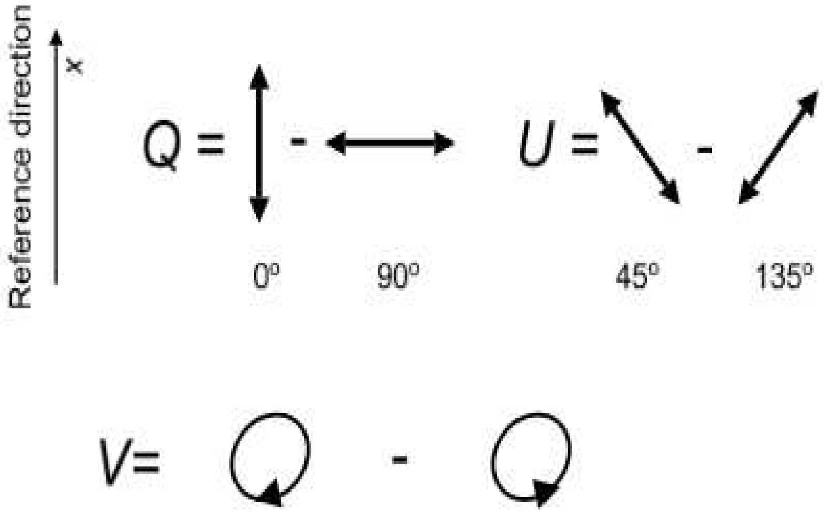

FIGURE 5.3: Geometrical definition of Stokes parameters considering that the observer is looking toward the source. Image credit: Landi Degl'Innocenti et al. (2007).

V describes the preponderance of circular dextrorotatory polarization over circular levorotatory polarization. A schematic definition of Stokes parameters is represented in Fig. 5.3.

In other words, the Stokes parameter V is connected to the eccentricity of the polarization ellipse and the Stokes parameters Q and U tell us how the polarization ellipse is oriented. Then, if linear polarization is zero, the polarization ellipse degenerates in a circle. If circular polarization is zero, the polarization ellipse degenerates in a segment. The Stokes parameters are usually expressed in quantities relative to the total intensity, i.e. I parameter in which case they are called reduced Stokes parameters:

$$P_V = \frac{V}{I} \quad , \quad P_Q = \frac{Q}{I} \quad \text{and} \quad P_U = \frac{U}{I} \tag{5.1}$$

On the other hand, the major and minor semi-axes of the polarization ellipse, a and b, and the tilt angle θ that the major semi-axis forms with the reference direction x, are related with the reduced Stokes parameters of the polarized component by the equations (see Landi Degl'Innocenti et al. (2007) and references therein):

$$\begin{aligned} a &= \frac{1}{2}\left((1-P_V)^{1/2} + (1+P_V)^{1/2}\right) \\ b &= \frac{1}{2}\left((1-P_V)^{1/2} - (1+P_V)^{1/2}\right) \\ \frac{P_U}{P_Q} &= \tan(2\theta) \end{aligned} \tag{5.2}$$

Due to the fact that scattering is much more efficient to produce linear than circular polarization by a factor ~ 100 (Siebenmorgen et al., 2014), in the field of AGN the circular polarization is usually null and linear polarization dominates. Q and U are then the most important parameters in this field. However it is important to note that if multiple scatterers or synchrotron emission are present, circular polarization could become important, although this is not common in Seyfert galaxies. The contribution of polarimetry to our understanding of the AGN environment is detailed below.

In general, P_Q and P_U are combined in two fundamental magnitudes which contain the whole information about the configuration of polarization: the degree of polarization (p), which measures the fraction of linearly polarized radiation and the PPA, or θ, which is coincident with the angle of maximum polarization, i.e., the angle that the major axis of the polarization ellipse forms with the x-axis of the reference system, reckoned counterclockwise for an observer looking at the radiation source.

They are expressed as:

$$p = \sqrt{P_Q^2 + P_U^2} \tag{5.3}$$

$$\theta = \frac{1}{2} \arctan\left(\frac{P_U}{P_Q}\right) + \theta_0 \tag{5.4}$$

$$\text{where} \quad \theta_0 = \begin{cases} 0 & \text{if} \quad P_Q > 0,\ P_U \geqslant 0 \\ \pi & \text{if} \quad P_Q > 0,\ P_U < 0 \\ \frac{\pi}{2} & \text{if} \quad P_Q < 0,\ P_U \gtrless 0 \end{cases} \quad \text{or} \quad \theta = \begin{cases} \frac{\pi}{4} & \text{if} \quad P_Q = 0,\ P_U > 0 \\ \frac{3\pi}{4} & \text{if} \quad P_Q = 0,\ P_U < 0 \end{cases}$$

This equations will be further explained in section 5.7.

5.3 Scattering models in Seyferts galaxies

Having introduced the meaning and potentiality of polarization parameters, we are now ready to understand and interpret the polarization properties of Seyfert galaxies so that the whole information provided by this powerful technique can be used up.

First of all, it is extremely important to underline that the intrinsic spectrum of polarization is likely to be modified by interstellar dust along the LOS in both the host galaxy and our own. Aligned dust grains can induce interstellar medium (ISM) polarization. There exist methods to estimate the induced ISM, p_{ISM} polarization by the Milky Way (see section 5.12.1), however the effects of dust in the host galaxy are more difficult to assess. According to the Serkowsky law p_{ISM} strongly depend on wavelength (Serkowski et al., 1975). It varies weakly in short wavelength ranges while the corresponding PPA is expected to show a constant value (Fossati et al., 2007). Therefore the detection of significant θ rotations or changes in p across a relatively short wavelength range would indicate that the polarization is at least partly intrinsic to the AGN.

As mentioned at the beginning of this chapter, although polar scattering is the norm in Sy2 galaxies while equatorial scattering appears to dominate in most Sy1 galaxies, a number of Sy1 galaxies have optical polarization orthogonal to their radio (or symmetry) axis, i.e. there appear to be a number of Sy1 galaxies where polar scattering dominates, as is the case for Sy2 galaxies.

From an observational point of view, the polarization spectra of "standard" equatorial-scattered Sy1 nuclei nearly always exhibit variations with wavelength along the broad H_α line in either the degree and position angle of polarization, or both (see left panel of Fig. 5.4, as noted above, these changes indicate that the Seyfert nucleus is intrinsically polarized). Rotations of PPA across the H_α line profile from the blue to the red wings mean that the orientation

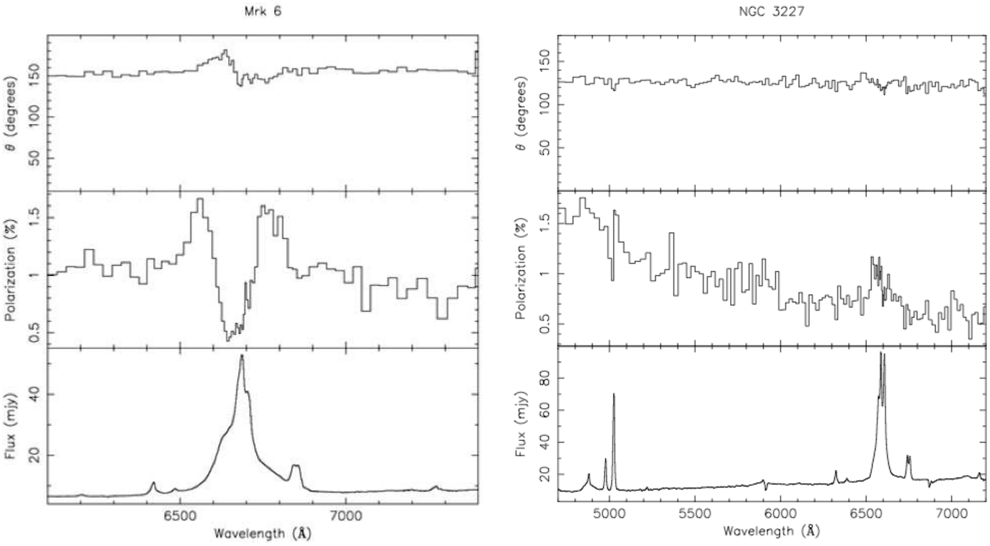

FIGURE 5.4: *Left:* Prototype of equatorial-scattered Sy1 (Mrk 6; Smith et al. (2005)). *Right:* Prototype of polar-scattered Sy1 (NGC 3227; Smith et al. (2004)).

of the scattering plane varies with the LOS velocities of the line emitting gas, which places constraints on the geometry and kinematics of the scattering and/or emitting regions. A velocity-dependent rotation in the PPA across the broad emission line requires either that the BLR is resolved by the scattering region or that it is subject to two distinct scattering regions that are arranged in order for their scattering planes to subtend a large angle between them. In both cases, the velocity field in the BLR and/or scatterers must also be perfectly ordered so that some discrimination in wavelength can lead rays following different scattering paths. Thus, if two scattering regions produce a line profile covering somewhat different wavelengths ranges (because, one is shifted, or broadened, with respect to the other), the ratio of polarized fluxes from each scattering geometry will vary across the total line profile, resulting in a θ rotation. At the same time if the BLR is confined to a rotating disc and is surrounded by a coplanar ring of scatterers , p will decrease in the core of the broad H_α line because the line profile in direct view (total flux) is narrower than in scattered view (polarized flux), due to the fact that direct LOS to the BLR has to pass within the opening angle of the circumnuclear torus and therefore provides a more face-on view, whereas the scatterers will have a edge-on view of the disc Smith et al. (2002). We will address this model further on the next subsection.

On the contrary, in Sy2 galaxies showing type 1 spectra in polarized light, the usual trend of p is to increase with respect to the continuum across the entire profile of H_α not only in the wings, while θ rotations across the broad lines are usually not observed. Therefore, in principle, this case seems simple to interpret. The nuclear continuum source and the BLR are hidden by the torus and only visible in scattered, and hence, polarized light. Thus, continuum and line emission are generally believed to be generated in the same scattering geometry made of dust and/or electrons along the polar axis of the torus. Since, there is only one intervening scatterer, continuum and line emission should exhibit the same polarization level. The increase in p along the broad Balmer lines is explained by the presence of a further, unpolarized continuum component, likely to be starlight from the host galaxy (Antonucci, 1993, González Delgado et al., 1998, Storchi-Bergmann et al., 1998), that dilutes the polarized light from both the nuclear continuum and the BLR. The contribution of polarized flux from the BLR lessens the effect of dilution over the broad-line profile, leading to an increase in percentage polarization. Finally, the continuum polarization is often seen to increase at shorter wavelengths. This is generally believed to be due to the combination of the unpolarized starlight contribution and of dust scattering of the light from the obscured AGN continuum (or, alternatively, to electron scattering combined with a red unpolarized continuum).

In Sy1 galaxies, we have the direct view of the nuclear continuum source and the BLR, hence the dilution effect of starlight would be smaller and dominated by the AGN continuum (Smith et al., 2002). Polar-scattered Sy1 galaxies do not exhibit significant θ rotations across the broad $H\alpha$ line. These trends on p and θ identied with PBL Sy2 are also plausible in polar-scattered Sy1 galaxies if the direct view of the AGN continuum passes through the upper layers of the of the dusty circumnuclear torus (see right panel of Fig 5.4). This one would act like a dusty far-field polar scattering region (Schmid et al., 2001).

Smith et al. (2002) argue that the observed polarization properties of Seyfert galaxies must follow the unification scheme which demands that all AGN are intrinsically the same, so that both polar and equatorial scattering routes should be present in all Seyferts. The question to be considered is: what is it that determines which of the two sources of scattered light dominates the observed polarization in both Sy1 and Sy2 nuclei? In order to answer this question, Smith et al. (2002) proposed a model in which the broad-line emission is generated in a rotating disc and then scattered by two distinct scattering regions that produce orthogonally polarized light. These two regions are:

(*i*) a near-field scattering region co-planar with the line-emitting disc and situated within the torus, in its equatorial plane: the *equatorial scattering region*.

(*ii*) a far-field scattering cone situated outside the torus but aligned with the torus/emission disc axis: the established *polar scattering region*.

This geometrical configuration is shown in Fig. 5.5. Equatorial scattering prints more complicated polarization features than polar scattering as the processes taking place in the equatorial scattering region are more complex. Consequently, we will first address the equatorial scattering model and then, separately, the polar one.

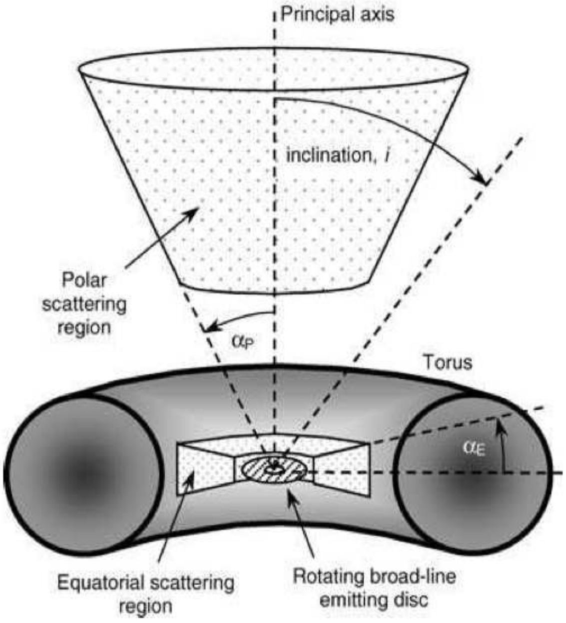

FIGURE 5.5: Two-component scattering geometry proposed by Smith et al. (2002) to explain the optical characteristics of Seyfert nuclei. The rotating disc is responsible for the emission of the broad Balmer lines. The equatorial scattered region is modeled as a flared disc of half-opening angle α_E surrounding the line-emitting disc. The polar scattering region is modeled as a truncated cone of half-opening angle α_p, aligned with the system simmetry axis. Inclination, i, is measured from the simmetry axis to the line of sight. Image credit: Smith et al. (2004).

5.3.1 Equatorial scattering model

A more detailed view of the equatorial scattering region is shown in Fig. 5.6. As noticed, the major role is played by the line-emitting disc which is centered on the point-like continuum source, C. The disc rotation axis is inclined at some intermediate angle to observer's LOS, which is perpendicular to the page. A co-planar ring of scatterers closely surrounds the disc. In turns, both the disc and ring are surrounded by the circumnuclear dusty torus, the key element of UM. Their three axes are co-aligned defining the system axis, assumed to be coincident with the symmetry axis of the AGN and, therefore, with the radio axis. This direction can be also called *principal axis* of the AGN.

For the sake of simplicity, let us start considering a single scattering element aligned with the major axis of the disc seen in projection. Light from the emitting disc and from the central continuum source is scattered from this scattering element into the observer's LOS and thereby becomes linearly polarized. The **E** vector of the scattered continuum light will be parallel, in projection, to the system axis. The scattering element will 'see' blue- and redshifted emission from points A and B, respectively. Keeping in mind that the broad-line emitting disc is inclined, the scattering planes for red- and blue-shifted rays and their corresponding **E** vectors are directed

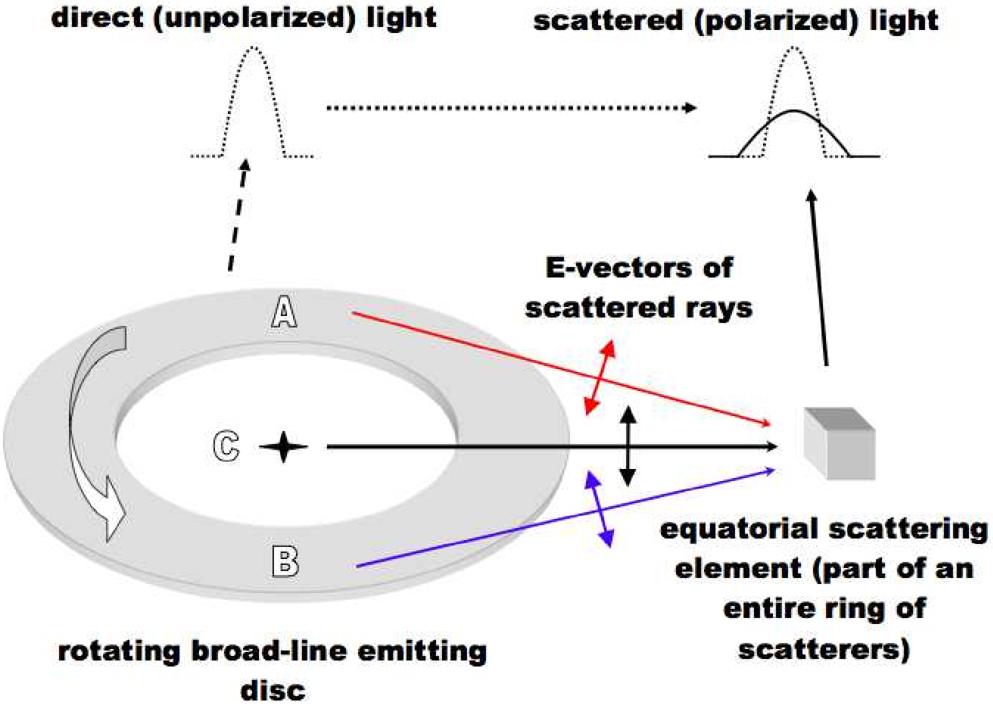

Figure 5.6: Scheme on the equatorial scattering model proposed by Smith et al. (2002). The disc rotation axis is inclined at some intermediate angle to observer's LOS, which is perpendicular to the page. The central continuum source, C, and the broad line emitting disc are surrounded by a coplanar ring of scattering medium. A single particle of the scattering ring is represented as well as polarization vectors, after scattering, of rays originating from opposite sides, A and B, of the emission disc and C. Image credit: Smith et al. (2005).

either side of the continuum E vector with equal but opposite offset angles. This leads to a rotation in PPA, θ, from blue to red across the line profile, centered on the continuum θ.

In general, the blue-to-red θ rotation is kept even considering scattering from the whole ring. When the disc is viewed face-on, circular symmetry ensures complete cancellation of the polarization produced by any scattering element by that of its orthogonal counterpart. On the contrary, when the disc is inclined, light scattered from elements aligned with the minor axis of the projected disc begins to get polarized due to the smaller scattering angles than those exhibited by the light scattered in elements aligned with the major axis. Thus, the symmetry is broken and leaves a net polarization with a PPA rotation similar to that expected for a single scattering element aligned with the major axis.

Distinctive variations in p with velocity shift across the line profile are also reproduced by the model. A simple rotating disc produces a line profile for which the width varies as $\sin i$, being i the inclination of rotation axis to the line of sight (Smith et al., 2002) . Since the scattering ring has an edge-on view of the line-emitting disc $i = 90°$, the scattered line profile collects the whole range in rotational velocity present in the disc, therefore all scattering elements within the ring will ‘see’ a broader emission-line profile than the direct LOS to the observer, which for a Sy1 nucleus, must pass within the torus opening.

The average torus opening angle in Seyfert galaxies is well established by reiterated observational evidences to be of the order of $\sim 45^\circ$ (e.g. Lawrence (1991)). Therefore, the LOS in Sy1 galaxies must have, typically, $i < 45^\circ$ which implies that the line profile in direct (unpolarized) light has a width $< 1/\sqrt{2}$ times that in scattered (polarized) light. It follows that the combination of scattered and direct line emission will result in wavelength-dependent dilution of the polarized component. With the addition of the underlying continuum, for which the polarization is wavelength independent, the observed percentage polarization will increase relative to the continuum level in the line wings, where the dilution of the direct and unpolarized light has little effect due to its narrower line profile, but will drop to a minimum in the core of the line.

In short, the equatorial scattering model based on a broad line-emitting disc proposed by Smith et al. (2002) reproduces the general polarization characteristics of equatorial-scattered Sy1 galaxies as described above:

(*i*) θ rotations from blue to red across the broad lines profiles, while the underlying continuum keeps a roughly constant PPA

(*ii*) The continuum PPA is aligned with the projected disc rotation axis and hence also with the symmetry and radio axis.

(*iii*) p peaks in the line wings and passes through a minimum in the line core, while the underlying continuum is polarized at an intermediate level.

A blue-to-red θ rotation across the line profile is not always observed. A plausible explanation according to the model is that increasing the scattering ring radius relative to that of the disc will decrease the angle subtended by the disc at a given scattering element and hence will reduce the PPA swing (Smith et al., 2002). Thus, a constant PPA in wavelength in some objects could mean that the scattering ring has a relatively large radius. Nevertheless, while the model predicts that the PPA swing has to bisect the continuum polarization in the center of the line profile, sometimes it occurs displaced from the center although still in the line. A scattering outflow along the system axis would produce redshifted scattered light, polarized orthogonally to the equatorial component. This would imply the expected amplitude of the red-wing polarization peak to be reduced (by cancellation) relative to that of the blue-wing peak and its PPA to be preferentially modified, breaking the symmetry of the blue- and red- θ swing relative to that of the continuum.

In conclusion, polarization features predicted by the equatorial scattering model are present to very different degrees in the observations (Smith et al., 2002). This is not surprising given the simple geometry of the model and the probable complexity of the real emission and scattering regions. Additional emission components or scatterers, perhaps with velocity shifts, will undoubtedly distort the polarization signatures of the disc/ring system. However, the equatorial model is generally successful in accounting for the typical observational properties of equatorial-scattered Sy1 galaxies.

5.3.2 Equatorial + polar scattering model

As already stated, Sy1 nuclei do not always exhibit their θ parallel to the principal axis. In some cases polarization spectra very similar to those observed in PBL Sy2 nuclei are observed. It follows that polar scattering and its corresponding ‘scattering mirror’, which is located above the circumnuclear torus and allows us to detect the obscured BLR in Sy2 galaxies, are also present in some type 1 ones (Goodrich & Miller, 1994). Following the idea that all AGN are intrinsically the same, the idea is that both an equatorial and a polar scattering region are always present in Seyfert galaxies. Therefore optical polarization properties of Sy1 nuclei should include both far-field polar and inner equatorial component.

According to the model developed by Young (2000), the polar scattering region is devised as a cone, containing dust and/or free electrons, which is co-axial with the torus and has a comparable opening angle. The observed polarization produced by the combination of equatorial and polar scattering will, in general, depend on the inclination of the system axis to the LOS.

Smith et al. (2004) carried out calculations using the scattering code of Young (2000) varying the inclination from $i = 0^\circ$ to 90°. At very small inclinations, with the system axis closely aligned with the LOS, a low p is obviously obtained, since the circular symmetry ensures that both components of scattered light will suffer almost complete cancellation. However, when i is increased, p increases more rapidly for the equatorial than for the polar component. Then, without considering the optically thick dusty torus, the equatorial component would dominate the observed polarization at all inclinations. Nevertheless, for inclinations $i > 45^\circ$, the LOS to the BLR and the equatorial scattering region is blocked by the torus. In this configuration we would observe a Sy2 nucleus with broad Balmer lines visible in polarized light as a result of scattering in the polar region.

For polar scattering to dominate in type 1 Seyferts, the equatorial component must be suppressed relative to the polar component. The polar scattering region is visible in both Sy1 and Sy2 galaxies because it is located outside the circumnuclear torus. Therefore polarized flux from this component will contribute to the observed net polarization in all Seyfert nuclei. This component is dominating in Sy2 galaxies, because the torus blocks the direct view of the continuum source, the BLR and the equatorial scattering region. Then, one would expect that when the direct view of the nuclear regions is not blocked by the torus, equatorial scattering tends to dominate the observed polarization. Why is this not the case in the polar-scattered Sy1 galaxies, in which we evidently have a direct view of the BLR? Two scenarios are contemplated by Smith et al. (2004). (1) The equatorial component is unusually weak in these objects, allowing the polar component to dominate. This could occur if, for example, the column density of scatterers is relatively small in the equatorial region, compared to the polar region. (2) A more interesting possibility in the context of the unification scheme, is that geometry plays a role in suppressing the equatorial component relative to the polar component. In the Sy1 nuclei exhibiting signatures of polar scattering, the direct line of sight to the AGN passes through the, presumably relatively tenuous, upper layers of the torus. Light from the equatorial scattering region might easily suffer sufficient extinction to allow polar scattering to dominate the observed polarization. Direct light from the AGN would, of course, also suffer extinction, although the extinction must not be strong enough to obscure the view of the BLR.

To sum up, much of the observed diversity in the optical polarization properties of Seyfert nuclei is well-explained by this model studied and probed by Smith et al. (2002), Smith et al. (2004) and Smith et al. (2005) in which the broad-line emission originates from a rotating disc and is scattered by two distinct scattering regions that produce orthogonally polarized light. These are the scattering region co-planar with the line-emitting disc and situated within the torus, in its equatorial plane, i.e. the so-called *equatorial scattering region* and a scattering cone situated outside the torus and aligned with the torus/emission disc axis, the well established *polar scattering region*.

5.4 Extinction through the torus atmosphere

The idea that polar-scattered Sy1 galaxies are objects viewed at intermediate inclinations, in which the direct LOS to the AGN passes at relatively small optical depth in the upper layers of the dusty torus, had already been studied in QSOs. Wills et al. (1992) showed that the polarization and spectral properties of the infrared-selected QSO IRAS 13349+2438 can be explained as a combination of a reddened spectrum transmitted through a dusty thick disc (conceptually equivalent to the torus) and a polarized component due to scattering of light escaping in the polar directions. Schmid et al. (2001) modeled the spectrum of Fairall 51 combining reddened direct light and dust-scattered polarized light. The polarized light emerged from a dusty polar scattering region while the LOS to the AGN went through a section of the torus with an optical depth $\tau \sim 1$.

Since equatorially scattered Sy1 show low polarizations, typically $p \sim 1\%$, relatively little extinction in the upper layers of the torus would be needed to allow polar scattering to dominate the observed polarization. After suffering this extinction the polarized flux from the equatorial scattering region would have to be less than the unattenuated polarized flux from the polar scattering cone.

The ratio of the polarized flux produced by equatorial scattering, $F_{eq}(i)$, to that produced by polar scattering, $F_{pol}(i)$, can be considered as a lower limit to the required optical depth through the torus atmosphere:

$$\tau \geq \ln \frac{F_{eq}(i)}{F_{pol}(i} \tag{5.5}$$

Smith et al. (2004) used this relation together with the generic scattering model for AGN developed by Young (2000) configured as in Fig. 5.5 to obtain estimates for $F_{eq}(i)$ and $F_{pol}(i)$. They considered well-established values for AGN parameters like opening angles for polar and equatorial scattering regions and torus as 45°, 20° and 45° respectively. Therefore, extinction through the upper layers of the torus is likely to become important for inclinations around $\sim 45°$. For this value of i, they find $\tau \approx 1$, corresponding to an optical extinction $A_V \sim 1$ mag. The BLR will be also exposed to the same extinction that the equatorial scattering region. However, they also derived that a much larger extinction, typically $A_V \geq 4$ would be needed to reduce the direct broad-line flux to undetectable levels against the underlying continuum. Despite the fact that these estimates of the necessary A_V are model-dependent, they show that it is possible for light from the equatorial scattering region to suffer enough attenuation to allow polar scattering to dominate the observed polarization spectrum, without causing significant obscuration of the BLR and AGN continuum source.

Considering the half-opening angle of the torus $i \approx 45°$, one could expect that the optical depth along the LOS will increase for $i > 45°$ as a result of both the path length through the torus and an increasing dust density towards the equatorial plane. Then, polar scattered Sy1 galaxies will be observed in some range in inclination governed by $\tau(i)$. The lower limit to this range will be the inclination at which $\tau(i)$ becomes large enough to attenuate the polarized flux from the equatorial scattering region to a level below that of the polar scattering region. The upper limit will be the inclination at which $\tau(i)$ is large enough to extinguish the direct broad line emission relative to the stellar continuum, leaving a PBL Sy2 spectrum.

It follows that, in general, polar-scattered objects should be more reddened than the equatorial-scattered ones amongst Sy1 population. Besides, it is worth mentioning that if the direct view of BLR and equatorial scattering region goes through the dusty atmosphere of the torus, dichroic absorption could imprint a certain amount of polarization. However, the strength of any dichroically polarized flux component will depend on the magnetic field structure in the upper atmosphere of the torus. The common increase of p to shorter wavelengths so characteristic of the polar-scattered Sy1 nuclei argues against significant dichroic polarization. Smith et al.

(2004) suggest the upper atmosphere of the torus can be turbulent, blocking any large-scale organization of the magnetic field and hence any significant dust grain alignment.

In brief, this two-component scattering geometry implies that the polar-scattered Sy1 galaxies represent the transition between unobscured (the majority of type 1) and obscured (type 2) Seyferts, showing inclinations of the system axis to our LOS comparable to the half-opening angle of the torus.

5.5 Classification of Seyfert galaxies according to orientation-dependent polarization

Within the scenario described up to now, the combination of a compact equatorial scattering region within the torus and an extended polar scattering region outside it, results in strongly orientation-dependent polarization properties. Smith et al. (2004) identify four inclination regimes, each one producing different polarization features (see Fig. 5.7), only assuming that the well-established value of $\sim 45^\circ$ for the torus opening angle. Since the geometrical configuration of the scattering regions, i.e their opening angles, are poorly constrained, the inclination range of each regimen is approximated. This classification is described below:

- **Unpolarized Seyfert 1 galaxies ($i \approx 0^\circ$)**

  When $i \approx 0^\circ$ (system viewed almost face-on), both the equatorial and polar scattering regions exhibit a high degree of circular symmetry in projection and therefore cancellation leads to null or very low polarization, within the uncertainty of the measurement of p. Hence, this type of objects shows featureless polarization spectra.

- **Seyfert 1 galaxies dominated by equatorial scattering ($0^\circ < i < 45^\circ$)**

  For inclinations $0^\circ < i < 45\circ$, the direct LOS to the nucleus does not suffer obscuration by the torus. Both scattering regions, as well as the broad-line emitting disc, are visible. The two scattering regions produce orthogonal polarization, therefore there will be cancellation between the two, and the net polarization will reflect that of the stronger component. In general, equatorial scattering is the dominant one at these inclinations.

  The predicted polarization features of this subgroup are:

  (*i*) A central dip in p in the line core, flanked by polarization peaks in the wing.
  (*ii*) A blue-red swing in θ across the Hα profile.
  (*iii*) The continuum and average Hα PPA should be parallel to the system axis.

  The amplitudes of these effects depend on different combinations of parameters and the presence of one does not necessarily imply the presence of the other.

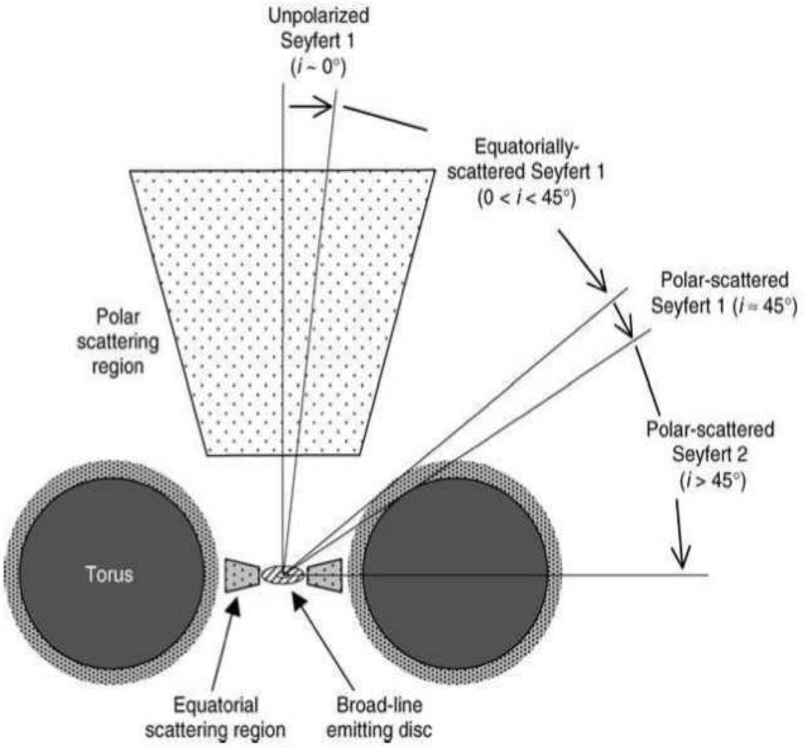

FIGURE 5.7: Schematic representation in which the broad lines polarization characteristics of Seyfert galaxies can be directly related with the LOS inclination. Image credit: Smith et al. (2004).

- **Seyfert 1 galaxies dominated by polar scattering ($i \approx 45°$)**

  When $i \approx 45°$, the LOS to the nucleus passes through the relatively tenuous upper layers of the torus attenuating the normally dominant equatorially scattered light and leading polar scattering to dominate the polarization spectrum. The total light spectrum is still that of a Sy1, but moderately reddened.

  In this category, the predicted polarization signatures are:

  (*i*) p rises for shorter wavelengths with local maxima associated with the broad Balmer lines.

  (*ii*) $\theta(\lambda)$ is generally constant over the spectrum or presents slight changes across the broad lines, but always small compared to the large swings seen in the equatorial-scattered Sy1 galaxies.

  (*iii*) The average PPA tends to be roughly perpendicular to the system axis.

  These general characteristics are shared with PBL Sy2 galaxies.

- **Seyfert 2 galaxies**

When the inclination is such that the LOS to the nucleus passes through the body of the torus. Both the BLR and the equatorial scattering region are completely obscured and only the polar scattering region remains unobscured. The broad lines are only visible in polarized light scattered from the polar scattering region.

- **Other objects**

  It is important to highlight that this classification described by Smith et al. (2004) is a general framework which can explain the broad range of polarization spectra exhibited by Seyfert nuclei. However, the detailed properties of a particular object may show variations and may not fit perfectly in this scheme.

5.6 Potential of ESO 362-G18 in polarimetric observations

As already noticed, the results reported up to now along this dissertation place ESO 362-G18 in a very interesting perspective within the polarization scenario outlined above. The multi-epoch X-ray analysis of ESO362-G18 carried out in Agís-González et al. (2014) and reported on Chapter 2 strongly suggests that the inclination of our LOS to the system axis is $i = 53° \pm 5°$. Moreover, the occultation events discussed in the previous chapters, driven by clumps likely located close to the dust sublimation radius (i.e. the inner edge of the dusty torus), strongly suggest that our LOS passes through the upper layers of the clumpy torus itself, confirming a grazing inclination which is one of the defining properties of the class of polar–scattered Sy1 galaxies identified by Smith et al. (2004). Moreover, as discussed in Chapter 4, we have seen that the observed extinction towards the BLR when the source exhibits both $H\alpha$ and H_β broad components (i.e. when ESO 362-G18 is classified as Sy1.5) is ${A_V}^{EMMI} = 0.99 \pm 0.15$ and ${A_V}^{FORS2} = 1.71 \pm 0.21$, precisely in the range of $A_V = 1 - 4$ mag that is capable of obscuring the equatorial scattering region while preserving the broad emission lines. Hence, the described picture of polar-scattered Sy1 galaxies fits very well with the previously presented results for ESO 362-G18 and, at the same time, it reinforces the scenario where absorption driven by clumps of the torus (or its upper layers) is responsible for the changes of look reported in former section.

The polarization properties of changing look Seyfert nuclei are still not studied, and they could provide us with a clearer view of these transitional objects within the unification scheme. With the aim of probing the picture described above for the special case of the changing look Seyfert ESO 362G-18, we applied for observations in polarized light with one of the most powerful instruments working in this field: FORS2 located at Very Large Telescope (VLT), and the observations were granted to us. The immediate objective of our observations was to obtain the polarization spectrum, and to classify the source according to the scheme given by Smith et al. (2004). To that end, we aim to measure the fraction of linear polarization and its angle as a function of wavelength. Since the change of polarization across the H_α line constrains the BLR geometry and kinematics, we also required a polarization spectrum at higher resolution around 6500 Å. Imaging polarimetry (through the same bands) of the field around the source is also needed to estimate the value of interstellar polarization (not intrinsic to the source).

As discussed in Chapter 4, our spectropolarimetric observation of the source with FORS2 revealed (in direct light) both Hα and Hβ broad emission lines in the optical spectrum, so that during that observation ESO 362-G18 is classified as a Sy1.5 galaxy. Hence, in principle, both scattering regions, the polar and the equatorial, are accessible for our study. Therefore, we will be able to derive the behavior of p(λ) and $\theta(\lambda)$ and to corroborate if our target can be classified as polar-scattered Sy1, as all previous results discussed so far seem to anticipate. It must be pointed out that the source is resolved and the morphological position angle known so that the polarization position angle can be directly compared to it. The radio axis of this source is not available in the literature presumably because the object is not resolved at radio wavelengths. However, the PA in [OIII] is thought to be aligned with the PA of the scattering cones and with the symmetry axis. Mulchaey et al. (1996a) give PA= 158° for [OIII]. Hence, the PPA of ESO 362G-18 can be compared to [OIII] PA to estimate the relative direction of its polarization. For this purpose, Smith et al. (2004) establish three arbitrary categories: *parallel objects* have $\Delta PA \leqslant 30^\circ$, *intermediate objects* have $30^\circ \leqslant \Delta PA \leqslant 60^\circ$ and *perpendicular objects* have $\Delta PA \geqslant 60^\circ$. We will follow these bins in ΔPA taking into account that their boundaries are general approximations.

As already discussed in the former chapter, observations in polarized light of ESO 362-G18 performed with EFOSC1@3.6m are also available at ESO archive. However with these data the goals on the source cannot be reached due to a configuration problem of the instrument which makes impossible to compute θ.

5.7 General set-up of polarimetric observations

The observations described in this chapter were obtained with instrumentation that follows the optical scheme of Appenzeller (1967), i.e. comprising a $\lambda/2$ retarder wave plate set at fixed positions and a Wollaston prism as beam splitting device (see Fig. 5.8). The $\lambda/2$ retarder wave plate can be rotated in 22.5^o steps. If $\alpha = 0^\circ, 45^\circ, 90^\circ, 135^\circ... = k45^\circ$ the retarder will select the linear polarization contained in the planes perpendicular and parallel to the direction of propagation, thus it will be measuring P_Q. If $\alpha = 22.5^\circ, 67.5^\circ, 112.5^\circ, 157.5^\circ, ... = k45^\circ + 22.5^\circ$ the retarder will select linear polarization with an inclination of 45° and −45° to the plane of reference, i.e it will be filtering P_U (Hough, 2005). The Wollaston prism splits up the incoming light in two beams orthogonally polarized: the *ordinary beam* and the *extraordinary beam*.

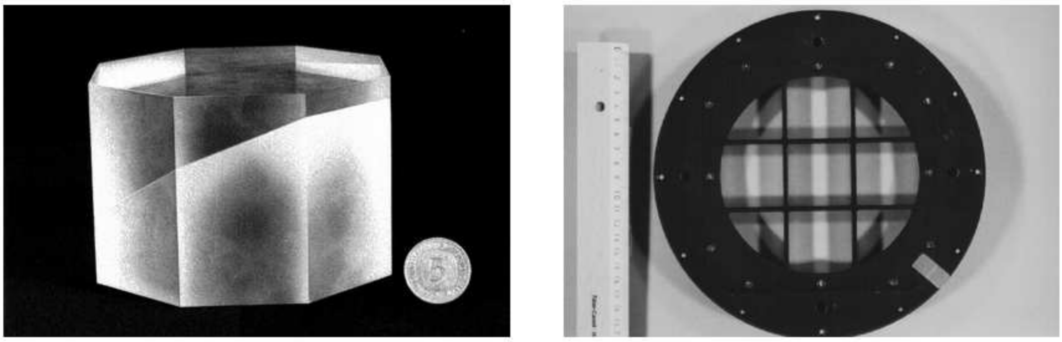

FIGURE 5.8: Optical devices required to split up polarized light in astronomical observations. *Left:* a Wollaston prism whose function is to separate orthogonal states of polarization detected simultaneoulsy. *Right:* the retarder wave plate allows to select the direction of the polarized light to enter in the optical system. Image credit: http://www.eso.org/sci/facilities/paranal/instruments/fors/inst/pola.html.

P_Q and P_U are measured by combining the photon counts (background subtracted) of ordinary and extraordinary beams (f° and f^e, respectively) observed at various retarder wave plate positions α, where α indicates the angle between the acceptance axis of the ordinary beam of the Wollaston prism and the fast axis of the retarder wave plate. In the ideal case, P_Q and P_U are obtained measuring the quantity

$$r = (-1)^k \frac{f^\circ - f^e}{f^\circ + f^e} \tag{5.6}$$

at any retarder wave plate position $\alpha = k45^\circ$ and $\alpha = k45^\circ + 22.5^\circ$ (k=0, 1, 2,..., 7.) respectively (Bagnulo et al. (2006) and references therein). In practice, there are several deviations from the ideal case. For instance, the actual retardance value of the retarder wave plate may deviate from its nominal value or the transmission of the ordinary and extraordinary beam can be not identical, even after flat field correction. In linear polarization, the effect of these and other sources of instrumental polarization can be largely reduced at the first order, carrying out four exposures at four angles of the retarder wave plate:

$$\begin{aligned} P_Q &= \frac{1}{2}\left\{\left(\frac{f^\circ - f^e}{f^\circ + f^e}\right)_{\alpha=0^\circ} - \left(\frac{f^\circ - f^e}{f^\circ + f^e}\right)_{\alpha=45^\circ}\right\} \\ P_U &= \frac{1}{2}\left\{\left(\frac{f^\circ - f^e}{f^\circ + f^e}\right)_{\alpha=22.5^\circ} - \left(\frac{f^\circ - f^e}{f^\circ + f^e}\right)_{\alpha=67.5^\circ}\right\} \end{aligned} \tag{5.7}$$

The corresponding errors, σ_{P_X} being X=Q, U, can be obtained through error propagation:

$$\begin{aligned}\sigma'^2_{P_X} \; = \; & \left(\left(\frac{f^\circ}{(f^\circ+f^e)^2}\right)^2 \sigma^2_{f^\circ} + \left(\frac{f^e}{(f^\circ+f^e)^2}\right)^2 \sigma^2_{f^e}\right)_{\alpha=\phi_0} + \\ & \left(\left(\frac{f^\circ}{(f^\circ+f^e)^2}\right)^2 \sigma^2_{f^\circ} + \left(\frac{f^e}{(f^\circ+f^e)^2}\right)^2 \sigma^2_{f^e}\right)_{\alpha=45^\circ+\phi_0}\end{aligned} \tag{5.8}$$

where $\phi_0 = 0^\circ$ if $X = Q$ and $\phi_0 = 22.5^\circ$ if $X = U$. P_Q and P_U can be obtained adding up N pairs of exposures. In that case the errors will be given by:

$$\sigma^2_{P_X} = \frac{1}{N}\sum_{i=1}^{N} \sigma'^2_{P_X} \tag{5.9}$$

Since the fluxes f^o and f^e are usually very similar (unless the source is really strongly polarized), one can can consider $f^o = f^e = f$ and $\sigma'_{P_X} = \sigma$ for all beams and positions intervening on the calculation of X. Thus, the error on σ_{P_X} can be simplified as:

$$\sigma_{P_X} = \frac{1}{2\sqrt{N}}\frac{\sigma}{f} \tag{5.10}$$

which means that the error bar for P_X is equal to the inverse of SN in one beam of one exposure divided by twice the square root of the number of pairs of exposures (Bagnulo et al., 2009).

As already mentioned, P_Q and P_U are generally combined in two fundamental magnitudes which contain the whole information about the configuration of polarization: the p, which measures the fraction of linearly polarized radiation and the PPA, or θ, which is coincident with the angle of maximum polarization, as:

$$p = \sqrt{P_Q^2 + P_U^2} \tag{5.11}$$

$$\theta = \frac{1}{2}\arctan\left(\frac{P_U}{P_Q}\right) + \theta_0 \tag{5.12}$$

$$\text{where} \quad \theta_0 = \begin{cases} 0 & \text{if} \quad P_Q > 0,\ P_U \geqslant 0 \\ \pi & \text{if} \quad P_Q > 0,\ P_U < 0 \\ \frac{\pi}{2} & \text{if} \quad P_Q < 0,\ P_U \geqslant 0 \end{cases} \quad \text{or} \quad \theta = \begin{cases} \frac{\pi}{4} & \text{if} \quad P_Q = 0,\ P_U > 0 \\ \frac{3\pi}{4} & \text{if} \quad P_Q = 0,\ P_U < 0 \end{cases}$$

Eq. 5.12 is the correct expression for obtaining the PPA since the *arctan* is a function defined between −90° and 90° what generates inconsistencies for the resulting value of the angle. This discrepancy is solved adding those turns of 90° or 180° according to the signs of P_U and P_Q. The arising θ is measured in the usual astronomical sense: 0° is north and 90° is east.

At the same time, P_Q and P_U can obviously be expressed as a function of p and θ (Bagnulo et al., 2009):

$$\begin{aligned} P_Q = & \quad p\cos 2\theta \\ P_U = & \quad p\sin 2\theta \end{aligned} \tag{5.13}$$

The associated errors, σ_p and σ_θ, are derived from the former equations by error propagation and the corresponding error bars will be given by:

$$\begin{aligned} \sigma_p = & \quad \sqrt{\cos^2(2\theta)\sigma^2_{P_Q} + \sin^2(2\theta)\sigma^2_{P_U}} \\ \sigma_\theta = & \quad \frac{1}{2}\frac{\sqrt{\sin^2(2\theta)\sigma^2_{P_Q} + \cos^2(2\theta)\sigma^2_{P_U}}}{p} \end{aligned} \tag{5.14}$$

Note that the expression for σ_p is only valid if $\sigma_p << p$. Besides if $\sigma_{P_Q} = \sigma_{P_U}$ then Eq. 5.13 are transformed into:

$$\begin{aligned} \sigma_p = \sigma_{P_Q} = \sigma_{P_U} \\ P_\theta = \frac{1}{2}\frac{\sigma_p}{p} \end{aligned} \tag{5.15}$$

It has to be noticed than linear polarization is a biased quantity. It describes the state of polarization (along with PPA) throughout the normalized Stokes parameters (P_Q, P_U), which due to the presence of errors are only estimates of the true normalized Stokes parameters (P_{Q_0}, P_{U_0}) (Simmons & Stewart, 1985). Using $p = \sqrt{P^2_Q + P^2_U}$ as estimator the true polarization, $p_0 = \sqrt{P^2_{Q_0} + P^2_{U_0}}$, will be overestimated. This is a common behavior for quantities defined as always positive. If $P_{Q_0} = P_{U_0} = 0$ and both parameter are considered randomly distributed between $\pm\sigma_{P_{Q_0}}$ and $\pm\sigma_{P_{U_0}}$, p_0 should be also zero. However, if one compute p_0 for each realization of P_{Q_0} and P_{U_0} within the intervals errors, the average value of p_0 will not be equal to zero.

Several 'debiasing' schemes have been discussed in the literature (see Simmons & Stewart (1985) for a review and for a detailed mathematical development). In order to get a analytical expression, let us consider the estimator $\langle p\rangle = \hat{p}_0 - f(\sigma, p_0)$, although $f(\sigma, p_0)$ excludes any analytical solution and where $\hat{p}_0$ is also an estimator for p_0. Serkowski (1958) propose to consider

$\langle p \rangle$ as the observed p so that $\hat{p}_0$ can be estimated from $\hat{p}_0 = p + f(\sigma, p)$ (maximum likelihood estimator). Simmons & Stewart (1985) found that this estimator has the least associated risk when $\sigma_p/p \lesssim 0.7$. On the contrary, when $\sigma_p/p \gtrsim 0.7$, the best suited estimator for $\hat{p}_0$ is that suggested by Wardle & Kronberg (1974), i.e $\hat{p}_0$ accomplishes that for that value of p_0 the actual p_{obs} is the most likely, which is similar but not identical to the maximum likelihood estimator.

It should be mentioned that the introduction of estimators compensates the bias effect partially but these estimators will not be totally free of bias. The key point is to choose the least biased estimators in the range of polarizations that interests us as well as the one which minimizes the square error $\langle (\hat{p}_0 - p_0)^2 \rangle$ (Simmons & Stewart, 1985).

5.8 Instrumentation: FORS2

FORS2 is the acronym for **FO**cal **R**educer and low dispersion v.2 **S**pectrograph (Appenzeller et al., 1998). It is a multi mode instrument (imaging, polarimetry, long slit and multi-object spectroscopy) working in optical and near UV ranges, 330-1100 nm and attached to the VLT of ESO, located at Paranal Observatory (Chile). Two versions of FORS have been built, FORS1 and FORS2, but nowadays only FORS2 is in operation, mounted on the UT1 (Antu) Cassegrain focus. It offers two different magnifications with pixel scales of 0.25″/pixel (with the standard resolution collimator) and 0.125″/pixel (with the high resolution collimator). The corresponding field sizes are 6.8’ x 6.8’ and 4.25’ x 4.25’ respectively. The two different magnifications are chosen by selecting one of the two different collimators, hence each magnification has to be calibrated independently. FORS2 also provides an unbinned readout mode for specific scientific cases.

The polarimetric modes allow for the measurement of linear and circular polarization, both for direct imaging, *IPOL*, and for spectroscopy, *PMOS*. The polarization optic is located in the parallel beam section and consists of a Wollaston prism as beam splitting analyser and two superachromatic phase retarder plate mosaics to measure linear and circular polarization respectively. Both mosaics are installed in rotatable mountings on a dedicated swing arm which can be moved in and out of the light path. The Wollaston prism is inserted in the uppermost wheel of the parallel beam section after the corresponding retarder and splits the incoming light into two orthogonally polarized beams separated by a small angle. Hence, every object in the field presents two images on the CCD detector (see, for instance, Fig. 5.12).

For imaging polarimetry (IPOL mode) of extended objects or crowded fields, an aperture strip mask is put at the focal plane of the telescope in order to avoid any overlapping of the two beams of polarized light on the CCD and to reduce the sky contribution (see Fig. 5.9). Then, by design, in IPOL observations, only half of the full field of view of the instrument is imaged on

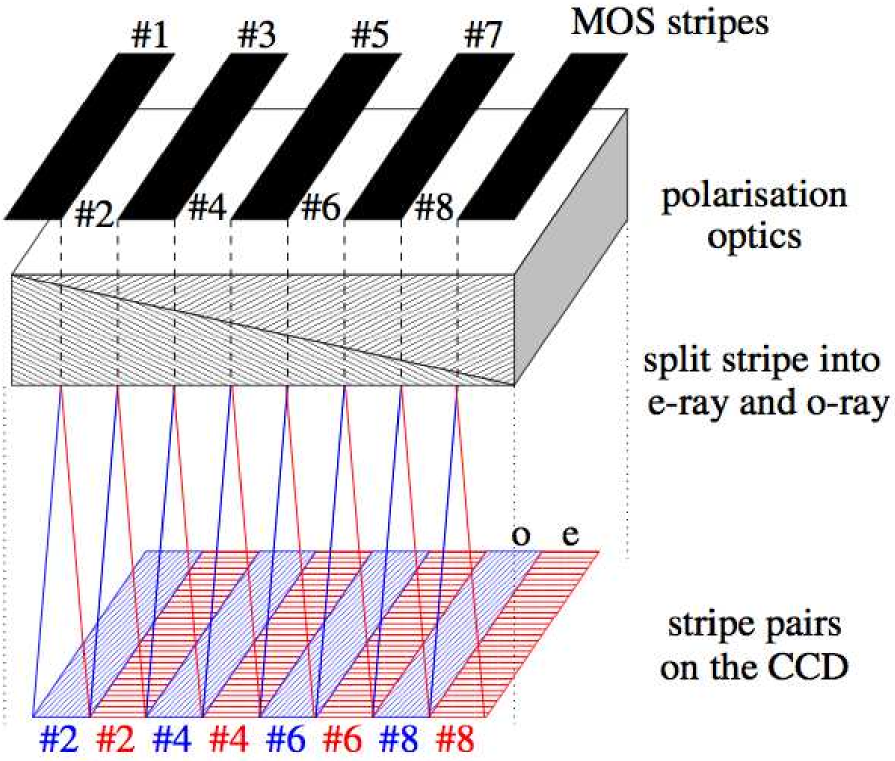

FIGURE 5.9: Strip mask to be inserted in the focal plane of FORS2 in IPOL mode to avoid overlapping of the two polarized beams. Image credit: FORS2 manual VLT-MAN-ESO-13100-1543_v96_0.

the CCD in one exposure. The complete field coverage can only be achieved if the user carries out an offset of the telescope accordingly in between exposures. The use of a stripped mask is also required for spectropolarimetry (PMOS mode) in order to avoid overlapping of the two beams polarized orthogonally.

As explained in section 5.7, the $\lambda/2$ retarder wave plate can be rotated in 22.5^o steps raging between the whole wheel, $\alpha = 0°, 22.5°, ..., 337.5°$, where α indicates the angle between the acceptance axis of the ordinary beam of the Wollaston prism and the fast axis of the retarder wave plate . Stokes parameters can be measured by combining the photon counts (background subtracted) of ordinary and extra-ordinary beams observed at various retarder wave plate α positions.

The polarization optics allows the determination of p to a relative error of $< 3 \times 10^{-4}$ and of PPA (depending on the target polarization) to about $\sim 2°$. For observations in the center of the field of view no instrumental polarization was found at the detection level of $< 3 \times 10^{-4}$. For off-axis measurements spurious polarization of up to $\sim 8 \times 10^{-4}$ was detected. It was modeled for V band and hence can be corrected (see section 5.11.2).

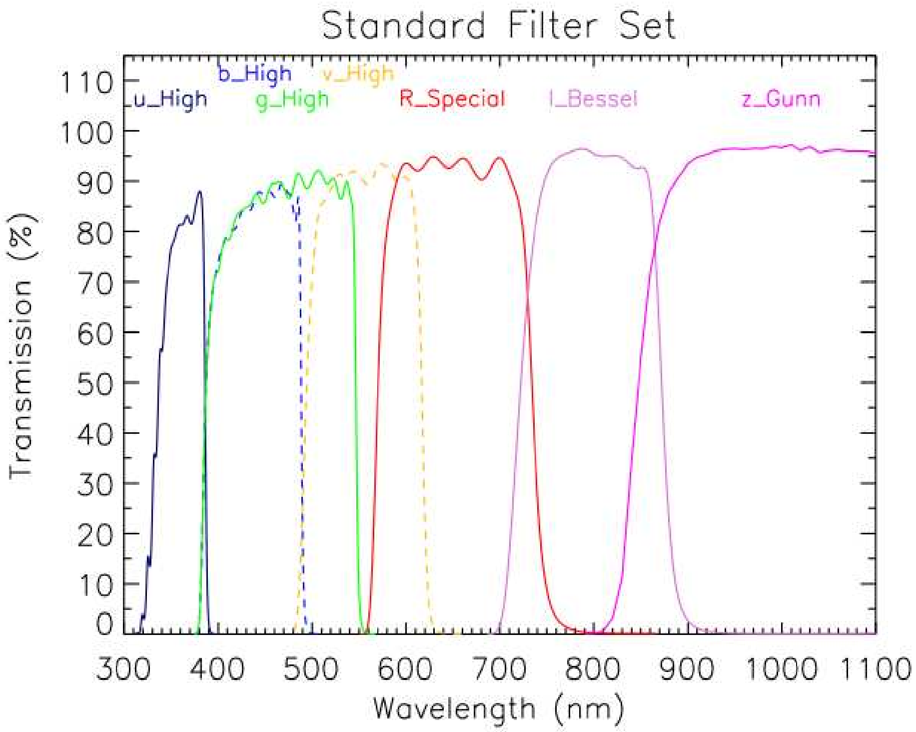

FIGURE 5.10: Transmission functions of the standard filter set in FORS2. We utilized v_HIGH and R_SPECIAL to measure the fraction of linear polarization and its orientation in the continuum. Image credit: FORS2 manual VLT-MAN-ESO-13100-1543_v96_0.

5.9 Observations

Our observations of ESO 362G-18 were performed in service mode during the night of March 29th 2016. Since the sky-background is highly polarized in presence of the Moon, we asked for grey time.

5.9.1 Imaging polarimetry: IPOL mode

The broadband polarization of ESO 362-G018 has been measured for filters v_HIGH+114 and R_SPECIAL+76 (see transmission functions in Fig. 5.10) in IPOL mode. The target was observed taking exposures of 3 s. at half wave plate angles of 0°, 22.5°, 45° and 67.5° for each filter at read-out mode 1×1, i.e. at scale pixel 0.125″/pixel, at standard resolution. In order to get polarization measurements in the field of view of the target with the aim of estimating the ISM polarization, another set of exposures, this time of 30 s., at the same half wave plate angles were performed, again in both filters but in read-out mode 2×2, i.e. at scale pixel 0.25″/pixel, at standard resolution. The exposure time and the read-out are changed since the field stars are much fainter than the target galaxy. For each Stokes parameter one pair of exposures were taken.

5.9.2 Spectropolarimetry: PMOS mode

Two grisms were used with two different mask. The grism 300V+10 (hereafter 300V) provides a spectral coverage from 4350 to 9300 Å, a central wavelength of 5900 Å, a dispersion of 112 [Å/mm] or 1.68 [Å/pixel] and a resolving power of $\lambda/\Delta\lambda$ = 440 for a slit width of 1". Together with the grism 300V, a stripped mask of 1.2" was used, then spectral resolution changes to $\lambda/\Delta\lambda$ = 367. These capabilities allow us to analyze the continuum of our target and the $H\alpha$ and $H\beta$ lines. Since changes of the polarization is expected along $H\alpha$, the 1200R+95 grism together with a stripped mask of 1" width were also requested to get spectra of high resolution around 6563 Å. Its spectral coverage is 5750 - 7300, its central wavelength 6500 Å, its dispersion 25.0 [Å/mm] or 0.38 [Å/pixel] and its resolving power $\lambda/\Delta\lambda$ = 2140.

In order to get the chromatic refraction due to the atmosphere along the slit, this one is set at the parallactic angle, i.e. along the hour circle. In this way, the position of the target will move within and along the slit from the blue to the red without risk of having the blue or the red image out of the slit. However, the reference plane established to calculate polarization is that in which the rotator/adapter coincides with N-S direction. Then, the P_Q-P_U plane has to be rotated by the parallactic angle value with respect to the N-S direction in each exposure. This rotation is not affecting the polarization degree as p is the quadratic sum of P_Q and P_U. The PPA can be obtained by a simple offset correction (Bagnulo et al., 2009): $\theta = \theta'$ *-rotator position*.

Exposures of 117 and 120 s., respectively for grisms 300V and 1200R, at half wave plate angles of 0°, 22.5°, 45°, 67.5°, 90°, 112.5°, 135° and 157.5° were taken to be combined and to compute average $P_Q(\lambda)$ and $P_U(\lambda)$.

5.10 Reduction of the data

All the calibration and science frames were bias subtracted using the corresponding master bias. No flat-field correction was carried out as it is irrelevant for the purpose of measuring the polarization through Eq. 5.7 and can induce additional noise. Besides, the beam-swapping technique described before largely reduce the errors introduced by a non-constant transmission function.

5.10.1 Procedure for IPOL data

Ordinary, f^o, and extra-ordinary, f^e, beams were bias-substracted and not flat-field corrected. Then, f^o and f^e fluxes were measured via simple aperture photometry that was performed using a procedure written within the ESO MIDAS reduction package combined with FORTRAN language and developed by Lamy & Hutsemékers (1999). This procedure allows to derive semi-automatically linear polarization data from CCD images obtained with beam-splitters such as the Wollaston prism available at FORS2. P_Q and P_U are then computed from the fluxes measured in the orthogonally polarized images according to Eq. 5.7. The associated errors, σ_{P_Q} and σ_{P_U} are calculated taking into account the photon noise in the object and the sky background. These errors are then propagated as Eq. 5.8 neglecting the readout noise.

Due to the fact that polarization observed in extragalatic objects is usually $\sim$ 1%, a careful subtraction of the sky background and an accurate determination of the object intensities f^o and f^e are essential to achieve reliable results for the Stokes parameters (Lamy & Hutsemékers, 1999). Since the sky background is usually polarized, the subtraction must be done independently for each orthogonally polarized image. For that purpose, two strips centered on each one of the two orthogonally-polarized images of the object are extracted. Then, the local sky is evaluated by fitting a bi-dimensional polynomial to values of background measured in small boxes free of cosmic rays and faint objects. Lamy & Hutsemékers (1999) showed that the best results were achieved with first grade polynomials. The small boxes are chosen in the upper and in the lower strips at exactly the same locations with respect to the object, taking care about a possible misalignment between the direction of the image splitting and the columns of the CCD. The center and the width of the object are determined at sub-pixel precision by fitting a bi-dimensional Gaussian profile. These results are injected in a FORTRAN code to integrate the flux in a circle of same center and arbitrary radius, taking into account only those fractions of pixels inside the circle. Thus, Stokes parameters are calculated for the desirable value of the aperture radius with a selected step in units of the mean Gaussian width $\sigma = (2\ln 2)^{-1/2} FWHM/2$, which is assumed to be identical for both the upper and lower images of the object. In this work a radius of $R/\sigma = 3$ was adopted in order to take as much flux as possible without too much sky. Polarization contribution coming from the host galaxy is thought to be insignificant as compared with that generated by the AGN if P_Q and P_U present a constant value when varying the aperture radius.

Although a super-achromatic half wave plate is used with FORS2, the position angle of the wave plate is slightly wavelength dependent. Therefore, all raw measurements θ are rotated by an angle of a few degrees due to this chromatism problem. For imaging polarimetry, the offset zero angles can be determined by convolving the filter response curves with the color dependence of the half wave plate zero angle. The results are recorded in table 4.7 of FORS2 manual VLT-MAN-ESO-13100-1543_v96_0. Thus, in order to correct this offset, a new position angle θ is obtained as

$$\theta = \theta' - \epsilon_\theta(F) \tag{5.16}$$

where $\epsilon_\theta(F)$ is the correction factor depending on the filter F and θ is the final corrected result for PPA. As noted in section 5.9.2, it is not necessary to apply this rotation correction for results on the degree of polarization, as p is calculated as the square sum of P_Q and P_U.

5.10.2 Procedure for PMOS data

PMOS data were pre-processed with the dedicated packages for spectra analysis implemented in IRAF. Spectra in the ordinary and extraordinary beams were bias-subtracted by the corresponding master-bias obtained from two series of 20 frames. As already noted, flat-field correction was not applied. The data were optimally extracted and wavelength calibrated using IRAF packages, and finally processed using dedicated IDL routines to calculate P_Q, P_U, p, and PPA, θ, with the corresponding errors following the procedure explained in section 5.1.

As in IPOL mode, the zero angle of the half wave plate in PMOS mode is not negligible. In this case, the chromatic dependence is determined with an aligned Glan-Thomson prism. The tabulated values can be downloaded from http://www.eso.org/sci/facilities/paranal/instruments/fors/inst/pola.html and are displayed in Fig. 5.11. The correction is applied following an analogous equation to Eq. 5.16, but for PMOS mode we have to take into account the rotation performed to keep the slit at the parallactic angle in order to keep both red and blue images shifted by the chromatic dispersion of the atmosphere within the slit. Then, for θ' derived from the PMOS data, the correction to be applied due to the different offsets is:

$$\theta(\lambda) = \theta'(\lambda) - \epsilon(\lambda) - \delta \tag{5.17}$$

where $\epsilon(\lambda)$ is the zero angle of the wave plate and δ is the position angle of the rotator.

5.11 Control quality of the data and results

5.11.1 Polarized standard star: offset of the polarization position angle

Studying scientific targets where polarization is involved, observations of standard stars are of crucial importance to calibrate and monitor instrument performances. At VLT, observations for standard stars considered to exhibit either zero polarization or substantial polarization are routinely performed within the context of the FORS2 calibration plan. Usually, a star known to exhibit a large signal of polarization, i.e. a *polarized standard star*, is observed during those nights when the polarimetric mode is working (Fossati et al., 2007). Vela 1 95 was the polarized standard star observed in IPOL mode on the night of 29th March 2016. Standard stars for PMOS mode are not performed so routinely since the PMOS mode is verified as very stable.

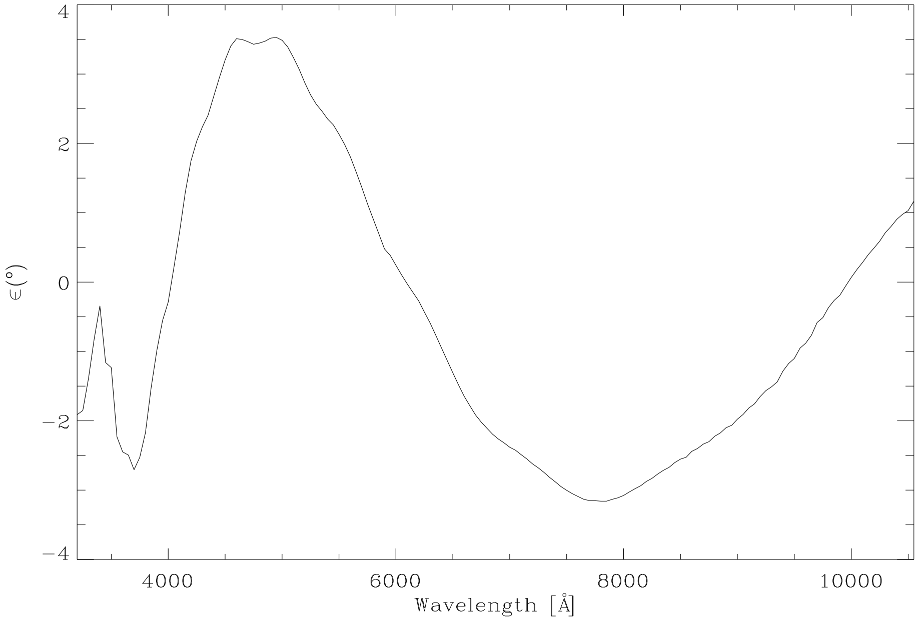

FIGURE 5.11: Tabulated values of the zero angle for the half wave plate determined with an aligned Glan-Thomson prism.

For IPOL mode, Vela 1 95 allows us to check the reduction procedure and to determine/verify the offset of the PPA, which is measured with respect to the instrument axis aligned with the N-S direction. As noted in section 5.10.1, the offset of the position angle of the wave plate for IPOL mode is stable and given as a function of the filter in FORS2 manual. Filters v_HIGH+114 and R_SPECIAL+76 are relatively new in the filter set of FORS2 but their response curves are very similar to those of Bessel V and R filters. Therefore, the established offsets given in FORS2 manual for Bessel V and R filters will be equivalent to those of v_HIGH+114 and R_SPECIAL+76 in terms for carrying out the chromatic correction of the resulting PPA.

P_Q and P_U for Vela 1 95 were computed through the MIDAS+FORTRAN procedure developed by Lamy & Hutsemékers (1999). The final results for its degree of polarization, p, and polarization position angle, θ, are shown in table 5.1. After having performed the chromatic correction due to the offset of the zero angle of the half wave plate following Eq. 5.16, the calculated quantities are in agreement with the tabulated values for that polarized standard star. This fact verifies the procedure carried out to derive the polarization parameters for the next targets is correct.

TABLE 5.1: Tabulated and measured values for the polarized standard star, Vela1 95, observed within the FORS2 calibration plan in mode IPOL during the night in which ESO 362-G018 data were taken, 29th May 2016.

POLARIZED STANDARD STAR: Vela1 95

Filter	p(%)	p_{tab}(%)	θ'	$\epsilon_\theta(F)$	θ	θ_{tab}
v_HIGH+114	8.24 ± 0.03	8.24 ± 0.03	$173.5° \pm 0.1°$	$+1.80°$	$171.7° \pm 0.1°$	$172.1° \pm 0.1°$
R_SPECIAL+76	7.95 ± 0.03	7.89 ± 0.04	$170.4^{o} \pm 0.1°$	$-1.19°$	$171.6° \pm 0.1°$	$172.1° \pm 0.2°$

p is the derived and final degree of polarization.
Subscript *tab* indicates that the corresponding magnitude is that tabulated.
θ' is the measured PPA.
$\epsilon_\theta(F)$ is the chromatic offset of the wave plate in function of the used filter.
θ is the corrected and final PPA.

5.11.2 Instrumental polarization

As noted in the former subsection, there exits a routine FORS2 quality control (see http://www.eso.org/observing/dfo/quality/FORS2/reports/HEALTH/trend_report_PMOS_angle_HC.html). The instrumental polarization of FORS2 is checked to be stable thanks to periodical polarized standard stars which ensure that, for IPOL mode, instrumental polarization can be considered zero in the center of instrument field of view. It should be noted that, in the corners of the CCD, FORS2 is affected by a problem of spurious linear instrumental polarization that cannot be eliminated even by performing several observations with the wave plate at various positions. This spurious polarization, due to the presence of curved lenses in the collimator, combined with the non complete removal of reflections by the coatings, has been analyzed in V band and shows a high degree of axial symmetry, increasing smoothly from less than 0.03% on the optical axis to 0.7% at an axis distance of 3 arcmin (Patat & Romaniello, 2006). This effect can be modeled with a correction function which depends on the radial distance from the center of the field of view in units of arcmin, $r = (x - x_c, y - y_c)$:

$$\begin{aligned} p_{ins}(r) &= 0.0057\ r^2 \quad [\%] \\ PA(x,y) &= \arctan\left(\frac{y - y_c}{x - x_c}\right) \end{aligned} \tag{5.18}$$

Note that this spurious polarization is filter-dependent and only applies for V filter. $p_{ins}(r)$ and $PA(x,y)$ must be decomposed in the corresponding P_{Q_ins} and P_{U_ins} through Eq. 5.13 in order to apply a "vectorial correction" where P_{Q_ins} and P_{U_ins} are subtracted from the observed P_Q and P_U. From there, the corrected p and PPA are computed. It must be underlined that polarimetric observations of single targets in the center of the field of view are not affected by these effects.

A grism-dependent instrumental polarization is also present in PMOS mode. For grism 300V a polarization offset for P_Q is well defined through unpolarized standard stars and established as $P_{Q_{off}} = (V)0.07\%$ by Fossati et al. (2007) and Cikota et al. (2016), while for P_U no spurious polarization is detected. For grism 1200R Siebenmorgen et al. (2014) measured an instrumental contribution $P_{Q_{off}}(R)$ which is linearly changing with wavelength from $\sim 0.2\%$ at $\lambda = 580$ nm to $\sim 0.32\%$ at $\lambda = 720$ nm, and $P_{U_{off}}(R) \sim -0.1\%$ that is nearly constant with wavelength. This instrumental contributions will be subtracted from the observed values of P_Q and P_U.

5.11.3 Unpolarized starlight from the host galaxy

The unpolarized starlight from the host galaxy can affect our measurements by diluting the intrinsic polarization of the AGN. Besides, the level of starlight contribution may not be constant across the wavelength range of our data and can lead to an apparent increase in polarization towards shorter wavelengths (Smith et al., 2002). However, in the analysis of the IPOL data we have noted that the computed P_Q and P_U are constant with the the aperture radius up to 10 σ (being σ the mean gaussian width of the source profile, see section 5.10.1). This result suggets that the host galaxy is not exerting a measurable dilution effect. We also consider this assumption for boht IPOL and PMOS modes.

5.12 Results from imaging polarimetry

5.12.1 Interstellar medium polarization

If between the target and the observer, there exist aligned dust grains in our LOS belonging to our Galaxy, ISM polarization can be induced. This effect is indeed more noticeable at low galactic latitude, but intermediate objects as ESO 362G-18 with latitude $b = -32.57$ are not exempt. Assuming that ISM polarization is constant over the FORS2 field of view, the induced p_{ISM} can be computed from the neighboring stars. Through SAOImage DS9 we have overlapped the GSC 2.2 Catalog over our acquisition images on R_SPECIAL+76 filter (see Fig. 5.12). We chose that catalog among the available options because it contains more stars of the field and also more information about them. In this way, we retrieved the coordinates of each star in the field (see table 5.2).

Nevertheless, it should be emphasize that our AGN is out of the Milky Way and therefore the light crosses a much larger portion of the Milky Way than the stars within the Galaxy. Then, it is not possible to know exactly the magnitude of the ISM polarization, only it is possible to get an estimated approximation. For this purpose, we tried the following methods:

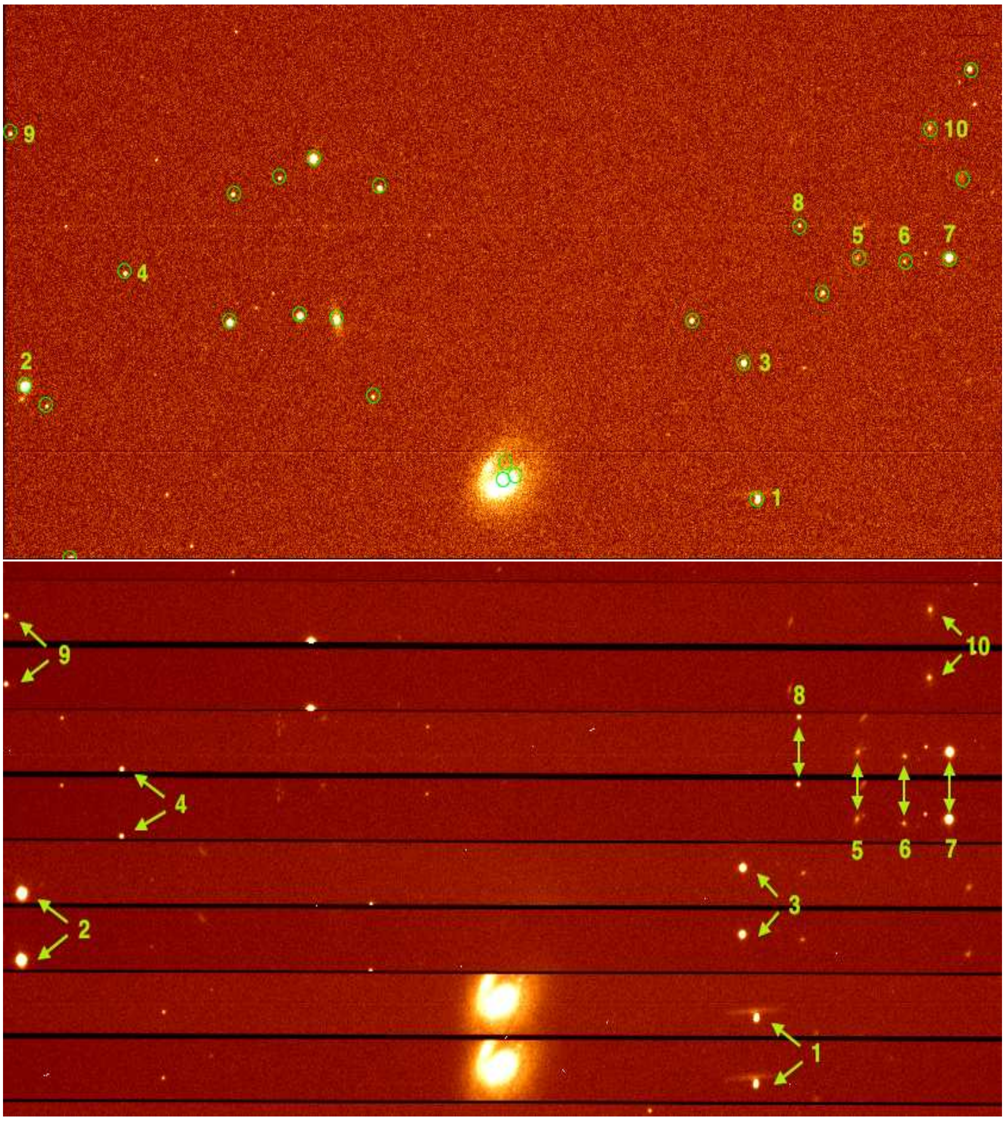

FIGURE 5.12: : *Top panel*: Acquisition image of ESO 362-G018 on R_SPECIAL+76 filter with 0.5 seconds of exposure time, which makes easier to recognize the field stars contained in GSC 2.2 Catalog. *Bottom panel:* Polarimetric image of ESO 362-G018 on v_HIGH+114 filter with 30 seconds of exposure time. With this exposure the galaxy is saturated but the flux of the field stars is suitable to measure their corresponding Q and U Stokes parameters and obtain an estimation on the ISM polarization.

- **Estimation from stellar catalogs**

  The most simple and direct way to get an estimation of the ISM polarization is to identify the neighboring stars in the field of the AGN and start a search in polarimetric catalogs. If several stars are going to exhibit similar p and PPA, very probably their polarization is due to ISM. We have identified the neighboring stars in the FOV of our images thanks to the coordinates given by the GSC 2.2 catalog. Unfortunately, none of the field stars are included in any type of catalog (polarimetric or not). An exhaustive search in SIMBAD did not deliver any match.

- **Estimation from stellar extinction**

  For lines of sight with $E(B-V) \gtrsim 0.1$ mag, Serkowski et al. (1975) showed that the maximum ISM polarization in per cent over the V band obeys $p_{ISM_{max}} \lesssim 9E(B-V)$. Making use of the Galactic Extinction Calculator tool provided by NED, we have found that the expected extinction for ESO 362-G18 is roughly $E(B-V) \sim 0.01$. The relation given by Serkowski et al. (1975) is less certain for low extincitons although still valid (see Fig. 9 of Serkowski et al. (1975)). In any case, an estimation of the maximum ISM polarization can be always derived and we have found $p_{ISM_{max}} \lesssim 0.14$ %, according to Schlafly & Finkbeiner (2011) and $p_{ISM_{max}} \lesssim 0.17$ %, according Schlegel et al. (1998), assuming $E(B-V) = A_v/3.1$ from the galactic extinction law by Cardelli et al. (1989). It should be emphasized that this estimation corresponds to the maximum polarization in the LOS. For typical conditions, where the dust grains are not highly aligned, the percentage of the induced polarization is $\approx 3E(B-V)$. In this case, the estimations result in $p_{ISM} \approx 0.05$ % for A_v data given by Schlafly & Finkbeiner (2011) and $p_{ISM} \approx 0.06$ % following Schlegel et al. (1998).

  When the magnitude of ISM polarization is known or estimated, Hoffman et al. (2005) showed that the maximum PPA difference given by that ISM can be inferred as:

  $$\Delta\theta_{max} = \frac{1}{2} \arcsin\left(\frac{p_{ISM}}{p_{obs}}\right) \tag{5.19}$$

  where p_{ISM} is the magnitude of the ISM polarization and p_{obs} is the degree of polarization observed for the target in question.

  An analogous estimate can be calculated for R band thanks to the empirical relation given by the Serkowski law (Whittet, 1992):

  $$P_\lambda = p_{ISM_{max}} \exp\left(-K \ln^2 \left\{\frac{\lambda_{max}}{\lambda}\right\}\right) \tag{5.20}$$

  where $K = (1.66 \pm 0.09)\lambda_{max} + (0.01 \pm 0.05)$ and λ_{max} is the wavelength of maximum polarization, which varies from star to star although is typically in the range of $0.3-0.8\mu m$ with a mean value of $0.55\mu m$ which will be adopted here. Taking into account the average for both results derived above for $p_{ISM_{max}}$ (hereafter p_{ISM_V}), we obtain $p_{ISM_R} \sim 0.151\%$ for $p_{ISM_V} \sim 0.155\%$.

- **Estimation from measurements in neighboring stars**

  The last attempt for achieving a reliable estimation of the ISM polarization is to apply the described MIDAS+FORTRAN procedure in order to find out if some field stars exhibit a similar state of polarization. If so, the most probable scenario would be that the polarization of the neighboring stars is caused by the ISM and its corresponding p would be that obtained.

> Since the neighboring stars on the polarimetric images of ESO 362-G18 are not in the center of the FOV, they will be affected by spurious instrumental polarization whose correction function is only available for V band (Eq.5.18). Then, our estimation can only be carried out for those images performed with the filter v_HIGH+114. For this purpose, the targets must be bright and cannot be placed close to the strip bonduaries. Otherwise, the sky background could not be computed and the aperture photometry could not be performed in favorable conditions. Unfortunately, only two field stars far off the edges of the polarized strips are bright enough so that polarization parameters can be obtained: those identified as 3 and 7 in Fig. 5.12. Star 1 also verifies these two requirements, however, in the fits file a kind of spurious horizontal band in the CCD can be noticed very close to it. This makes very difficult to compute the corresponding Stokes parameters and star 1 turns into not usable. Star 2 is saturated, hence invalid too. The log of the corresponding results can be found in table 5.2.
>
> After applying the adequate instrumental correction available for V band and given by Eq.5.18, we found that Star 3 shows $p = 0.31 \pm 0.01\%$ and $\theta = 125^\circ \pm 5^\circ$, whereas the another usable neighboring star, Star 7, seems to suffer a degree of polarization polarization significantly higher, $p = 1.13 \pm 0.05\%$, and a consistent PPA with $\theta = 133^\circ \pm 2^\circ$. Hence, both polarization position angles are aligned but due to the p difference we are unable to get a reliable conclusion about the induced p_{ISM}. However, it s worth to highlight that the measured θ for our AGN is not consistent with that derived for the usable field stars what should indicate that the direction of the electric field coming from ESO 362-G18 is not induced by the dust belonging to our Galaxy.
>
> The measurements of polarization of Star 3 in both V and R band do not allow us to perform a meaningful comparison since a correction function of the instrumental polarization induced by R filter is not available. It can only be concluded that the observed (including instrumental polarizations) are consistent.

In conclusion, there is evidence for intrinsic polarization of the neighboring stars and a substantial contribution from ISM cannot be ruled out. The galactic extinction on the LOS suggest that $p_{ISM_{max}}$ is comparable with the degree of polarization computed for ESO 362-G18, whereas the p for the analyzed field stars is considerably higher, what can indicate that the field stars exhibit intrinsic polarization, at least Star 7. In the view of these results, we decide to assume a rough estimate of the ISM polarization on V band considering the average value calculated for $p_{ISM_{max}}$ taking into account the absorptions given by Schlegel et al. (1998) and Schlafly & Finkbeiner (2011). Namely, hereafter we will consider the contribution of the ISM polarization to our measurements as $p_{ISM_V} \sim 0.155\%$ for V band. From this, we obtain $p_{ISM_R} \sim 0.151\%$ for R band according to the Serskowky law (Eq. 5.20) and assuming λ as the effective wavelength of filter R_SPECIAL+76 filter.

TABLE 5.2: Estimate of ISM polarization from the field stars in both V and R filters.

			v_HIGH+114						R_SPECIAL+76 filter			
Object	RA	DEC	P_Q	P_U	p_V (%)	θ_V	$p_{V_{corr}}$ (%)	$\theta_{V_{coor}}$	P_Q	P_U	p_R (%)	θ_R
AGN	05h19m35.80s	−32°39′27.31”	−0.22 ± 0.02	0.03 ± 0.02	0.22 ± 0.02	86° ± 13°	-	-	−0.19 ± 0.02	0.13 ± 0.01	0.23 ± 0.06	73° ± 9°
Star 1	05h19m27.29s	−32°39′33.98”			anomaly					anomaly		
Star 2	05h19m51.84s	−32°38′49.82”			SATURATED					SATURATED		
Star 3	05h19m27.74s	−32°38′41.56”	−0.23 ± 0.01	−0.14 ± 0.01	0.28 ± 0.01	105° ± 9°	0.31 ± 0.01	125° ± 9°	−0.11 ± 0.01	−0.17 ± 0.02	0.20 ± 0.07	118° ± 10°
Star 4	05h19m48.47s	−32°38′05.98”			on the edge					on the edge		
Star 5	05h19m23.87s	−32°38′01.05”			not bright enough					not bright enough		
Star 6	05h19m22.32s	−32°38′02.71”			not bright enough					not bright enough		
Star 7	05h19m20.83s	−32°38′01.27”	−0.49 ± 0.01	−0.62 ± 0.02	0.78 ± 0.05	115° ± 2°	1.13 ± 0.05	133° ± 2°		SATURATED		
Star 8	05h19m25.84s	−32°37′48.82”			on the edge					on the edge		
Star 9	05h19m52.30s	−32°37′12.54”			on the edge					on the edge		
Star 10	05h19m21.46s	−32°37′11.57”			not bright enough					not bright enough		

p_V is the observed degree of polarization on band V.
θ_V is the obsrerved polarization position angle on band V.
$p_{V_{corr}}$ is the degree of polarization corrected by instrumental polarization.
$\theta_{V_{corr}}$ is the polarization position angle corrected by instrumental polarization.
p_R is the observed degree of polarization on R band.
θ_R is the observed polarization position angle corrected by instrumental polarization.

TABLE 5.3: Polarization parameters for ESO 362-G018 derived from imaging polarimetry.

ESO 362-G018

Filter	v_HIGH+114	R_SPECIAL+76
P_Q	-0.22 ± 0.02	-0.19 ± 0.02
P_U	0.03 ± 0.02	0.13 ± 0.01
$p(\%)$	0.22 ± 0.02	0.23 ± 0.06
$p_{deb}(\%)$	0.219 ± 0.02	0.229 ± 0.06
$p_{corr_{ISM}}(\%)$	0.35 ± 0.02	0.34 ± 0.06
$p_{corr_{ISMdeb}}(\%)$	0.349 ± 0.02	0.339 ± 0.06
θ'	$86° \pm 13°$	$73° \pm 9°$
$\epsilon_\theta(F)$	$-1.19°$	$+1.80°$
θ	$87° \pm 13°$	$71° \pm 9°$
$\Delta\theta_{max}$	$22°$	$21°$
ΔPA	$\sim 71°$	$\sim 87°$

p is the observed degree of polarization.
p_{deb} is the debiased observed degree of polarization.
$p_{corr_{ISM}}$ is the observed degree of polarization corrected by our estimates of ISM poalrization.
$p_{corr_{ISMdeb}}$ is the observed degree of polarization corrected by our estimates of ISM poalrization and by bias.
θ' is the observed PPA.
$\epsilon_\theta(F)$ is the chromatic offset of the wave plate in function of the used filter.
θ is the PPA corrected by offset induced by the corresponding filter.
$\Delta\theta$ is the expected maximun change on θ induced by the estimated p_{ISM} .
ΔPA is the difference between the symmetry axis of the AGN (considered here as the PA for [OIII]) and θ.

5.12.2 Imaging polarimetry for ESO 362-G18: results

The polarization parameters for ESO 362-G18 are derived from the described MIDAS+FORTRAN procedure developed by Lamy & Hutsemékers (1999) and are shown in table 5.3. We have applied corrections for ISM polarization taking into account the estimates described on Section 5.12.1 and the bias of p. The observed ratio σ_p/p lead us to use the "debiasing" scheme given by Wardle & Kronberg (1974). In Table 5.3 we record the degrees of polarization observed (p) and corrected by the estimated ISM polarization ($p_{corr_{ISM}}$) and, in turn, also both quantities debiased (p_{deb} and $p_{corr_{ISMdeb}}$), although this last correction appears to be negligible here.

The PPA is corrected by the given instrumental offset of the corresponding filter ($\epsilon_\theta(F)$). As already mentioned in section 5.6, ESO 362-G18 is not resolved at radio wavelengths. Consequently, we make use of another measurement of the direction of the system axis of our target, the PA for [OIII] $\sim 158°$, provided by Mulchaey et al. (1996a). Hence, the PPA of ESO 362G-18 can be compared to [OIII] PA. ΔPA measures this difference in Table 5.3.

According to the results listed in this table, it can be inferred that PPA is roughly orthogonal to the system axis in both analyzed bands. $\Delta\theta_{max}$ is the possible rotation in the PPA induced by the estimated ISM polarization in both bands. Taking into account these values and the statistical errors, the derived PPAs are approximately constant along V and R filters and perpendicular to the system axis.

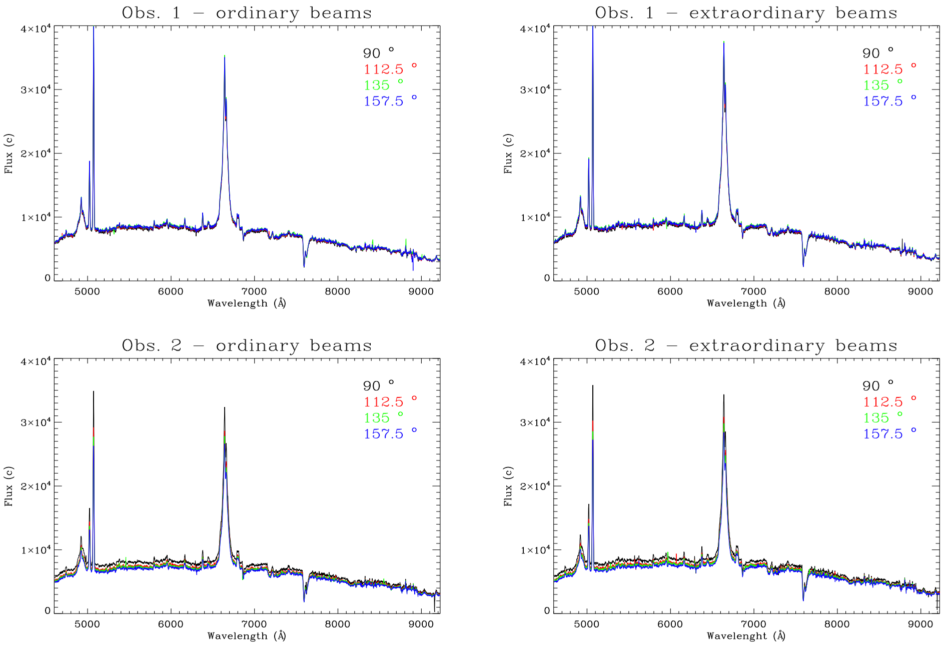

FIGURE 5.13: Ordinary and extraordinary spectra performed with grism 300V.

On the other hand, the degree of polarization of ES0 362-G18 seems to be constant in both bands with a observed value of ∼ 0.22%. When the estimated ISM polarization is taking into account p increases up to ∼ 0.34%, still quite low for a polar-scattered object. The increase in p after applying the ISM polarization correction can be possible if the PPA of the ISM is roughly perpendicular to that of the AGN, which results in a depolarizing effect. Then, the corrected p is expected to be higher.

Hence, the derived θ places ESO 362-G18 in the class of polar-scattered Seyfert galaxies. Besides, this value of θ is different from the PPA found for the field stars, which gives some confidence, that the measured polarization although weak is intrinsic to the source. On the order hand, the computed p for ESO 362-G18 is quite low for a polar-scattered object. A plausible explanation could be that the analysis of polar-scattered Seyfert galaxies carried out so far was most probably done by selecting objects significantly polarized, i.e. on the basis of their polarization properties, which may induce a bias.

5.13 Results from spectropolarimetry

As noted in section 5.9.2, exposures at half wave plate angles of 0°, 22.5°, 45°, 67.5°, 90°, 112.5°, 135° and 157.5° were taken to be combined and form average P_Q and P_U spectra from which p and θ were calculated for each wavelength bin. All ordinary and extraordinary spectra are shown in FIg.5.13.

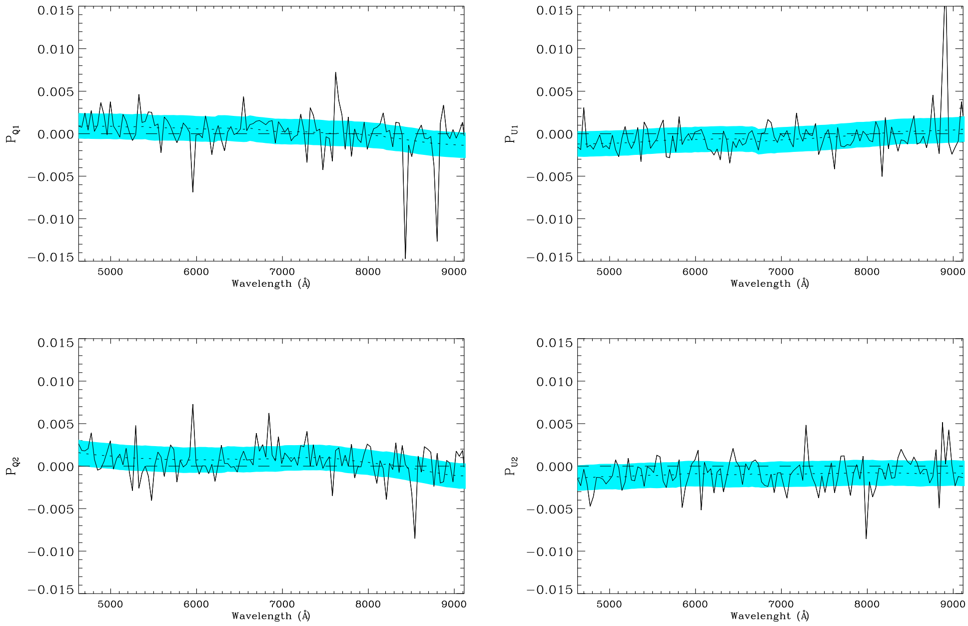

FIGURE 5.14: P_Q and P_U taken with grism 300V are shown for each two pairs of exposures. In top panels P_Q and P_U for exposures corresponding to the positions of the retarder of 0°, 22.°, 45° and 67.5° are represented. In bottom panels P_Q and P_U for exposures of 90°, 112.5°, 135° and 157.5° are shown.The blue regions represent the estimated error for each parameter.

The unavoidable and well established instrumental polarization measured by Fossati et al. (2007) and Siebenmorgen et al. (2014) for P_Q and P_U (see section 5.11.2) in both 300V and 1200R grisms is removed for the corresponding measurements, simply applying:

$$P_x = P'_x - P_{off_x} \tag{5.21}$$

The offset generated from maintaining the slit at the parallactic angle, δ, is also taken into account as well as the chromatic rotation induced by the half wave plate (Eq. 5.17). Since two pairs of exposures were taken in order to calculate P_Q and P_U (see Fig. 5.14), these were added up for deriving average p and PPA (see Fig. 5.15). The corresponding errors were estimated according to Eqs.5.10, 5.14 and 5.15.

Taking into account the strong noise, the four quantities present a rough constant value along λ. The average values of p and PPA along the wavelength range, $\sim$ 0.2% and $\sim$ 85°, are in very good agreement with those values computed from IPOL data. Then, here the correction for ISM polarization will give the same result of $p_{corr_{ISM}}$ and constant along wavelength.

As in IPOL data, the bias correction suggested by Wardle & Kronberg (1974) was applied, however since σ_p is always higher than p, the debiased values are most often null and they are not shown by lack of meaning.

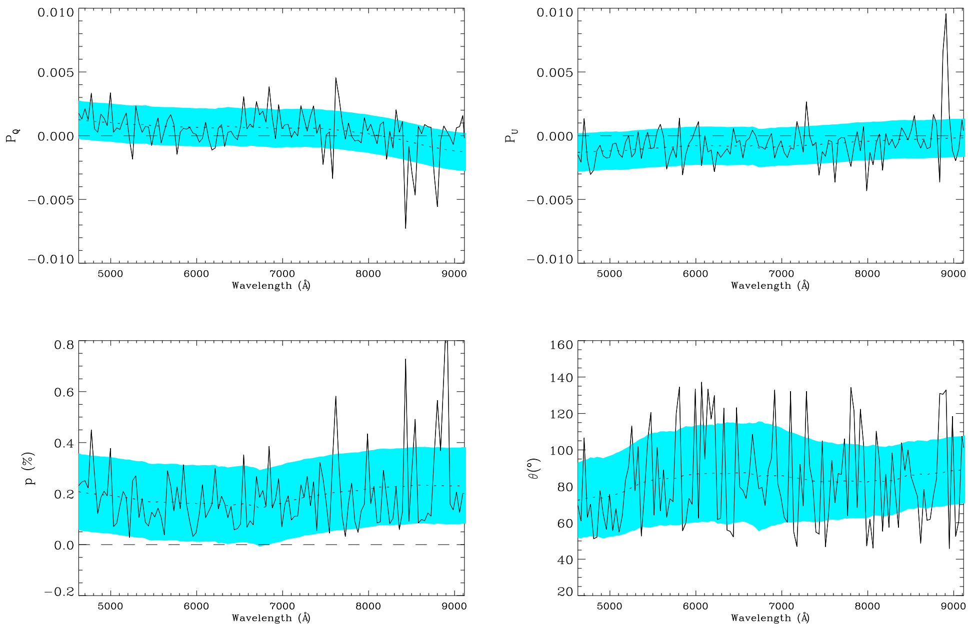

Figure 5.15: From right to left and from top to bottom: mean P_Q, mean P_U, mean polarization degree and mean polarization position angle. The blue regions represent the estimated error for each parameter.

5.13.1 High spectral resolution

Exactly the same procedure used for the 300V grism is followed for the analysis of the data taken with 1200R. Since this is a narrower grism, the SN ratio is lower and consequently the errors are higher. In Fig 5.16 all ordinary and extraordinary spectra for the same eight positions of the waveplate are represented. P_Q and P_U for each two pairs of exposures are shown in Fig. 5.17, while the corresponding mean values and the derived p and PPA are plotted in Fig. 5.18. Although errors are large, we conclude that the four polarimetric parameters are consistent with being constant with wavelength and, in broad agreement with the results obtained with the R filter in IPOL mode, $p \sim 0.2\%$, $\theta \sim 90°$ and $p_{corr_{ISM}} \sim 0.35\%$. The debiased p is also zero in most bins and is not plotted because it would not provide any information.

5.13.2 Conclusions from the spectropolarimetric observations of ESO 362-G18

Despite the large errors in PMOS data, the results are consistent with the values obtained from imaging polarimetry with IPOL data. Both $p(\lambda)$ and $\theta(\lambda)$ are constant over the full wavelength range in both grisms. However, the high errors do not allow us to establish solid conclusion about small changes with wavelength.

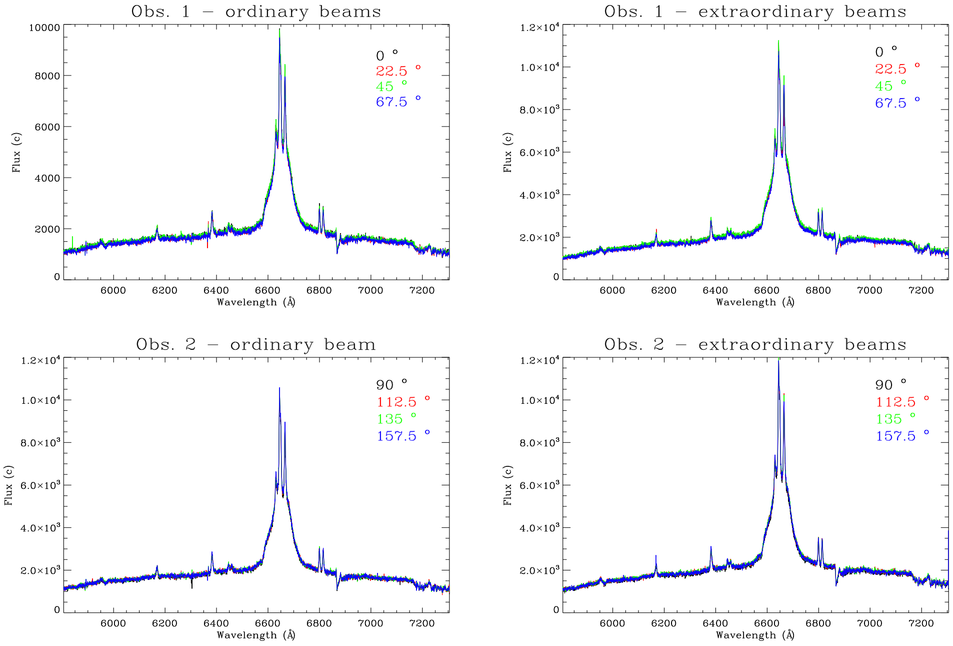

FIGURE 5.16: Ordinary and extraordinary spectra of high resolution around $H\alpha$.

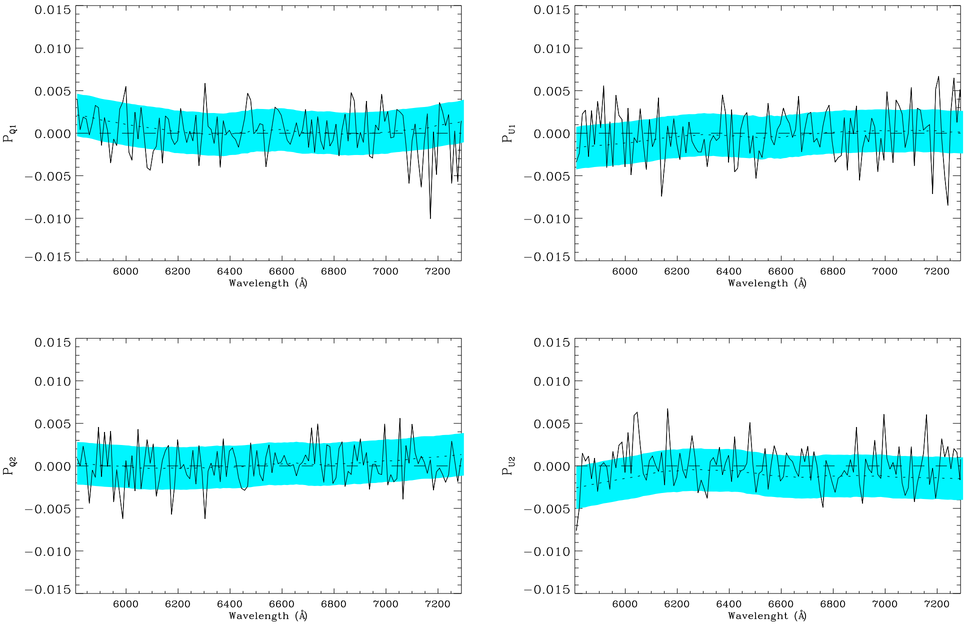

FIGURE 5.17: P_Q and P_U taken with grsim 1200R are shown in top panels for observation 1 and in bottom panels for observation 2. The blue regions represent the estimated error for each parameter.

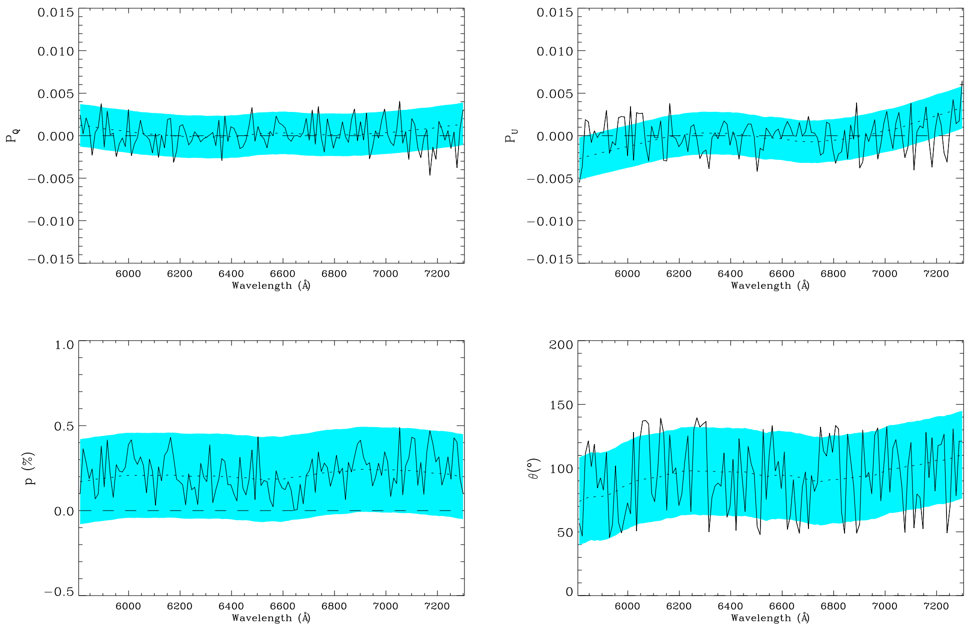

FIGURE 5.18: From right to left and from top to bottom: mean P_Q, mean P_U, mean polarization degree and mean polarization position angle around the $H\alpha$ line. The blue regions represent the estimated error for each parameter.

On the other hand, PMOS data reinforce the conclusion obtained for IPOL data that ESO 362-G18 exhibits a PPA perpendicular to the system axis, as it is expected for polar-scattered Sy1 galaxies. $p(\lambda)$ generally exhibits an increase towards the blue in polar-scattered Sy1 galaxies, however, the relatively large uncertainties in our derived quantities may mask any subtle trend of p with λ.

5.14 EFOSC1 data

As already mentioned, we have also retrieved spectropolarimetric data of ESO 362-G18 performed with EFOSC1@3.6m from the ESO archive. Particularly, two pairs of exposures in V band taken on 21^{th} September 2006 were available. As noted, ESO 362-G18 exhibits a typical type 1.9 optical spectrum at that epoch, with undetected broad H_β. It would therefore be of great interest to obtain information on the polarimetric properties of the source in that different optical state.

Several standard stars taken around the observation night were studied (Vela 1 95, HDE 316232, HD 94851 and Hiltner 652) in order to determine the instrumental offsets and polarization by comparing the measured values of PPA and p with the literature. The results provided by the standards were inconsistent since the offset between the measured PPA and the tabulated one was different for each star. Hence, we are not able to derive the variable offset that EFOSC1 imprint to P_Q and P_U and we cannot compute the PPA for ESO 362-G18. However, since offset rotations do not affect the degree of polarization we could still measure p for this additional observation.

5.14.1 Instrumentation: EFOSC1

The **E**SO **F**aint **O**bject **S**pectrograph and **C**amera (v.**1**) is a multi-mode instrument including normal/polarimetric imaging/spectroscopy (several submodes in each), multi-object spectroscopy and coronography. It was attached to the Cassegrain focus of the ESO-3.6m telescope (La Silla, Chile), but it was moved to the Nasmyht focus of the NTT in April 2008. Since EFOSC1 was permanently mounted at the Cassegrain focus (like FORS2 al the VLT) of thevESO-3.6m, the EFOSC1 instrumental polarization is expected to be comparable to that of FORS2. Moreover, EFOSC1 also performs polarimetry using a Wollaston prism as beam splitting analyser and a retarder waveplate in order to measure linear polarimetry.

Its wavelength range of operation is between 305 nm and 1100 nm and its FOV is $4.1'\times4.1'$. The size of its CCD is 2048×2048 pixel, the pixel size being $15m\mu \times 15m\mu$, or $0.12'' \times 0.12''$ on the sky.

5.14.2 Results from spectropolarimetric data of EFOSC2

For EFOSC1 there is no literature on instrumental polarization, although it is expected to be comparable to that of FORS2, i.e. $< 1\%$, since both instruments are mounted at the Cassegrain focus and perform polarimetry which analogous devices. Our purpose here will be to derive an estimation of the degree of polarization of ESO 362-G18 in its configuration of Sy1.9, which in principle is thought to be higher than in Sy1.5 configuration.

We computed P_Q and P_U following the same procedure than that detailed for FORS2 data, but without applying spurious polarization which will be expected to be, as noted, $< 1\%$. Then, detections of $p >> 1\%$ will imply a noticeable increase on the polarization degree of ESO 362-G18 with respect to its Sy1.5 state.

Our calculations found a mean p$\sim$ 3% for V grism. Although this is a rough estimate, with a factor higher than 2 comparing with p derived for FORS2 data, we can conclude that ESO 362-G18 exhibit a higher degree of polarization in its Sy1.9 configuration.

5.15 Summary and outcomes of this chapter

In this chapter we have analyzed the polarization properties of a changing look Seyfert galaxy for the first time. It is clear that this type of objects represent a powerful probe of the UM of AGN (and, most importantly, of its possible modifications) and polarimetry potentially adds important information which could allow us to have a clearer view of these objects. In the particular case of ESO 362-G18, the optical changes from type 1.5 to 1.9 Seyfert, as well as the occultation events observed in the X-rays and of the inclination angle derived from X-ray spectroscopy, place the source in the highly interesting region of intermediate objects, with a LOS of the order of 45° which is likely passing through the upper layers of the obscuring dusty torus. From a polarimetric point of view, this type of objects should be dominated by polar scattering, as even low extinction levels in the torus atmosphere can reduce the contribution of the equatorial scattering region.

The FORS2 data, however, measure low levels of polarization and it is difficult to say with any confidence whether the measured polarization is intrinsic to the AGN or induced by the ISM. By means of a detailed and careful analysis of IPOL data we have performed a rough estimation of the polarization induced by the ISM of our Galaxy. As already discussed, it is difficult to obtain accurate determinations since the light coming from our extragalactic source will always suffer more interaction with the ISM than the stars within the Galaxy. We estimate $p_{ISM_{V,R}} \sim 0.15\%$ and an expected maximum change on the PPA induced by the ISM paolrization of $\Delta\theta \sim 20°$ for both studied bands, V and R. At the same time, for ESO 362-G18 we derived $p \sim 0.2$ also for both bands. Nevertheless, applying the corresponding correction, $p_{ISM_{corr}}$ increases up to $\sim 0.35\%$, probably due to a depolarizing effect of the ISM which can take place if the intervening PPA, that of the AGN and that of the ISM, are perpendicular. No variation of polarization with λ is seen in the spectropolarimetric data, although the noise in our data could mask subtle changes across the broad emission lines.

On the other hand, even considering the maximum possible rotation induced by the ISM, ESO 362-G18 presents a PPA orthogonal to the system axis (considering the system axis as the [O III] PA given by Mulchaey et al. (1996a)). Besides, the ESO 362-G18 PPA is different from the PPA found for the field stars, which gives some confidence, that the measured polarization although weak is intrinsic to the source. Although the computed p for ESO 362-G18 is quite low for a polar-scattered object, a plausible explanation could be that the analysis of polar-scattered Seyfert galaxies carried out so far was most probably done by selecting objects significantly polarized, i.e. on the basis of their polarization properties, which may induce a bias.

Moreover, the extinction that we could measure towards the BLR from optical spectroscopy in the two observations where ESO 362-G18 is in its Sy1.5 state is consistent with that estimated by Smith et al. (2004) for polar scattered Sy1 galaxies ($A_V \sim 1 - 4$) reinforcing that classification.

Finally, from EFOSC1 date, we were able to perform a rough estimate of the degree of polarization of our changing look Seyfert galaxy in its Sy1.9 configuration. We tentatively detect a much higher p than in the Sy1.5 state which could possibly indicate that the low level of p in the latter state may be due to cancellation effects that are only present when the equatorial scattering region is also visible.

Chapter 6

Conclusions and Future Work

This dissertation is based on the detailed analysis of multi-epoch observations of the Seyfert galaxy ESO 362-G18 in the X-rays and UV using a number of different X-ray observatories (sometimes carrying optical/UV telescopes and detectors on board) and in the optical we made use of long slit spectroscopy at low and intermediate resolutions and also a detailed analysis in polarized light. As a whole, our observations span a very long temporal baseline, starting with a first optical observation on January 2003 from the 6dFGS and ending on March 2016 with the last spectropolarimetric observation. In between, 45 X-ray observations (from the X-ray observatories *XMM-Newton*, *Chandra*, *Suzaku*, and *Swift*) and two other optical data sets have been analyzed in this work. Although most data have been retrieved from the X-ray and optical archives, a number of observations were obtained by us (one long X-ray observation with the *XMM-Newton* X-ray observatory, five with the *Chandra* X-ray observatory, and one spectropolarimetric observation with the FORS2 instrument at the VLT).

6.1 Main results

The global X-ray data set can be divided into two main blocks. The first comprises individual pointed observations obtained with *Swift* (1 observation), *XMM-Newton* (2 observations), *Suzaku* (1 observation), and *Chandra* (5 observations) that allow us to probe the X-ray global properties of the source and its X-ray flux and spectral variability on timescales of months to years (as well as, thanks to a long and continuous *XMM-Newton* observation, timescales of minutes to hours). The second block, comprising 36 *Swift* observations covering about 2 months, enables us to probe timescales ranging from days to weeks.

From the analysis of the highest quality available X-ray observations (a long *XMM-Newton* and a *Suzaku* observation) that are associated with unabsorbed or only mildly absorbed states, we are able to decompose the complex X-ray spectrum of ESO 362-G18 into its different components. Here we mention only the most important ones. Besides the standard X-ray power law like continuum, we detect a narrow Fe Kα emission line (that is ubiquitous in the X-ray spectra of AGN) due to X-ray reflection from distant material such as, for example, the illuminated and visible face of the obscuring torus. The spectral shape of the source, however, is characterized by three additional features: a soft excess (i.e. an excess of X-ray emission below $\sim$ 1keV with respect to the extrapolation of the power law continuum), a broad feature around the energy of the Fe Kα line, and a hard X-ray excess around 20-30 keV. The first two features are detected in both the *XMM-Newton* and *Suzaku* data, while the third one can only be seen in the *Suzaku* spectrum, as *XMM-Newton* is not sensitive above $\sim$ 10 keV. All three features are extremely well reproduced when a X-ray reflection component off the inner accretion disc is included in our spectral model. The rest-frame reflection spectrum is characterized by a series of fluorescent emission lines both in the soft X-rays and at Fe K energies, but the spectral distortions caused by relativistic effects close to the black hole produce a smooth spectral shape that fits the data extremely well. The disc reflection features can then be used to infer some of the most relevant properties of the black hole and inner accretion disc. We measure a black hole spin $a \geqslant 0.92$ at the 99.99% (statistical) confidence level, which implies that the super massive black hole powering ESO 362-G18 is a nearly maximally rotating Kerr black hole.. The disc-reflection emissivity profile is steep, with $q = 4.3^{+0.8}_{-0.6}$, suggesting that the primary source of X-rays (the so called X-ray corona) is compact and centrally concentrated. On the other hand, the inclination between the disc axis and our LOS is measured to be $53° \pm 5°$ via disc reflection modeling of the X-ray spectra. Such high inclination is further supported by different estimates based on virial assumptions as well as on the relationship between black hole mass and stellar velocity dispersion of the super massive black hole mass which become all consistent with each other only for inclinations $\geq 43°$, providing independent support for the disc reflection interpretation of the spectral features seen in the X-ray spectrum. An unavoidable consequence of disc reflection is that this reprocessed component should exhibit a time delay with respect to the primary continuum which may be used to infer the light-crossing distance between the primary X-rays emitting site (the X-ray corona) and the reprocessing site (the inner disc). By analyzing the energy-selected intra-band variability on different timescale during the continuous *XMM-Newton* observation we are able to detect a time lag of the order of 650 s between the energy band dominated by the continuum and that dominated by reflection. Considering dilution effects (as in reality both bands have contributions from both components), we infer an intrinsic lag of $\sim$ 1600 s which implies that the reprocessing site is located at distances of the order of few gravitational radii from the X-ray continuum source (the corona). This strongly supports our interpretation in terms of delayed relativistic reflection off the inner accretion disc in ESO 362-G18 and confirms beautifully and independently (no spectral modeling is performed to derived the time delays) that relativistic reflection is present in this active nucleus.

Moreover, the relatively high inclination we derive is consistent with the idea that our LOS is grazing the obscuring torus (which has a typical half-opening angle of the order of 45° or so). If the torus is not homogeneous but clumpy (as spectral modeling of AGN in the infrared is starting to show), such high inclination may intercept from time to time some of the clumps of the obscuring torus (or of its atmosphere, or upper layers) possibly explaining why ESO 362-G18 exhibits changes of look from type 1 to type 2 in its optical spectra taken only 1 year and 8 months apart, as mentioned above.

In fact, a subsequent *XMM-Newton* observation caught the source in a much more heavliy absorbed state consistent with full coverage of an extra neutral column density of $3-4\times 10^{23}$ cm^{-2} with respect to a basically unabsorbed observation performed with *Swift* just two months before. By analyzing in detail this absorption event in the X-rays also making use of the simultaneous optical/UV photometric data of the two optical monitors on board *XMM-Newton* and *Swift*, we were able to infer that the absorbed observation is affected by a transient occultation event produced by a cloud of the dusty torus. Moreover, such analysis allowed us to estimate the size of the X-ray emitting region, confirming that X-rays come from within about 50 gravitational radii from the black hole, thus supporting the compact nature of the X-ray emission in AGN. Such result holds not only for the primary X-ray continuum emitting region, but also for the soft excess, demonstrating that this component is also associated with a compact emitting region and supporting our interpretation in terms of relativistic reflection off the inner accretion disc.

Such occultation event was not isolated, and the *Swift* monitoring campaign over 2 months, comprising 36 pointed observations, caught another occultation events. In this case, we were able to follow the occultation almost completely from ingress to egress. This allowed us to infer with good accuracy all the relevant properties of both the X-ray emitting regions (that resulted to be slightly more compact than the upper limit of 50 gravitational radii derived above) and of the cloud responsible for the eclipse confirming the dynamic and clumpy nature of the X-ray absorbers towards ESO 362-G18.

Our analysis of ESO 362-G18 also includes four low-resolution long slit optical spectra which show the source exhibiting broad Balmer lines in two of the four observations, while these broad lines disappear in the two remaining spectra leading to a changing look classification for the source (between Sy1.5 and Sy1.9) as anticipated above. In detail, ESO 362–G18 is detected as a Sy1.9 in January 2003, then as a Sy1.5 in September 2004, again as a Sy1.9 two years later, and finally, as a Sy1.5 in our last observation performed in March 2016. The minimum observed timescale for a change of look is therefore 1 year and 8 months. We do not see any evidence for dramatic changes in the nuclear activity (this is also demonstrated by the stability of the X-ray intrinsic luminosity over few years), so that the most natural explanation for the change of look is that intervening dusty absorbing structures are present into our LOS towards the BLR at the epochs when the source exhibits a Sy1.9 optical spectrum. As the BLR is much more extended than the X-ray emittin region, it is unlikely that we are observing exactly the same intervening structures in the optical and X-rays. As demonstrated by the full eclipse monitored with *Swift*, the cloud size affecting the X-rays is of the order of 3×10^{14} cm (about 50 gravitational radii), likely too small to significantly affect the BLR. On the other hand, the very fact that broad Hα emission is detected in the optical even at epochs affected by absorption means that we are likely dealing with a structure that absorbs most but not all the BLR flux, i.e. an extended (but not too extended) dusty cloud or clump. Extinction variability towards the BLR is detected when comparing the two optical spectra during Sy1.5 states, pointing (as expected) towards two different absorbing structures in 2003 and 2006 with an equivalent change in column density of the order of $\sim 2 \times 10^{21}$ cm^{-2}.

No polarimetric observations of changing look nuclei have been performed to date, despite the obvious potential of this kind of measurements in the context of understanding the circumnuclear geometry and gas/dust distribution. We have then proposed (and obtained) an imaging and spectropolarimetric observation of ESO 362-G18 with the FORS2 at the VLT. Unfortunately, in FORS2 data ESO 362-G18 does not seem to exhibit highly significant intrinsic polarization despite its previously studied properties pointed to wards to a polar-scattered classification. However, ESO 362-G18 shows other properties characteristic of polar-scattered Seyerts, like a PPA orthogonal to the system axis and an estimated $A_V \sim 1.8$ towards the BLR when in a Sy1.5 state, an A_V that is sufficient to block the polarized light from the equatorial scattering region while preserving the broad optical emission lines, as expected in sources where the LOS is passing through the upper layers of the circumnuclear torus. This can suggest that ESO 362-G18 presents, in reality, a ‘inefficient” polar-scattered Sy1, with a polar-scattering region not well orientated, badly placed or simply not efficient, as it is the case in many Seyfert 2 galaxies observed in polarized light and that do not exhibit any polarized broad emission component. On the other hand, we also carried out an estimate of the polarization degree during one of the Sy1.9 states of ESO 362-G18, and we measured a clear increase with respect to the Sy1.5 case, possibly indicating that the only marginal detection of polarization during Sy1.5 states is due to cancellation effects when more than one scattering region is contributing.

In the appendix attached to this thesis, we present what can be considered as work-in-progress. We have explored in detail the capabilities of the robust mathematical tool of PCA, which provide us with a model-independent way to assess spectral components in the AGN X-ray spectrum. We highlight that this technique can be used to study not only the X-ray spectral variability in general, but also its crucial flux-dependence as well as its sensitivity to subtle absorption events. The mathematical and numerical tools developed here will be used routinely in future data analysis of X-ray data from AGN complementing the information that can be obtained from more traditional spectroscopic and timing analysis.

6.2 Future Work

Apart from the work included and described in this thesis, we have been also involved in other side projects related to the main topic of this dissertation. In the following, we briefly point out some highlights concerning this future work :

- **True 2 Seyfert galaxies**
  We are interested to analyze the paradigm of the true Sy2 galaxies in polarized light. In particular, we will try to assess a detectability limit on the HBLRs, which is essential in the definition of true Sy2 galaxies. Often the hidden broad lines are present but are difficult to detect.
- **Changing-look quasars**
  As already noted, the degree of polarization can provide information about the configuration of a changing look AGN. We will exploit the potential of the polarized light to further study the properties of this special AGN type.
- **X-ray polarization**
  If the optical polarization can provide us with valuable information about the unresolved scatters far from the SMBH, X-ray polarimetry will allow a completely new view of the X-ray scatterers like the accretion disc and the inner regions of the torus.

List of Publications

In the course of this thesis, I have participated in 5 refereed articles so far, one of them as first author. The list of publications is presented below in inverse chronological order of publication. Currently, I have one more paper in preparation (as first author and not listed below). My contributions to scientific conferences are also listed below.

Refereed publications

[1] **“Black hole spin and size of the X-ray emitting region(s) in the Seyfert 1.5 galaxy ESO 362-G18”**
Agís-González B., Miniutti G., Kara, E., Fabian A. C., Sanfrutos M., Risaliti G., Bianchi S., Strotjohann, N. L., Saxton R. D & Parker M. L., 2014, MNRAS, 443, 2862.

[2] **“Eclipsing the innermost accretion disc regions in AGN”**
Sanfrutos M., Miniutti G., Dovciak M., & Agís-González B., 2016, AN, 337, 546.

[3] **“X–ray outflowing torus in ESO 323-G77: low–ionization clumps confined by homogeneous warm absorbers”**
Sanfrutos M., Miniutti G., Krongold Y. & Agís-González B. & Longinotti A. L, 2015, MNRAS, 457, 510.

[4] **“The properties of the clumpy torus and BLR in the polar-scattered Seyfert 1 galaxy ESO 323-G77 through X-ray absorption variability”**
Miniutti G., Sanfrutos M., Beuchert T., Agís-González B., Longinotti A. L., Piconcelli E., Krongold Y., Guainazzi M., Bianchi S., Matt G. & Jiménez-Bailón, E., 2014, MNRAS, 437,1776.

[5] **“The size of the X-ray emitting region in SWIFT J2127.4+5654 via a broad line region cloud X-ray eclipse”**
Sanfrutos M., Miniutti G., Agís-González B., Fabian A. C., Miller J. M., Panessa F. & Zoghbi, A., 2013, MNRAS, 436, 1588.

[6] **“The Dust Environment of Main-Belt Comet P/2010 R2 (La Sagra)”**
Moreno F., Lara L. M, Licandro J., Ortiz J. L., de León J., Alí-Lagoa, V. , Agís-González B. & Molina A., 2011, ApJ, 738,16.

Appendix A

Probing X-ray spectral variability in AGN throughout principal component analysis (PCA)

This appendix comprises the work initiated during a 3-months stay at the "Osservatorio Astrofisico di Arcetri" in collaboration with the research group led by Dr. Guido Risaliti. The main goal of this study is to analyze the X-ray spectral variability of AGN in the most model-independent way as possible, using the mathematical tool known as PCA. We will describe briefly its functioning, why it is useful and how to interpret the results. Subsequently, we will apply this technique on data retrieved from the *XMM-Newton* archive of the Sy1 galaxy NGC 4051, known to perform rapid X-ray variability (Vaughan et al., 2011).

A.1 Introduction

As widely discussed along this dissertation, AGN can show extreme variability in X-ray wavelengths at timescales as short as the light travel time over a few gravitational radii, which ranges from days to minutes, depending on the black hole mass. As also already noted on Section 1.7.2, AGNs show a complex X-ray spectrum which is normally interepreted as a combination of a large variety of spectral components produced by very different physical processes. As a result, AGN X-ray spectra can be very complex, with multiple different models providing acceptable fits to the same data, meaning that spectral fitting alone often cannot discern between alternative physical models. PCA is a powerful tool for distinguishing different patterns of variability in AGN (Mittaz et al., 1990). It reduces the dimensionality of the data without loosing information and yields the directions that maximize the variance of the data. It works transforming a data set where variables correlate with each other into a new coordinate system, defined by a smaller

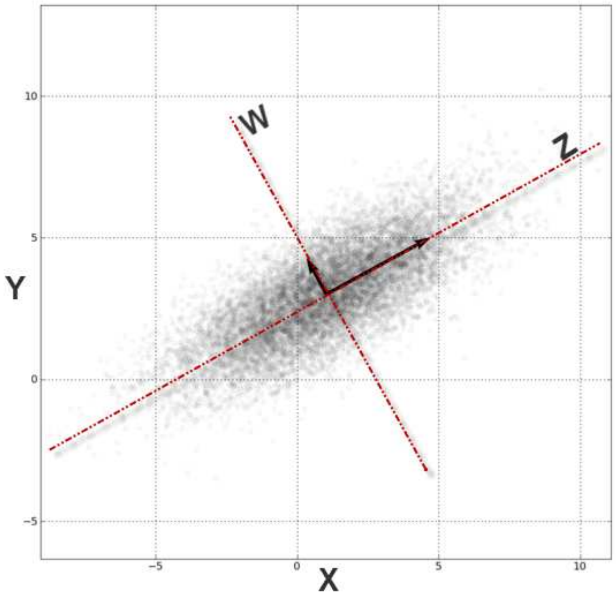

FIGURE A.1: Schematic representation of the coordinate rotation implicit to the PCA technique. *Z* lies in the direction of the most variance in the dataset, i.e. it represents the first principal component, while the second principal component *W* is perpendicular to the former one and its direction is along the next largest variance. For the sake of clarity, only two coordinates are plotted, then the reduction of dimensionality is not represented. *Image credit:* http://strata.uga.edu/6370/lecturenotes/principalComponents.html

number of uncorrelated variables called *principal components* or *eigenvectors*. In other words, it consists in a coordinate rotation so that one axis in the rotated system lies in the direction for which the distribution has the largest variance (Malzac et al., 2006). This functioning is shown in Fig. A.1, where for simplicity of vision there are only two initial variables, so the reduction of the dimensionality is not represented. The two resulting principal components (PCs) make a new set of axis where *Z* lies along the maximal direction of variability. This direction is known as the *first principal component* and accounts for most of the variance in the data . The *second principal component* is orthogonal to the first one and is the axis along which the distribution has the next largest variance, the same would be valid for a third component and so on. In this way, the variability is summed up in as few principal components as possible. These few "relevant" principal components can be linearly combined to reconstruct the initial data set. If the spectrum is made up of a linear sum of variable, uncorrelated, and spectrally distinct physical components, then with enough data quality, PCA will reproduce an exact description of those components. Hence, the undeniable advantage is that this technique provide us with detailed spectra of each variable component in a model independent way (Parker et al., 2015).

This powerful technique has already been used for the analysis of X-ray binary variability (Malzac et al., 2006, Koljonen et al., 2013b, Koljonen, 2015) . PCA has been also performed understand AGN spectral variability (e.g. (Vaughan & Fabian, 2004, Miller et al., 2007)), but in most cases with only one component confidently identified. More recently, Parker et al. (2015, 2014b, 2015) have demonstrated that, given a dataset with high-enough quality on relevant timescales of the order of 10 ks, the PCA can isolate several several spectral components. These authors carried out a systematic analysis of variable AGNs, using PCA to determine patterns of variability and relate them to the physical processes in AGN.

NGC 4051 is probed to be an exceptionally good candidate for this technique to be applied due its high-amplitude and fast flux and spectral X-ray variability (e.g. Vaughan et al. (2011)). NGC 4051 is among the sources systematically analyzed by Parker et al. (2015) in a time-slicing of 10 ks. These authors analyze a global data set comprising 14 individual observations of this target (of about $\sim$ 40 ks per observation). We will go further and study another observation of NGC 4051 dated in May of 2001 with $\sim$ 120 ks of *XMM-Newton* data in order to investigate the usefulness of the PCA at timescales as short as 1ks.

A.2 The procedure

We developed a PYTHON procedure to apply the PCA on any possible chosen timescales, following the methods discussed in Parker et al. (2014a), i.e:

(*i*) We divide the observation(s) in spectra at the intended timescale and the data are arranged into a matrix $n \times m$ (Matrix M), where n is the number of energy bins for each spectra and m is the number of spectra.

(*ii*) Deviations from the mean for the whole set of spectra are computed.

(*iii*) We then apply the Singular Value Decomposition (SVD) (Press et al., 1986, Mittaz et al., 1990, Miller et al., 2007), a method which decomposes the arranged matrix into orthogonal eigenvectors in order to find the set of principal components factorizing the matrix $M = UAV^*$ (see Parker et al. (2014a)), where * refers to the corresponding conjugate transpose matrix. This factorization does not require a unique solution, which implies that it is not necessary to have more spectra than energy bins in the analysis, which is analogous to having more unknowns than equations. Hence, the full instrumental resolution can be preserved and also the number of bins (logarithmically space) can be changed in order to optimize the signal to noise ratio (SNR) of the resulting components.

Then, in order to carry out the PCA we must first divide the data into time-sliced spectra binned in energy and also regularize the SNR versus the spectral resolution . The energy bins cannot be infinitesimally small because otherwise shot noise would dominate over intrinsic sources variations.

The rows of U and the columns of V coincide with the orthogonal eigenvectors of the matrices and M^*M, and the diagonal elements of A are the corresponding eigenvalues. In this context, where M is a matrix of spectra, the eigenvectors give each variable spectral component, and the square root of each eigenvalue gives the variability of their corresponding component (Parker et al., 2014a). The fractional variability of each component is computed by dividing each eigenvalue by the sum of all eigenvalues. When the fractional variability is plotted in a logarithmical scale, which is known as log-eigenvalue (LEV) diagram, the components due to noise are predicted to decay geometrically, so deviations from a geometrically progression will be the variant principal components. Thus, the initial matrix M can be reconstructed taking into account the variable principal components while the "noisy" components can be neglected for further analysis. Each component show the strength of the correlation between energy bins, thus any coherent component is extremely unlikely to be produced by random noise which is independent of bins. Therefore a flat (positive or negative, since the sign of the y-axis is arbitrary) component shows that all bins vary equally. On the contrary, a component that changes its sign along the spectral range will represents a pivoting effect. The first component is by convention defined to be positive.

A.3 A example of how PCA works

A simple and illustrative example of this functioning is performed by Parker et al. (2015) (see Fig. A.2). These authors add together three synthetic sinusoidal functions ($y_1(x) = 0.3 + \frac{x}{8}$, $y_2(x) = \sin(x)$ and $y_3(x) = \sin(2x)$) along with random noise (left panel in Fig. A.2) in order to create 50 new functions (middle panel i) according to $y(xi) = 0.6a_1y_1(x_i) + 0.2a_2y_2(xi) + 0.1a_3y_3(xi) + 0.1a_4$ with a_i and $x_i$being random values between ±0.5 and x_i and $[0,6\pi]$. The functions recovered by the PCA are shown in the right panel of the same figure, while the corresponding LEV diagram is displayed in Fig. A.3 which probes that exactly three components are significant, with 47% of the variability falling in the first component, 7% in the second and 3% in the third.

A.4 Need of simulations

The advantage of PCA is that it produces detailed spectra of each variable component in a model independent way. On the contrary, calculating the RMS spectra can show the total variability as a function of energy, but cannot be used to determine how many variable components of the initial

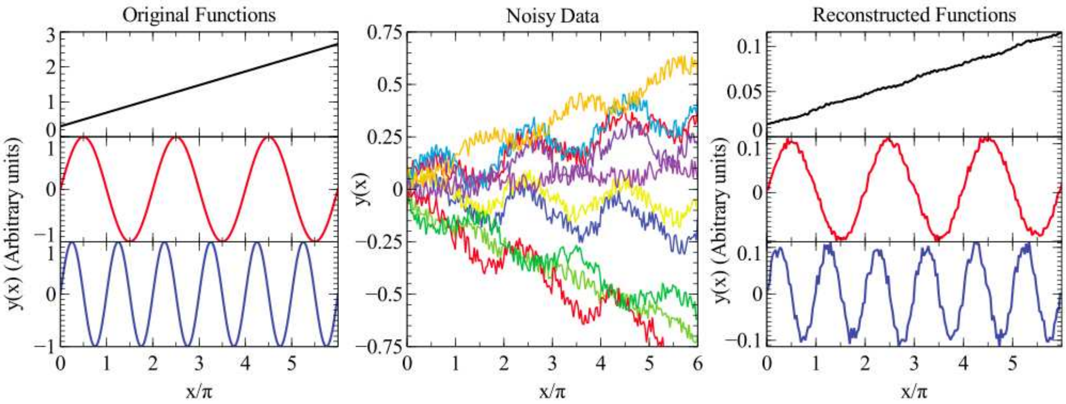

Figure A.2: On the left panel are represented three synthetic function which are added together along random noise in order to created the 50 functions displayed in the middle panel. The three initial functions are retrieved by PCA in the right panel. *Image credit:* this example was performed by Parker et al. (2015)

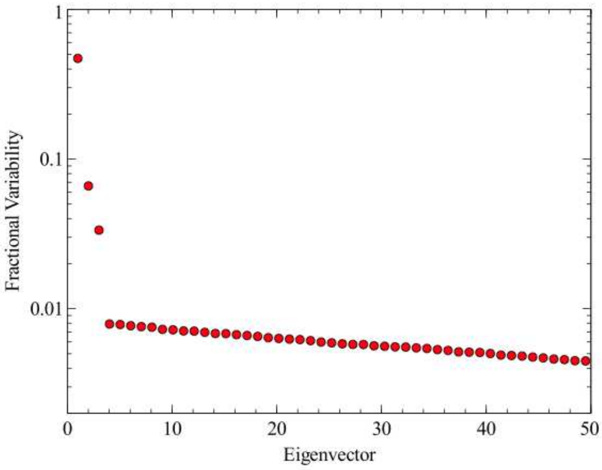

Figure A.3: LEV diagram corresponding to the example shown in Fig A.2. *Image credit:* Parker et al. (2015)

spectrum contribute to the variability or to isolate contributions from different mechanisms. However there exists a small disadvantage: the interpretation of these variable components is not always immediate. They do not have to correspond to physical components, since there is no requirement for the true physical components to vary independently. Thus, a same PC can be generated by more that one parameter or physical process varying.

To solve this inconvenience and keep the independence from the models one has to turn to numerical simulations. This technique was introduced by Koljonen et al. (2013b) and it is based on the idea of creating simulated variable spectra based on physical models that are allowed to vary within ranges of given parameters. Then, the PCA is applied to these simulated spectra of models and produces the corresponding PCs. From these PCs, patterns from each spectral

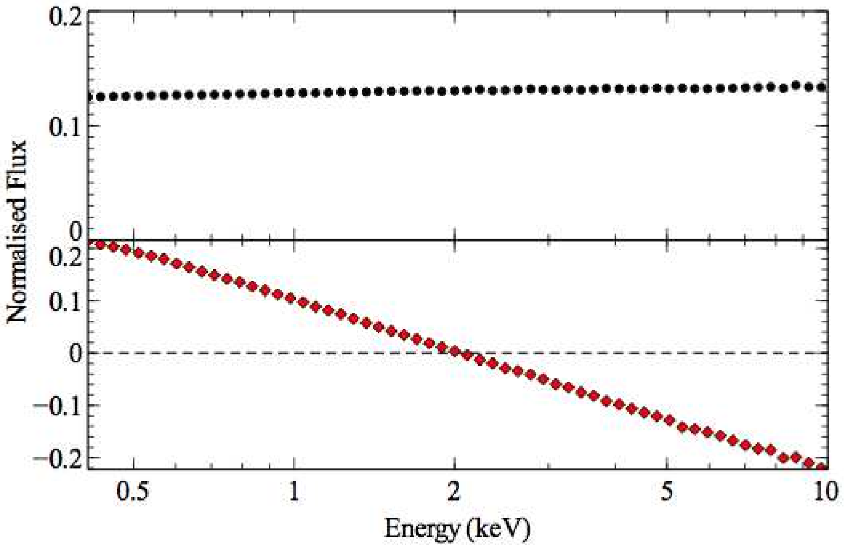

FIGURE A.4: Simulated PCs computed by using PCA on a spectra of a power law which varies both in normalization and photon index. Here the effect on both parameters can be easily disentangled. The first component (top, black) reveals to changes in normalization whereas the second component (bottom, red) represents the pivoting changes of the power law due the variation of the photon index. *Image credit:* Parker et al. (2015)

model can be determined. Then, they can be matched to the PCs found from the real data for each source.

In order to perform simulations we used the XSPEC command “FAKEIT”. The resulting fake spectra was processed by PCA so that the corresponding fake PCs could be computed. The flux of the models was always exaggerated in order to get more prominent features in the PCs as what really matters is the relative flux between the different physical models and their variability amplitude and typical timescale, rather than the total flux.

Simulations becoming important to understand the analysis of this particular work are outlined below. Parker et al. (2015) also performed simulations in order to create a “catalog” of fake PCs so that the real PCs can be rapidly disentangled. These authors initially consider the baseline AGN model: a variable power law, and then investigate the effect of additional spectral components. Here we review some of their work which we have been able to reproduce within the framework of our numerical simulations and PCs reconstruction.

- **Baseline model: power law varying photon index and normalization**

  A simulation of a simple variable power law produces the PCs shown in Fig. A.4. They are completely straight, without features of any kind, although there is a slight increase with energy in the primary component, due to a correlation between flux and photon index

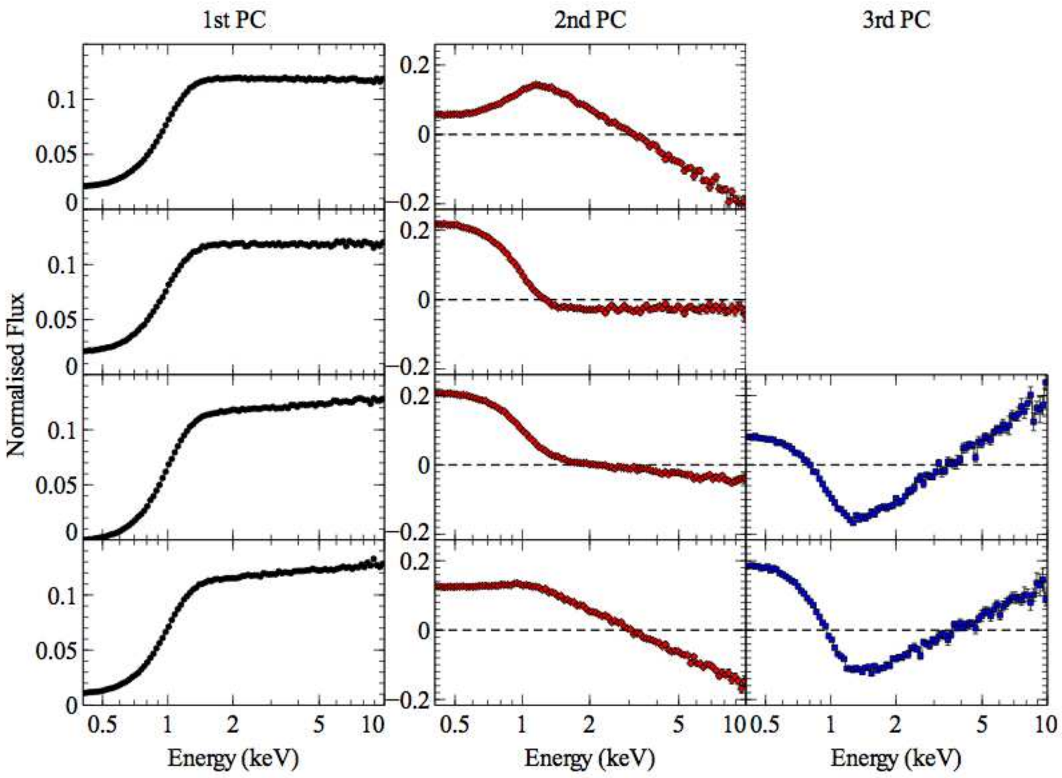

Figure A.5: Simulated PCs computed by using PCA on spectra comprising a power law and a black body modeling the soft excess. *Top row:* Constant black body plus a variable power law. *Second row:* both power law and black body varying their normalizations. *Third row:* power law varying both photon index and normalization and black body varying only its normalization but with stronger changes than that of the power law. *Bottom row:* The same conditions than in third row, but this time the power law exhibits stronger changes of normalization. *Image credit:* Parker et al. (2015)

in the model. The photon index is allowed to vary between 1.9 and 2.1 randomly, and the normalization is allow to change up to a factor of 2.

- **Variable power law + black body modeling the soft excess**

  The next natural step is to investigate a soft excess component. To this end, Parker et al. (2015) consider a black body for simplicity, however the resulting PCs will be equivalent to those that would be produced by any other models accounting for the soft excess in terms of an additional component that only contributes at low energies (e.g. Comptonization and bremsstrahlung models). Fig A.5 shows the resulting PCs for different scenarios.

  In the top row, a variable power law plus a constant black body is considered. The effect of this constant component is to suppress the variability seen in the variable components of Fig A.4, pushing the bins where the blackbody dominates towards zero. In the second row, the power law photon index is fixed, and the blackbody is allowed to vary its normalization. This produces a different second component with the same shape as the

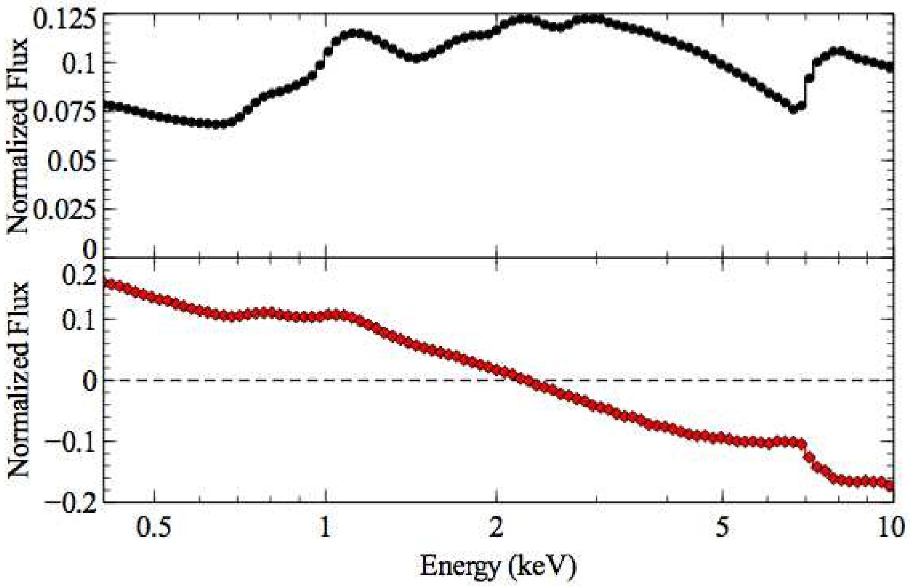

FIGURE A.6: *Image credit:* Parker et al. (2015)

blackbody at low energies and negative but close to zero at high energies. The negative values arise from the orthogonality constraint of PCA (the dot-product of any two PCs has to be zero). In practice, this means that if the primary component is entirely positive, approximately 50% of the energy bins of all subsequent PCs must be below zero.

Allowing also the photon index to vary weakly produces the PCs shown in third row. The first two components keep almost the same (both component slightly increase their slopes at high energies) but a third component arises. This thrid PC seems to act as a correction factor to the second component, which no longer describes all of the pivoting itself. This assumption is probed in the bottom row where the photon index varies strongly. This does not change the third component but affects the second one. Hence, the third component is not a direct match to a single physical component. As already noticed, this is a inherent weakness of the PCA: if two physical components have a similar effect on the spectrum, then they will not be expressed as two separate PCs, there will be one PC describing the average effect, and another one describing the differences between them. In this model, the increase of flux in the blackbody and the increase of photon index produce a steeper spectrum which is imprinted on the second component (see Parker et al. (2015) for details).

- **Relativistic reflection component**

  Another main feature in the X-ray spectrum of the AGN is the relativistic reflection from the inner accretion disc. Fig A.6 shows the PCs from a model comprising a variable power law and a constant reflection component. The first PC (top panel) can be thought

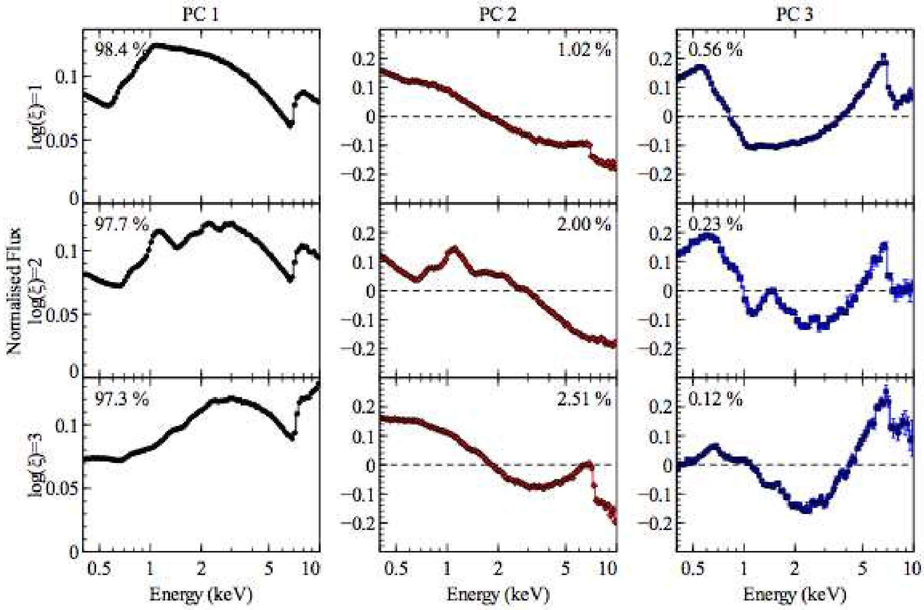

Figure A.7: Simulated PCs computed by using PCA on spectra comprising a power law and a relativistic reflection component, where the power-law flus is allowed to vary by a factor 4 and the reflected flux by a factor 1.5. In each row it is represented the PCs for a different ionization parameter and the fractional variability attributed to each component is labeled in each plot. *Image credit:* Parker et al. (2015)

of as a flat line with the reflection component subtracted, representing the suppression of variability at energies where the relativistic reflection make a substantial contribution to the total flux. The same interpretation can be given for the second PC, although starting from a diagonal flat line.

Allowing the relativistic reflection component to vary, but eith lower amplitude than the power law, produces a third component as shown in Fig A.7. The first two PCs are equivalent to those shown in Fig. A.6. In this case, the third component appears to represents all the reflection and displays the correlated soft excess and broad iron line typical of relativistic reflection.

A.5 Previous results for NGC 4051 applying PCA

NGC 4051 is classified in the literature as a narrow line Seyfert 1 (NLS1) extremely variable on all timescales. Ponti et al. (2006) found that the variable spectrum to be well-described by a power law plus relativistic reflection model. Alston et al. (2013a) also detected strongly flux-dependent time lags, what suggests models involving intrinsic variability and relativistic reflection over reprocessing by distant material.

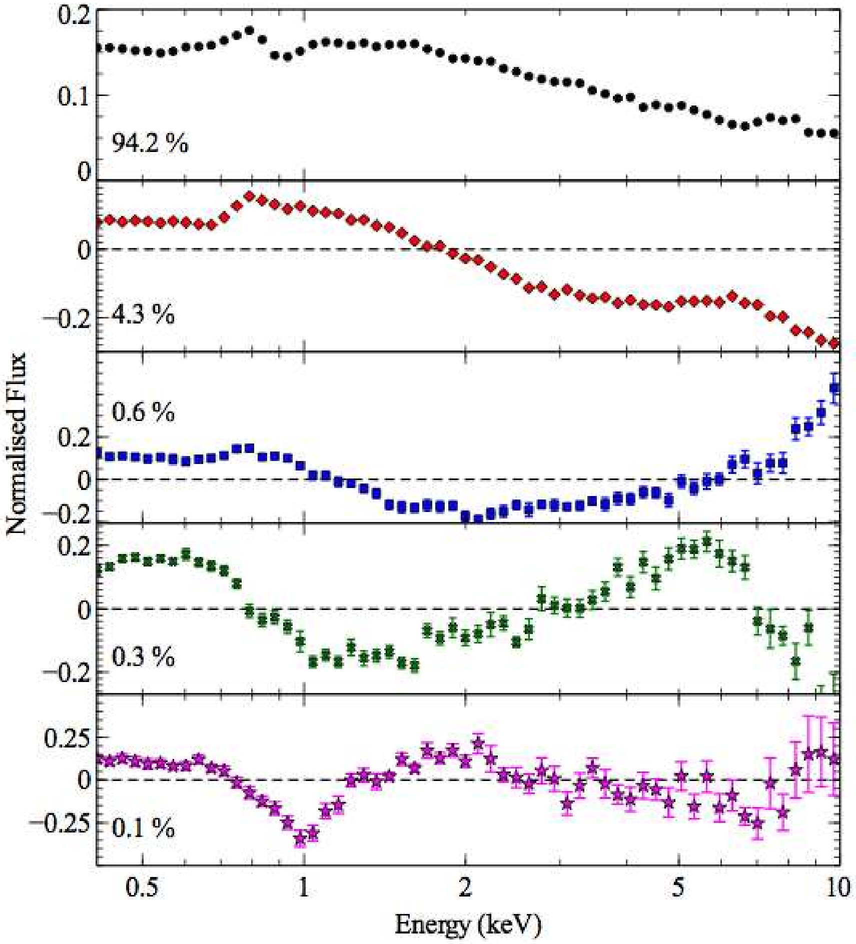

FIGURE A.8: Principal components computed by Parker et al. (2015) for $14 \times 40ks$ observations of NGC 4051. *Image credit:* Parker et al. (2015)

(Parker et al., 2015) carried out a general classification of 26 AGN matching the patterns shown by their PCs with those derived from model simulations. 14 *XMM-Newton* observations retrieved from archive of ∼ 40 ks each one, one of them from November of 2002 and the remaining from May and June of 2009 were added by these authors in order to computed the corresponding PCs. Their results, performed with a time binning of 10 ks, are shown in Fig. A.8 and reveals five PCs. Comparing with the simulated PCs shown in the former section, the first and second components can be interpreted as a power law varying in photon index and normalization, where the suppression of variability at energies of the soft excess and iron line indicates the presence of a strong relatively constant spectral component at these energies. The third and fourth PCs match with variations from relativistic reflection. The fifth PC appears to be an absorption edge at 1 KeV with no other strong features visible in the spectrum.

A partially covered power law can reproduce the spectrum of this source, but not the spectral shape of the observed PCs. Fig. A.9 shows the simulated PCs for a variable power law

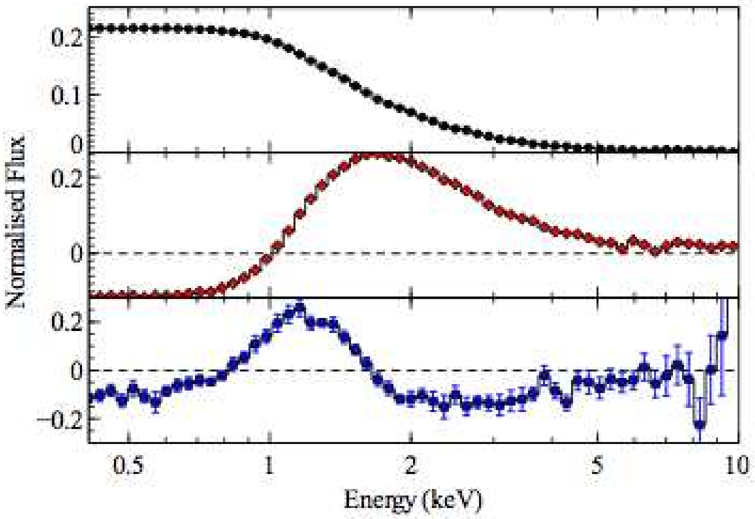

Figure A.9: Simulated principal components for a variable power law convolved with neutral partial covering absorption model. The column density and covering fraction of the absorber vary. The first PC correlates well with the covering fraction, however, the other two components do not correspond directly to a single parameter and represent changes in the column density at different covering fractions. *Image credit:* Parker et al. (2015)

convolved with neutral partial covering absorption model. Hence, the PCs of NGC 4051 do not accept partial covering absorption and PCA rejects the absorption interpretation.

A.6 Another observation

We retrieved from *XMM-Newton* archive another observation of NGC 4051 which was not analyzed by Parker et al. (2015). This data has ~ 120 ks of exposure time and the observation was performed in November 2001. We sliced the spectrum source in small spectra of 10 ks and, in order to maximize the spectral information, we adapt the energy bin size so that the lower flux spectrum has at least 25 counts at high energies. Errors on the resulting PCs are obtained by the Monte-Carlo method, in which the observed photon counts binned in energy and time are perturbed by a random amount proportional to Poisson photon noise following a normal distribution. Then we use PCA on the perturbed data set. This process is repeated 50 times. The computed PCs for this 'new' observation are displayed in Fig. A.10. They are equivalent to those found by Parker et al. (2016). Due to the minor amount of data (~ 120 ks vs. 560 ks) the fourth and fifth PCs are lost while the first three are softened. This corroborates the relativistic reflection interpretation given by (Ponti et al., 2006) and Parker et al. (2015) of NGC 4051 for this 120 ks *XMM-newton* observation performing PCA with a time binning of 10 ks.

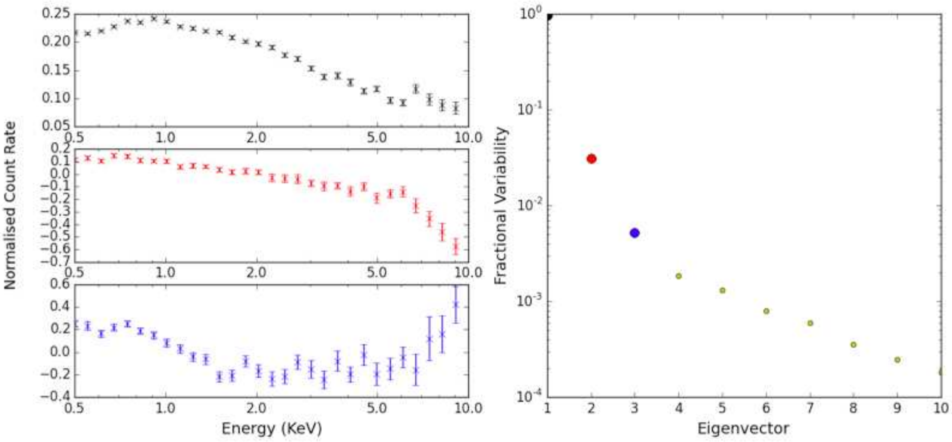

FIGURE A.10: Computed PCs for the 120 ks *XMM-newton* observation of NGC 4015.

As NGC 4051 is known to vary on timescales s as short as 100 s, we have also applied the same technique to spectra extracted in shorter time bins than 10 ks. We tried several different time bins between 10 ks and 1 ks, shorter time bins were not possible to keep at least 25 counts per energy bin. However we found that the obtained PCs were always consistent with those derived with a time-slicing of 10ks.

A.7 Discussion

On the other hand the data set analyzed by Parker et al. (2015) obviously comprises observations in very different flux levels, but results will obviously be dominated by the higher fluxes with little contribution from the low flux observations. At this point, we decided to investigate other possible capabilities of this robust mathematical tool and investigated the resulting PCs of individual observations of NGC 4051 analyzed by Parker et al. (2015). In figure A.11 we show the PCs with a time bin of 10 ks for the highest-flux observation analyzed by Parker et al. (2015). The second and third PCs are dominated by noise due to the short exposure which is 40 ks, then only the first component is reliable. We reproduced this PC with a simulation of a variable power law convolved with a constant relativistic reflection model.

We also applied PCA on the lowest-flux observation used by citeParkerML2015 with a time bin of 10 ks to explore whether different variability patterns are imprinted as a function of the source overall flux level. The corresponding PCs are shown in Fig. A.12. Again the second and third PCs are dominated by noise due the relatively exposure time, but the first component appears to be clearly different from the case of the high flux observation. The variability is suppressed at low energies and rises at high energies compared with the PC shown in Fig. A.11 for the highest-flux observation. These changes can be simulated from the highest-flux simulation simply increasing the relative flux of the constant reflection component and adding a constant

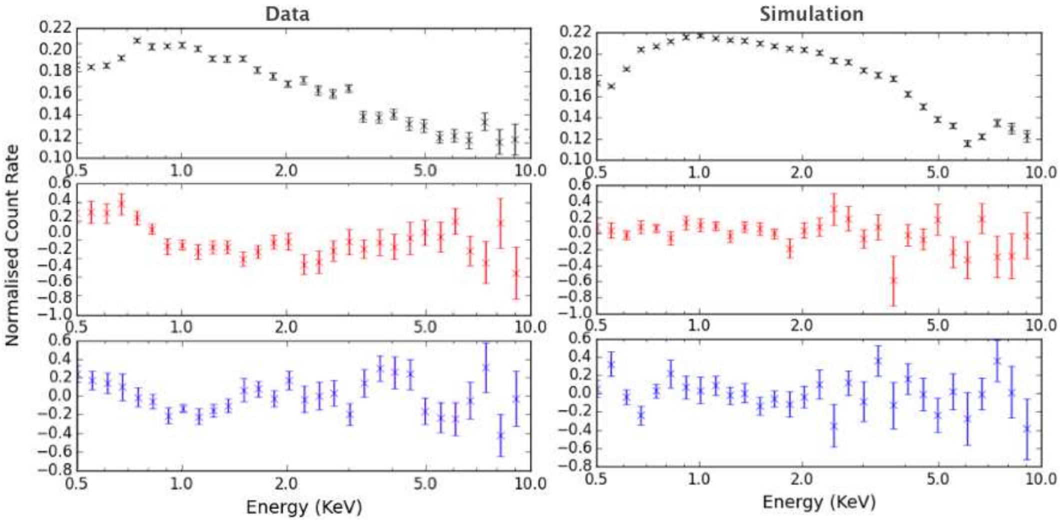

Figure A.11: Computed PCs for the highest-flux 40 ks observation analyzed by Parker et al. (2015). The second and third PCs are dominated by noise due the relatively exposure time (see text for details).

soft excess, modeled by a black body, which suppresses the variability at low energies. Besides, this constant soft excess is also found by Vaughan et al. (2011) calculating the rms spectrum of NGC 4051. This is likely an emission component from an extended emitting region whose flux is generally much lower than that of the continuum and that is only revealed as a constant component when the nuclear continuum flux level is extremely low, as it is the case during the considered observation. The relativistic reflection component is constant, but its relative flux increases with respect to that during the higher flux observation, in other words the spectrum is likely more reflection dominated during the low flux periods. Hence, with a 10ks time bin over a individual observation PCA reinforces the a previous conclusion derived through the rms spectrum.

A.8 Summary and outcomes of this chapter

Along this chapter, apart from confirming the PCs interpretation for NGC 4051 given by Parker et al. (2015) using a different available observation and a variety of different time-slices, we have corroborated the model proposed by Vaughan et al. (2011) for NGC 4051 using PCA.

Besides, we have explored the capabilities of the robust mathematical tool of PCA, which provide us with a model-independent way to assess spectral components in the AGN X-ray spectrum. The technique can be used to isolate contributions from different physical mechanism, although it should be noted that there is no need of the PCs to correspond to unique physical components, since there is no requirement for the true physical components to vary

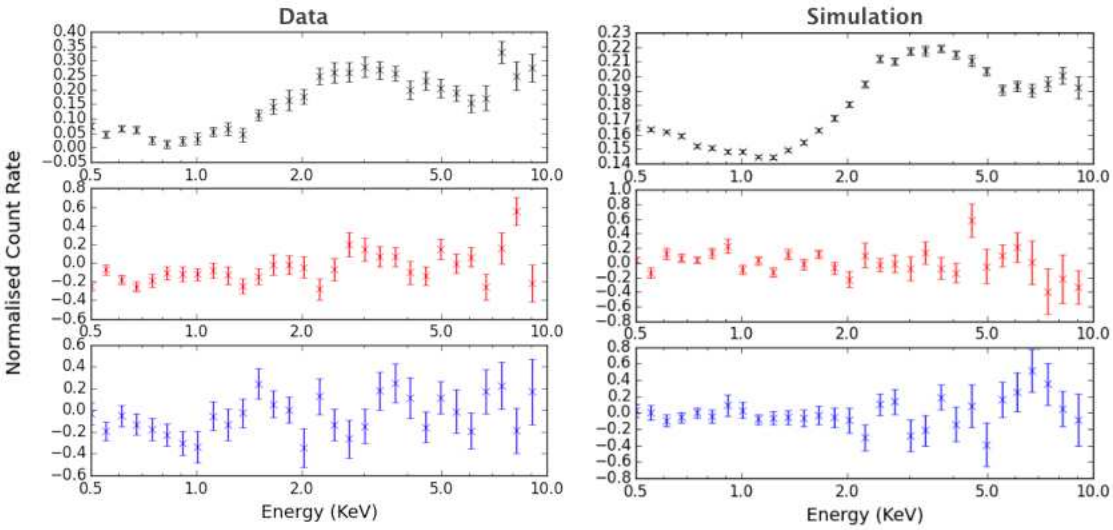

Figure A.12: Computed PCs for the lowest-flux 40 ks observation analyzed by Parker et al. (2015). The second and third PCs are dominated by noise due the relatively exposure time (see text for details).

independently. Thus, a same PC can be generated by more that one parameter or physical process varying. This is why numerical simulations are needed in order to interpret physically the results obtained through the PCA. Moreover, with the study carried out here we can conclude that PCA provides additional information about the spectral components at play if flux-selected observation are considered revealing which are more dominant in and at which flux level(s).

On the other hand, we have seen that, at least for NGC 4051, no difference in the PC are obtained by varying the timescale of interest in the range between 1 and 10 ks. This probably implies that the contribution of the different spectral components to the variability patterns is already established on timescales as short as 1 ks and that, in order to see the building up of the spectral variability in NGC 4051, one should consider shorter timescales, which will only be reachable with larger collecting area X-ray missions in the future.

Then, the main conclusions can be outlined as follows:

(1) We have not been able to probe different PCs at shorter timescales (< 10 ks) in a source as NGC 4051, expected to be variable at those timescales.

(2) We have corroborated the model suggested by Vaughan et al. (2011) using PCA

(3) We have found an unexplored capability of PCA: its dependence with flux, at least in the case of NGC 4051, which enables us to infer that a constant soft component (likely from an extended emitting region) emerges at low flux levels and that the overall X-ray spectrum is likely more dominated by the disc relativistic reflection component at low fluxes.

Our work with the PCA has just started and the results presented here should be considered as a first step of a longer term work in progress. We will continue to apply this technique to other sources exploring both different time-slices and different flux levels to reveal what are the physical mechanisms behind the often extraordinary variability of active nuclei in the X-rays. This type of anlaysis will be routinely used in our X-ray data analysis work in the future.

Bibliography

Agís-González, B., Miniutti, G., Kara, E., et al. 2014, MNRAS, 443, 2862

Alexander, D. M. & Hickox, R. C. 2012, New Astronomy Reviews, 56, 93

Alston, W. N., Vaughan, S., & Uttley, P. 2013a, MNRAS, 435, 1511

Alston, W. N., Vaughan, S., & Uttley, P. 2013b, MNRAS, 429, 75

Antonucci, R. 1993, A&A Annual Review, 31, 473

Antonucci, R. 2015, ArXiv e-prints

Antonucci, R. R. J. 1983, Nature, 303, 158

Antonucci, R. R. J. & Miller, J. S. 1985, ApJ, 297, 621

Appenzeller, I. 1967, PASP, 79, 136

Appenzeller, I., Fricke, K., Fürtig, W., et al. 1998, The Messenger, 94, 1

Aretxaga, I., Joguet, B., Kunth, D., Melnick, J., & Terlevich, R. J. 1999, ApJ Letters, 519, L123

Arévalo, P. & Uttley, P. 2006, MNRAS, 367, 801

Arévalo, P., Uttley, P., Lira, P., et al. 2009, MNRAS, 397, 2004

Arnaud, K. A., Branduardi-Raymont, G., Culhane, J. L., et al. 1985, MNRAS, 217, 105

Awaki, H., Kunieda, H., Tawara, Y., & Koyama, K. 1991, PASJ, 43, L37

Bagnulo, S., Boehnhardt, H., Muinonen, K., et al. 2006, A&A, 450, 1239

Bagnulo, S., Landolfi, M., Landstreet, J. D., et al. 2009, PASP, 121, 993

Balbus, S. A. & Hawley, J. F. 1998, Reviews of Modern Physics, 70, 1

Barcons, X., Barret, D., Decourchelle, A., et al. 2012, ArXiv e-prints

Barthelmy, S. D. & Swift/BAT Instrument Team. 2004, in Bulletin of the American Astronomical Society, Vol. 36, American Astronomical Society Meeting Abstracts, 1611

Barvainis, R. 1987, ApJ, 320, 537

Beckmann, V. & Shrader, C. 2013, in Proceedings of "An INTEGRAL view of the high-energy sky (the first 10 years)"

Beckmann, V. & Shrader, C. R. 2012, Active Galactic Nuclei (Wiley-VHC)

Bennert, N., Falcke, H., Shchekinov, Y., & Wilson, A. S. 2004, in IAU Symposium, Vol. 222, The Interplay Among Black Holes, Stars and ISM in Galactic Nuclei, ed. T. Storchi-Bergmann, L. C. Ho, & H. R. Schmitt, 307–308

Bennert, N., Jungwiert, B., Komossa, S., Haas, M., & Chini, R. 2006a, A&A, 459, 55

Bennert, N., Jungwiert, B., Komossa, S., Haas, M., & Chini, R. 2006b, A&A, 456, 953

Bennett, A. S. 1962, MmRAS, 68, 163

Bentz, M. C., Walsh, J. L., Barth, A. J., et al. 2009, ApJ, 705, 199

Best, P. N., Kauffmann, G., Heckman, T. M., et al. 2005, MNRAS, 362, 25

Bianchi, S., Corral, A., Panessa, F., et al. 2008, MNRAS, 385, 195

Bianchi, S., Maiolino, R., & Risaliti, G. 2012, Advances in Astronomy, 2012, 782030

Bianchi, S., Miniutti, G., Fabian, A. C., & Iwasawa, K. 2005, MNRAS, 360, 380

Bianchi, S., Piconcelli, E., Chiaberge, M., et al. 2009, ApJ, 695, 781

Blandford, R. D. & McKee, C. F. 1982, ApJ, 255, 419

Blustin, A. J., Page, M. J., Fuerst, S. V., Branduardi-Raymont, G., & Ashton, C. E. 2005, A&A, 431, 111

Brenneman, L. W. & Reynolds, C. S. 2006, ApJ, 652, 1028

Brindle, C., Hough, J. H., Bailey, J. A., et al. 1990, MNRAS, 244, 577

Burrows, D. N., Hill, J. E., Nousek, J. A., et al. 2005, Space Science Reviews, 120, 165

Cackett, E. M., Fabian, A. C., Zogbhi, A., et al. 2013, ApJ Letters, 764, L9

Cackett, E. M., Horne, K., & Winkler, H. 2007, MNRAS, 380, 669

Campbell, L. A., Lucey, J. R., Colless, M., et al. 2014, MNRAS, 443, 1231

Capetti, A., Macchetto, F., Axon, D. J., Sparks, W. B., & Boksenberg, A. 1995, ApJ Letters, 452, L87

Cappi, M., Panessa, F., Bassani, L., et al. 2006, A&A, 446, 459

Cardelli, J. A., Clayton, G. C., & Mathis, J. S. 1989, ApJ, 345, 245

Chartas, G., Kochanek, C. S., Dai, X., Poindexter, S., & Garmire, G. 2009, ApJ, 693, 174

Cikota, A., Patat, F., Cikota, S., & Faran, T. 2016, MNRAS

Cohen, R. D., Puetter, R. C., Rudy, R. J., Ake, T. B., & Foltz, C. B. 1986, ApJ, 311, 135

Collier, S., Horne, K., Wanders, I., & Peterson, B. M. 1999, MNRAS, 302, L24

Collin-Souffrin, S., Alloin, D., & Andrillat, Y. 1973, A&A, 22, 343

Crummy, J., Fabian, A. C., Gallo, L., & Ross, R. R. 2006, MNRAS, 365, 1067

Dai, X., Kochanek, C. S., Chartas, G., et al. 2010, ApJ, 709, 278

De Marco, B., Ponti, G., Cappi, M., et al. 2013, MNRAS, 431, 2441

de Marco, B., Ponti, G., Uttley, P., et al. 2011, MNRAS, 417, L98

del Toro Iniesta, J. C. 2004, Introduction to Spectropolarimetry (Cambridge University Press)

den Herder, J. W., Brinkman, A. C., Kahn, S. M., et al. 2001, A&A, 365, L7

Denney, K. D., De Rosa, G., Croxall, K., et al. 2014, ApJ, 796, 134

Dewangan, G. C., Griffiths, R. E., Dasgupta, S., & Rao, A. R. 2007, ApJ, 671, 1284

Dewey, D. 2003, Chandra News, 10, 11

Done, C., Gierliński, M., Sobolewska, M., & Schurch, N. 2007, in Astronomical Society of the Pacific Conference Series, Vol. 373, The Central Engine of Active Galactic Nuclei, ed. L. C. Ho & J.-W. Wang, 121

Drake, J. 2002, Chandra News, 9, 14

Edge, D. O., Shakeshaft, J. R., McAdam, W. B., Baldwin, J. E., & Archer, S. 1959, MmRAS, 68, 37

Elitzur, M. 2012, ApJ Letters, 747, L33

Elitzur, M. & Ho, L. C. 2009, ApJ Letters, 701, L91

Elitzur, M., Ho, L. C., & Trump, J. R. 2014, MNRAS, 438, 3340

Elitzur, M. & Shlosman, I. 2006, ApJ Letters, 648, L101

Elvis, M., Risaliti, G., Nicastro, F., et al. 2004, ApJ Letters, 615, L25

Emmanoulopoulos, D., McHardy, I. M., & Papadakis, I. E. 2011, MNRAS, 416, L94

Fabian, A. C. 1999, Proceedings of the National Academy of Science, 96, 4749

Fabian, A. C., Iwasawa, K., Reynolds, C. S., & Young, A. J. 2000, PASP, 112, 1145

Fabian, A. C., Kara, E., Walton, D. J., et al. 2013, MNRAS, 429, 2917

Fabian, A. C. & Miniutti, G. 2005, ArXiv Astrophysics e-prints

Fabian, A. C., Rees, M. J., Stella, L., & White, N. E. 1989, MNRAS, 238, 729

Fabian, A. C., Zoghbi, A., Ross, R. R., et al. 2009, Nature, 459, 540

Fath, E. A. 1909, Lick Observatory Bulletin, 5, 71

Ferrarese, L. & Merritt, D. 2000, ApJ Letters, 539, L9

Fossati, L., Bagnulo, S., Mason, E., & Landi Degl'Innocenti, E. 2007, in Astronomical Society of the Pacific Conference Series, Vol. 364, The Future of Photometric, Spectrophotometric and Polarimetric Standardization, ed. C. Sterken, 503

Fraquelli, H. A., Storchi-Bergmann, T., & Binette, L. 2000, ApJ, 532, 867

Garcia-Rissmann, A., Vega, L. R., Asari, N. V., et al. 2005, MNRAS, 359, 765

Garmire, G. P., Bautz, M. W., Ford, P. G., Nousek, J. A., & Ricker, Jr., G. R. 2003, in X-Ray and Gamma-Ray Telescopes and Instruments for Astronomy., ed. J. E. Truemper & H. D. Tananbaum, Vol. 4851, 28–44

Gaskell, C. M. 2015, ArXiv e-prints

George, I. M. & Fabian, A. C. 1991, MNRAS, 249, 352

Giacconi, R., Branduardi, G., Briel, U., et al. 1979, ApJ, 230, 540

Giacconi, R., Gursky, H., Paolini, F. R., & Rossi, B. B. 1962, Physical Review Letters, 9, 439

Giacconi, R., Kellogg, E., Gorenstein, P., Gursky, H., & Tananbaum, H. 1971, ApJ Letters, 165, L27

Gilli, R., Comastri, A., & Hasinger, G. 2007, A&A, 463, 79

González Delgado, R. M., Heckman, T., Leitherer, C., et al. 1998, ApJ, 505, 174

González-Martín, O., Masegosa, J., Márquez, I., et al. 2015, A&A, 578, A74

Goodrich, R. W. 1989, ApJ, 340, 190

Goodrich, R. W. & Miller, J. S. 1994, ApJ, 434, 82

Greene, J. E. & Ho, L. C. 2004, ApJ, 610, 722

Greene, J. E., Ho, L. C., & Barth, A. J. 2008, ApJ, 688, 159

Greene, J. E., Peng, C. Y., Kim, M., et al. 2010, ApJ, 721, 26

Greenstein, J. L. & Schmidt, M. 1964, ApJ, 140, 1

Guainazzi, M., Perola, G. C., Matt, G., et al. 1999, A&A, 346, 407

Guilbert, P. W. & Rees, M. J. 1988, MNRAS, 233, 475

Güver, T. & Özel, F. 2009, MNRAS, 400, 2050

Haardt, F. & Maraschi, L. 1991, ApJ Letters, 380, L51

Halpern, J. P. 1984, ApJ, 281, 90

Harrison, F. A., Craig, W. W., Christensen, F. E., et al. 2013, ApJ, 770, 103

Hawkins, M. R. S. 2004, A&A, 424, 519

Heard, C. Z. P. & Gaskell, C. M. 2016, MNRAS, 461, 4227

Heckman, T., Krolik, J., Meurer, G., et al. 1995, ApJ, 452, 549

Heisler, C. A., Lumsden, S. L., & Bailey, J. A. 1997, Nature, 385, 700

Hill, J., Burrows, D., Nousek, J., et al. 2004, in APS Meeting Abstracts

Ho, L. C. 2008, A&A Annual Review, 46, 475

Ho, L. C., Filippenko, A. V., & Sargent, W. L. W. 1993, ApJ, 417, 63

Ho, L. C., Filippenko, A. V., & Sargent, W. L. W. 1997, ApJ Supplements, 112, 315

Hoffman, J. L., Chornock, R., Leonard, D. C., & Filippenko, A. V. 2005, MNRAS, 363, 1241

Hough, J. H. 2005, in Astronomical Society of the Pacific Conference Series, Vol. 343, Astronomical Polarimetry: Current Status and Future Directions, ed. A. Adamson, C. Aspin, C. Davis, & T. Fujiyoshi, 3

Hubble, E. 1923, Popular Astronomy, 31, 644

Hunt, L. K., Malkan, M. A., Rush, B., et al. 1999, ApJ Supplements, 125, 349

Iwasawa, K., Fabian, A. C., Mushotzky, R. F., et al. 1996, MNRAS, 279, 837

Jansen, F., Lumb, D., Altieri, B., et al. 2001, A&A, 365, L1

Jones, D. H., Read, M. A., Saunders, W., et al. 2009, MNRAS, 399, 683

Jones, D. H., Saunders, W., Colless, M., et al. 2004, MNRAS, 355, 747

Kalberla, P. M. W., Burton, W. B., Hartmann, D., et al. 2005, A&A, 440, 775

Kara, E., Fabian, A. C., Cackett, E. M., Miniutti, G., & Uttley, P. 2013a, MNRAS, 430, 1408

Kara, E., Fabian, A. C., Cackett, E. M., et al. 2013b, MNRAS, 428, 2795

Kara, E., Fabian, A. C., Cackett, E. M., et al. 2013c, MNRAS, 434, 1129

Kaspi, S., Maoz, D., Netzer, H., et al. 2005, ApJ, 629, 61

Kaspi, S., Smith, P. S., Netzer, H., et al. 2000, ApJ, 533, 631

Kawaharada, M., Hong, S., Murashima, M. M., et al. 2004, in High-Energy Detectors in Astronomy, ed. A. D. Holland, Vol. 5501, 286–295

Kellermann, K. I., Sramek, R., Schmidt, M., Shaffer, D. B., & Green, R. 1989, AJ, 98, 1195

Khachikian, E. Y. & Weedman, D. W. 1974, ApJ Letters, 189, L99

Kitchin, C. R. 1991, Space Science Reviews, 55, 497

Koay, J. Y., Vestergaard, M., Casasola, V., Lawther, D., & Peterson, B. M. 2016, MNRAS, 455, 2745

Koljonen, K. I. I. 2015, MNRAS, 447, 2981

Koljonen, K. I. I., Hannikainen, D. C., McCollough, M. L., et al. 2013a, in IAU Symposium, Vol. 290, Feeding Compact Objects: Accretion on All Scales, ed. C. M. Zhang, T. Belloni, M. Méndez, & S. N. Zhang, 237–238

Koljonen, K. I. I., McCollough, M. L., Hannikainen, D. C., & Droulans, R. 2013b, MNRAS, 429, 1173

Kollatschny, W. & Fricke, K. J. 1985, A&A, 146, L11

Kormendy, J. 1988, ApJ, 325, 128

Krolik, J. H. 2001, ApJ, 551, 72

Krolik, J. H., Horne, K., Kallman, T. R., et al. 1991, ApJ, 371, 541

Krolik, J. H. & Kallman, T. R. 1987, ApJ Letters, 320, L5

Krongold, Y., Nicastro, F., Elvis, M., et al. 2007, ApJ, 659, 1022

Kwan, J. & Krolik, J. H. 1981, ApJ, 250, 478

LaMassa, S. M., Cales, S., Moran, E. C., et al. 2015, ApJ, 800, 144

Lamer, G., Uttley, P., & McHardy, I. M. 2003, MNRAS, 342, L41

Lamy, H. & Hutsemékers, D. 1999, The Messenger, 96, 25

Landi Degl'Innocenti, E., Bagnulo, S., & Fossati, L. 2007, in Astronomical Society of the Pacific Conference Series, Vol. 364, The Future of Photometric, Spectrophotometric and Polarimetric Standardization, ed. C. Sterken, 495

Laor, A. 1991, ApJ, 376, 90

Lawrence, A. 1991, Starlink Bulletin, 8, 25

Legg, E., Miller, L., Turner, T. J., et al. 2012, ApJ, 760, 73

Leighly, K. M., Cooper, E., Grupe, D., Terndrup, D. M., & Komossa, S. 2015, ApJ Letters, 809, L13

Lira, P., Arévalo, P., Uttley, P., McHardy, I., & Breedt, E. 2010, in IAU Symposium, Vol. 267, Co-Evolution of Central Black Holes and Galaxies, ed. B. M. Peterson, R. S. Somerville, & T. Storchi-Bergmann, 90–95

Lira, P., Arévalo, P., Uttley, P., McHardy, I., & Breedt, E. 2011, MNRAS, 415, 1290

Lumsden, S. L. & Alexander, D. M. 2001, MNRAS, 328, L32

Lynden-Bell, D. 1969, Nature, 223, 690

Madejski, G. M., Zdziarski, A. A., Turner, T. J., et al. 1995, ApJ, 438, 672

Maiolino, R. & Rieke, G. H. 1995, ApJ, 454, 95

Maiolino, R., Risaliti, G., Salvati, M., et al. 2010, A&A, 517, A47

Malizia, A., Landi, R., Bassani, L., et al. 2007, ApJ, 668, 81

Malkan, M. A. & Sargent, W. L. W. 1982, ApJ, 254, 22

Malzac, J., Petrucci, P. O., Jourdain, E., et al. 2006, A&A, 448, 1125

Marinucci, A., Risaliti, G., Wang, J., et al. 2013, MNRAS, 429, 2581

Markowitz, A. G., Krumpe, M., & Nikutta, R. 2014, MNRAS, 439, 1403

Martel, A. R. 1996, PhD thesis, , Univ. California at Santa Cruz, (1996)

Martin-Carrillo, A., Kirsch, M. G. F., Caballero, I., et al. 2012, A&A, 545, A126

Martocchia, A., Karas, V., & Matt, G. 2000, MNRAS, 312, 817

Mason, K. O., Breeveld, A., Much, R., et al. 2001, A&A, 365, L36

Matsumoto, H., Koyama, K., Tsuru, T. G., et al. 2005, Nuclear Instruments and Methods in Physics Research A, 541, 357

Matt, G., Fabian, A. C., & Ross, R. R. 1993, MNRAS, 264, 839

Matt, G., Fiore, F., Perola, G. C., et al. 1996, MNRAS, 281, L69

Matt, G., Guainazzi, M., & Maiolino, R. 2003, MNRAS, 342, 422

Matt, G., Perola, G. C., & Piro, L. 1991, A&A, 247, 25

Matthews, T. A. & Sandage, A. R. 1963, ApJ, 138, 30

McElroy, R. E., Husemann, B., Croom, S. M., et al. 2016, A&A, 593, L8

McHardy, I. M., Connolly, S. D., Peterson, B. M., et al. 2016, Astronomische Nachrichten, 337, 500

Merritt, D. & Ferrarese, L. 2001, ApJ, 547, 140

Miller, J. S. & Antonucci, R. R. J. 1983, ApJ Letters, 271, L7

Miller, J. S. & Goodrich, R. W. 1990, ApJ, 355, 456

Miller, J. S., Goodrich, R. W., & Mathews, W. G. 1991, ApJ, 378, 47

Miller, L., Turner, T. J., Reeves, J. N., & Braito, V. 2010, MNRAS, 408, 1928

Miller, L., Turner, T. J., Reeves, J. N., et al. 2007, A&A, 463, 131

Miniutti, G. & Fabian, A. C. 2006, MNRAS, 366, 115

Miniutti, G., Fabian, A. C., & Miller, J. M. 2004, MNRAS, 351, 466

Miniutti, G., Sanfrutos, M., Beuchert, T., et al. 2014, MNRAS, 437, 1776

Miniutti, G., Saxton, R. D., Rodríguez-Pascual, P. M., et al. 2013, MNRAS, 433, 1764

Mitsuda, K., Bautz, M., Inoue, H., et al. 2007, PASJ, 59, 1

Mittaz, J. P. D., Penston, M. V., & Snijders, M. A. J. 1990, MNRAS, 242, 370

Miyoshi, M., Moran, J., Herrnstein, J., et al. 1995, Nature, 373, 127

Momjian, E., Carilli, C. L., Walter, F., & Venemans, B. 2014, AJ, 147, 6

Moran, E. C., Kay, L. E., Davis, M., Filippenko, A. V., & Barth, A. J. 2001, ApJ Letters, 556, L75

Morgan, C. W., Hainline, L. J., Chen, B., et al. 2012, ApJ, 756, 52

Morgan, C. W., Kochanek, C. S., Dai, X., Morgan, N. D., & Falco, E. E. 2008, ApJ, 689, 755

Mosquera, A. M., Kochanek, C. S., Chen, B., et al. 2013, ApJ, 769, 53

Mulchaey, J. S., Wilson, A. S., & Tsvetanov, Z. 1996a, ApJ Supplements, 102, 309

Mulchaey, J. S., Wilson, A. S., & Tsvetanov, Z. 1996b, ApJ, 467, 197

Murray, S. S. & HRC Team. 1999, in Bulletin of the American Astronomical Society, Vol. 31, American Astronomical Society Meeting Abstracts, 1515

Mushotzky, R. F., Done, C., & Pounds, K. A. 1993, A&A Annual Review, 31, 717

Nandra, K. 2001, Advances in Space Research, 28, 295

Nandra, K. 2006, MNRAS, 368, L62

Nandra, K. & Pounds, K. A. 1994, MNRAS, 268, 405

Nandra, K., Pounds, K. A., & Stewart, G. C. 1990, MNRAS, 242, 660

Narayan, R. & Yi, I. 1994, ApJ Letters, 428, L13

Nayakshin, S. & Melia, F. 1997, ApJ Letters, 490, L13

Nenkova, M., Sirocky, M. M., Ivezić, Ž., & Elitzur, M. 2008a, ApJ, 685, 147

Nenkova, M., Sirocky, M. M., Nikutta, R., Ivezić, Ž., & Elitzur, M. 2008b, ApJ, 685, 160

Netzer, H. 2013, The Physics and Evolution of Active Galactic Nuclei (Cambridge University Press)

Netzer, H. 2015, A&A Annual Review, 53, 365

Netzer, H. & Laor, A. 1993, ApJ Letters, 404, L51

Nicastro, F. 2000, ApJ Letters, 530, L65

Nicastro, F., Piro, L., De Rosa, A., et al. 2000, ApJ, 536, 718

Nowak, M. A., Vaughan, B. A., Wilms, J., Dove, J. B., & Begelman, M. C. 1999, ApJ, 510, 874

Osterbrock, D. E. 1981, ApJ, 249, 462

Osterbrock, D. E. 1989, Astrophysics of gaseous nebulae and active galactic nuclei (University Science Books)

Packham, C., Young, S., Hough, J. H., Axon, D. J., & Bailey, J. A. 1997, MNRAS, 288, 375

Panessa, F., Carrera, F. J., Bianchi, S., et al. 2009, MNRAS, 398, 1951

Pappa, A., Georgantopoulos, I., Stewart, G. C., & Zezas, A. L. 2001, MNRAS, 326, 995

Parisi, P., Masetti, N., Jiménez-Bailón, E., et al. 2009, A&A, 507, 1345

Park, D., Kelly, B. C., Woo, J.-H., & Treu, T. 2012, ApJ Supplements, 203, 6

Parker, M. L., Fabian, A. C., Matt, G., et al. 2015, MNRAS, 447, 72

Parker, M. L., Komossa, S., Kollatschny, W., et al. 2016, MNRAS, 461, 1927

Parker, M. L., Marinucci, A., Brenneman, L., et al. 2014a, MNRAS, 437, 721

Parker, M. L., Walton, D. J., Fabian, A. C., & Risaliti, G. 2014b, MNRAS, 441, 1817

Patat, F. & Romaniello, M. 2006, PASP, 118, 146

Penston, M. V. & Perez, E. 1984, MNRAS, 211, 33P

Peterson, B. A. 1997, Cambridge University Press, 117, 314

Peterson, B. M. 1988, PASP, 100, 18

Peterson, B. M. 1993, PASP, 105, 247

Peterson, B. M. 2001, in Advanced Lectures on the Starburst-AGN, ed. I. Aretxaga, D. Kunth, & R. Mújica, 3

Piconcelli, E., Bianchi, S., Guainazzi, M., Fiore, F., & Chiaberge, M. 2007, A&A, 466, 855

Piconcelli, E., Jimenez-Bailón, E., Guainazzi, M., et al. 2005, A&A, 432, 15

Pier, E. A. & Krolik, J. H. 1992, ApJ, 401, 99

Piro, L., Yamauchi, M., & Matsuoka, M. 1990, ApJ Letters, 360, L35

Pogge, R. W. 1988, ApJ, 328, 519

Ponti, G., Miniutti, G., Cappi, M., et al. 2006, MNRAS, 368, 903

Porquet, D. & Dubau, J. 2000, A&A, Supplement, 143, 495

Poutanen, J. & Fabian, A. C. 1999, MNRAS, 306, L31

Press, W. H., Flannery, B. P., & Teukolsky, S. A. 1986, Numerical recipes. The art of scientific computing (Cambridge: University Press, 1986)

Puccetti, S., Fiore, F., Risaliti, G., et al. 2007, MNRAS, 377, 607

Quataert, E. 2004, in Astronomical Society of the Pacific Conference Series, Vol. 311, AGN Physics with the Sloan Digital Sky Survey, ed. G. T. Richards & P. B. Hall, 131

Ramos Almeida, C., Levenson, N. A., Alonso-Herrero, A., et al. 2011, ApJ, 731, 92

Reynolds, C. S. 1996, PhD thesis, University of Cambridge

Reynolds, C. S. 1997, MNRAS, 286, 513

Reynolds, C. S. 1999, in Astronomical Society of the Pacific Conference Series, Vol. 161, High Energy Processes in Accreting Black Holes, ed. J. Poutanen & R. Svensson, 178

Reynolds, C. S., Fabian, A. C., Makishima, K., Fukazawa, Y., & Tamura, T. 1994, MNRAS, 268, L55

Reynolds, C. S. & Nowak, M. A. 2003, Phys. Rep., 377, 389

Reynolds, C. S., Ward, M. J., Fabian, A. C., & Celotti, A. 1997, MNRAS, 291, 403

Ricci, C. 2011, PhD thesis, ISDC, University of Geneva

Risaliti, G. 2002, A&A, 386, 379

Risaliti, G., Elvis, M., Fabbiano, G., Baldi, A., & Zezas, A. 2005, ApJ Letters, 623, L93

Risaliti, G., Elvis, M., Fabbiano, G., et al. 2007, ApJ Letters, 659, L111

Risaliti, G., Elvis, M., & Nicastro, F. 2002, ApJ, 571, 234

Risaliti, G., Miniutti, G., Elvis, M., et al. 2009, ApJ, 696, 160

Risaliti, G., Nardini, E., Salvati, M., et al. 2011, MNRAS, 410, 1027

Rivers, E., Markowitz, A., & Rothschild, R. 2011, ApJ Letters, 742, L29

Roming, P. W. A., Hunsberger, S. D., Nousek, J. A., et al. 2004, in American Institute of Physics Conference Series, Vol. 727, Gamma-Ray Bursts: 30 Years of Discovery, ed. E. Fenimore & M. Galassi, 651–654

Ross, R. R. & Fabian, A. C. 2005, MNRAS, 358, 211

Runnoe, J. C., Cales, S., Ruan, J. J., et al. 2016, MNRAS, 455, 1691

Rybicki, G. B. & Lightman, A. P. 1979, Radiative processes in astrophysics (New York, Wiley-Interscience, 1979. 393 p.)

Salpeter, E. E. 1964, ApJ, 140, 796

Sandage, A. 1964, ApJ, 139, 416

Sanders, D. B., Phinney, E. S., Neugebauer, G., Soifer, B. T., & Matthews, K. 1989, ApJ, 347, 29

Sanfrutos, M., Miniutti, G., Agís-González, B., et al. 2013, MNRAS, 436, 1588

Sanfrutos, M., Miniutti, G., Krongold, Y., Agís-González, B., & Longinotti, A. L. 2016, MNRAS, 457, 510

Scarsi, L. 1997, in Data Analysis in Astronomy, ed. V. Di Gesu, M. J. B. Duff, A. Heck, M. C. Maccarone, L. Scarsi, & H. U. Zimmerman, 65–78

Schlafly, E. F. & Finkbeiner, D. P. 2011, ApJ, 737, 103

Schlegel, D. J., Finkbeiner, D. P., & Davis, M. 1998, ApJ, 500, 525

Schmid, H. M., Appenzeller, I., Camenzind, M., et al. 2001, A&A, 372, 59

Schmidt, M. 1963, Nature, 197, 1040

Schmidt, M. & Green, R. F. 1983, ApJ, 269, 352

Schulz, H. & Henkel, C. 2003, A&A, 400, 41

Schwarzschild, K. 1916, Abh. Konigl. Preuss. Akad. Wissenschaften Jahre 1906,92, Berlin,1907, 1916

Serkowski, K. 1958, Acta Astronomica, 8, 135

Serkowski, K., Mathewson, D. S., & Ford, V. L. 1975, ApJ, 196, 261

Seyfert, C. K. 1943, ApJ, 97, 28

Shapiro, S. L., Lightman, A. P., & Eardley, D. M. 1976, ApJ, 204, 187

Shappee, B. J., Prieto, J. L., Grupe, D., et al. 2014, ApJ, 788, 48

Shemmer, O., Netzer, H., Maiolino, R., et al. 2004, ApJ, 614, 547

Shi, Y., Rieke, G. H., Smith, P., et al. 2010, ApJ, 714, 115

Shields, G. A. 1978, Nature, 272, 706

Shu, X. W., Wang, J. X., Jiang, P., Fan, L. L., & Wang, T. G. 2007, ApJ, 657, 167

Siebenmorgen, R., Voshchinnikov, N. V., & Bagnulo, S. 2014, A&A, 561, A82

Simkin, S. M., Su, H. J., & Schwarz, M. P. 1980, ApJ, 237, 404

Simmons, J. F. L. & Stewart, B. G. 1985, A&A, 142, 100

Simpson, J. P., Colgan, S. W. J., Erickson, E. F., et al. 2002, ApJ, 574, 95

Singh, K. P., Garmire, G. P., & Nousek, J. 1985, ApJ, 297, 633

Singh, V., Ishwara-Chandra, C. H., Sievers, J., et al. 2015, MNRAS, 454, 1556

Smith, E. P., Heckman, T. M., Bothun, G. D., Romanishin, W., & Balick, B. 1986, ApJ, 306, 64

Smith, H. J. & Hoffleit, D. 1963, Nature, 198, 650

Smith, J. E., Robinson, A., Alexander, D. M., et al. 2004, MNRAS, 350, 140

Smith, J. E., Robinson, A., Young, S., Axon, D. J., & Corbett, E. A. 2005, MNRAS, 359, 846

Smith, J. E., Young, S., Robinson, A., et al. 2002, MNRAS, 335, 773

Stalevski, M., Fritz, J., Baes, M., Nakos, T., & Popović, L. Č. 2012, MNRAS, 420, 2756

Stokes, G. G. 1852, Trans. Cambridge Phil. Soc., 9

Storchi-Bergmann, T., Baldwin, J. A., & Wilson, A. S. 1993, ApJ Letters, 410, L11

Storchi-Bergmann, T., Fernandes, R. C., & Schmitt, H. R. 1998, ApJ, 501, 94

Storchi-Bergmann, T., Mulchaey, J. S., & Wilson, A. S. 1992, ApJ Letters, 395, L73

Strüder, L., Briel, U., Dennerl, K., et al. 2001, A&A, 365, L18

Suganuma, M., Yoshii, Y., Kobayashi, Y., et al. 2006, ApJ, 639, 46

Sulentic, J. W., Marziani, P., Zamanov, R., et al. 2002, ApJ Letters, 566, L71

Tanaka, Y., Inoue, H., & Holt, S. S. 1994, PASJ, 46, L37

Tanaka, Y., Nandra, K., Fabian, A. C., et al. 1995, Nature, 375, 659

Taylor, B. G., Andresen, R. D., Peacock, A., & Zobl, R. 1981, Space Science Reviews, 30, 479

Terashima, Y., Kamizasa, N., Awaki, H., Kubota, A., & Ueda, Y. 2012, ApJ, 752, 154

Tohline, J. E. & Osterbrock, D. E. 1976, ApJ Letters, 210, L117

Tran, H. D. 2001, ApJ Letters, 554, L19

Tran, H. D. 2003, ApJ, 583, 632

Tran, H. D., Osterbrock, D. E., & Martel, A. 1992, AJ, 104, 2072

Tremaine, S., Gebhardt, K., Bender, R., et al. 2002, ApJ, 574, 740

Truemper, J. 1982, Advances in Space Research, 2, 241

Trump, J. R., Impey, C. D., Kelly, B. C., et al. 2011, ApJ, 733, 60

Turner, M. J. L., Abbey, A., Arnaud, M., et al. 2001, A&A, 365, L27

Turner, T. J., George, I. M., Nandra, K., & Mushotzky, R. F. 1998, ApJ, 493, 91

Ulrich, M.-H., Maraschi, L., & Urry, C. M. 1997, A&A Annual Review, 35, 445

Urry, C. M. & Padovani, P. 1995, PASP, 107, 803

Uttley, P., Edelson, R., McHardy, I. M., Peterson, B. M., & Markowitz, A. 2003, ApJ Letters, 584, L53

Valencia-S., M., Zuther, J., Eckart, A., et al. 2012, A&A, 544, A129

Vasudevan, R. V., Mushotzky, R. F., Winter, L. M., & Fabian, A. C. 2009, MNRAS, 399, 1553

Vaughan, S. & Fabian, A. C. 2004, MNRAS, 348, 1415

Vaughan, S., Fabian, A. C., & Nandra, K. 2003, MNRAS, 339, 1237

Vaughan, S., Uttley, P., Pounds, K. A., Nandra, K., & Strohmayer, T. E. 2011, MNRAS, 413, 2489

Vrtilek, J. M. & Carleton, N. P. 1985, ApJ, 294, 106

Wandel, A., Peterson, B. M., & Malkan, M. A. 1999, ApJ, 526, 579

Wardle, J. F. C. & Kronberg, P. P. 1974, ApJ, 194, 249

Weaver, K. A., Krolik, J. H., & Pier, E. A. 1998, ApJ, 498, 213

Weisskopf, M. C., Aldcroft, T. L., Bautz, M., et al. 2003, Experimental Astronomy, 16, 1

Whittet, D. C. B. 1992, Science, 257, 1148

Wilkins, D. R. & Fabian, A. C. 2013, MNRAS, 430, 247

Wills, B. J., Wills, D., Evans, II, N. J., et al. 1992, ApJ, 400, 96

Wilson, A. S. & Colbert, E. J. M. 1995a, ApJ, 438, 62

Wilson, A. S. & Colbert, E. J. M. 1995b, ApJ, 438, 62

Winter, L. M., Mushotzky, R. F., Tueller, J., & Markwardt, C. 2008, ApJ, 674, 686

Woltjer, L. 1959, ApJ, 130, 38

Woo, J.-H., Treu, T., Barth, A. J., et al. 2010, ApJ, 716, 269

Woo, J.-H. & Urry, C. M. 2002, ApJ, 579, 530

Wu, Y.-Z., Zhang, E.-P., Liang, Y.-C., Zhang, C.-M., & Zhao, Y.-H. 2011, ApJ, 730, 121

Xiao, T., Barth, A. J., Greene, J. E., et al. 2011, ApJ, 739, 28

Yaqoob, T. & Padmanabhan, U. 2004, ApJ, 604, 63

Young, S. 2000, MNRAS, 312, 567

Young, S., Hough, J. H., Axon, D. J., Bailey, J. A., & Ward, M. J. 1995, MNRAS, 272, 513

Young, S., Hough, J. H., Axon, D. J., Ward, M. J., & Bailey, J. A. 1996, MNRAS, 280, 291

Zdziarski, A. A., Fabian, A. C., Nandra, K., et al. 1994, MNRAS, 269, L55

Zoghbi, A., Fabian, A. C., Reynolds, C. S., & Cackett, E. M. 2012, MNRAS, 422, 129

Zoghbi, A., Fabian, A. C., Uttley, P., et al. 2010, MNRAS, 401, 2419

Zoghbi, A., Reynolds, C., Cackett, E. M., et al. 2013, ApJ, 767, 121